TESIS DE LA UNIVERSIDAD
DE ZARAGOZA

2020

34

Lucía Candela Díaz Pérez

Positioning Control System for a Large Range 2D Platform with Submicrometre Accuracy for Metrological and Manufacturing Applications

Departamento
Ingeniería de Diseño y Fabricación

Director/es
Albajez García, José Antonio
Yagüe Fabra, José Antonio

ISSN 2254-7606

Prensas de la Universidad
Universidad Zaragoza

ISSN 2254-7606

Tesis Doctoral

POSITIONING CONTROL SYSTEM FOR A LARGE RANGE 2D PLATFORM WITH SUBMICROMETRE ACCURACY FOR METROLOGICAL AND MANUFACTURING APPLICATIONS

Autor

Lucía Candela Díaz Pérez

Director/es

Albajez García, José Antonio
Yagüe Fabra, José Antonio

UNIVERSIDAD DE ZARAGOZA
Ingeniería de Diseño y Fabricación

2019

Universidad Zaragoza

1542

TESIS DOCTORAL

Positioning Control System for a Large Range 2D Platform with Submicrometre Accuracy for Metrological and Manufacturing Applications

Lucía Candela Díaz Pérez

Zaragoza, 2019

Positioning Control System for a Large Range 2D Platform with Submicrometre Accuracy for Metrological and Manufacturing Applications

Lucía Candela Díaz Pérez

Dirigida por

Dr. José Antonio Yagüe Fabra

Dr. José Antonio Albajez García

Para la obtención del Título de Doctora
por la Universidad de Zaragoza

Zaragoza, Julio de 2019

This doctoral thesis is presented as a compendium of the following publications:

- **Sensors 2017**: “Geometrical characterisation of a 2D laser system and calibration of a cross-grid encoder by means of a self-calibration methodology”. Marta Torralba, Lucía C. Díaz-Pérez, Margarita Valenzuela, José A. Albajez, José A. Yagüe-Fabra. Sensors, 2017, 17, 1992.
- **Micromachines 2018**: “One dimensional control system for a linear motor of a two dimensional nanopositioning stage using a commercial control hardware”. Lucía C. Díaz-Pérez, Marta Torralba, José A. Albajez, José A. Yagüe-Fabra. Micromachines, 2018, 9, 421.
- **Electronics 2018**: “Vector control strategy for a Halbach linear motor implemented in a commercial control hardware”. Lucía C. Díaz-Pérez, José A. Albajez, Marta Torralba, José A. Yagüe-Fabra. Electronics, 2018, 7, 232.
- **Procedia Manufacturing 2019**: “Positioning uncertainty of the control system for the planar motion of a nanopositioning platform”. Lucía C. Díaz-Pérez, Marta Torralba, José A. Albajez, José A. Yagüe. Procedia Manufacturing, 2019, accepted.

The work developed in this thesis is part of the projects:

- DPI2010-21629-C02-01, Desarrollo y calibración de una etapa para nanoposicionado 2D de amplio rango, “NanoPla”, of the Ministry of Economy and Competitiveness of the Spanish Government.
- DPI2015-69403-C3-1-R, Caracterización Metrológica de Superficies Microestructuradas, “MetroSurf”, of the Ministry of Economy and Competitiveness of the Spanish Government.

In addition, the FPU (Formación de Profesorado Universitario) Program of the Ministry of Education, Culture and Sports of the Spanish Government sponsored the author.

Departamento de
Ingeniería de
Diseño y Fabricación
Universidad Zaragoza

D. **José Antonio Yagüe Fabra**, Doctor por la Universidad de Zaragoza y Profesor Titular del departamento de Ingeniería de Diseño y Fabricación de la Universidad de Zaragoza.

INFORMA:

Que la tesis titulada "**Positioning Control System for a Large Range 2D Platform with Submicrometre Accuracy for Metrological and Manufacturing Applications**", elaborada por Dña. **Lucía Candela Díaz Pérez**, ha sido realizada bajo mi dirección, se ajusta al proyecto de tesis inicialmente presentado y cumple los requisitos exigidos por la legislación vigente para optar al grado de Doctora por la Universidad de Zaragoza. Una vez finalizada, autorizo su presentación en la modalidad de compendio de publicaciones para ser evaluada por el tribunal correspondiente.

Zaragoza, a 12 de Julio,

Fdo. D. José Antonio Yagüe Fabra

Departamento de
Ingeniería de
Diseño y Fabricación
Universidad Zaragoza

D. **José Antonio Albajez García**, Doctor por la Universidad de Zaragoza y Profesor Titular del departamento de Ingeniería de Diseño y Fabricación de la Universidad de Zaragoza.

INFORMA:

Que la tesis titulada "**Positioning Control System for a Large Range 2D Platform with Submicrometre Accuracy for Metrological and Manufacturing Applications**", elaborada por Dña. **Lucía Candela Díaz Pérez**, ha sido realizada bajo mi dirección, se ajusta al proyecto de tesis inicialmente presentado y cumple los requisitos exigidos por la legislación vigente para optar al grado de Doctora por la Universidad de Zaragoza. Una vez finalizada, autorizo su presentación en la modalidad de compendio de publicaciones para ser evaluada por el tribunal correspondiente.

Zaragoza, a 12 de Julio,

Fdo. D. José Antonio Albajez García

AGRADECIMIENTOS / ACKNOWLEDGEMENTS

En primer lugar, mi más sincero agradecimiento a mis directores de tesis por su dedicación, tiempo, paciencia e inestimable ayuda, tanto personal como profesionalmente. Sin su persistente labor, esta tesis no habría sido posible. Muchísimas gracias también a Marta por su meticuloso trabajo previo, por proporcionarme todas las facilidades para retomar el proyecto y por su apoyo y consejos durante todo este tiempo.

También debo agradecer a todos mis compañeros del departamento de Ingeniería de Diseño y Fabricación por haberme tratado con tanto cariño, en especial a Ismael y Tomás por estar siempre disponibles y dispuestos a echar una mano.

I would like to acknowledge Professor Guido Tosello for giving me the opportunity to learn and work at the Department of Mechanical Engineering of the Technical University of Denmark and to Ali Davoudinejad for allowing me to participate in his project. I would also like to thank Danilo Quagliotti for sharing his time and knowledge with me, and to all the colleagues that work at the Section of Manufacturing Engineering for making me feel welcome.

In the same way, my sincere thanks to Professor Stuart Smith for accepting and hosting me at the Center for Precision Metrology at the University of North Caroline at Charlotte, learning from him has been a privilege. I would also like to thank Masoud Arablu and Kumar Arumugam for patiently teaching me all I needed to know to participate in the project and for being my colleagues and friends during my time there. I am also grateful to all the colleagues that work at the Center for Precision Metrology, who made me feel welcome.

Por último, pero no menos importante, deseo expresar mi agradecimiento a mi familia, en especial a mi madre y a mi padre que me han inculcado su pasión por aprender y enseñar. Mi agradecimiento más profundo es para Marek por darme su apoyo y motivación constante e incondicional en todos los proyectos que he decidido emprender.

Contents

List of Figures

List of Tables

List of Abbreviations

1D	One dimensional
2D	Two dimensional
3D	Three dimensional
ADC	Analogue to digital converter
AFM	Atomic force microscope
BLDC	Brushless DC motor
CAGD	Computer aided and geometrical design
CMP	Compare value
DAC	Digital to analogue converter
DAQ	Data acquisition
DC	Direct current
DMC	Digital motor control
DO	Digital output
DSP	Data signal processor
DTU	Technical University of Denmark
d-q	Direct and quadrature
HRA	High relative accuracy
HRPWM	High resolution pulse width modulation
MCU	Microcontroller unit
MEP	Micro edge positioning
NanoPla	Nanopositioning platform stage
NC	Numerical control
PC	Personal computer
PID	Proportional-integral-derivative

PVDD	Supply voltage of the three-phase inverter power stage
PWM	Pulse width modulation
RMS	Root mean square
SCI	Serial communication interface
SYSCLKOUT	System clock
TBCLK	Time-base clock
TBPRD	Time-base period
TI	Texas Instruments
UNCC	University of North Carolina at Charlotte
VCM	Voice coil motor

1. Introduction

Nanotechnology has been defined by the National Nanotechnology Initiative, as the manipulation of matter with at least one dimension sized from 1 to 100 nanometres. It is a growing field that, in the recent decades, has impacted the world of Science and Technology [1]. Nanotechnology applications such as nanomanufacturing or nanometrology require positioning systems capable of operating at a submicrometre scale, where they act as supplementary stages for measuring or manipulating samples [2, 3, 4, 5]. The performance of these processes depends directly on the accuracy of the positioning systems and their working ranges [6].

Several positioning systems capable of obtaining effective and accurate positioning are currently available [7]. Nonetheless, their application is limited to a short positioning range [8, 9]. The accurate positioning control in a large 2D plane is one of the main necessities of applications such as scanned probe microscopes, lithography and surface profilometers [10], in a variety of industries such as electronics, aerospace, power generation and astronomy [11, 12, 13] in which nanostructures and features form objects with dimensions in the centimetre range . For this reason, the demand of accurate, repeatable and long travel range positioning systems is rapidly increasing [14, 15].

In this line of research, a Nanopositioning platform stage (NanoPla) was designed in two previous theses [16, 17], and its first prototype was built at the Department of Design and Manufacturing Engineering at the University of Zaragoza. The NanoPla is expected to achieve positioning submicrometre accuracy along a large working range of 50 mm × 50 mm. It is designed to work together with different kinds of tools and probes in various applications such as metrology or nanomanufacturing. In this thesis, the NanoPla positioning control system is developed and implemented. The development process of the 2D positioning control system can be divided into the following phases:

- Dynamic characterisation of the control system actuators.
- Development of a 1D positioning control system for one actuator and implementation in the selected control hardware.
- Analysis and optimisation of the performance of the NanoPla 2D positioning sensor.
- Development and implementation of a 2D positioning control system for the NanoPla.
- Analysis and verification of the performance of the 2D positioning control system.

In the introduction of this thesis, firstly, the state of the art of accurate long travel range positioning system components is reviewed. Then, the motivation of the thesis is justified.

1.1. State of the art

Positioning systems main components are actuators, control hardware and positioning sensors. The selection of these components conditions the control system of nanopositioning stages and it is based on the positioning stage required precision, operating range and structure of the stage. The advantages and disadvantages of each of them must be analysed to select the most suitable for each application. In addition, the implementation of the components in the positioning control system can be optimised to leverage the capabilities of each of them in order to obtain the maximum positioning accuracy.

This section analyses the advantages and disadvantages of positioning system components and their applicability in large range accurate positioning. In this work, a positioning stage is considered to work in a large range when its travel range is between 10 mm and 100 mm, and it is considered to be accurate when its resolution is at a submicrometre scale.

The following subsections are divided as follows:

- Actuators in large range accurate positioning systems. Nanopositioning actuators are listed and compared. Special emphasis is made in Halbach linear motors, which allow implementing planar motion for accurate positioning in large travel ranges.

- Control of Halbach linear motors. The control requirements and solutions for Halbach linear motors are presented and analysed.

- Positioning sensors in large range accurate positioning systems. Positioning sensors, their applicability and accuracy are analysed. Plane mirror laser interferometer systems are presented as the best option for achieving accuracy and traceability in a 2D long range. Accuracy and calibration procedures for laser systems are also assessed.

1.1.1. Actuators in large range accurate positioning systems

The selection of the actuators of a nanopositioning stage is a crucial part that affects the whole stage design, from the architecture to the control strategy. The length of the travel range and the required accuracy must be the main selection criteria in nanopositioning applications.

Piezo actuators and electromagnetic motors are able to generate linear motion in accurate applications. On the one hand, piezo actuators, are capable of providing position resolutions of less than one nanometre, can achieve extremely high accelerations, are frictionless and backlash-free [18]. They are currently used in many nanopositioning stages based on flexure mechanisms [19, 20, 21]. Even though their travel range is small, a lever displacement amplifier can be employed to amplify its working range [22]. Nevertheless, the maximum stroke is usually limited to one millimetre [23, 24]. Thus, they are not adequate to carry out large travels [25, 26]. For this reason, they can be used as auxiliary fine nanopositioning units to improve the performance of the large travel positioning stage, in a two-stage scheme [27].

On the other hand, electromagnetic actuators can convert electrical energy into mechanical energy without friction [28]. In addition, the generated force is adjustable without affecting the displacement output by acting on the phase currents, a property that can be leveraged by the control system. Nevertheless, only some of the generally used electromagnetic motors are suitable for accurate applications. Some stepper motors can achieve a 1 µm accuracy over a 25 mm travel range. However, they generate a significant amount of unwanted heat and do not provide smooth continuous motion [29]. Brushless DC (BLDC) motors are also frictionless solutions that combine a coil and a permanent magnet. The interaction between the DC current flowing through the coils and the magnetic field generated by the permanent magnets, results in a thrust force that generates a relative motion, according to the motor law. However, traditional brushless DC rotary motors present many disadvantages in accurate positioning systems because they need additional mechanical systems as ball screws to convert rotary motion in linear motion. The mechanical tolerance of these transmission systems introduce backlash and setting errors [30]. In addition, rotary motors typically use mechanical contact bearings, which are not frictionless [31] and difficult the control task [32]**.** Nevertheless, they are often used as actuators for low-precision coarse motions in a two-stage scheme [33]. For precision positioning, linear drives are preferred because they do not use drive screws or gearheads and are backlash-free. Furthermore, they can also be frictionless [28] when combined with air bearings [34, 35]; magnetic levitation [36] or flexure bearings, which makes them capable of achieving high-precision positioning [37]**.** In [38], a flexure-based electromagnetic actuator able to achieve a stroke range of 2 mm with a positioning accuracy of ±10 nm was presented. The absence of friction between moving parts presents numerous advantages, such as, absence of mechanical wear and less number of elements. Thus, the resulting positioning accuracy of the overall system is only affected by the accuracy of the control system and the guides. For this reason, electromagnetic linear actuators are employed in large range high-precision nanopositioning.

Voice coil motors (VCM) are frictionless electromagnetic linear actuators characterised by their good dynamics and relatively low holding force. The VCM consists of a tubular coil immerse in the radially oriented magnetic field of a permanent magnet. When the current flows through the coil, the interaction with the magnetic field results in a linear force generated according to the Lorentz force law. VCM are capable of achieving fast responses and high precision positioning without cogging or hysteresis. They have been applied in flexure linear and parallel XY stages [39, 40, 41]. Nevertheless, their motion range is limited and they produce small output forces. To increase the stroke, the diameter and length of the motor must also increase and this results in a poor performance. The nanopositioning system described in [26] integrates these actuators. It has been developed for heavy payloads and its XY-drive system is a stacked configuration of VCMs and linear guides. A flexure structure of four degrees of freedom micro-range stage ($ZR_xR_yR_z$) is assembled over the platform for fine positioning. It has a working range of 20 mm × 20 mm, with a positioning error of 23 µm in X-axis and 22 µm in Y-axis.

In contrast to VCM, in linear brushless DC (BLDC) motors, non-contact parts are flat and parallel surfaces and they are capable of producing high forces and high speeds keeping a compact design. The positioning control of these motors is performed by commutating the phase currents, which results in low stiffness and vibrations. The different types of linear brushless DC motors can be classified according to their guiding requirements. In commercially available linear motors, the linear displacement is guided by the architecture of the magnet track or the motor design, which can be flat, U-shaped or tubular [42]. However, the guiding system impedes the displacement of the motor along the orthogonal direction of its driving axes, thus, the implementation of planar motion becomes unfeasible. Therefore, they can only be mounted in stacked nanopositioning stages, characterised by comprising one axis of displacement over the other one. A macro-positioning system that implements stacked configuration using U-shaped motors was presented by [43]. The coarse motion performed by the stacked stage is complemented by the fine motion of an ultra-precision piezo positioning system, achieving an accuracy better than 3 µm in a working range of 300 mm × 300 mm.

Nevertheless, stacked linear axes result in longer kinematic chains with an unfavourable transfer behaviour [44, 33]. Thus, planar motion is the best solution to obtain an accurate performance [45]. In a planar configuration, the movement of the X and Y-axes takes place in the same plane, minimising geometrical errors and improving the dynamics of the system [46]. A linear motor must be capable of attaining displacement not only along its drive axis, but also along the orthogonal direction in order to allow planar motion. Therefore, only unguided linear motors can be implemented in a planar stage. Halbach linear motors designed by Trumper et al. [47] are considered to be a solution. In Figure 1.1, a Halbach linear motor has been represented. As it can be seen, it consists of a Halbach magnet array and the stator, where the coil windings are wrapped around a core.

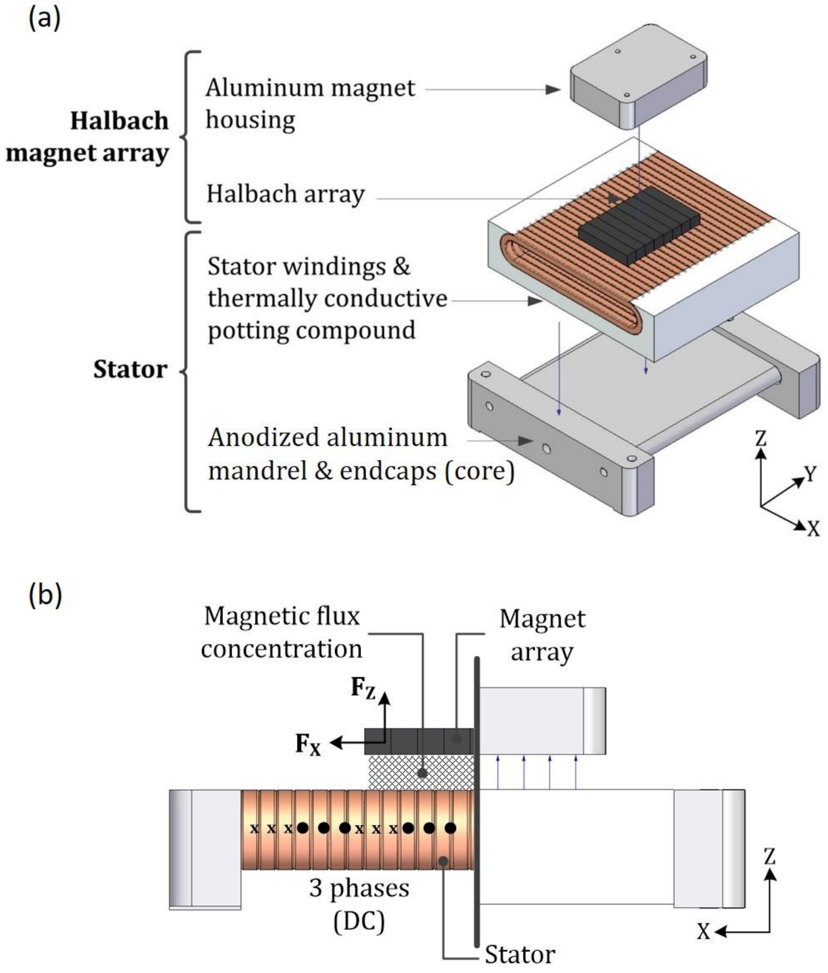

Figure 1.1*. Exploded (**a**) and lateral (**b**) view of a Halbach linear motor [17].*

Halbach linear motors are a type of permanent magnet synchronous motors (PMSM). Their main advantage is that they are unguided and allow the displacement along the orthogonal direction, only limited by size of the effective winding area. Therefore, planar motion is possible in all the positions that permit the interaction between the coil and the permanent magnet array. Apart from enabling planar motion without contact between parts, another advantage of Halbach linear motors is that, additionally to the thrust force, they generate a vertical force, perpendicular to the stator plane, that favours the levitation of the magnet array [48], as shown in Figure 1.1b. The resultant generated vertical and horizontal forces are dependent on the phase currents and the relative position between stator and magnet array, as defined by the motor law. Currently, unguided Halbach linear motors are not commercialised and, thus, they are custom-made for each application. The Multi-scale Alignment and Positioning System (MAPS) developed at the University of North Caroline at Charlotte (UNCC) [49, 50], implements these type of linear actuators in a planar configuration. This ultra-precision stage has a working range of 10 mm × 10 mm and an accuracy lower than 2 nm. Similarly, the 6D planar magnetic levitation system PIMag6D [51] is actuated and fully levitated by three coil pairs mounted at the stator which interact with three Halbach arrays in the moving platform, achieving a positioning stability of ±10 nm in X and Y-axes in a range of 100 mm × 100 mm. Similar motors are used in [52] for 2D positioning in a ϕ 100 mm travel range, nevertheless, in that work, levitation is performed by three vacuum preloaded airbearings.

Table 1.1. Summary of actuators options for large range accurate positioning systems

Actuator	Pros	Limitations	Uses
Piezo actuators	- Linear motion - Nanometre resolution - Frictionless and backlash-free	- Small travel range (<1 mm)	- Auxiliary fine nanopositioning units in a two-stage scheme
Rotary BLDC motors	- Frictionless	- Need of additional mechanical systems as ball screws	- Low-precision coarse motors in a two-stage scheme
VCM	- Linear motion - Frictionless	- Small output forces - Limited travel range (typically < 20 mm)	- Actuators in flexure stages
Linear BLDC motors	- Linear motion - Frictionless	- Guided displacement that impedes planar motion	- Stacked-axis nanopositioning stages
Halbach linear motors	- Linear motion - Frictionless - Favours levitation - Unguided (allow planar motion)	- Not commercialised	- Nanopositioning stages with planar configuration - Magnetic levitation

Table 1.1 shows a summary of the actuators that have been reviewed in this subsection and the advantages and disadvantages of their use in large range accurate positioning stages. Piezo actuators are able to provide linear motion with nanometre resolution. Nevertheless, due to their small travel range limitation, they are commonly used in auxiliary fine nanopositioning stages in positioning systems that implement a two-stage scheme. On the contrary, rotary BLDC motors present a lower precision but can perform large travel ranges. Therefore, they are commonly used for low-precision coarse positioning in a two-stage scheme. VCM provide an intermediate solution; they can perform precise positioning in a limited travel range. On the

other hand, linear BLDC motors can provide linear motion in large travel ranges. However, the available commercial solutions are guided and impede planar motion. Thus, they can only be implemented in a stacked-axis configuration.

As shown, Halbach linear motors provide the best solution for accurate positioning in a large range. In addition, they allow implementing planar motion which is preferred over stacked-axes for accurate positioning. Therefore, they can be used to perform high-precision coarse positioning in a large range, that could be complemented by the fine positioning of a piezostage. The main limitation of unguided Halbach linear motors is that they are not commercialised, hence, they are custom-made for each application. For instance, the Center for Precision Metrology of the UNCC has manufactured the linear motors used in [50]. As a consequence, a commercial solution for the control of these Halbach linear motors is not available and, thus, the authors of nanopositioning systems implementing Halbach linear motors specifically designed and developed the control system hardware and software of their positioning systems. The next subsection reviews the control strategies and available solutions for this type of actuators.

1.1.2. Control of Halbach linear motors

The performance of the control strategies used for nanopositioning is crucial in the final positioning accuracy of the stage. For this reason, they have been widely studied. Most of these studies focus on short range nanopositioning with piezo actuators. The work presented in [53] reviewed some of the control-related research in nanopositioning with piezoelectric actuators and discussed their performance. Similarly, in [54, 55, 56] driving methods and design methodologies for piezoelectric actuators were reviewed. However, as mentioned in the previous subsection, Halbach linear motors are a better solution for long range accurate planar motion. Halbach linear motors are a type of permanent magnet synchronous motors. PMSM and brushless DC motors are differentiated by the fact that in the second one, the magnet flux in the air gap is rectangular, while in a permanent magnet machine, the magnet flux has a sinusoidal distribution [57]. Therefore, whereas the current waveform in a three phase brushless DC motor is a 120º square wave, the current waveform in a three phase PMSM is sinusoidal. For this reason, the control of a power electronic device for driving BLDC motors is less complex than the control of the one for driving PMSMs.

As previously noted, when current flows through the coils, in a Halbach linear motor, two orthogonal forces, a horizontal and a vertical force, are generated (Figure 1.1b) and their magnitudes depend on the relative position between stator and magnet array. The motor law is defined as the mapping from phase currents to force for each motor position. Subsection 2.2.1 of this thesis explains in detail the working principle of Halbach linear motors and the motor law. In a positioning stage, the horizontal force generated by the actuators must be controlled to perform the motion to a desired position (thrust force). In addition, in nanopositioning systems, the vertical force can be leveraged either to help the air bearings to levitate the moving platform or even to perform the complete levitation [51]. Then, the required thrust force and the levitation force must be transformed by the control system to the corresponding phase currents to be sent to the motor phases. This transformation is performed according to the commutation law, that is defined as the inverse of the motor law, also explained in Subsection 2.2.1.

The resultant forces in a Halbach linear motor is the sum of the forces produced by all phases, thus, the commutation law depends on the number of phases that the motor has and their respective wiring. Considering a three-phase motor, there are two possible wirings: independent phase currents or start-connection. Motors with independent phase currents require more expensive servo amplifiers than a motor with star connection. This is due to the fact that in motors with independent phase currents, each phase current is driven by a servo amplifier which needs one command signal for each of the three phases [58]. In this configuration, the inverse of the motor law is an under-determined system which has an infinite set of solutions. This gives the flexibility of choosing one more constraint for the commutation. In [59], the constraints of minimum power and power symmetry optimisation were studied. The power symmetry commutation scheme was preferred because it reduced accuracy errors due to non-symmetric thermal deformation in the platen top. On the other hand, star-connection of phases includes an additional constraint: the sum of the three current phases must be null, according to Kirchhoff law. Hence, it is not possible to add any additional optimisation constraint in a star-connection configuration.

The position of the motor is defined by the thrust force because it is the only force acting on the axis of movement. The thrust force generated by a PMSM is affected by two major disturbances when implementing sinusoidal commutation: cogging force and ripple force [60], which are position dependent. Cogging force results from the interaction between the moving magnet array and an iron core stator (slotted) [61]. Cogging force can be avoided by using a non-ferrous core (slotless). Even though the power density of slotless motors is typically lower, in [62], four slotless Halbach linear motors were proven to be sufficient to suspend a platen and drive it at a one-g acceleration. On the other hand, ripple force is an electromagnetic effect and it is defined as the error between the desired and the actual force output due to the fact that the back electromagnetic forces (EMF) of the phases are not exactly sinusoidal. The ripple force is dependent on the number of phases, the magnet array type and the non-ideality of phase currents and magnetic field. The ripple force can affect the motor positioning performance and is to be made as small as possible [62]. A method to optimise the waveform of the phase currents in linear PMSM for force ripple compensation in order to generate smooth force was presented in [63]. Moreover, an adaptive compensation method for friction and force ripple in linear PMSM was proposed in [64]. Nevertheless, the work presented in [62], estimated the force ripple in the slotless surface-wound surface-magnet linear synchronous motor, such as Halbach linear motors, and it proceed to be negligible. Similarly, in [59], it was stated that a Halbach magnet array results in a purely sinusoidal magnetic field, and as a result, planar motion may have a little effect from the force ripple and obtain better power efficiency.

In certain applications, apart from controlling the thrust force for positioning, it can be important to regulate the vertical force generated by the motor because it provides support for levitation [65]. Nevertheless, it is unfeasible to regulate the thrust force and the levitation force separately by acting directly on the phase currents. A similar problem arises in rotary PMSM for the separate control of the torque and the magnetic flux [66]. In rotary motors, a solution, known as vector control, is to apply a Clarke-Park transformation that permits the decoupling of these two variables by defining direct and quadrature (d-q) virtual axes that rotate with the spinning rotor at a speed identical to that of the rotating flux vector [67]. Then, the quadrature axis component (I_q) produces the torque, and the direct axis component (I_d) exerts a magnetising effect on the reference flux. In these systems, the common practice is to magnify the torque production and minimise the magnetic flux [68]. Similarly, as stated in [48], in a Halbach linear motor, a Clarke-Park transformation permits decoupling the control of the thrust (produced by I_d) and levitation force (produced by I_q).

The use of unguided Halbach linear motors is not widespread yet, thus, they are custom-made for each application. Subsequently, a commercial control system for this type of motors is not available. For this reason, the authors of nanopositioning systems implementing Halbach linear motors specifically designed and developed the control system hardware and software. In [62], a high-precision magnetically levitated stage was presented. This stage is actuated by four Halbach linear motors that provide both, levitation and thrust forces, in a working range of 50 mm × 50 mm in X and Y-axes and of 400 µm in Z-axis, achieving a positioning noise of 5 nm in XY-plane. In this work, the controller sends the commutation command through digital to analogue converters (DAC) as voltage signals to transconductance power amplifiers. Each of these power amplifiers independently supplies the commanded phase current to the stator coils. Thus, the power amplifiers act as a controlled current source and the phase currents are controlled directly and independently with the DAC signals. The same solution is proposed for the positioning stage presented in [69]. In [70], the design and control of a 6 degree of freedom precision positioner was presented. As in the previous case, power amplifiers were designed and built for the application, and they act as independent controlled current sources for each individual phase current. The same power amplifiers were used in [71] to control the phase currents of a similar stage. In [59], Shalom proposed a similar solution for the previously mentioned MAPS based on linear power amplifiers driven by a DAC voltage signal that independently controlled each of the phase currents of the motor.

In conclusion, when current flows through the phases of Halbach linear motors, they generate two orthogonal forces, a thrust force and a levitation force. In order to perform motion, it is necessary to control the thrust, which can be done by variating the phase currents according to the motor law. Although most nanopositioning stages using these motors implement a hybrid suspension combining the magnetic suspension with air bearings, Halbach motors are capable of providing complete suspension of the moving platen. Thus, it would be of interest to develop a vector control strategy capable of decoupling the control of the thrust force and the levitation force. Due to the absence of a commercial control hardware for unguided Halbach linear motors, the current solutions have been specifically developed and built for each application. These solutions drive each phase current with an independent current source. Even though, this allows implementing an additional constraint in the system, like power symmetry optimisation, independent phase currents require more expensive servo amplifiers than a motor with star connection. Phase currents can also be controlled by commercial hardware based on three-phase voltage-source pulse width modulated converters [72], commonly used for the control and drive of rotary motors. Therefore, a completely generic control hardware could be implemented for the control and drive of Halbach linear motor phase voltages. The use of only one commercial piece of hardware and no custom-made electronics is a novelty that would facilitate the applicability and replication of the developed control system. In order to implement vector control, the control hardware should include a current sensing module capable of reading phase currents.

1.1.3. Positioning sensors in large range accurate positioning systems

Positioning sensors are a crucial component in control systems of nanopositioning stages. Accuracy of the positioning sensor directly affects the total positioning uncertainty of the system [73, 74]. The different sensor solutions can be classified according to the type of displacement that is measured: rotation or translation; working range and accuracy [75]. Rotation can be measured with autocollimators, whereas short range displacements (less than 10 mm) can be measured by capacitive or inductive sensors. These short-range devices are typically used for measuring spurious motions in out-of-plane positions in nanopositioning stages [76]. The commercially available options for measuring planar 2D displacement in a long range are 2D grid encoders, combinations of 1D linear encoders and laser interferometers.

Linear encoders (Figure 1.2a) are more accurate than grid encoders (Figure 1.2b), because linear scale errors can be evaluated and compensated by software. For the evaluation of these linear errors heterodyne or homodyne laser interferometers are widely used [77, 78]. Nevertheless, due to the narrowness of the linear scale in the orthogonal direction, they are not appropriate for planar designs. Grid encoders typically consist of a scanning head and a grid plate with a reference pattern on the surface. Surface encoders are capable of measuring XY-positions along a plane [79]. Their accuracy and resolution is dependent on the quality of the pattern. This results in an incremental error that increases in long range applications. In [80], a grid encoder was used as positioning sensor in a 40 mm × 40 mm planar stage, achieving a XY-resolution of 20 nm, before calibration and compensation. The 6D planar magnetic levitation system PIMag6D [51] measures the planar degrees of freedom with a grid encoder. The grid plate is mounted on the bottom side of the moving part, whereas the scanning head is fixed.

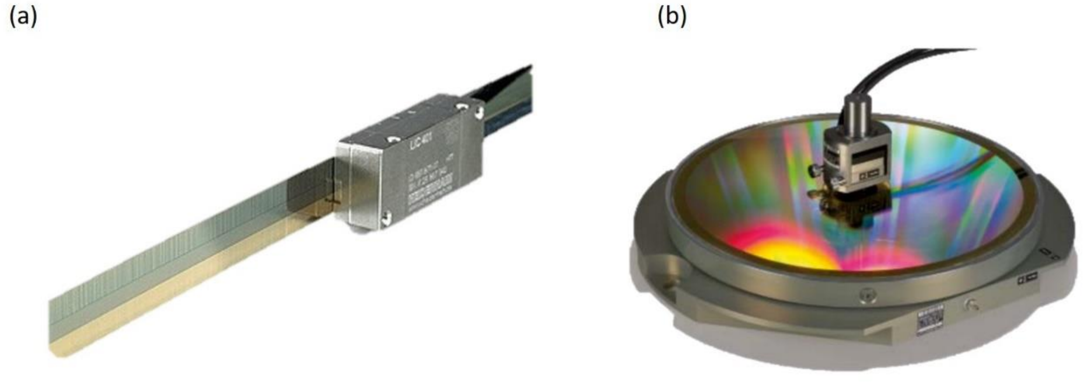

Figure 1.2. *Linear encoder (**a**) and grid encoder (**b**) from Heidenhain.*

On the other hand, laser interferometer systems provide highly accurate, non-contact measurements and they are capable of working in long distances [81]. In addition, they present direct traceability to the fundamental standard of length and an excellent dynamic range, limited only by the fluctuations of the refractive index of air [82], achieving nanometre or even subnanometre resolution. The measure beam can be considered as a virtual axis that can pass directly through the measurement point of interest to eliminate Abbe offset errors [83]. The measure beam and the reference beam are recombined in the interferometer and the phase difference between the two signals is recorded by a photodetector and processed. The phase difference is caused by the displacement of the measure beam and results in either constructive or destructive interference [84]. Then, displacement is measured by counting the number of cycles and, thus, higher resolution can be achieved by phase interpolation.

Moreover, using plane mirrors as retroreflectors in a laser system allows measuring planar displacement [85]. Thus, 1D plane mirror laser interferometer systems can be combined to result in a 2D positioning sensor. As a drawback, in plane mirror laser interferometer systems, the plane mirror acting as retroreflector must be always kept perpendicular to the beam to obtain a normal interference between measurement beam and reference beam. Therefore, in a 2D plane mirror laser interferometer system, planar motion is permitted in large ranges only as the translation in X and Y-axes, but rotation around Z-axis (θ_z) is limited to a very small angle. The range of the permitted misalignment angle (θ_z) can be increased by offsetting the second beam in a double pass configuration [83]. 2D plane mirror laser systems have been selected as positioning sensors in positioning stages as the already mentioned MAPS [49, 50], which implements Halbach linear motors as actuators. The Nanopositioning and Nanomeasuring Machine [10] implements plane mirror laser systems for the measurement of the displacement in 3D: in X, Y and Z-axes. This machine has a travel range of 25 mm × 25 mm × 5 mm that is obtained with a stacked arrangement, achieving closed-loop positioning stability of approximately 0.3 nm.

The accuracy of the positioning sensor system is crucial when working at a nanometre scale. Accuracy is defined by the International Organisation for Standardisation as the description of random and systematic errors [86]. Random errors cannot be corrected but only quantified by taking numerous measurements and processing the resulting data in order to determine the measurement uncertainty. However, systematic errors can be identified and corrected. The principle of interferometry is dependent on the wavelength of the laser light, which is calibrated by the manufacturer, resulting in direct traceability. Nevertheless, the wavelength of a laser interferometer system working in a non-vacuum environment is affected by the variations of temperature, pressure and humidity. These parameters change the air refractive index [87] and, thus, the wavelength of the laser light. Nevertheless, this is a systematic error that can be minimised by monitoring the environment parameters and correcting the refractive index.

Measurement errors of 1D laser interferometers are mainly caused by misalignments between laser beam and retroreflectors; misalignments between laser beam and motion axis, and Abbe errors. In [88], a better straightness measurement accuracy was obtained through compensating for pitch and yaw angles of the target retroreflector. As previously noted, in a 1D plane mirror laser interferometer, it needs to be a normal interference between measure beam and reference beam for the system to work [89]. Typically, the manufacturer defines a tight alignment tolerance between laser beam and the normal vector of the plane mirror. Therefore, the deviations caused by the orthogonality (pitch and yaw) error between laser beam and plane mirror are limited by the alignment tolerance and the maximum possible distance between laser head and plane mirror in working conditions, and it tends to be negligible. In a 1D plane mirror laser interferometer system configuration, the main geometrical error is the pitch misalignment between the laser beam and the motion axis (α_{pitch}), as represented in Figure 1.3.

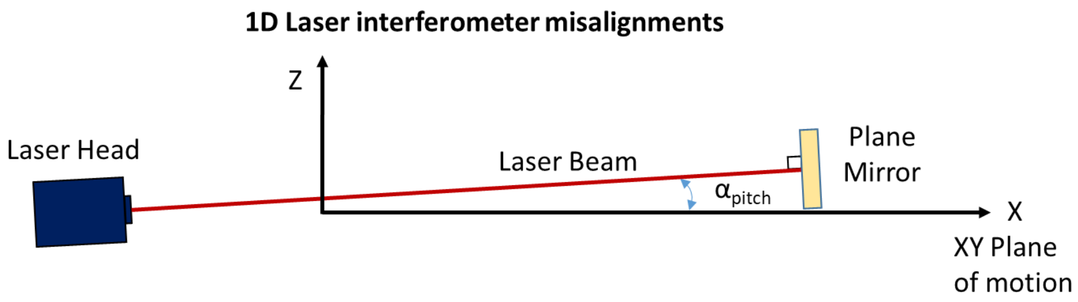

Figure 1.3. *Pitch error in a 1D laser interferometer.*

A 2D laser system consists of the combination of more than one 1D laser interferometer. Two laser interferometers are sufficient to measure the displacement in X and Y-axes, whereas an additional laser interferometer is necessary to measure the rotation around Z-axis. Thus, in a 2D laser system, apart from the own 1D errors of each laser interferometer, misalignment errors appear due to the impossible perfect assembly of both components. In a 2D positioning stage, the laser system defines the reference X and Y-axes for the motion control. Hence, besides the pitch misalignments between each laser beam and the motion plane, there will be an additional 2D error caused by the lack of squareness between X and Y-axes (α_{xy}), as represented in Figure 1.4. Therefore, the final positioning error will be affected by the combination of 1D and 2D errors.

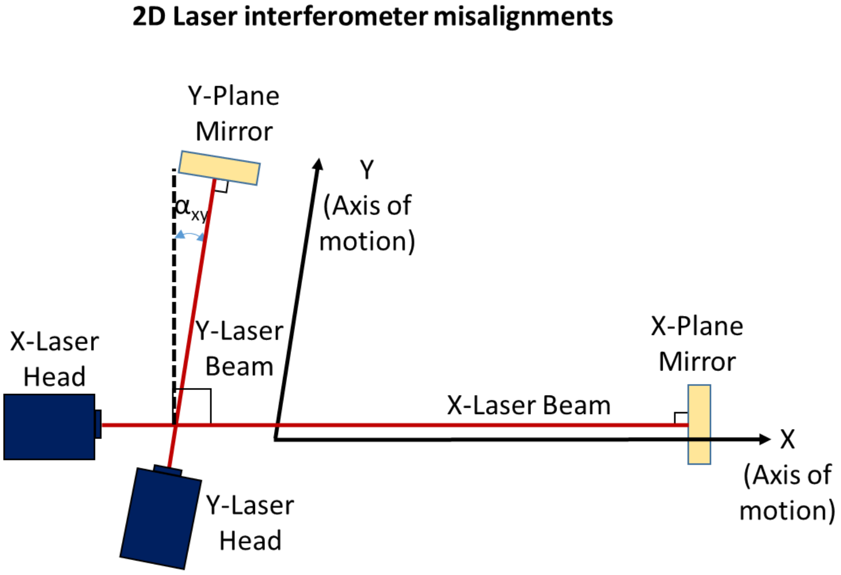

Figure 1.4. *2D laser system misalignments in XY-plane of motion.*

As previously mentioned, Abbe errors are also the cause of alignment errors. Nevertheless, Abbe errors are not dependent on the 2D laser system assembly but on the location of elements (such as sensor probes, targets, etc.) and they can be minimised by design. In [90], the design of a 2D nanopositioning platform (NanoPla) was presented. The NanoPla uses four Halbach linear motors as actuators and a 2D plane mirror laser interferometer system as positioning sensor. In [91], the accuracy of the NanoPla was improved by eliminating the Abbe error in the horizontal plane. This was achieved because the design forces the sensor probe (an atomic force microscope tip, in this case) to be coincident with the centre of the reference system. As a result, a submicrometre uncertainty was obtained in the whole working range of 50 mm × 50 mm.

Misalignment errors, as well as other systematic errors of 2D positioning systems that cannot be eliminated by design or during the assembly, can be obtained through calibration methods and subsequently corrected by error compensation techniques. Calibration methods are selected depending on the accuracy required, the size of the working range and the available equipment. Direct calibration is the most commonly used calibration method, it essentially consists in comparing the measurements of the system that is being calibrated to the length of a calibrated artefact of known accuracy [92]. Thus, the accuracy of the calibrated artefact should be better than the system to be calibrated, which can be difficult to obtain when working at a submicrometre scale in large working ranges [93]. On the other hand, self-calibration methods extract the systematic errors of the system to be calibrated by relating views of a non-calibrated artefact [94], thus, solving the problem of finding a calibrated artefact at submicrometre scale [95]. Therefore, self-calibration offers a suitable procedure for extracting systematic errors of large range nanopositioning sensors [96, 97]. The only calibrated pattern required in a self-calibration procedure is the absolute 1D length scale, to obtain the scale factor of the system to be calibrated. As a solution, the use of a calibrated reference rod was proposed in [98]. Nevertheless, in a laser system, the wavelength of the laser beam is already calibrated by the manufacturer, thus, a scale factor correction is not needed.

Table 1.2. Summary of positioning sensors options for large range accurate positioning systems

Sensor	Pros	Limitations	Uses
Capacitive and inductive	- Non-contact measurements - High resolution	- Short range displacements (< 10 mm)	- Measurement of spurious motions in large range nanopositioning stages
Linear encoders	- Long range linear displacements - Systematic errors can be corrected by software	- Not appropriate for planar designs	- Measurement of linear displacement in stacked-axis nanopositioning stages
Grid encoders	- Long range planar displacements	- The error increases in long range applications	- Measurement of 2D displacement in planar stages
Laser interferometer system	- Direct traceability - Non-contact measurements - Plane mirror retroreflectors allow planar motion - 1D plane mirror laser interferometers can be combined for 2D measurement	- The laser beam must be perpendicular to the plane mirror - Misalignment errors derived from the assembly	- Measurement of 2D displacement in planar stages - Calibration of linear and grid encoders

Table 1.2 shows a summary of the positioning sensors that have been reviewed in this subsection and the advantages and disadvantages of their use in large range accurate

positioning stages. Capacitive and inductive sensors provide a high resolution in short range displacements, hence, they are used for measuring out-of-plane spurious motions. Linear encoders are capable of measuring large range linear displacements but displacement is impeded in the orthogonal axis, thus, they are not appropriate for planar designs. On the other hand, grid encoders are capable of measuring large range planar displacements but their errors increase in large range applications. Finally, 1D plane mirror laser interferometers can be combined to measure 2D planar displacements in a large range. Their use provides many advantages, such as direct traceability and non-contact motion. Nevertheless, they present some limitations: The laser beam must be always kept perpendicular to the plane mirrors, for the laser system to read. Therefore, rotation of the moving part should be impeded by the positioning control system. In addition, 2D laser system assemblies are affected by 1D and 2D misalignment errors in the setup that need to be known and corrected in order to provide accurate displacement measurements. Systematic errors can be obtained by calibration methods. The main disadvantage of commonly used direct calibration methods is the need of a calibrated artefact at submicrometre scale for large working ranges. This limitation can be overcome by implementing self-calibration methods that can isolate the systematic errors of the system by relating different views of a non-calibrated artefact.

1.2. Thesis motivation

At the Design and Manufacturing Engineering Department of the University of Zaragoza (Spain), a two-dimensional nanopositioning platform (NanoPla) has been developed and the first prototype has already been manufactured. It is designed to achieve nanometre resolution and submicrometre accuracy in a large working range of 50 mm × 50 mm. This work has been subject of two published theses: [16, 17].

The NanoPla has been designed to work together with different kinds of tools and probes in various applications such as metrology or nanomanufacturing. In particular, the main application of this first prototype is surface topography characterisation at atomic scale of samples with relative big planar areas, using an atomic force microscope (AFM). The AFM will be attached to the moving platform that performs the large displacement of 50 mm × 50 mm (coarse motion). The NanoPla architecture is based on the scheme for the four integrated Halbach linear motors that perform the planar motion of the moving stage. The XY-position of the platform is measured by a 2D plane mirror laser interferometer system, whereas out-of-plane spurious motions are measured by capacitive sensors. The NanoPla implements a two-stage structure, where a commercial piezostage provides precise positioning of the sample in a shorter range of 100 µm × 100 µm × 10 µm (fine motion). An exploded view of the NanoPla has been represented in Figure 1.5.

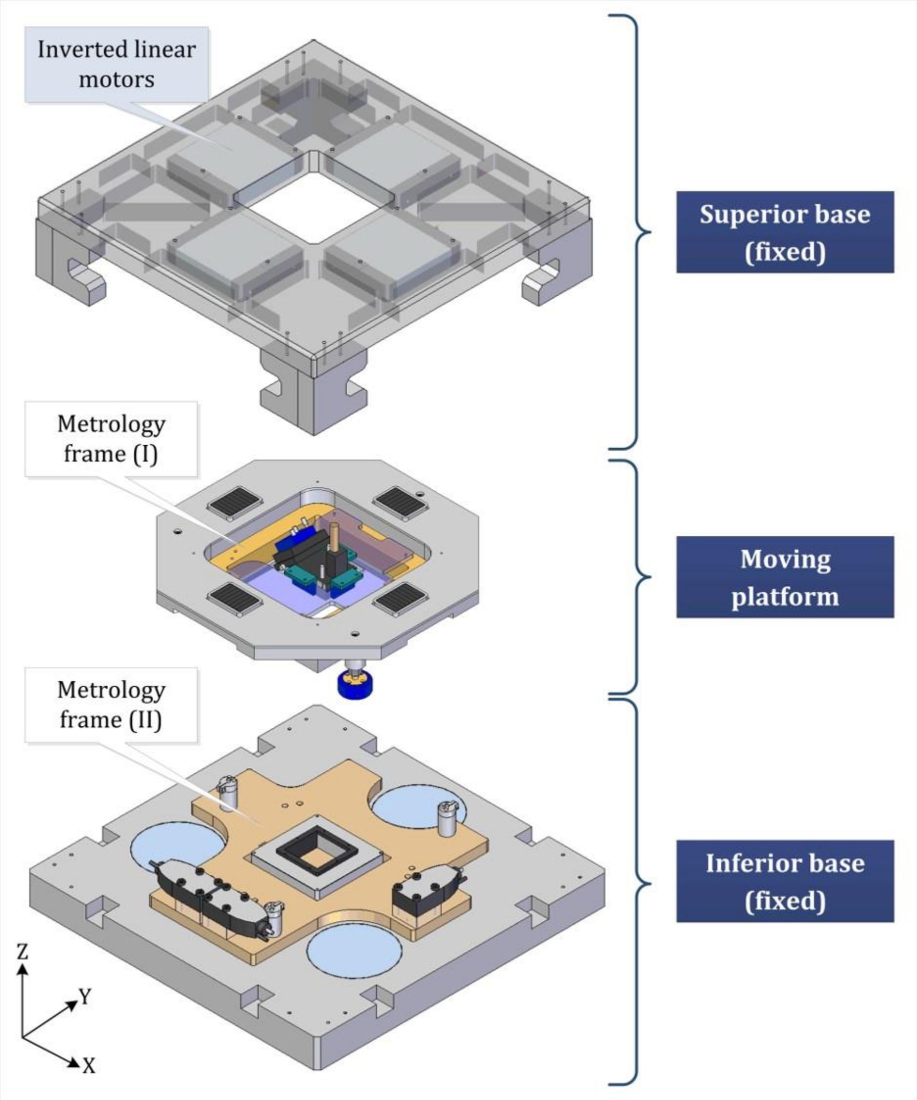

Figure 1.5. *NanoPla exploded view [17].*

The NanoPla is comprised of three main structural parts: two fixed bases and the moving platform. The metrology loop consists of two metrology frames, one in the moving platform (I) and the other in the inferior base (II). The design and function of these parts are following described:

- Inferior base: The inferior base incorporates the airbearing surfaces and the metrology frame (II). The airbearing surfaces are made of steel and over them the moving platform levitates, thus, their size is dependent on the working range. In the metrology frame, the three laser heads and capacitance probes are located. In addition, the fine-motion nanopositioning piezostage is also placed on the metrology frame (II) when the two-stage structure is implemented (see Figure 1.6).

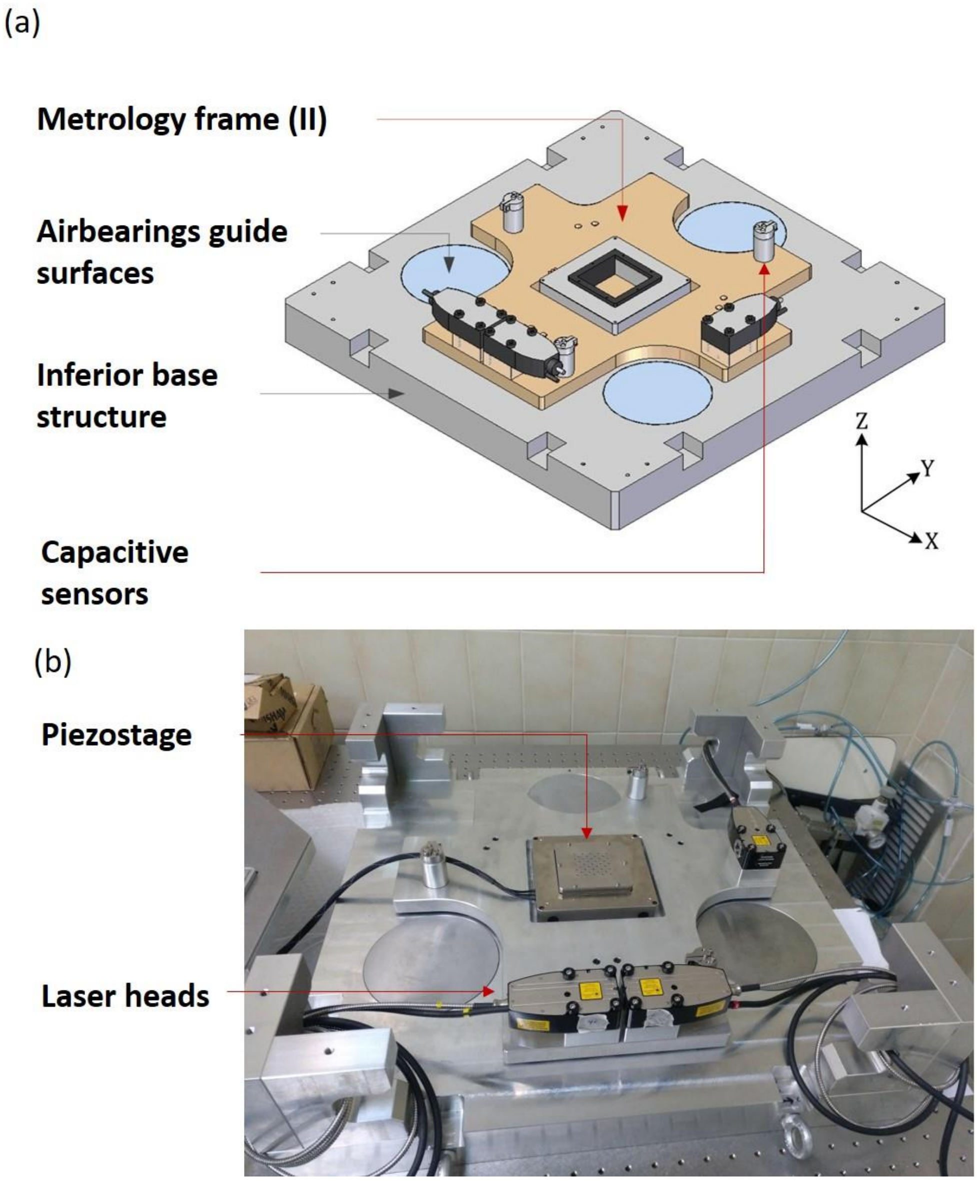

Figure 1.6. *NanoPla inferior base: (**a**) 3D model [17] and (**b**) photograph.*

- Superior base: The purpose of the superior base (Figure 1.7) is to locate the stators of the four linear motors, which are upside-down, in comparison to other reviewed stages [49, 51, 65, 70], in which the stators are placed in the main inferior base. The reason for this novel design is to reduce the size of the stage and to improve metrological features.

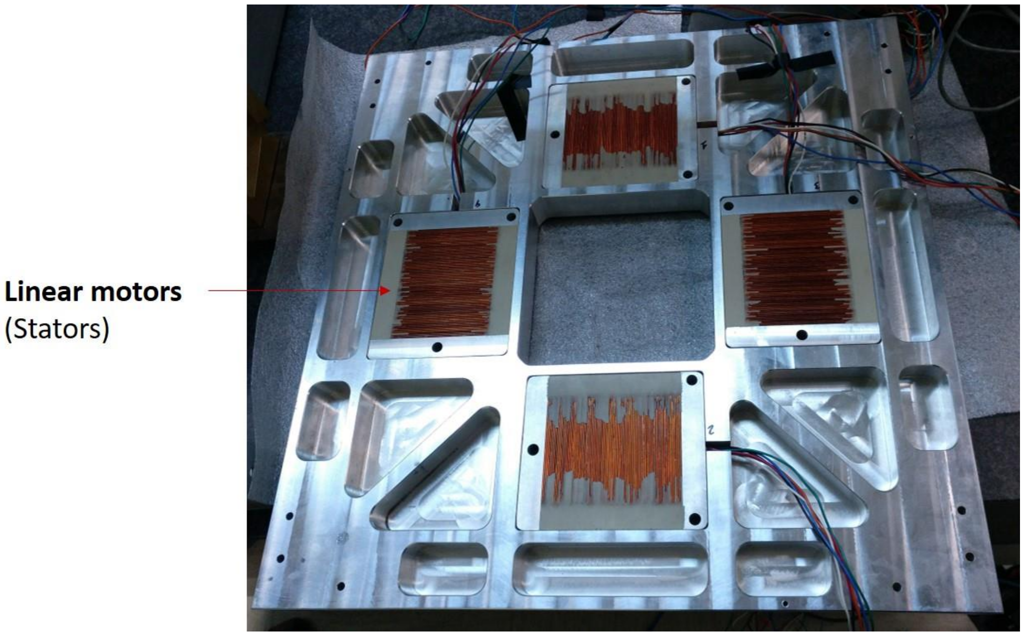

Figure 1.7. *NanoPla superior base bottom side photograph.*

- <u>Moving platform</u>: The moving platform performs the long range displacements of 50 mm × 50 mm. The platform is levitated by three airbearings that allow frictionless motion between parts. The three airbearings are vacuum preloaded and are equally spaced 120º. The Halbach magnet arrays of the linear motors are integrated over the platform, and the capacitive sensors targets are placed at the bottom. In the centre of this part is the metrology frame (I), which supports the measuring device (e.g.: AFM, confocal sensor) and the plane mirrors. The metrology frame (I) is connected to the platform structure by three identically spaced flexure mounts to diminish thermal gradient effects. In Figure 1.8, the moving platform has been represented in detail.

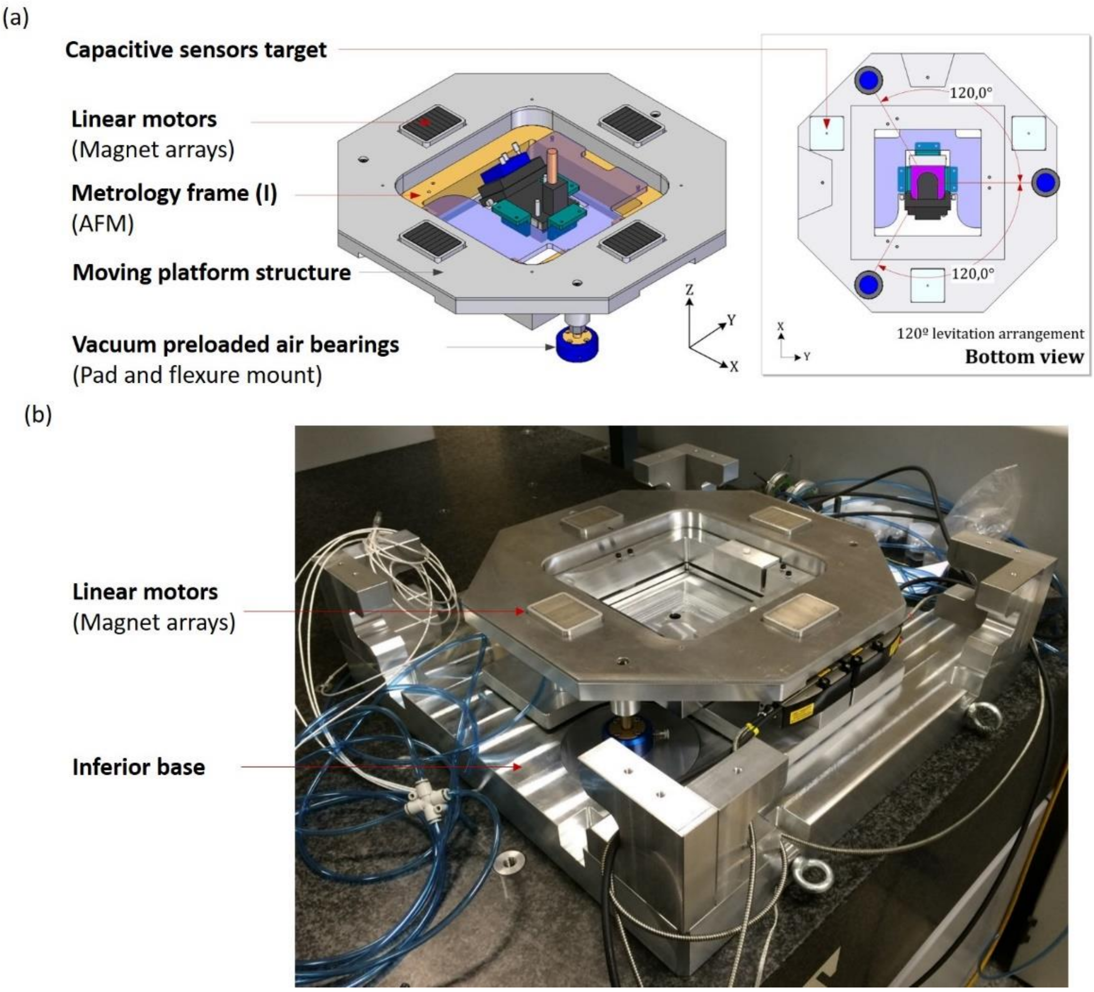

Figure 1.8. *Moving platform: (**a**) 3D model [17] and (**b**) photograph.*

The structural parts of the NanoPla are made of aluminium alloy 7075-T6, due to its strength comparable to many steels. In this first prototype for preliminary tests, the metrology frame is made of the same aluminium. Nevertheless, the selected material for its final design is Zerodur, due to low thermal expansion coefficient that assures negligible dimensional changes caused by temperature variation.

The design of the NanoPla was completely stablished and the first prototype was manufactured and assembled in [16, 17]. This design is the result of an extended research process, which includes state-of-art study of similar systems and precision engineering principles. One of the design criterions of the NanoPla is to use commercial systems for the integrated devices, whenever possible. The aim is to obtain a more standard system for future industrial application. An exception has been made with the four Halbach linear motors which are custom-made. The reason is that, even though they are not commercially available, they are the best option to perform planar motion in a long range.

During the scanning task, the NanoPla will perform the high-precision coarse motion that allows the metrological characterisations of a large range of the sample, up to 50 mm × 50 mm. Then, the moving platform would remain static (air bearings off) while the piezostage will perform the fine motion required for the AFM measurement. In working conditions, the NanoPla would be set to move in a trajectory and stop at defined positions. Therefore, its positioning system is required to displace to positions along the whole working range with the minimum positioning error.

The work presented in this dissertation is the continuation of the mentioned theses [16, 17], and deals with the design and implementation of an accurate 2D positioning control system for the whole working range of the NanoPla. The target of this thesis is to achieve accurate 2D positioning of the NanoPla along its working range. The development of the control strategy is constrained by the positioning system components defined by the NanoPla design, which are summarised below:

- Actuators: In the NanoPla, the movement is performed by four unguided Halbach linear motors developed by Trumper et al. [47] and custom-made in the Center for Precision Metrology of the University of North Carolina at Charlotte. Each of the stators of these motors have three phase windings wrapped around an anodized aluminium mandrel, in order to avoid cogging. The motors are placed in parallel pairs, so that each pair performs the motion in X and Y-axes, respectively, as represented in Figure 1.9. Despite the fact that this design allows leveraging the vertical forces generated by the motors to provide the levitation, airbearings provide the main support of the moving platform due to their stiffness. The custom-made design of the magnet array and the stator of these motors allows planar motion in the whole working range of 50 mm × 50 mm.

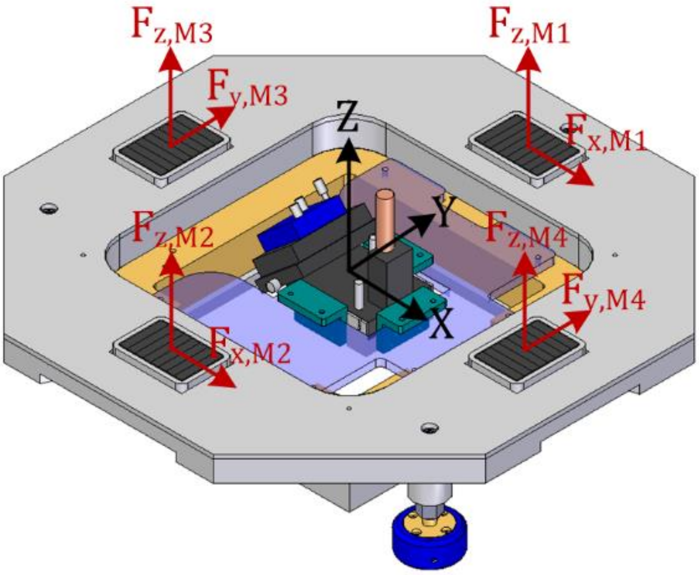

Figure 1.9. *Linear motors magnet arrays in the moving platform and resultant forces [17].*

- Control hardware: As previously mentioned, there is no available commercial solution to perform the control and driving task of the NanoPla Halbach linear motors. For this reason, other reviewed stages integrating these motors specifically designed and developed control hardware and software for this purpose [59, 62, 70, 71]. In these stages, the control strategies are based on individually and independently controlling each of the phase currents of the motors with transconductance power amplifiers. However, following the NanoPla design principle of integrating commercial devices when possible, in [17], the use of only commercial hardware and no custom-made electronics was proposed. Thus, the Digital Motor Control Kit (DMC) DRV8302-HC-C2-KIT from Texas Instruments was selected as control hardware. The DMC kit consists of the F28035 control card and the DRV8302 board, as shown in Figure 1.10. This DMC kit has been designed for rotary BLDC and PMSM three-phase motors, where the aim is to control the rotation speed or the torque generated. The board includes a three-phase power stage that drives and generates phase-voltages by pulse width modulation (PWM), in contrast to [59, 62, 70, 71], where the hardware acted as a controlled current source. Additionally, the control hardware forces the star-connection of the phases, impeding the phase currents to be controlled independently, as it was done in [59, 62, 70, 71]. The hardware includes a current sensing module capable of reading phase currents in real time, which allows the implementation of a vector control strategy. This hardware has been selected due to its relative low cost and the advantages of the associated software. The control of the used microcontroller from Texas Instruments is based on the Target Support Package™ for Embedded Code. This Package integrates MATLAB® and Simulink® with Texas Instrument tools and C2000 processors, to generate, compile, implement and execute the optimised control code with a user-friendly graphic interface and without programming in a specific language.

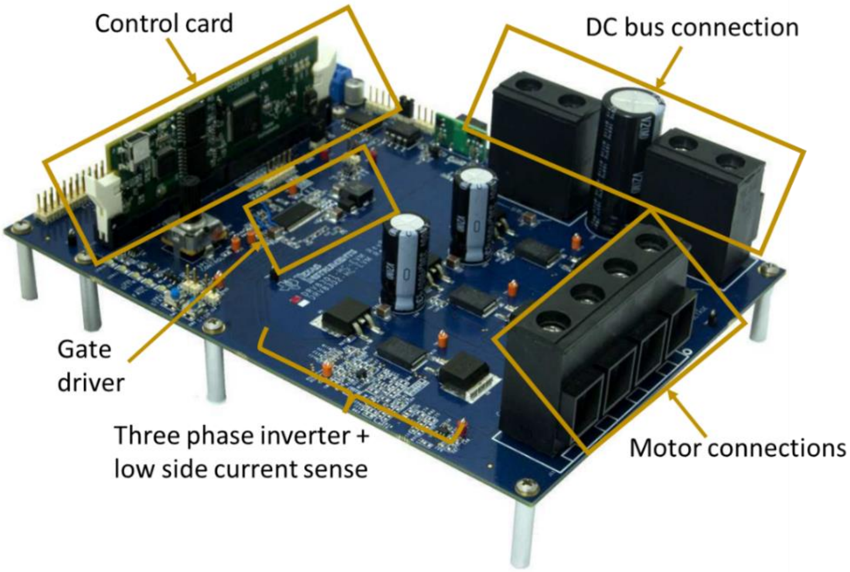

Figure 1.10. *Digital Motor Control Kit from Texas Instruments.*

- <u>Positioning sensor</u>: A 2D laser system is used as positioning sensor in the XY-plane of the NanoPla. This 2D laser system is the combination of three 1D plane mirror laser interferometer systems. Two laser beams are needed to measure the displacement in X and Y-axes, respectively. In addition, one more beam is needed to determine the rotation around Z-axis. Thus, one laser head is placed projecting its beam in the X-axis (L_x), aligned with the reference system of the travel range, while the other two laser heads project their beams (L_{y1} and L_{y2}) parallel to Y-axis, symmetrically to the orthogonal axis of the reference system, as represented in Figure 1.11. The two parallel beams are reflected in the same plane mirror, thus, only one mirror per axis is needed.

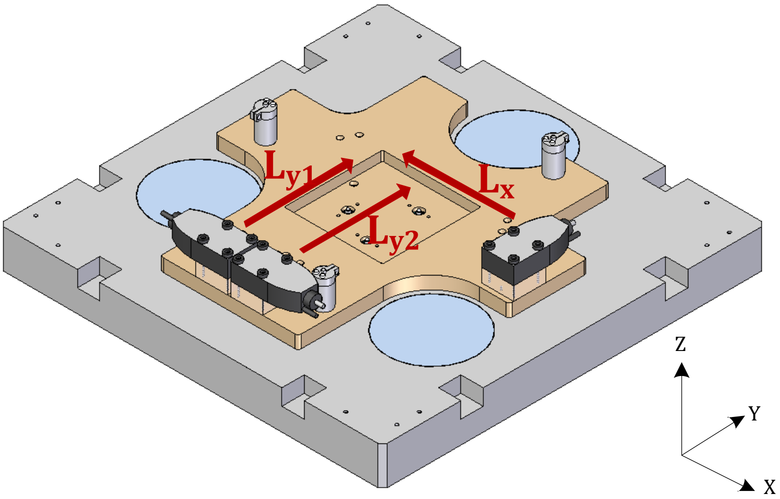

Figure 1.11. *Laser beam representation of the 2D laser system of the NanoPla.*

The system belongs to the Renishaw RLE10 laser interferometer family. Apart from two laser units (RLU); three sensor heads (RLD) and two plane mirrors (one per axis), an environmental control unit (RCU) and three interpolators have been acquired. The environmental unit is capable of monitoring environmental error sources (temperature, pressure and humidity changes) to correct in real time the deviations in the laser wavelength due to refractive index variations, which improves accuracy and repeatability. Moreover, the interpolators reduce the expected resolution of the system from 9.88 nm to 1.58 nm. The components of the whole system are shown in Figure 1.12, in the specific case of the NanoPla, the motion controller is the host PC that extracts the laser system readouts.

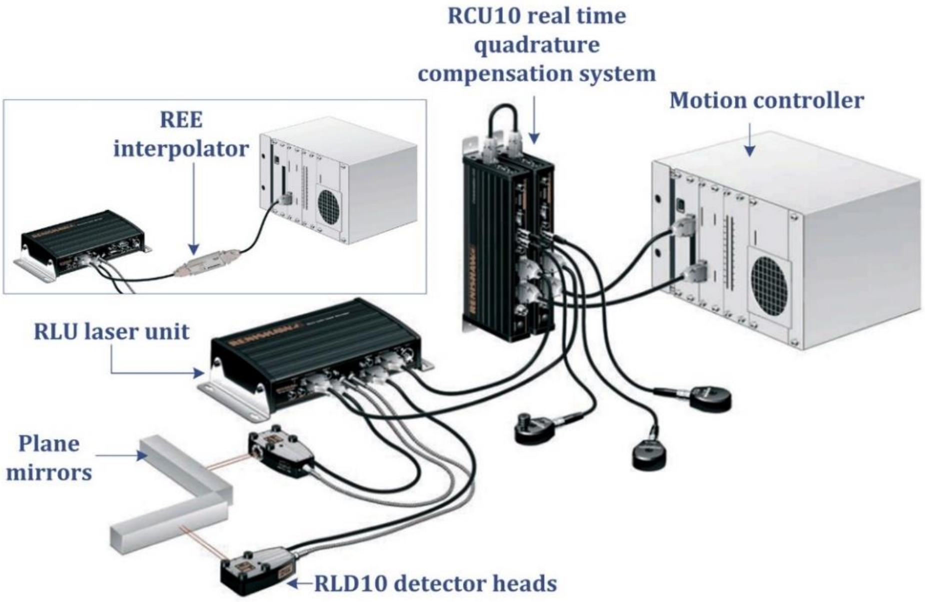

***Figure 1.12**. NanoPla plane mirror laser interferometer system of Renishaw [17].*

Therefore, the target of this thesis is the design and implementation of an accurate 2D positioning control system for the whole working range of the NanoPla. The NanoPla actuators are four Halbach linear motors and the positioning sensor is a 2D plane mirror laser interferometer system. The selected control hardware to drive the linear motors phase voltages is a generic DMC kit for the control of three-phase motors.

In the previous subsection, it was stated that Halbach linear motors have many benefits in large range precision positioning, such as allowing the implementation of planar motion. Nevertheless, their main disadvantage is that they are not commercialised yet and, thus, there is not a commercial control solution available. According to the NanoPla design requirement of implementing commercial devices when possible, a commercial generic solution has been proposed as control hardware for the linear motors. Due to the complexity of controlling a pneumatically levitated Halbach linear motor and the absence of literature addressing the position control of Halbach linear motors with commercial control hardware, the thesis first focuses on the development of a 1D positioning control strategy for Halbach linear motors and its implementation in the DMC kit. This includes a dynamic modelling of the system, which facilitates the design of the control strategy. Moreover, in order to overcome the limitations of using a generic hardware for precision positioning, the configuration of the voltage generation must be optimised.

Similarly, in the previous subsection, plane mirror laser interferometers were presented as the best option for measuring planar displacements due to their direct traceability and high resolution. However, the use of these sensors implies one additional constraint; the control system must impede the rotation of the moving part in order to maintain the orthogonality of the laser beams and the plane mirrors. In order to provide accurate positioning, it is necessary to correct the systematic errors of the readouts. There are two main contributors to the laser system systematic errors: the refractive index variations and the geometrical errors derived from the assembly. The NanoPla laser system includes an environmental control unit that corrects the refractive index variations, whereas the geometrical errors can be obtained by calibration methods and, then, corrected in the system readouts. In this thesis, a self-calibration procedure for the geometrical characterisation of a 2D laser system assembly is proposed. The main advantage of this procedure over commonly used direct calibration methods is that it does not require a calibrated artefact at a submicrometre scale, which is costly and difficult to obtain.

Finally, this thesis develops and implements a 2D positioning control system for the NanoPla, which coordinates the four Halbach linear motors and integrates the 2D laser system for positioning feedback. In addition, the positioning uncertainty of the 2D positioning control system is assessed and minimised.

2. Presentation of the publications

This doctoral thesis is presented as a compendium of publications. This section, first, justifies the thematic unit of the publications. Then, each of the publications is summarised.

2.1. Justification of the thematic unit

The work presented in this thesis focuses on the development and implementation of the positioning control system for a nanopositioning platform (NanoPla) capable of providing accurate positioning along its large working range of 50 mm × 50 mm. The actuators of the positioning system are four Halbach linear motors that have been custom-made at the UNCC for this application, fulfilling the requirement of providing planar motion in the whole working range. In the NanoPla, a 2D plane mirror laser interferometer system works as positioning sensor, measuring the displacement in X and Y-coordinates and the rotation around the Z-axis. The control hardware selected for driving the motors is a generic commercial digital motor control kit for rotary BLDC and PMSM motors that generates phase voltages by pulse width modulation (PWM). The aim is to achieve accurate 2D positioning control by optimising the control strategy and the performance of the control system components, that is, the control hardware, the actuators and the positioning sensor.

The research contributions of this thesis can be divided into three blocks: development of a 1D control system for a Halbach linear motor using generic hardware for the control of three-phase motors; characterisation and error compensation of the 2D laser system assembly and, finally, the integration of the previous results to achieve accurate 2D positioning of the NanoPla. The published articles that best represent the work accomplished in these three blocks are listed below:

- **Block 1:** Development of a 1D control system for a Halbach linear motor:
  - **Micromachines 2018:** One-dimensional control system for a linear motor of a two-dimensional nanopositioning stage using commercial control hardware
  - **Electronics 2018:** Vector control strategy for Halbach linear motor implemented in a commercial control hardware
- **Block 2:** Characterisation and error compensation of the 2D laser system assembly
  - **Sensors 2017:** Geometrical characterisation of a 2D laser system and calibration of a cross-grid encoder by means of a self-calibration methodology
- **Block 3:** Accurate 2D positioning of the NanoPla
  - **Procedia Manufacturing 2019:** Positioning uncertainty of the control system for the planar motion of a nanopositioning platform

Intermediate results have also been published and they are referenced in this thesis. Nevertheless, they are not part of the compendium of publication of this thesis. Those publications are detailed in Section 5.

The 2D positioning control system of the NanoPla must integrate the control and drive of four Halbach linear motors acting on the two orthogonal axes of the XY-plane. Thus, it seemed necessary to start first with a one-dimensional approach. In this manner, the works published in **Micromachines 2018** and **Electronics 2018** propose two alternative control strategies for positioning a Halbach linear motor in one axis with generic hardware for the control of rotary motors. These control strategies are experimentally validated in a separate setup consisting on a linear guide that allows frictionless motion and a laser interferometer that provides position feedback.

In **Micromachines 2018**, firstly, an overview of the NanoPla is presented, this is necessary to define the working requirements of the control system. The moving platform of the NanoPla is actuated by four Halbach linear motors that perform planar motion in the XY-plane along the working range of 50 mm × 50 mm. Moreover, the NanoPla design includes a commercial piezostage that performs fine motion in a range of 100 µm × 100 µm × 10 µm, in a two-stage scheme. Therefore, the 1D linear motion strategy must be able to work in a range of 50 mm, with a positioning error at least one order of magnitude smaller than the maximum XY range of the commercial piezostage, that is 10 µm. In addition, due to the fragility of some of the NanoPla components (e.g. Zerodur plane mirrors of the laser system), oscillations should be avoided. Then, the working principles of the Halbach linear motors of the NanoPla are described, that is, the motor law and the commutation law. The experimental setup used for validation is explained and the commercial control hardware used for the implementation is presented. As mentioned, the selected control hardware is a commercial Digital Motor Control (DMC) Kit from Texas Instruments designed to control the torque or the rotational speed of rotary three-phase motors. A dynamic characterisation of the linear motor is performed, in contrast to other works, that focus on the electromechanical modelling of the motor. Leveraging the dynamic properties of the motor allows developing an open-loop positioning strategy that works as a sensorless solution. Afterwards, a closed-loop positioning control strategy is proposed. Both strategies are implemented in the control hardware, using a laser system as positioning sensor. According to the literature, the integration of completely generic control hardware for the position control of these linear motors is a novelty that this study presents. The limitations of using a generic hardware are overcome by optimising the control system design. In this work, it is verified that the proposed 1D positioning control system achieves and surpasses the NanoPla working requirements: it is able to work in a range of 50 mm and perform a minimum incremental motion of 1 µm.

As described, the work presented in **Micromachines 2018** focuses on the positioning control of Halbach linear motors where motion is performed by acting on the generated thrust force. Nevertheless, Halbach linear motors generate an additional vertical force that can be leveraged as support for levitation of the moving part of the stage. Thus, in some applications, it can be of interest controlling the fluctuations of the levitation force during the positioning task. Therefore, in **Electronics 2018**, a vector control strategy for Halbach linear motors was proposed. Vector control allows decoupling the vertical and the horizontal forces generated by the motor. Thus, this strategy enables the positioning of the motor while regulating the generated vertical force. The strategy is implemented in the DMC Kit from Texas Instruments. Vector control is a strategy commonly applied in rotary PMSM motors to control the generated torque and magnetic flux separately. The DMC kit is designed for rotary PMSM motors and integrates low-side current sensing circuit components for reading phase currents in real-time which is necessary for vector control. The article, first, describes Halbach linear motors operating principle and the motor is identified as a servosystem when it acts as a positioning actuator. Then, the vector control strategy is presented. The implementation of the vector control strategy in the control hardware is more complex than in **Micromachines 2018**. This is due to the fact that, apart from driving and generating phase voltages, the hardware is required to integrate the readouts of the analogue to digital converters (ADC) of the current sensing amplifiers, as feedback for the vector control. Thus, in the article, voltage generation and current sensing modules of the hardware are analysed and its settings are optimised. Subsequently, the control system performance is validated, first, virtually and, then, experimentally. In the experimental setup, a cell load that measures the vertical force generated by the motor has been added, this allows verifying the performance of the vertical force controller. The results show that vector control strategy enables controlling the position of the motor and the levitation force separately and simultaneously. In the virtual analysis, it is shown how the current sensing resolution and noise affect the final positioning error.

In brief, the vector control strategy presented in **Electronics 2018** enables regulating the levitation force generated by a Halbach linear motor as well as controlling the position by acting on its thrust force. Vector control requires reading the phase currents which are used as feedback in the strategy. As a result, in this specific control strategy, the positioning system accuracy is affected by the current sampling noise and errors. On the other hand, the position control strategy of **Micromachines 2018** leaves the generation of the vertical force unregulated in open-loop and, hence, does not require reading phase currents. This results in less positioning error noise. Therefore, two alternative strategies with different functionalities are proposed. The advantages and disadvantages of each of them must be analysed for each application. In the specific case of the NanoPla, levitation is provided by the airbearings which have a stiffness of 13 N/µm that will counteract the variations of the vertical force generated by the motors. Thus, in this case, positioning accuracy is preferred over levitation force control.

The positioning sensor of the NanoPla is a 2D laser system consisting of the combination of three commercial plane mirror interferometers. Two beams are needed to measure the displacement in X and Y-axes, respectively. In addition, the displacement in Y-axis is measured by two parallel beams that reflect on the same plane mirror. This allows measuring the rotation in the XY-plane, apart from the X and Y-displacements. The accuracy of the laser system measurements depends on the accuracy to which the laser beam wavelength is determined. The wavelengths of the three laser interferometers of the NanoPla have been calibrated by the manufacturer and their traceability is direct. Furthermore, the laser system includes an environmental control unit that corrects the errors caused by the refractive index variations. Nevertheless, in a 2D laser system there are also geometrical errors derived from the laser system assembly that need to be corrected to obtain an accurate measurement. In **Sensors 2017**, a self-calibration procedure for the geometrical characterisation of a 2D laser system operating along a range of 50 mm × 50 mm is presented. The advantage of self-calibration respect to direct calibration methods is that a calibrated artefact is not required. This is especially relevant when working in submicrometre scale in a large range, due to the difficulty in finding a reliable calibrated artefact at this scale. In the developed procedure, a grid encoder is proposed as non-calibrated artefact. The target of this procedure is to know and correct the geometric errors of a 2D laser system setup generated when positioning the laser heads and the plane mirrors in the assembly. The article, first, describes the methods and materials used for the procedure, including the experimental setup. Then, the mathematical model of the 2D laser system assembly is analysed. There are three geometrical errors that need to be corrected: the pitch errors of the X and Y-laser beams, that are a 1D error that appears when the laser beams are not coplanar to the XY-plane of motion, and the orthogonality error, that is a 2D error caused by the non-orthogonality between the X and Y plane mirrors. Afterwards, the self-calibration procedure is described: by recording measurements of the grid encoder at three different positions it is possible to isolate the laser system errors, and, thus, correct them. Once the laser system geometrical errors are known, its corrected readouts can be used to calculate the measurement and squareness errors of the grid encoder. The correct performance of the self-calibration procedure is experimentally validated by comparing the errors obtained for the grid encoder with the ones specified by the manufacturer for the main axes in its calibration certificate. The standard uncertainty of the calibrated laser system is calculated to be 99 nm in both axes. Finally, the article assesses the expanded calibration uncertainty of the grid encoder.

The results obtained in **Micromachines 2018**, **Electronics 2018** and **Sensors 2017** are integrated in the work presented in **Procedia Manufacturing 2019**. In this article, the positioning control system is extended to the four Halbach linear motors of the NanoPla that generate 2D planar movement in the whole working range. Firstly, the components of the control system and the connections between them are described. The four Halbach linear motors are set in parallel pairs, in a manner that each pair generates a force in X and Y-axes, respectively. The previously introduced 2D plane mirror laser interferometer system works as positioning sensor in the XY-plane. Moreover, a DMC kit from Texas Instruments drives and generates the phase voltages of each linear motor. The control strategy is computed in a host PC that communicates with the control hardware and the positioning sensor, and includes a user interface to input the target position. Then, in the article, the 2D positioning control strategy is presented. Positioning of the platform in the XY-plane is achieved by acting on the total forces generated in X and Y-axes by the motor pairs. To prevent the misalignment of laser beams and plane mirrors, the rotation around Z-axis is constrained by acting on the torque generated by the four motors. The control strategy is implemented in the NanoPla and the experimental results are shown to demonstrate its correct performance. Finally, in the article, the positioning uncertainty of the control system is assessed. The main contributors to the positioning uncertainty are the resolution of the voltage generation modules, the errors derived from the electronic devices noise and the standard uncertainty of the 2D laser system, once the geometrical errors have been corrected by means of the self-calibration procedure previously proposed. The obtained positioning uncertainty in the XY-plane ($k=2$) is equal to ±0.50 µm in each axis and in all the working range of the NanoPla, 50 mm × 50 mm. The resultant positioning uncertainty of the control system is much lower than the NanoPla initially required accuracy, broadening the applicability scope of the designed positioning system.

The NanoPla has been designed to work together with different kinds of tools and probes in various applications such as metrology or nanomanufacturing. In some nanomanufacturing applications, nanopositioning stages are required to follow a predefined trajectory with a submicrometre precision [99]. Defining a complex trajectory in a CAD/CAM system is not always a simple task. They are commonly defined by curve fitting which results in fitting errors that, even though in traditional manufacturing systems are negligible, in nanopositioning stages like the NanoPla, can be of the same order or greater than the positioning control system error. In the specific case of the NanoPla, the trajectory definition errors are required to be one order of magnitude lower than the positioning uncertainty of the control system, that is 0.05 µm, in order not to significantly affect the final positioning accuracy of the system.

Therefore, an accurate curve fitting method capable of offering high accuracy in the position definition along the whole trajectory is required. In order to address this problematic, a collaborative project was started with a research group of the Department of Applied Mathematics at the University of Zaragoza that is focused on Computer Aided and Geometrical Design (CAGD). In this project, a novel method for the parametric representation of curves allowing curve fitting with high relative accuracy (HRA) was proposed for the definition of curve trajectories in CAGD. This work is presented in the Subsection 3.3.3 of this thesis. Sets of given data points are curve fitted by interpolation and least squares approximation with the proposed HRA method and CAD/CAM software. In every case, the curve fitting operation is required to fulfil the tolerance of 0.05 µm. The resultant fitting errors and the complexity of the fitting curve, i.e. the number of control points, are analysed for every case. In contrast to traditional CAD/CAM methods, the HRA method is capable of obtaining a fitting curve with fewer number of control points without compromising the fitting errors. As a result, the proposed HRA method offers a better trajectory definition accuracy than commonly used CAD/CAM methods when defining a trajectory by curve fitting (interpolation or least squares approximation). In conclusion, the implementation of the HRA method in CAD/CAM systems can be highly beneficial when defining trajectories for nanopositioning systems with a submicrometre accuracy, like the NanoPla.

2.2. Summary of the publications

2.2.1. Micromachines 2018: One-dimensional control system for a linear motor of a two-dimensional nanopositioning stage using commercial control hardware

This article introduces the positioning system of the NanoPla and its requirements. As a first approach to the 2D positioning control system problematic, it presents a 1D positioning control system of a Halbach linear motor using a commercial hardware to drive and generate phase voltages. The integration of a completely generic control hardware with unguided linear motor actuators is a novelty that could not be found in the literature. Such integration facilitates the applicability and reproducibility of the developed control system. Nevertheless, it presents many limitations that need to be overcome by adapting and optimising the design of the control strategy and its implementation. The article is organised as follows:

- Introduction
- NanoPla overview
- Halbach linear motors
- Experimental setup and hardware description
- Dynamic characterisation
- One-dimensional control strategy and hardware implementation
- Experimental results
- Conclusions

Introduction and NanoPla overview

Firstly, the article introduces the NanoPla and justifies the selection of Halbach linear motors as actuators and a commercial solution as control hardware. In the NanoPla, Halbach linear motors enable planar motion in the large working range of 50 mm × 50 mm. Halbach linear motors are not commercialised, thus, they have been custom-made for this application. Nevertheless, one of the design criterions of the NanoPla is to implement as many commercial components as possible to facilitate a future industrial applicability of the developed system. Therefore, instead of designing and building the control hardware for the linear motors, as it has been done in other works [59, 62, 70, 71], a commercial solution for the hardware has been selected. That is the Digital Motor Control kit from Texas Instruments, a generic hardware for the control and drive of rotary BLDC and PMSM where the aim is to control the torque and speed of the rotor.

In order to define the working requirements of the positioning control system, an overview of the NanoPla is presented. The positioning system needs to be able to work in a range of 50 mm, the positioning error should be less than 10 µm and oscillation in the transient response should be avoided.

Halbach linear motors

This section describes the working principle of the Halbach linear motors of the NanoPla. The linear actuators used in the NanoPla were developed by Trumper et al. [47] and are custom-made in the Center for Precision Metrology of the University of North Carolina at

Charlotte. These Halbach linear motors consist of a three-phase ironless stator and a Halbach permanent magnet array, as shown in Figure 2.1.

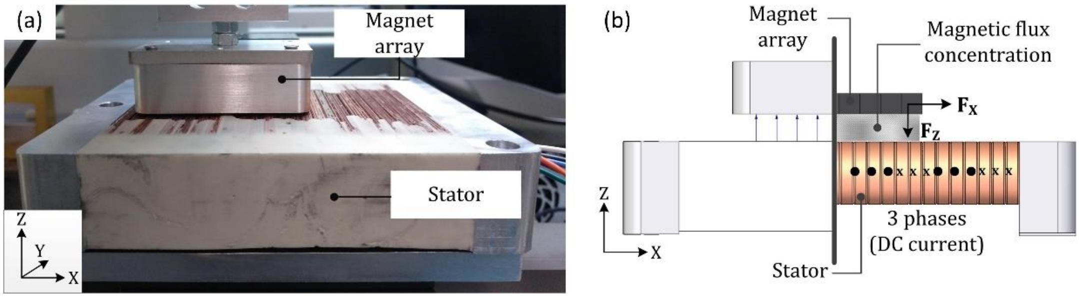

Figure 2.1. *(**a**) Halbach motor (magnet array and stator); (**b**) graphical representation of the dual forces generated by the Halbach motor.*

In a Halbach linear motor, when the current flows through the three-phase coils, they generate an electromagnetic interaction together with the magnetic flux generated by the Halbach permanent magnet array, resulting in two orthogonal forces, one horizontal (F_x) and the other, vertical (F_z). The amplitude of the generated forces is dependent on the magnitude of the phase currents (I_a, I_b and I_c), as well as, on the relative position between stator and magnet array (x_0), along the axis of movement, as defined by the motor law (Equation 1):

$$\begin{bmatrix} F_x \\ F_z \end{bmatrix} = A \begin{pmatrix} \cos\left(kx_o+\varphi\right) & \cos\left(kx_o-\frac{2\pi}{3}+\varphi\right) & \cos\left(kx_o+\frac{2\pi}{3}+\varphi\right) \\ \sin\left(kx_o+\varphi\right) & \sin\left(kx_o-\frac{2\pi}{3}+\varphi\right) & \sin\left(kx_o+\frac{2\pi}{3}+\varphi\right) \end{pmatrix} \begin{bmatrix} I_a \\ I_b \\ I_c \end{bmatrix} \qquad (1)$$

where A and k are constant parameters that depend on the motor design, specifically, k is the fundamental wave number which defines the spatial period of the motor, called pitch. In [17], the NanoPla linear motors were experimentally characterised and the value of these parameters was obtained. The article provides a description of these parameters and their theoretical and experimental value. In addition, the initial position of the motor ($x_0=0$) can be adjusted by changing the phase difference φ. In this paper, for simplicity reasons, the value of φ is considered null.

The phase currents that are required to generated certain forces (F_x and F_z) in a specific position (x_0) can be calculated by performing the inverse of the motor law, that is, the commutation law. Nevertheless, the inverse of Equation 1 has an infinite set of solutions. Other works [59, 62, 70, 71] where the phase currents were controlled independently by transconductance power amplifiers, implemented constraints of minimum power and power symmetry optimisation. Nevertheless, in the NanoPla application, phase voltages are controlled by the DMC kit from Texas Instruments. This control hardware forces the star-connection of the phases, impeding controlling the three phases independently and imposing the following constraint:

$$I_a + I_b + I_c = 0 \tag{2}$$

Therefore, the commutation law of the Halbach linear motors considering the control hardware constraint is defined as follows:

$$\begin{bmatrix} I_a \\ I_b \\ I_c \end{bmatrix} = \frac{2}{3A} \begin{pmatrix} \cos kx_o & \sin kx_o \\ \cos\left(kx_o - \frac{2\pi}{3}\right) & \sin\left(kx_o - \frac{2\pi}{3}\right) \\ \cos\left(kx_o + \frac{2\pi}{3}\right) & \sin\left(kx_o + \frac{2\pi}{3}\right) \end{pmatrix} \begin{bmatrix} F_x \\ F_z \end{bmatrix} \tag{3}$$

Experimental setup and hardware description

The validation of the 1D positioning control system of a Halbach linear motor has been carried out in an experimental setup separated from the NanoPla. The setup consists of a pneumatic linear guide that allows frictionless linear motion between parts. The stator is mounted over the linear guide, while the magnet array is fixed to a static bridge part, as shown in Figure 2.2. The control hardware is the same DMC kit that is considered for the NanoPla positioning system. In addition, as positioning sensor, a Renishaw XL-80 interferometer has been used. The readouts of the laser sensor are send to a host PC that communicates with the control hardware and also acts as an interface for the user.

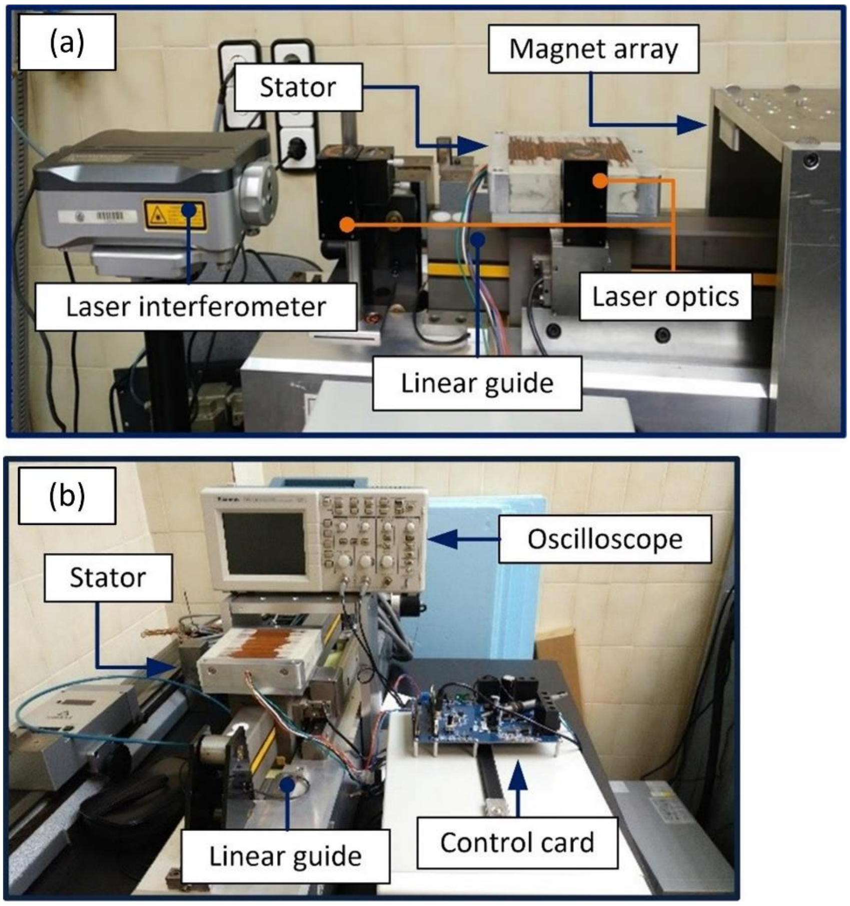

***Figure 2.2**. Lateral (**a**) and front (**b**) view of the experimental setup for the implementation of the control system of one linear motor.*

Dynamic characterisation

In this section, the system is characterised by observing and understanding its dynamic behaviour, in contrast to other works that focus on an electromechanical modelling [47]. The conditions at the equilibrium position of the motor are analysed and, based on this, an open-loop positioning system is proposed.

The magnitudes of the resultant horizontal and vertical forces generated by certain phase current values along the axis of movement (X) have been represented in Figure 2.3. Each of the three phase currents generates a horizontal force (F_{X1}, F_{X2} and F_{X3}) and a vertical force (F_{Z1}, F_{Z2} and F_{Z3}), whose sum is the total horizontal force F_X and the total vertical force F_Z. The horizontal force F_x is the only thrust force that acts along the axis of movement, and, thus, is the one that performs the motion. Therefore, the moving part of the motor remains motionless in the equilibrium positons where the trust force is null. There are two types of equilibrium positions, depending on the slope of the force at that point: stable equilibrium position (negative slope) and unstable equilibrium position (positive slope). As can be observed in the Figure, in stable equilibrium positions, the levitation force is positive, that is, the stator attracts the magnet array, favouring its levitation when the motor is placed in an upside-down position, as in the NanoPla.

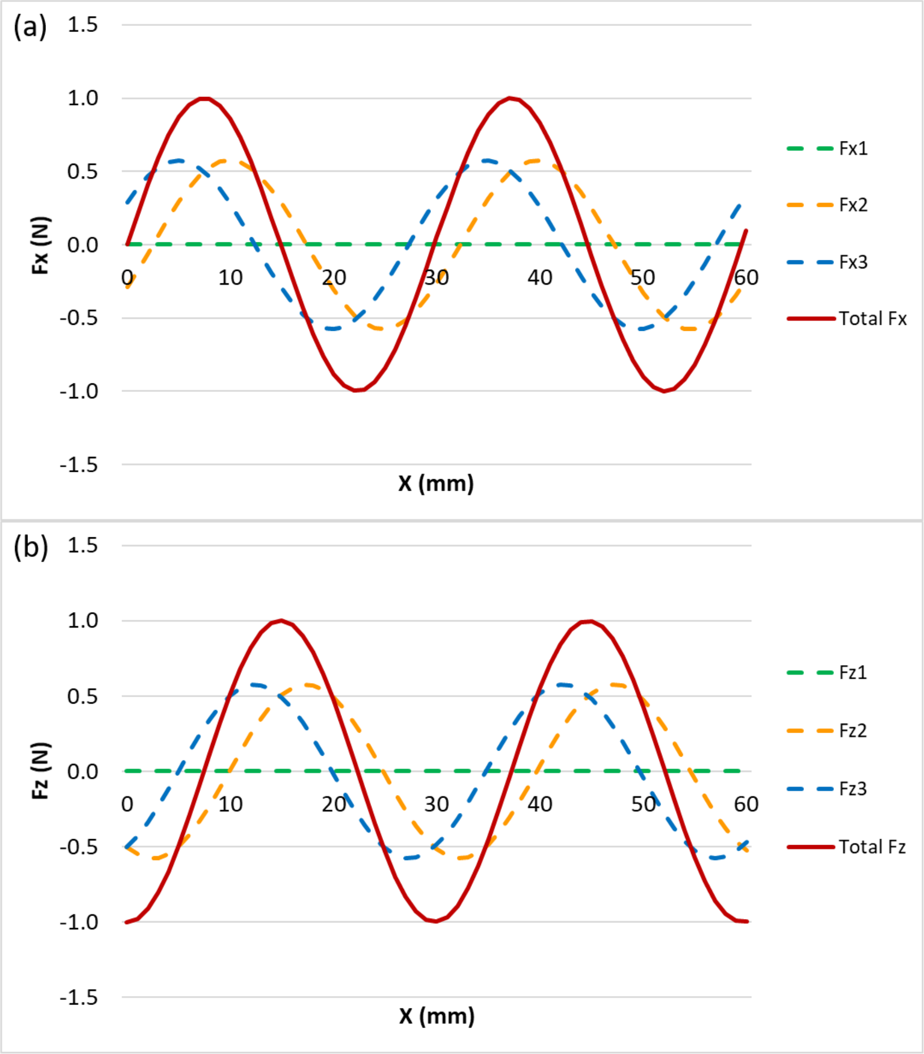

Figure 2.3. *F_x (**a**) and F_z (**b**) along the axis of movement, for $I_a = 0$ A; $I_b = 0.3593$ A; $I_c = -0.3593$ A.*

In a stable equilibrium position, when displaced from equilibrium, the electromagnetic thrust force acts as a controller that opposes to this displacement, returning it back to the stable equilibrium position. At this position, the vertical force results in attraction between stator and magnet array and the thrust force is null. By introducing these conditions in the commutation law (Equation 3), the required currents that create this state of stable equilibrium at a certain position ($x_0=x_{ref}$ in the equation) can be obtained. This electromagnetic controller does not require a positioning sensor. Nevertheless, the most significant disadvantage of this sensorless controller is its inaccuracy, since, without a positioning sensor, it cannot correct the positioning error. Moreover, the sensorless controller displaces the motor to the nearest stable equilibrium state, hence, it cannot perform steps longer than half pitch, that is 14.88 mm. The scheme of the open-loop positioning strategy has been represented in Figure 2.4.

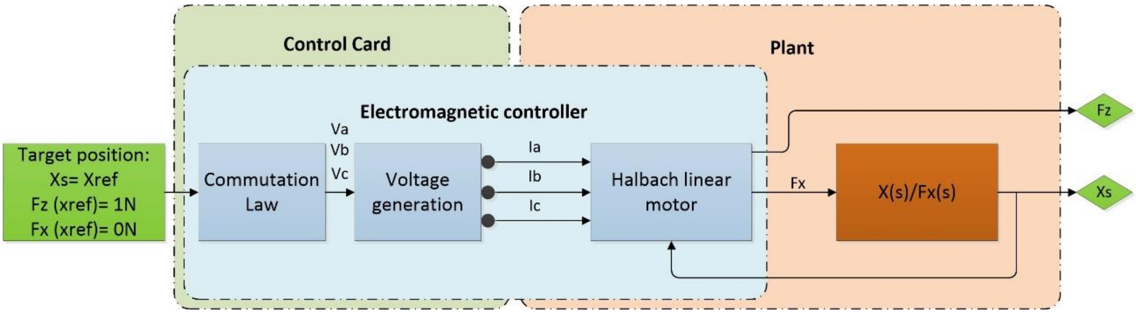

Figure 2.4. *Scheme of the linear motor system working as an electromagnetic controller.*

One-dimensional control strategy and hardware implementation

After studying the dynamic behaviour of the system, a closed-loop control strategy is proposed in this section. Firstly, a positioning sensor is implemented. The readouts of this positioning sensor are used as feedback in a proportional-integral-derivative (PID) controller that has as input the reference position. The PID controller corrects the positioning error by acting on the thrust force generated by the motor. The phase currents that are required to produce this force must be generated by the control hardware. As mentioned, the control hardware drives and generates phase voltages by high-resolution PWM and forces the star-connection of the phases. The control system resulting from the implementation of the control strategy in the hardware has been represented in Figure 2.5. The details of this implementation are explained in the article.

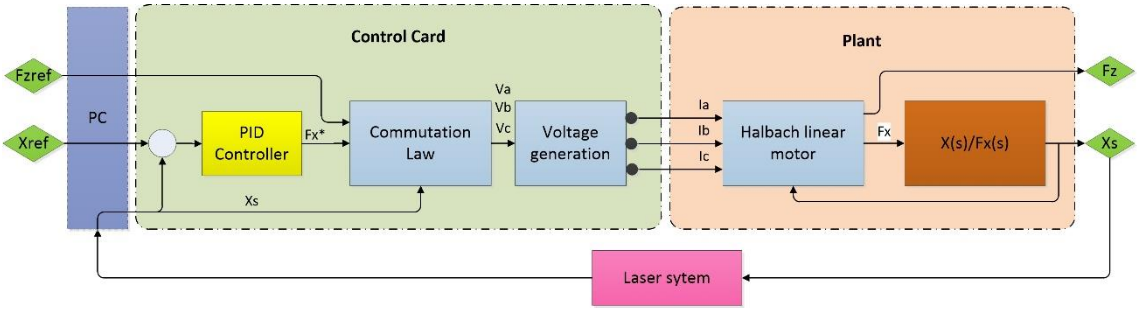

Figure 2.5. *Implementation of the one-dimensional (1D) control strategy in the control hardware.*

Experimental results and conclusions

Once the control strategy has been implemented in the control hardware, the performance of the control system is experimentally validated. Firstly, the performance of the electromagnetic sensorless controller is analysed. It is confirmed that the sensorless positioning system is able to work in the full range of 50 mm when the input is introduced as a ramp instead of as a step. Nevertheless, as predicted, it is unable to correct the positioning error, which increases for longer travels.

Then, the positioning sensor and the closed-loop control strategy are implemented and the PID is experimentally tuned. It has been verified that the system fulfils the working requirements of the NanoPla, which is a working range of 50 mm (Figure 2.6a) and a step response of 10 µm. It was also tested that the system is able to respond to steps of 1 µm (Figure 2.6b).

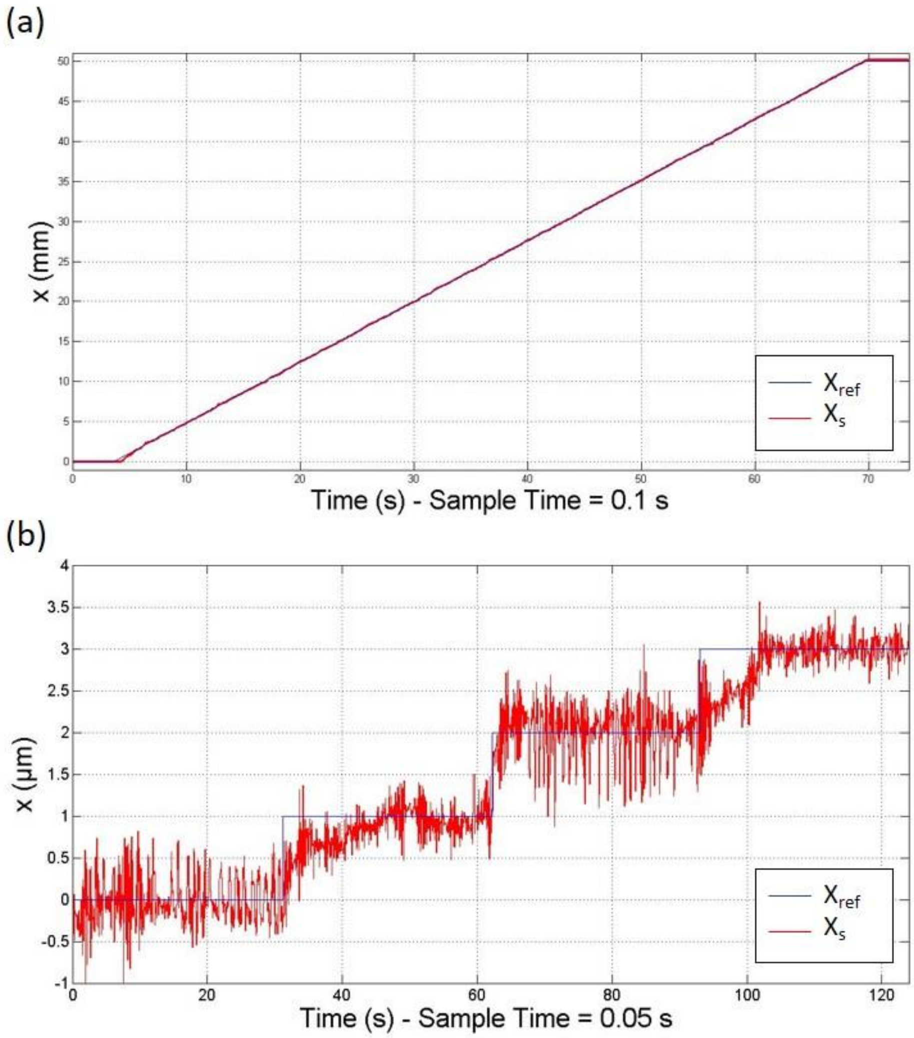

Figure 2.6. *(**a**) Closed-loop PID controller: 50 mm travel range at constant speed; (**b**) Closed-loop PID controller: 1-µm staircase response.*

This control strategy controls the position by acting on the thrust force, while leaving the control of the levitation force in open-loop. Namely, a reference value is set for the levitation force but its real value is not monitored nor corrected. Nevertheless, the vertical force generated by the motor has been experimentally measured with a load cell: it is constant at steady state and it varies slightly (+7%) during the transient period of a 5-mm step response, that is, when the motor is moving to the target position. In the NanoPla, although the motors favour the levitation of the moving platform, the main support is provided by three air bearings, with a stiffness of 13 N/µm. Thus, the airbearings are able to absorb the variations of the linear motor levitation forces, considering that the they are set to a maximum value of 2 N.

In conclusion, the performance of the developed control strategy implemented in the generic DMC kit is capable of fulfilling the working requirements of the NanoPla. Therefore, the use of more advance control devices is unnecessary for this application.

2.2.2. Electronics 2018: Vector control strategy for Halbach linear motor implemented in a commercial control hardware

The control strategy presented in **Micromachines 2018** controlled the position by acting on the thrust force, while leaving the generation of the levitation force uncontrolled in open-loop. Nevertheless, in some applications, controlling the levitation force during the transient and stationary state can be of interest. Therefore, **Electronics 2018** proposes a vector control strategy that decouples the control of the vertical and horizontal forces generated by a Halbach linear motor. Thus, it enables the positioning of the motor by acting on the thrust force, while regulating the vertical force that can be used as support for levitation. This strategy is implemented in the DMC kit from Texas Instruments for generic three-phase PMSM. The control strategy is first validated by a simulation that includes the plant modelling, hardware modules and the error contributors. Then, performance of the vector control strategy implemented in the control hardware is experimentally validated. The article is organised as follows:

- Introduction
- Halbach linear motors
- Experimental setup
- Vector control strategy
- Control hardware implementation
- Experimental results
- Conclusions

<u>Introduction</u>

Halbach linear motors present highly effective advantages in precision engineering, such as being capable of providing planar motion in large range applications. For this reason, they have been implemented as actuators in nanopositioning stages, like the NanoPla. Apart from the thrust force necessary for positioning, Halbach linear motors provide a vertical force that can be leverage for the levitation of the moving part. In the specific case of the NanoPla, this levitation force is combined with airbearings that provide the main support for levitation. Nevertheless, in other applications [65], the moving part is magnetically levitated solely by Halbach linear motors. Therefore, this article proposes a vector strategy that allows separately controlling the vertical and the horizontal force generated by the motor. In addition, the proposed control strategy is implemented in a commercial control hardware, which facilitates the applicability and replication of the developed control strategy.

<u>Halbach linear motors</u>

The working principle of Halbach linear motors was explained in the previous subsection: The interaction between the magnetic field of the magnet array and the currents flowing through the phases results in two orthogonal forces, one vertical and the other horizontal. The magnitude of the generated forces depends on the phase currents values and the relative position between stator and magnet array, as defined by the motor law (Equation 1).

In **Micromachines 2018**, a dynamic characterisation of the system, when functioning as a positioning actuator, was performed and the conditions to create a stable equilibrium state at a certain position were defined. That is, the thrust force must be null with a negative slope and the vertical force has to result in attraction between stator and magnet array, favouring the levitation of the magnet array when the motor is positioned upside-down, like in the NanoPla. In this article, the behaviour of the linear motor around the equilibrium position is modelled as a servosystem that consists in the electromagnetic force that depends on the relative position between stator and magnet array, and the load elements of the setup. Moreover, around the equilibrium position, the electromagnetic force can be considered lineal (see Figure 2.7), thus, it behaves as a proportional controller (K). The value of the proportional constant K is calculated in the linear zone as the slope of the thrust force (F_x). The value of K is defined by the magnitude of the vertical and horizontal forces that is dependent on the maximum value set for the vertical force at stationary state, that is, at the target position.

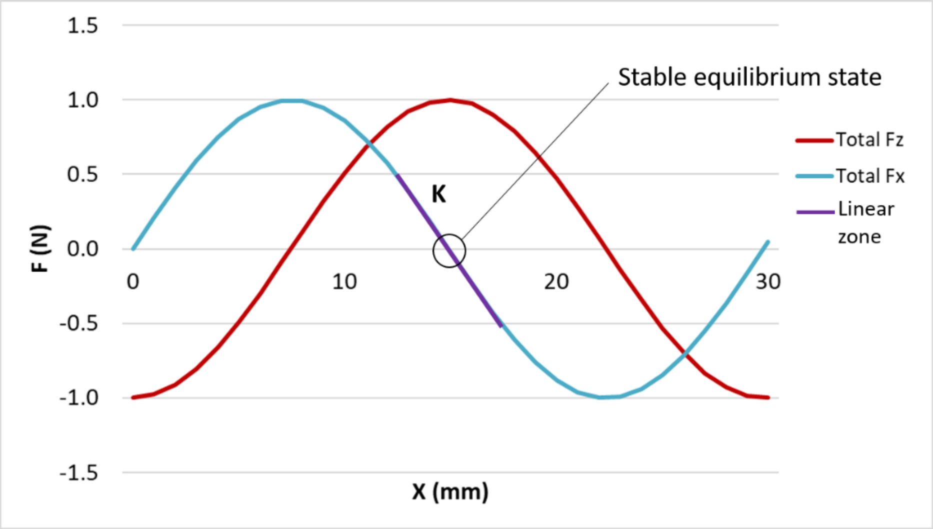

Figure 2.7. *Linear zone around the stable equilibrium position.*

Then, the electromagnetic force generated by the motor is dependent on its position and acts on the moving part, keeping it at stable equilibrium state. Moreover, the moving part of the system that has frictionless motion can be modelled as an inertia-damping system, that includes the mass of the moving part (m) and the viscous-friction elements (b) of the setup. In Figure 2.8, the model of the system has been simplified for the linear zone.

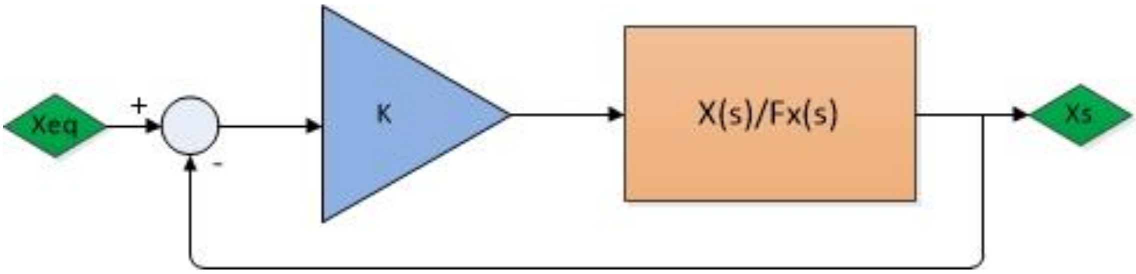

Figure 2.8. *Plant model in the linear zone of the electromagnetic force.*

The closed-loop transfer function models the final position of the system (X_s) as a function of the stable equilibrium position that has been set (X_{eq}), and, in the linear zone, it is expressed by Equation 4.

$$\frac{X(s)}{X_{eq}(s)} = \frac{\frac{K}{m}}{s^2 + \frac{b}{m}s + \frac{K}{m}} \tag{4}$$

Experimental setup

The setup used for the experimental validation of the control strategy implements the same pneumatic linear guide that was used in **Micromachines 2018** to provide frictionless linear motion to the stator, while the magnet array remains static. Nevertheless, in this setup, the magnet array has been attached to a load cell, in order to measure the vertical force generated by the motor. A scheme of the experimental setup is represented in Figure 2.9. In this setup, as in the previous case, the Renishaw XL80 laser system has been used to provide position feedback and the control hardware is the DMC kit from Texas Instruments that will be implemented in the NanoPla.

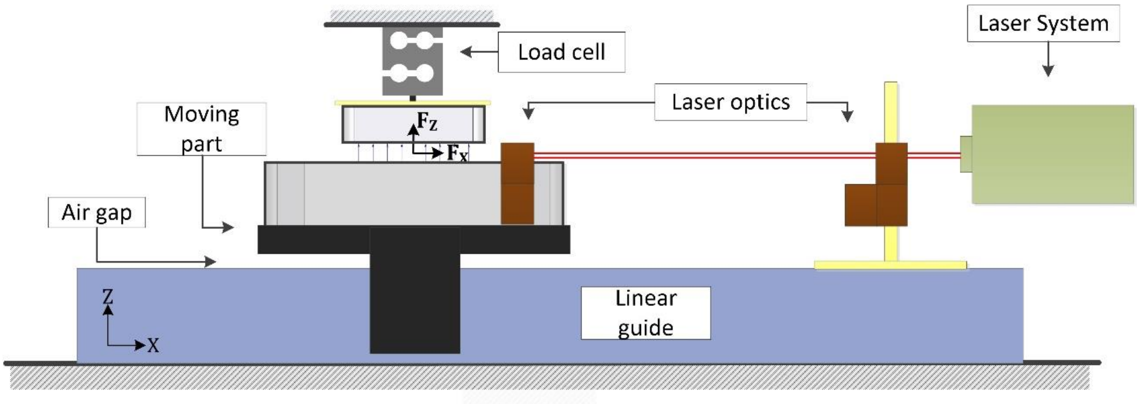

Figure 2.9. *Experimental setup scheme.*

Vector control strategy

When current flows through the phases of a linear motor, two orthogonal forces are generated, a horizontal force and a vertical force. While the horizontal force is the thrust force that displaces the motor to the target position, the vertical force can be used for levitation of the moving part. Therefore, in order to control the position of the motor and the levitation force separately, it is necessary to decouple the generation of the vertical and the horizontal forces. Nevertheless, according to the motor law (Equation 1), it is unfeasible to do so by acting directly on the phase currents.

A similar issue arises in rotary motors, where the electromagnetic interaction results in torque and magnetic flux. In these motors, the torque production is magnified when the magnetizing flux generation is kept minimal. Therefore, the control of the rotor magnetizing flux and the torque needs to be decoupled. This is done by means of a Clarke-Park transformation (Equation 5), that defines a direct and a quadrature (d-q) virtual axes that rotate with the rotor at the rotating flux vector speed. By a change of basis, the phase currents are transformed into the direct axis component (I_d) that exerts a magnetizing effect on the reference flux and the quadrature axis component (I_q) that produces the torque.

$$\begin{bmatrix} I_d \\ I_q \end{bmatrix} = \begin{pmatrix} \cos kx_o & \cos\left(kx_o - \frac{2\pi}{3}\right) & \cos\left(kx_o + \frac{2\pi}{3}\right) \\ \sin kx_o & \sin\left(kx_o - \frac{2\pi}{3}\right) & \sin\left(kx_o + \frac{2\pi}{3}\right) \end{pmatrix} \begin{bmatrix} I_a \\ I_b \\ I_c \end{bmatrix} \tag{5}$$

In a three-phase Halbach linear motor, the motor law (Equation 1) can be combined with the Clarke-Park transform (Equation 5) to decouple the generation of the vertical (F_z) and horizontal (F_x) forces:

$$\begin{bmatrix} F_x \\ F_z \end{bmatrix} = A \begin{bmatrix} I_d \\ I_q \end{bmatrix} \tag{6}$$

The Clarke-Park transform exerts a different effect in Halbach linear motors than in rotary motors. The virtual direct current (I_d) produces the thrust force, hence, I_d naturally tends to zero as the motor reaches the target position. The virtual quadrature current (I_q) produces the levitation force, that should be kept at a constant value and it attains its maximum value when F_x is null.

Once the generation of the two forces is decoupled, each of them can be regulated by two independent proportional-integral (PI) controllers having as input the reference virtual currents, I_{dref} and I_{qref}, and the actual virtual currents, I_d and I_q. The reference virtual currents are proportional to the desired horizontal and vertical forces. The actual virtual currents feedback is obtained by measuring the phase voltages and performing the Clarke-Park transform. In addition, the controllers correct the values of the virtual currents by acting on the direct and quadrature voltages. Nevertheless, the control hardware power stage generates phase voltages, thus, the phase voltages that correspond to the virtual direct and quadrature voltages at a certain position need to be calculated. This is achieved by performing an inverse Clarke-Park transform that considers the star-connection of phases (Equation 2) constraint. The inverse Clarke-Park transform is represented in Equation 7 and, as it can be seen, it is similar to the commutation law obtained in **Micromachines 2018**.

$$\begin{bmatrix} V_a \\ V_b \\ V_c \end{bmatrix} = \frac{2}{3} \begin{pmatrix} \cos kx_o & \sin kx_o \\ \cos\left(kx_o - \frac{2\pi}{3}\right) & \sin\left(kx_o - \frac{2\pi}{3}\right) \\ \cos\left(kx_o + \frac{2\pi}{3}\right) & \sin\left(kx_o + \frac{2\pi}{3}\right) \end{pmatrix} \begin{bmatrix} V_d \\ V_q \end{bmatrix} \tag{7}$$

Therefore, the control strategy is computed as follows: The resultant vector control strategy implements a main PID controller that corrects the positioning error by acting on the thrust force. Subsequently, a PI controller regulates the thrust force by acting on V_d. Simultaneously, another PI controller regulates the levitation force by acting on V_q. By performing a Clarke-Park transform, the corresponding phase voltages that need to be generated are obtained. In order to obtain the feedback for the PI controllers, the phase currents must be sampled and, by an inverse Clarke-Park transform, transformed into the virtual currents I_d and I_q. An scheme of the vector control strategy has been represented in Figure 2.10. As shown, the position of the motor must be known at every moment to perform the Clarke-Park transformation and its inverse.

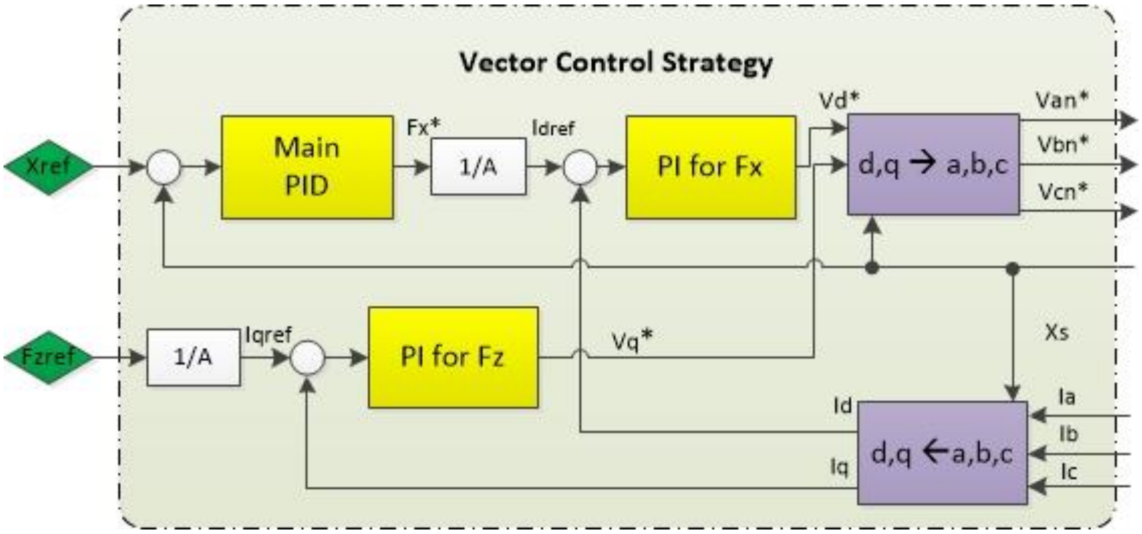

***Figure 2.10**. Scheme of the vector control strategy.*

Control hardware implementation

The vector control strategy is implemented in the selected DMC kit. As mentioned, this control hardware has been designed for generic rotary motors. Vector control is a common control strategy in rotary motors, thus, the hardware integrates a module that enables current sensing for vector control. The article explains the control hardware characteristics and control strategy implementation. It is stated that voltage generation and current sensing are the two main functions that affect the performance of the control system.

The selected control hardware generates phase voltages by pulse width modulation (PWM). The performance of the PWM module can be optimised by adjusting its settings to maximise its resolution and minimise the current ripple. In addition, the digital signal processor (DSP) includes a high resolution PWM (HRPWM) function that extends the time resolution capabilities of the PWM module.

The control hardware also includes a current sensing module. The phase currents are sensed at the inverter legs low side of the three-phase transistors bridge, then, analogue to digital converters (ADC) convert the measurements into a 12-bit integer. The ADCs must be synchronised with the PWM in order to measure the average current. In the article, the resolution and stability of the current sensing module is assessed.

Experimental results and conclusions

The vector control strategy implementation in the control hardware is validated, first, virtually and, then, experimentally. The virtual validation is carried out in Simulink®, in a simulation that includes the dynamic model of the plant that has been experimentally obtained, the resolution limitations of the control hardware and the current sensing noise. This simulation allows determining the effects of each error introduced in the model. It reveals that the main contributors are the current sensing noise; that includes the own phase currents noise, the positioning sensor noise and its sample time.

The correct performance of the positioning control system has been experimentally validated along the working range of the linear motors of 50 mm. In addition, to verify that the vector control is performed correctly, the variation of the vertical force when the motor moves from being static to a target position has been measured and compared for different cases: open-loop positioning, closed-loop with a position controller (strategy presented in **Micromachines 2018**) and closed-loop with the vector control strategy presented in this work. The results for a displacement of 5 mm have been represented in Figure 2.11. In this Figure the two variables that are being controlled (displacement in X-axis and F_z) have been represented during the transient response. As it can be seen, when vector control is not applied, the vertical force is not regulated and it does not attain its target value. In contrast, when applying vector control the target value is attained and the variations of F_z during the transient response can be adjusted and minimised by tuning its controller.

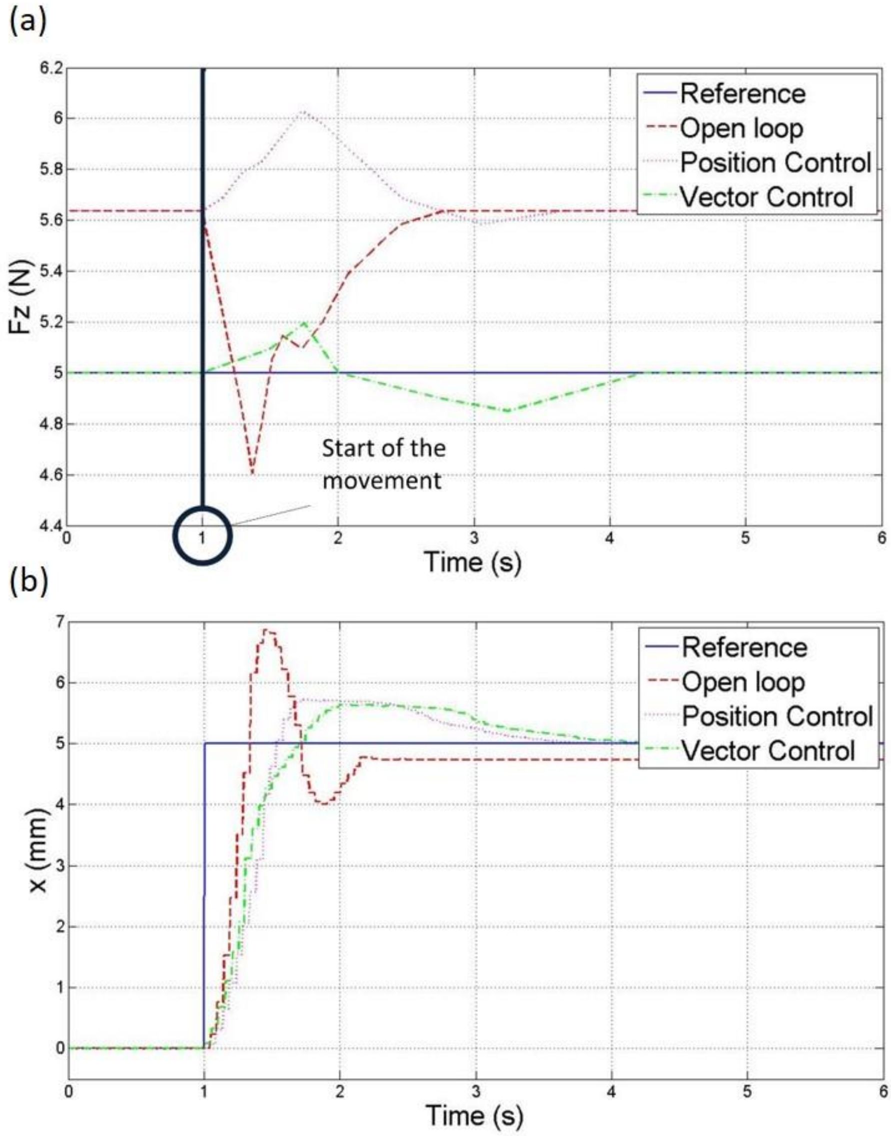

***Figure 2.11**. Experimental result: Variation of vertical force (**a**) and position (**b**) during movement of motor.*

In conclusion, in **Electronics 2018** a vector control strategy typically applied in rotary motors has been implemented in a Halbach linear motor. The proposed vector control strategy decouples the control of the two orthogonal forces generated by the motor. Thus, position control can be performed while simultaneously regulating the levitation force. The proposed control strategy has been implemented in the selected commercial control hardware, which facilitates the future replication of the system. Nevertheless, the performance of the control system is limited by the resolution and noise of the current sensing module of the hardware. In the positioning control strategy presented in **Micromachines 2018**, this error contributor was not present because current sensing was not implemented. Therefore, in the two articles, alternative control strategies are proposed. Each of them presents advantages and disadvantages that need to be studied for each application. That is, the positioning control strategy presented in **Micromachines 2018** has less error contributors and, thus, better positioning accuracy. Nevertheless, the levitation force is left uncontrolled in open-loop, in contrast to the vector control strategy presented in **Electronics 2018**.

2.2.3. Sensors 2017: Geometrical characterisation of a 2D Laser system and calibration of a cross-grid encoder by means of a self-calibration methodology

In the NanoPla, a 2D laser system consisting of the combination of three commercial plane mirror interferometers works as positioning sensor. In a positioning system, the positioning sensor accuracy is one of the main contributors to the final positioning system uncertainty. Although each laser interferometer of the NanoPla has been individually calibrated by the manufacturer, the 2D laser system assembly presents geometrical errors that need to be corrected in order to perform accurate 2D positioning. In **Sensors 2017**, a self-calibration procedure that characterises the geometrical errors of a 2D laser system assembly is proposed. Once the geometrical errors are known, the laser system readouts can be corrected, improving its accuracy. The article is divided as follows:

- Introduction
- Description of the methods and materials used for the procedure
- Mathematical model of the laser system
- Self-calibration procedure
- Geometrical characterisation of the laser system setup
- Calibration of the grid encoder
- Discussion and conclusions

Introduction

In the NanoPla, the positioning sensor is based on a combination of plane mirror laser interferometers. These sensors have been selected for its suitability to measure planar motion and to achieve excellent accuracy in large working ranges. In addition, they offer direct traceability. Nevertheless, the geometrical errors caused by the difference between the theoretical alignments and the real assembly result in systematic errors that increase the measurement uncertainty of the system. Calibration techniques are capable of determining the systematic errors in positioning sensors. However, commonly used direct calibration methods require a calibrated artefact more accurate than the system to be calibrated, which can be complicated and costly when working in such a small scale in a large range. Self-calibration methods provide a solution to this issue. By relating views of a non-calibrated artefact, they are able to isolate systematic errors. Therefore, this work presents a self-calibration procedure for the characterisation of the geometrical errors of a 2D laser system assembly, where a grid encoder is used as a non-calibrated artefact.

Description of the methods and materials used for the procedure

The 2D laser system belongs to the Renishaw RLE10 laser interferometer family. It consists of a laser unit (RLU), two sensor heads (RLD), two plane mirrors (one per axis), and an environmental control unit (RCU). In addition, an external interpolator is used to reduce the expected resolution of the system from 9.88 nm to 1.58 nm. In the 2D laser system that has been subject of the calibration, two laser beams are considered. The non-calibrated artefact is a KGM 181 cross-grid encoder (Heidenhain GmbH) with a circular working range of 140 mm in diameter. Although the whole range of the grid encoder is not calibrated, the manufacturer provides a calibration certificate of its central X and Y-axes.

The methodology has been the following: The laser system and the grid encoder are moved simultaneously along a mesh of points in the considered working range, equal to the working range of the NanoPla (50 mm × 50 mm), while taking measurements. This step has been repeated for different views (positions) of the grid encoder. Then, the self-calibration procedure explained in the following sections is applied. Once the geometric errors are isolated and the laser system readouts are corrected, the corrected laser system measurements are used to calibrate the grid encoder. The uncertainty of the laser system as well as the uncertainty of the calibration of the grid encoder are assessed. Finally, the self-calibration procedure is validated by comparing the errors along the axes of the grid encoder obtained through the calibration with the ones provided by the calibration certificate of the manufacturer.

In a calibration performed at a submicrometre resolution, the design of the experimental setup can significantly affect the accuracy of the final result. In this procedure, the experimental setup designed in a previous work [100] has been used. It consists of a metrology frame that has two thermally stable parts that are placed one above the other. The metrology frame is attached to a positioning machine that provides relative motion between the two parts. The plane mirrors and the grid encoder scanning head are fixed to the upper metrology frame that, in turn, is attached to the arm of the machine that remains static during the procedure. The laser heads and the grid plate of the grid encoder are fixed to the lower metrology frame, which is placed in the positioning table that moves in the XY-plane. The experimental setup is shown in Figure 2.12. In addition, Abbe errors in the X and Y-axes have been minimised by aligning the grid encoder scanning head and the X and Y laser sensors in Z-axis at the central position of the measuring range.

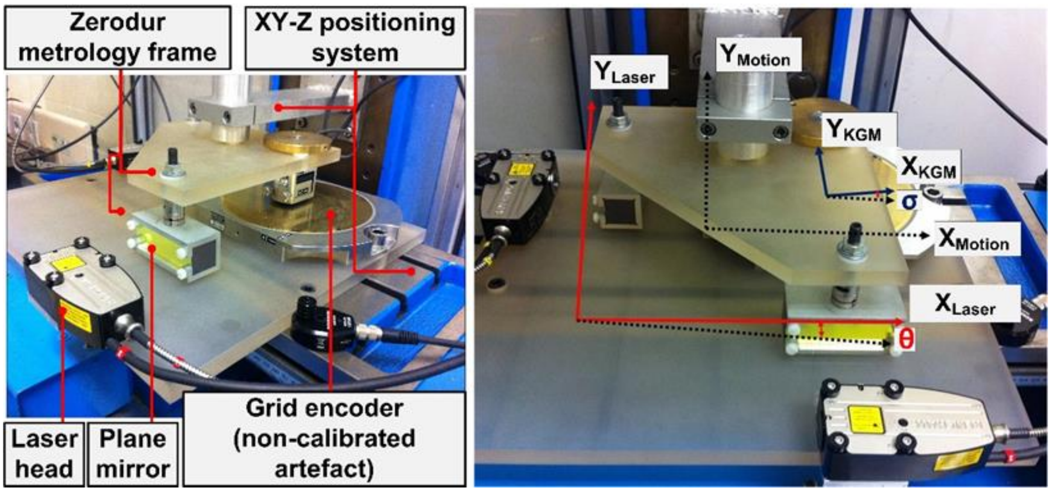

***Figure 2.12**. Experimental setup for the calibration procedure: main components (left); and defined geometric relationships between reference systems of the 2D sensors (right).*

Mathematical model of the laser system

This section analyses the mathematical model of the laser system in order to identify the geometrical errors that are present in the assembly. The laser system essentially consists of two laser beams and two plane mirrors. Each of the laser beams is theoretically aligned with the X and Y-axes, respectively, and thus, theoretically coplanar to the plane of movement and orthogonal to each other. Therefore, there are two different geometric errors that need to be compensated. The first one is the pitch error, present in every 1D laser interferometer measurement, that appears when the laser beam is not coplanar to the plane of movement (represented as α_{xpitch} in Figure 2.13). The second one is the squareness error, a 2D error caused by the non-orthogonality of the X and Y plane mirror interferometers (α_{xy} in Figure 2.13).

In this geometrical model it is assumed that the laser beam is always perpendicular to the plane mirror, this is justified by the tight alignment tolerance between laser beam and plane mirror (1.2×10^{-4} rad), defined by the manufacturer.

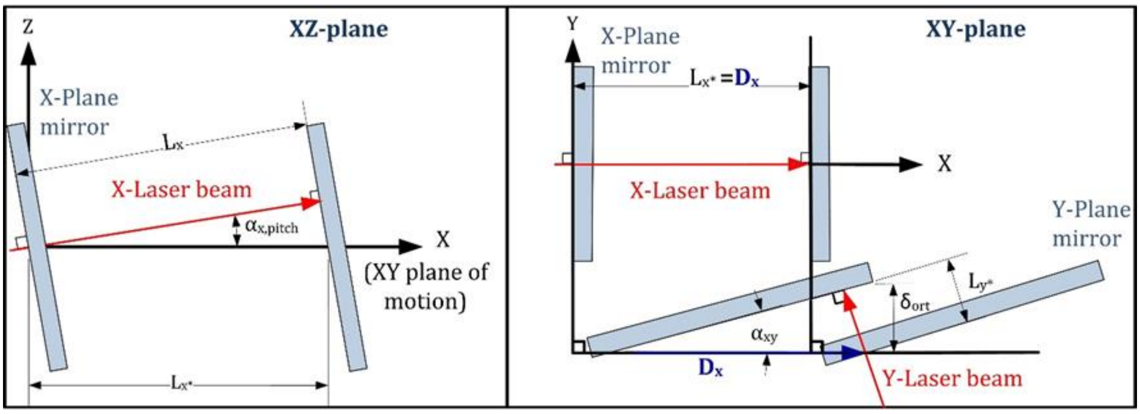

Figure 2.13. *Geometric model of the 2D laser system.*

The measurements recorded by the laser system (L_x and L_y) are affected by the geometrical errors (α_{xpitch}, α_{ypitch} and α_{xy}), and, thus, they present a measurement error in respect to the actual displacements (D_x and D_y). Once the geometrical errors are obtained through the self-calibration procedure, knowing the geometric relations of the model (expounded in the article), it is possible to correct the laser system readouts.

Self-calibration procedure

The calibration procedure presented in the article is based on reversal techniques capable of obtaining a submicrometre uncertainty along the working range. These techniques consist in measuring the features of a non-calibrated artefact in different views. The pattern of the measurement features remains invariant over the different views and, thus, the error of the system to be calibrated can be isolated. The only calibrated pattern required is a 1D-length scale, necessary to correct the scale factor of the system to be calibrated.

As a novelty, in the specific case of study, the non-calibrated artefact is a grid encoder that instead of measuring features has a measuring grid that, when read by the scanning head, provides measuring points. Therefore, the input data to the self-calibration procedure are the readouts of the laser system and the grid encoder at the same positions. The readouts of the grid encoder are mathematically aligned to the laser system reference axes in order to be comparable. Then, the global error at each position, V(x, y), is expressed as the addition of the laser system errors, M(x, y), plus the intrinsic errors of the grid encoder measurement, E(x, y). In Equation 8, the global error for the initial view (View 0) has been represented.

$$V_0(x, y) = M_0(x, y) + E_0(x, y) \tag{8}$$

According to the mathematical model presented in the previous section, three factors (α_{xpitch}, α_{ypitch} and α_{xy}) must be calculated through the self-calibration procedure. As expounded in the article, at least three different views of the grid encoder are required to cancel its systematic errors, that is, the initial view (View 0), the X-axis translation view (View 1) and the Y-axis translation view (View 2), represented in Figure 2.14.

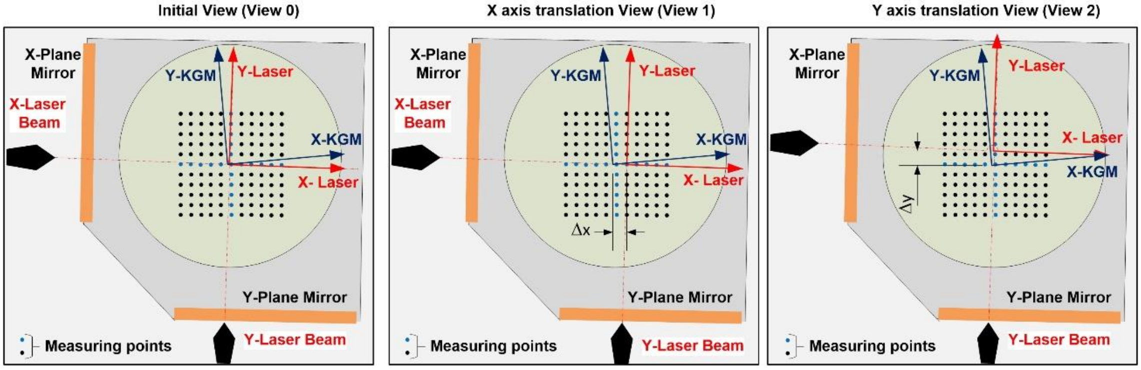

Figure 2.14. *Schematic of the initial and translation views, including the reference systems and their geometric relationships and the mesh of the measuring points.*

View 1 is obtained by displacing the grid encoder approximately 5 mm (Δ_x) in X-axis, at this view, the laser system systematic errors are displaced the same distance in X-axis, as shown in Equation 9. Similarly, View 2 is obtained by displacing the grid encoder approximately 5 mm (Δ_y) in Y-axis, at this view, the laser systematic errors are displaced the same distance in Y-axis, as shown in Equation 10. The actual value of the displacements Δ_x and Δ_y needs to be known to perform the procedure. The systematic error of the grid encoder remains invariant over the different views. Thus, by relating the different views, the systematic error of the grid encoder can be cancelled, but not the ones of the laser system. Then, the geometrical errors of the laser system can be obtained.

$$V_1(x, y) = M_0(x+\Delta_x, y) + E_0(x, y) \tag{9}$$

$$V_2(x, y) = M_0(x, y+\Delta_y) + E_0(x, y) \tag{10}$$

Before performing the procedure with experimental data, the proposed algorithm is validated by a simulation with virtual data. The virtual data represents the grid encoder and laser system readouts recorded at different views along the working range, including its systematic and random errors. The simulation proves that the proposed method works within all the expected ranges for the angles. Moreover, it provides a clear insight of the good theoretical repeatability of the system in a submicrometre range. Hence, the algorithm is considered to be valid.

Geometrical characterisation of the laser system setup and calibration of the grid encoder

Once the self-calibration algorithm has been developed and virtually validated, the 2D laser system can be experimentally calibrated. To minimise random errors of the laser system and the grid encoder during the calibration procedure, 100 readouts were recorded and averaged at each measured point. As mentioned, the actual values of the displacements in X and Y-axes in the translation views need to be known. They can be easily obtained with the calibrated central axes of the grid encoder, without using any additional calibrated length.

In the experiment, the readouts of the laser system and the grid encoder are taken at the same positions, distributed in a mesh of 11 × 11 points in a range of 50 mm × 50 mm. Once the measurements are obtained, the reference system of the laser system and the grid encoder are mathematically aligned in the same reference axes. Then, by combining the global errors obtained at different views, the errors of the grid encoder are cancelled and the geometrical errors of the laser system are obtained (α_{xpitch}, α_{ypitch} and α_{xy}). Finally, the geometrical errors of the laser system readouts (L_x and L_y) can be corrected, and the actual displacements are obtained (D_x and D_y).

The grid encoder acting as a non-calibrated artefact in this procedure is also a measuring instrument. As mentioned, the manufacturer provides a calibration certificate of its central axes. Nevertheless, the grid encoder is used in many applications that require high accuracy along its whole working range. Therefore, once the laser system is calibrated and its measurements corrected, it is possible to calculate the error of the grid encoder at each point. This work proposes a procedure for calibrating the grid encoder: First, the corrected laser readouts are aligned with the reference system of the grid encoder by aligning the X-axes of both systems. In this manner, the squareness errors of the grid encoder are taken to its Y-axis. Then, the grid encoder errors, including its squareness errors, are calculated as the difference between the two measurements. By this procedure, it is confirmed that the grid encoder errors remain invariant in the three different views used in the self-calibration (View 0, View 1 and View 2).

In addition, to experimentally validate the calibration procedure, the errors of the grid encoder are also calculated in an additional view (View 3) that was not used and in the self-calibration procedure. This view is obtained by rotating the grid encoder 180º around its Z-axis. It is verified that the grid encoder error map obtained for the views used in the self-calibration (View 0, View 1 and View 2) and the additional view (View 3) have similar trends and orders of magnitude. The small difference between error maps can be attributed to random errors and to the fact that the measured points are not exactly the same in all the views.

Moreover, as mentioned, the manufactured provides a calibration certificate of the grid encoder central axes. Then, the errors obtained for the central axes of the grid encoder are compared to the ones provided by its calibration certificate. As shown in the article, both errors are highly comparable, thus, the self-calibration procedure for the grid encoder calibration can be considered validated.

The article evaluates the expanded uncertainty of the calibration of the grid encoder according to [101]. For this, the expanded uncertainty of the 2D laser system once the geometrical errors have been corrected also needs to be calculated. In [100], the laser system uncertainty was already evaluated considering the uncertainty of the flatness of the mirrors and the laser resolution. In addition, the repeatability of the laser system during the self-calibration procedure, as well as the uncertainty of the calculation of the geometrical errors in the self-calibration procedure, also need to be considered. The resultant standard uncertainty of the calibrated 2D laser system is 99 nm in both axes and the calibration uncertainty of the grid encoder is $U_{95,x}[nm]=226+4\cdot x[mm]$ and $U_{95,y}[nm]=410+15\cdot y[mm]$ for errors in the X and Y-axes, respectively, which reduces the uncertainty of the grid encoder measurements.

Discussion and conclusion

This article proposes a self-calibration procedure for the geometrical characterisation of a 2D laser system. In self-calibration techniques, different views of a non-calibrated artefact are measured to isolate the error of the system to be calibrated. As a novelty, this study proposed the use of a grid encoder, which is also a measuring instrument, as a non-calibrated artefact.

The mathematical model of a 2D laser system was described, identifying three geometrical errors: the pitch error present in X and Y-axes and the squareness error between axes. The self-calibration procedure was performed by simultaneously recording measurements of both measuring systems along a mesh of points covering the working range. Three different views were sufficient to cancel the grid encoder errors by reversal techniques: the initial view and translation views in X and Y-axes. Once the geometrical errors of the 2D laser system were obtained, its measurements were corrected and were used to calibrate the grid encoder.

The self-calibration procedure presented in this article was validated in three different ways: Firstly, by a virtual validation that simulated the measurements and errors of both measuring system. Then, the procedure was validated by comparing the grid encoder error map obtained in the self-calibration views to a fourth view that was not used during the calibration. Finally, the errors obtained for the grid encoder central axes were compared to the errors defined in its calibration certificate. As shown in the article, the errors present the same trend and order of magnitude in every case. Thus, the self-calibration procedure presented in this work is valid and presents many advantages over direct calibration.

In the article, the calibration procedure is performed in a 2D laser system with two beams. The same procedure could be applied to the 2D laser system of the NanoPla consisting of three beams. That is because the two beams of Y-axis (L_{Y1} and L_{Y2}) are reflected in the same plane mirror, and, thus, considering the aforementioned assumption that the beams must be perpendicular to the plane mirrors, the two laser beams are parallel and have the same pitch errors respect to the plane of motion and the same orthogonality error respect to the X-axis laser beam. This assumption results in negligible errors (<< 1 nm) in X and Y coordinated. Nevertheless, the rotation around Z-axis (θ_z) can be affected by the misalignment errors between the two laser beams and the plane mirror. In the worst case scenario this error would be 25 arc s (1.2×10^{-4} rad). However, the target of monitoring θ_z is that the control system can keep the rotation around Z-axis null to avoid laser system misalignments. Therefore, as long as the 2D laser system is able to provide measurements in the whole working range of the NanoPla, errors in the definition of this angle can be disregarded.

2.2.4. Procedia Manufacturing 2019: Positioning uncertainty of the control system for the planar motion of a nanopositioning platform

The NanoPla positioning system must be able to provide accurate positioning along its whole working range of 50 mm × 50 mm. Its main components are four Halbach motors that work as actuators, the commercial control hardware (DMC kit from Texas Instruments) that drive the motors and the 2D laser system that acts as positioning sensor. Moreover, three vacuum preloaded airbearings provide support for the levitation of the moving platform. In the previous articles, the positioning control strategy for a Halbach linear motor using the commercial control hardware was developed and its correct performance was verified (**Micromachines 2018** and **Electronics 2018**). Additionally, a self-calibration procedure for the 2D laser system was presented in **Sensors 2017**. The self-calibration procedure allows correcting the geometrical errors of the 2D laser system assembly and, thus, improving the positioning accuracy of the whole positioning system. Finally, the work presented in the previous articles can be integrated in the positioning system of the NanoPla in order to obtain accurate positioning along its whole working range.

Firstly, the performance of the 2D laser system integrated in the NanoPla was analysed in order to verify its suitability as feedback positioning sensor. This work was presented in **Euspen 2017**. As mentioned, the 2D-laser system belongs to the Renishaw RLE10 laser interferometer family. It consists of a RLE system that comprises two laser units (RLU), three detector heads (RLD), one per axis and one more in Y-axis to measure the rotation around Z-axis (R_z), two plane mirrors and an environmental control unit (RCU), which compensates the effect of the environmental conditions in the refractive index and thermal expansion. In addition, one external interpolator (REE) is connected to each detector head, and reduces the expected resolution of the system from 9.88 nm to 1.58 nm. The two plane mirrors of the laser system are attached to the metrology frame (I) that is fixed to the moving platform. In turn, the laser heads are attached to metrology frame (II) which is fixed to the inferior base that remains static (see Figure 1.5). Although the original design of the NanoPla considers the metrology frame to be made of Zerodur due to its low thermal expansion, in the first built prototype, which has been used for the experiments, the metrology frames are made of aluminium. The performance analysis presented in **Euspen 2017** was done in MATLAB®, the same environment that is used for the control system of the NanoPla. Besides the readouts of the three detector heads, the system also provides the readout of the RCU sensors: air temperature, material temperature and air pressure. The measurement of each signal takes approximately 0.04 seconds, thus, the maximum speed at which it is possible to record the six measurements is every 0.25 seconds. When the refractive index correction is not performed, only displacement measurements are recorded at a speed of 0.12 seconds. This study verified that the resolution of the system is 1.58 nm and studied the short-term and long-term stability of the system. On both cases, stable measurements were obtained, thus, confirming the suitability of the 2D laser system to be implemented in the control loop as positioning sensors.

Before integrating the positioning sensor in the control system, it is necessary to align the laser beam with the plane mirrors and to define an initial position of the moving platform. For this purpose, the sensorless electromagnetic controller presented in **Micromachines 2018** was implemented in each of the four Halbach linear motors of the NanoPla. For the implementation, a DMC kit was connected to each of the motors. The sensorless electromagnetic controller is an open-loop positioning strategy that does not require positioning feedback. Therefore, this strategy can be used before laser beams and plane mirrors are aligned (when the laser system cannot read) to position the moving platform in the NanoPla central position and align it in X and Y-axes. This is done by adjusting the position of each of the four motors independently. Afterwards, the resultant position of each of the motors is set as their initial position (x_0=0) by changing the phase difference φ in the motor law (Equation 1) of each motor, as was described in **Micromachines 2018**. When the initial position of the four motors is defined, the moving platform is aligned in X and Y axis and, thus, the laser beams are perpendicular to the mirrors and positioning feedback can be implemented.

After defining the initial position of the moving platform, the 1D positioning strategy defined in **Micromachines 2018** is implemented in each of the motors using the positioning feedback of the 2D laser system. The four motors are placed in parallel pairs, thus, as long as the motor pairs displace the same distance, the moving platform remains aligned. It was experimentally verified that the moving platform can be positioned along its working range by controlling each of the motors individually with the 1D positioning strategy implemented in each motor. Nevertheless, independently controlling each motor results in undesired rotations around the Z-axis during the transient response, that is, when the platform is moving from one position to other. Undesired rotations cause misalignment between laser beams and plane mirrors which can affect the performance of the laser system and even impede the displacement measurement.

Therefore, in order to prevent undesired rotations of the moving platform during motion, it is necessary to coordinate the control of the four motors in a 2D control strategy. In **Procedia Manufacturing 2019**, a 2D control strategy is implemented in the 2D positioning system of the NanoPla. In addition, the final positioning uncertainty of the control system is assessed. The article is organised as follows:

- Introduction
- Methods and materials
- 2D positioning control
- Positioning uncertainty of the control system
- Conclusions

Introduction and methods and materials

These first sections introduce the NanoPla design and define its working requirements. As mentioned, the NanoPla presents a two-stage scheme, that is, the XY-long range positioning of the moving platform is complemented by an additional piezo-nanopositioning stage that is fixed to the metrology frame of the inferior base. This second stage is a commercial piezo-nanopositioning device with a working range of 100 µm × 100 µm × 10 µm, which will perform the motion of the sample during the scanning operation. Therefore, it has been decided that the position control system accuracy should have a positioning error at least one order of magnitude smaller than the maximum XY range of the commercial piezo-nanopositioning stage, i.e., 10 µm, along its whole working range of 50 mm × 50 mm. So that, this error could be corrected by the fine motion of the piezostage.

In addition, the connections between components and the host PC are described. The user inputs the target position (X_{ref}, Y_{ref}) in a graphic interface of Simulink® (MATLAB®). In the same Simulink® program, the position feedback from the laser system is extracted and the control strategy is computed. The same program communicates with the control hardware of the motors and sends them instructions. In turn, each control hardware drives the three phases of a motor of the NanoPla. The plane mirrors are the moving target of the 2D laser system and the magnet arrays are the part of the linear motors that perform the relative movement respect to the stator that is fixed. The plane mirrors as well as the magnet arrays belong to the moving platform and are wireless. In Figure 2.15, a photograph of the NanoPla and the control system components is shown.

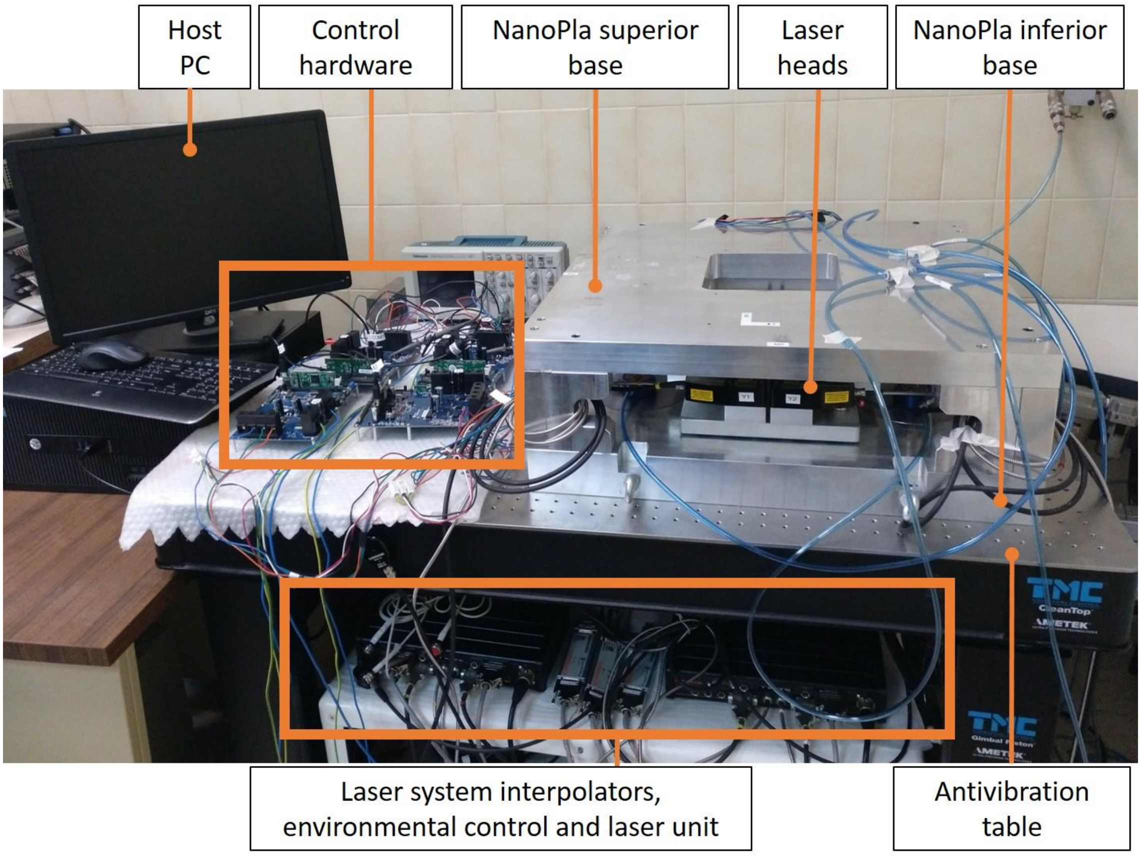

Figure 2.15. *Photograph of the NanoPla and the control system components: host PC, control hardware and 2D laser system units.*

2D positioning control

In the NanoPla, the motors are placed in parallel pairs, as shown in Figure 2.16a. Each motor generates a horizontal force in the moving platform that is longitudinal to its magnet array. Thus, motor 1 and motor 2 (M1 and M2 in the Figure) generate forces in X-axis ($F_{x,M1}$ and $F_{x,M2}$) that move the platform along X-axis. Similarly, motor 3 and motor 4 generate forces in Y-axis ($F_{Y,M3}$ and $F_{Y,M4}$ that move the platform in Y-axis. Additionally, the four motors are placed at the same distance R (169.9 mm) from the centre of the moving platform (see Figure 2.16b) and together they generate a torque around its Z-axis (T_z).

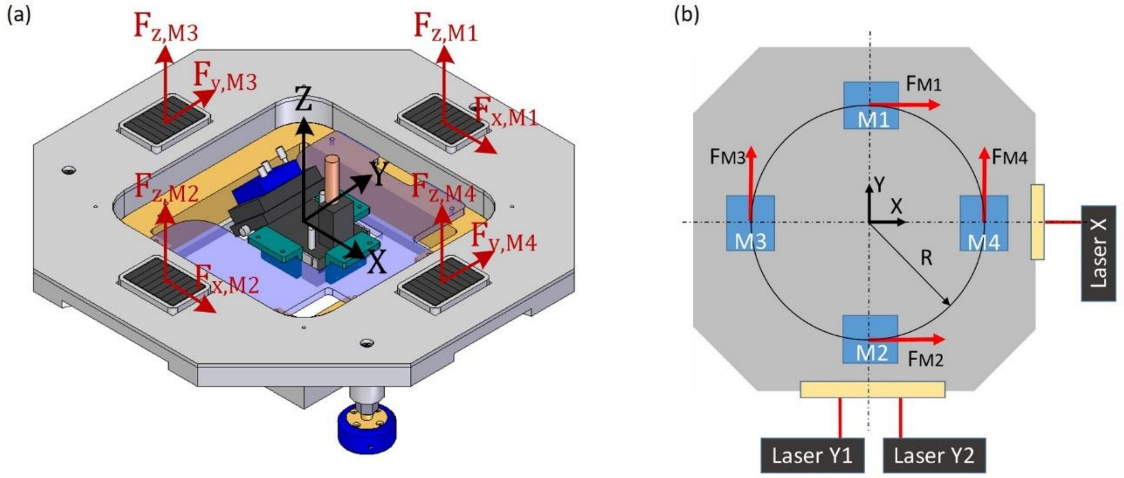

Figure 2.16. *Scheme of the forces that act on the moving platform: (**a**) isometric view; (**b**) top view scheme.*

Therefore, the total forces in X and Y-axes that act on the moving platform and the torque around its Z-axis can be calculated according to the following equations

$$F_x = F_{M1} + F_{M2} \tag{11}$$

$$F_y = F_{M3} + F_{M4} \tag{12}$$

$$T_z = -F_{M1} \cdot R + F_{M2} \cdot R - F_{M3} \cdot R + F_{M4} \cdot R \tag{13}$$

The control strategy positions the platform in X and Y-axes and minimises rotations around the Z-axis (θ_{zref}=0), to prevent laser system misalignments. This is done with three independent PID controllers that act on the forces generated in X and Y-axes by the motor pairs (F_x and F_y) and on the torque (T_z) generated by the four motors. The positioning feedback (X_s, Y_s and θ_s) is provided by the three laser beams (Laser Y1, Y2 and X) of the laser system. Considering symmetry of the moving platform, the total forces and torque are divided between the four motors and the horizontal force that each of the motor needs to generate is computed. Then, the control strategy computes the phase voltages that each DMC kit needs to generate, according to the commutation law of each motor. Then, the instructions of each motor are sent to its DMC kit, that generates the required phase voltages. Once the phase currents flow through the stators coils, the electromagnetic interaction with the magnet arrays of the moving platform generates the horizontal forces that move the platform. In addition, the motors also generate a vertical force that favours the levitation. An scheme of the control system has been represented in Figure 2.17.

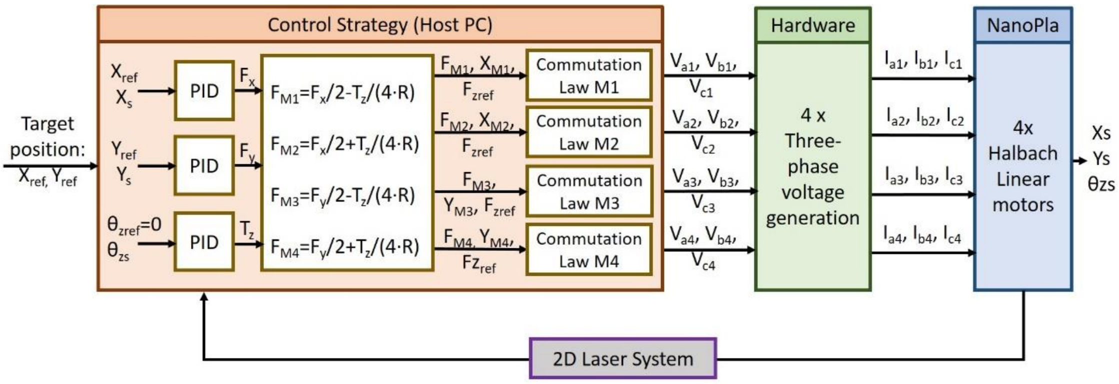

Figure 2.17. *Scheme of the 2D position control system.*

The 2D control strategy has been implemented in the NanoPla. The performance of the controls system has been tested in stationary and transient state, that is, when performing motion. Figure 2.18a shows the displacement of 100 µm in X-axis at a constant speed. When the NanoPla achieves the target position, the positioning error is 0.02 µm and the root mean square (RMS) deviation positioning error is 0.11 µm. In addition, the control system is capable of moving the platform in X and Y-axes simultaneously without losing the alignment of the laser beams and the plane mirrors, that is, keeping the rotation around Z-axis, θ_{zs}, minimal. In Figure 2.18b a displacement describing a 4-mm diameter circumference, moving simultaneously in the two axes, has been represented.

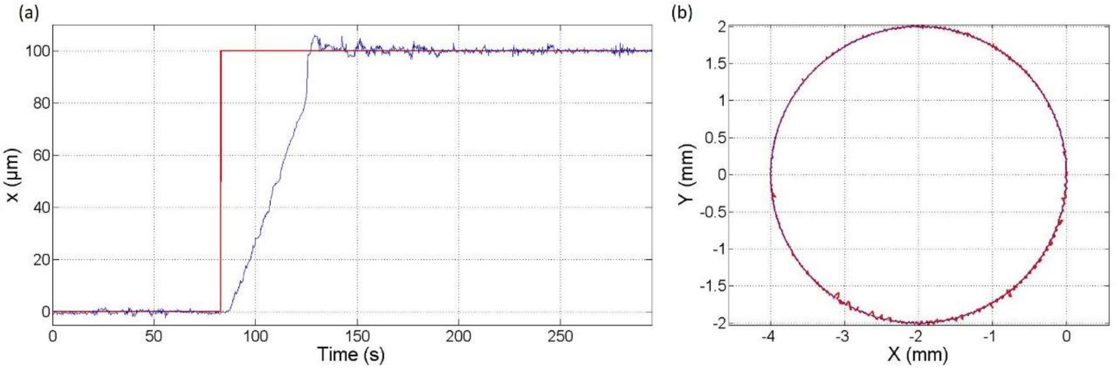

Figure 2.18. *(**a**) 100-µm displacement in X-axis, while Y-axis is kept static; (**b**) Simultaneous displacement in X and Y-axes describing a circumference.*

Positioning uncertainty of the control system

The control system of the NanoPla has been optimised in order to reduce the positioning errors. This section assesses the position uncertainty of the NanoPla and analyses the different contributors. The main contributors are the resolution of the HRPWM module of the DMC kit (control hardware), the uncertainty of the laser system, the phase currents noise and the NanoPla vibrations. Nevertheless, the contributors can be divided in two categories: The ones whose contribution to the final positioning error is known, like resolution of the phase voltages generation (analysed in **Electronics 2018**) and the laser system (analysed in **Euspen 2017**) and the errors in the laser system that are still present after the corrections of the geometrical errors obtained by the self-calibration procedure defined in **Sensors 2017**. The other type of errors are the ones whose contribution to the final positioning error cannot be calculated separately, such as the noise present in the phase current generation and the dynamic vibrations of the NanoPla. In addition, when measuring this error, the laser system noise is also present. These errors cause the root mean square (RMS) deviations of the positioning error, which can be experimentally measured in open-loop. Table 2.1 represents the contributors of the positioning uncertainty and its calculation based on [86]. Even though the laser system resolution is included inside the standard uncertainty of the laser system, its value is also shown separately in the table, so it can be compared to the other contributors magnitude.

Table 2.1. NanoPla positioning uncertainty contributors and calculation.

Source	**Justification**	**Value**
Resolution at the HRPWM u_{HRPWM}	Resolution of 26.2 µV	700/√12 nm
Laser system resolution u_{Lres}	Resolution of 1.58 nm	(1.58/√12 nm)
Calibrated laser system u_{Lcal}	Standard uncertainty of the laser system	99 nm
RMS positioning error u_{RMS}	Laser system noise + phase currents noise + NanoPla vibrations	110 nm
Positioning uncertainty $U_{XY}(k=2)$	$U_{XY}(k=2)=k\sqrt{u_{HRPWM}^2+u_{Lcal}^2+u_{RMS}^2}$	500 nm

Conclusions

The 2D positioning control system of the NanoPla was defined and implemented in this article. Its performance has been experimentally validated, being able to perform motion simultaneously in X and Y-axes while keeping the rotation around Z-axis minimal and avoiding the laser system misalignment. In addition, the positioning uncertainty in the XY-plane $U_X = U_Y = U_{XY}$ (k=2) has been calculated to be ±0.50 µm in each axis and in all the working range of the NanoPla, 50 mm × 50 mm. Therefore, the target of obtaining an accurate positioning control system that fulfils the NanoPla requirements by implementing the commercial hardware and without any additional electronics has been achieved. Furthermore, the resultant uncertainty of the positioning control system is much lower than the NanoPla initially required positioning accuracy, broadening its applicability scope.

2.3. Micromachines 2018

micromachines

Article

One-Dimensional Control System for a Linear Motor of a Two-Dimensional Nanopositioning Stage Using Commercial Control Hardware

Lucía Candela Díaz Pérez [1,*], Marta Torralba Gracia [2], José Antonio Albajez García [1] and José Antonio Yagüe Fabra [1]

[1] I3A, University of Zaragoza, C/María de Luna 3, 50018 Zaragoza, Spain; jalbajez@unizar.es (J.A.A.G.); jyague@unizar.es (J.A.Y.F.)
[2] Centro Universitario de la Defensa, Ctra. Huesca s/n, 50090 Zaragoza, Spain; martatg@unizar.es
* Correspondence: lcdiaz@unizar.es; Tel.: +34-97-676-2561

Received: 16 July 2018; Accepted: 21 August 2018; Published: 22 August 2018

Abstract: A two-dimensional (2D) nanopositioning platform stage (NanoPla) is in development at the University of Zaragoza. To provide a long travel range, the actuators of the NanoPla are four Halbach linear motors. These motors present many advantages in precision engineering, and they are custom made for this application. In this work, a one-dimensional (1D) control strategy for positioning a Halbach linear motor has been developed, implemented, and experimentally validated. The chosen control hardware is a commercial Digital Motor Control (DMC) Kit from Texas Instruments that has been designed to control the torque or the rotational speed of rotative motors. Using a commercial control hardware facilitates the applicability of the developed control system. Nevertheless, it constrains the design, which needs to be adapted to the hardware and optimized. Firstly, a dynamic characterization of the linear motor has been performed. By leveraging the dynamic properties of the motor, a sensorless controller is proposed. Then, a closed-loop control strategy is developed. Finally, this control strategy is implemented in the control hardware. It was verified that the control system achieves the working requirements of the NanoPla. It is able to work in a range of 50 mm and perform a minimum incremental motion of 1 μm.

Keywords: positioning platform; Halbach linear motor; commercial control hardware

---

1. Introduction

Positioning stages are becoming fundamental devices in nanotechnology and nanomanufacturing processes [1,2], where they act as a supplementary unit for measuring or manipulating samples [3,4]. Depending on the application, a certain combination of working range and metrological performance is required [5]. To obtain effective positioning, several metrological systems are currently available [6–8]. These systems have been designed for demanding and accurate operations. Nevertheless, their measuring and positioning range is often very limited [9,10]. Other applications such as measuring or manipulating solar cells or silicon wafers require working with larger areas in a planar part, where cutting of specific samples may be necessary. Therefore, the nanotechnology industry is demanding not only more accurate positioning systems but also larger working ranges [11]. Within this line of research, a nanopositioning platform stage (NanoPla) has been developed and manufactured at the University of Zaragoza [12,13]. It is expected to provide effective positioning at the nanometre scale inside a large working range of 50 mm × 50 mm. Its first application integrates an atomic force microscope (AFM) as a suitable technique for micro- and nanometrology [14], due to the high vertical as well as lateral resolution in the topographic characterization task of specimens.

Depending on their structure, nanopositioning stages can be classified into stages with stacked linear axes and plane stages. Stages with stacked linear axes are characterized for long kinematic chains with an unfavourable force transfer behaviour [15,16]. Whereas the absence of linear motion in plane stages minimizes geometrical errors and presents many other advantages in precision engineering [17]. For these reasons, it has already been implemented in multiple systems [18,19].

In the NanoPla design, the principles of precision engineering have been applied, including planar motion. However, planar motion conditions the actuator selection, since the motor design or its guiding system should not impede the displacement of the motor along the orthogonal direction of its driving axes. Halbach linear motors [20] suppose a solution to this issue, whose movement in the 2D plane is only limited by the size of its winding area. Other advantages of Halbach linear motors are that they provide non-contact motion and, in addition to the propulsion force, they generate a levitation force. Although one of the design criterions of the NanoPla is to implement as many commercial devices as possible, unguided Halbach linear motors are not commercialised yet. Therefore, they have been custom-made for this application due to the advantages of performing accurate and long travel range positioning.

The fact that the use of this kind of Halbach linear motors is not yet widespread means that there is no available commercial solution for the driving task. In other positioning stages described in the literature [6,21], the control hardware and software were specifically designed and built for this purpose. Nevertheless, as was mentioned, one of the targets of the NanoPla design is to develop it with commercial devices when possible, which will facilitate a future industrial applicability of the developed system. Thus, a commercial generic solution for the hardware has been chosen: a Digital Motor Control (DMC) Kit from Texas Instruments (Dallas, TX, USA). This control hardware has been designed for rotary permanent magnet synchronous motors (PMSM), where the aim is to control the rotation speed or the torque generated. According to the literature, the integration of completely generic control hardware with linear motor actuators is a novelty that is presented in this study. Such integration presents many limitations that need to be overcome by optimizing the control system design. Nevertheless, this has been done in this work always by using the available options of the control hardware modules. The hardware has not been modified and no additional electronic has been required. The use of only one commercial hardware and no custom-made electronics facilitates the applicability and replication of the developed control strategy, which is in line with the targets of the NanoPla design. This work can be very useful for other developers willing to implement commercial devices for the control of linear motors.

This article presents and experimentally validates a challenging one-dimensional (1D) control system for a custom-made Halbach linear motor that works as an actuator in the two-dimensional (2D) long working range NanoPla. The control system is characterized by the integration of a commercial solution hardware which is commonly implemented with rotary actuators. Thus, this paper first presents an overview of the NanoPla, which is necessary to define the working requirements of the control system. Secondly, the working principle of Halbach linear motors is described, and the materials used in this work are presented. Then, a dynamic characterization of these motors is performed, and a sensorless open-loop solution is proposed. Afterwards, the 1D control strategy is defined, and the proposed control strategy is implemented in the chosen commercial control hardware. Finally, the experimental results are shown and conclusions are withdrawn.

2. Two-Dimensional Nanopositioning Platform Stage (NanoPla) Overview

As shown in Figure 1a, the NanoPla consists of a three-layered architecture: an inferior and a superior base that are fixed, and a moving platform that is placed in the middle. Three air bearings lift the moving platform and levitate it. The planar motion is performed by four Halbach linear motors that are symmetrically assembled in an inverted position. In other words, the stators are fixed to the superior base, and the magnet arrays are assembled to the moving platform (see Figure 1a). The horizontal forces of each pair of parallel motors will move the platform in the X and Y direction, as Figure 1b shows. In addition, the vertical forces of the four motors will favour the levitation of the moving platform. A 2D laser interferometer system works as positioning sensor. The laser heads are fixed to the inferior base, and the mirrors are placed in the moving platform. In addition, in the NanoPla, a two-stage scheme has been applied. That means that the XY-long range positioning of the moving platform is complemented by an additional fine nanopositioning system for the more demanding scanning operations. This second stage is a commercial piezo-nanopositioning device with a working range of 100 × 100 × 10 µm^3, which increases the number and variety of applications of the NanoPla.

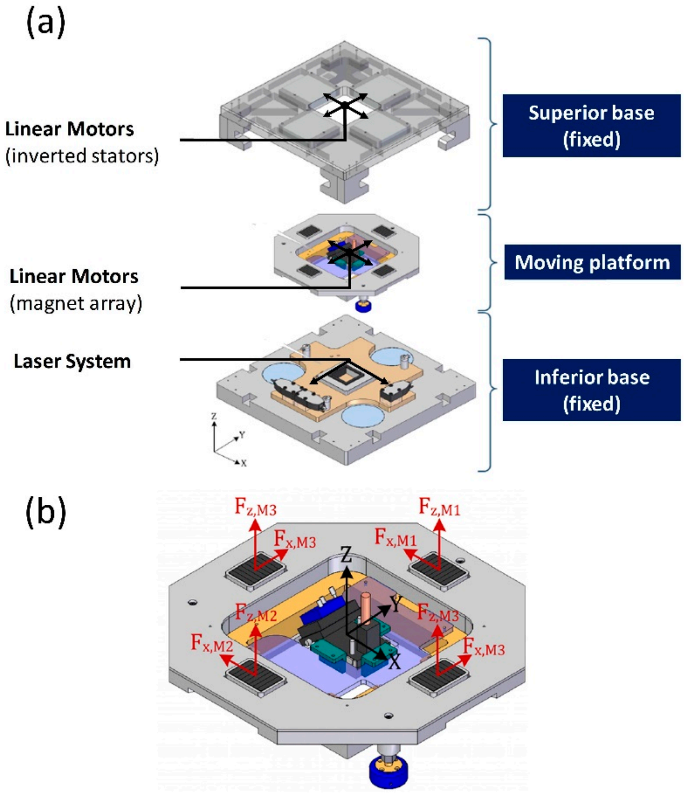

Figure 1. (**a**) Nanopositioning platform (NanoPla) prototype; (**b**) vertical and horizontal forces generated by the motors in the moving platform.

The first device that is going to be integrated in the NanoPla is an AFM, which will be placed on the moving platform. The NanoPla will position the AFM along the working range of 50 mm × 50 mm. The sample will be placed in the commercial piezo-nanopositioning stage fixed to the inferior base. During the scanning task, the moving platform and the AFM will be static (air bearings off) and the commercial nanopositioning stage will perform the fine motion of the sample.

A preliminary modelling of the 2D positioning control of the NanoPla was presented in [22] with a different approach. The input currents are controlled independently, which is not possible with the commercial control hardware solution proposed. Nevertheless, the control strategy requirements were initially defined. According to this, the 1D linear motion control strategy must be able to work in a range of 50 mm. In addition, the positioning error must be at least on order of magnitude smaller than the maximum XY range of the commercial piezo-nanopositioning stage, i.e., 10 µm. The settling time is not critical. Finally, other considerations are related to the transient behaviour of the positioning response. In addition, oscillation should be avoided.

3. Halbach Linear Motors

The linear motors used as actuators in the NanoPla were developed by Trumper et al. [20] and custom-made in the Center for Precision Metrology of the University of North Carolina at Charlotte (Charlotte, NC, USA). They consist of a Halbach permanent magnet array and three-phase ironless coils (stator). In this section, the motor law and the commutation law that define the working principle of the motor are described.

3.1. Motor Law

In a Halbach array of permanent magnets, the configuration of the magnets augments the magnetic field generated on one side and nullifies the magnetic field on the other side. That is, the rotating pattern of the permanent magnets forces the cancellation of magnetic components resulting in a one-sided flux. In a Halbach linear motor (Figure 2a), this flux is concentrated between the magnet array and the stator. When a DC current flows through the coils of the stator, these currents interact with the magnetic field of the magnet array. The electromagnetic interaction generates two orthogonal forces: one is horizontal (F_X) and the other is vertical (F_Z), as can be seen in Figure 2b.

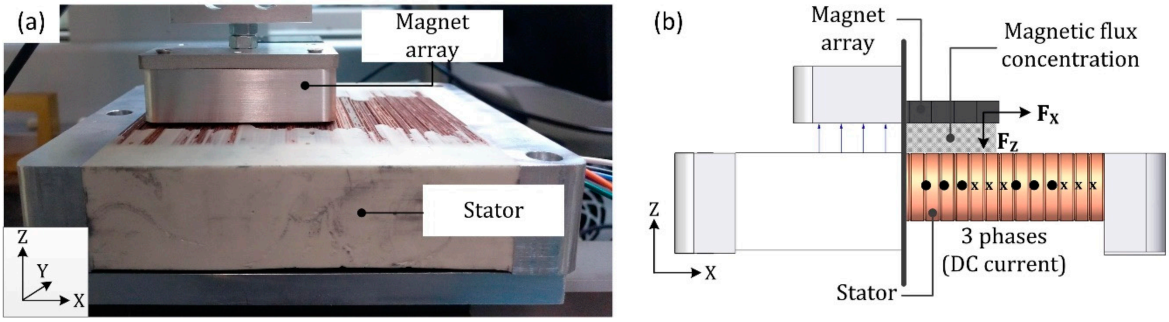

Figure 2. (**a**) Halbach motor (magnet array and stator); (**b**) graphical representation of the dual forces generated by the Halbach motor.

The direction and amplitude of the two forces depend on the relative position between the magnet array and the coils as well as on the magnitude of the DC phase currents flowing through the coils. The motor law (Equation (1)) represents the mathematical relationship between the generated forces (F_X and F_Z), the input phase currents (I_a, I_b and I_c) and the relative position between the stator and the magnet array (x_0), along the axis of movement.

$$\begin{bmatrix} F_X \\ F_Z \end{bmatrix} = A \begin{bmatrix} \cos(kx_0+\varphi) & \cos\left(kx_0-\frac{2\pi}{3}+\varphi\right) & \cos\left(kx_0+\frac{2\pi}{3}+\varphi\right) \\ \sin(kx_0+\varphi) & \sin\left(kx_0-\frac{2\pi}{3}+\varphi\right) & \sin\left(kx_0+\frac{2\pi}{3}+\varphi\right) \end{bmatrix} \begin{bmatrix} I_a \\ I_b \\ I_c \end{bmatrix} \quad (1)$$

In Equation (1), A and k are constant parameters of the motor. The constant of the motor, A, depends on design parameters of the motor, as represented in Equation (2). On the other hand, k is the fundamental wave number, which is calculated according to Equation (3), where l is the pitch or the spatial period of the array wavelength. In Table 1, a description of all these parameters is provided [23].

$$A = N_m \eta_0 \mu_0 M_0 G e^{-kz_o} \quad (2)$$

$$k = \frac{2\pi}{l} \quad (3)$$

Table 1. Description and theoretical values of the motor parameters.

Parameter	Description	Theoretical Value
N_m	Number of spatial periods of the magnet array	2
η_0	Winding density of the stator coil	832,400 turns/m^2
$\mu_0 M_0$	Remanence of the permanent magnets	0.4 T
G	Effects of the motor geometry	2.62×10^{-6}
k	Fundamental wave number	211.1285 rad/m
z_0	Separation gap between stator-magnets array	400 µm
l	Spatial period of the array wavelength	29.76 mm

Their values were calculated first theoretically and then experimentally in a previous work [24]. This was done by measuring with a load cell, along the travel range of the motor, the vertical and horizontal force generated by certain known phase currents. These results are shown in Table 2. The initial position $x_0 = 0$ can be adjusted by changing the phase difference φ in Equation (1). φ must have the same value in the F_x row as in the F_z row because the two forces are orthogonal. In this paper, for simplicity reasons, the value of φ will be considered null. φ acts as an initial offset and, thus, this assumption only affects the absolute initial position of the motor but not the results.

Table 2. Theoretical and experimental fitting parameters of the motor law.

Parameter	Theoretical Value	Experimental Value
A (N/A)	1.6	1.6067
k (rad/m)	211.1285	211.0001
l (mm)	29.760	29.778

3.2. Commutation Law

The commutation law is defined as the inverse of the motor law (Equation (1)), and it allows the calculation of the phase currents that are required in order to generate a certain F_x and F_z in a specific position. On the basis of Equation (1), the phase currents can be determined with one degree of freedom (three unknowns, two equations). As there are three input currents, one more equation needs to be considered to uniquely determine them. In [25], an additional constraint was proposed for power minimization, which is possible due to the fact that the control strategy acts independently on the input currents using linear transconductance power amplifiers built for that purpose. By contrast, this paper proposes the use of a generic DMC Kit from Texas Instruments. This control hardware imposes a star-connection on the phases of the motor, which adds an additional constraint (Equation (4)) that prevents the control of the three currents independently. Thus, it also impedes the implementation of the power minimization constraint.

$$I_a + I_b + I_c = 0 \tag{4}$$

Therefore, combining Equations (1) and (4) and considering $\varphi = 0$, the commutation law for the case of this study is defined as in Equation (5):

$$\begin{bmatrix} I_a \\ I_b \\ I_c \end{bmatrix} = \frac{2}{3A} \begin{pmatrix} \cos kx_0 & \sin kx_0 \\ \cos\left(kx_0 - \frac{2\pi}{3}\right) & \sin\left(kx_0 - \frac{2\pi}{3}\right) \\ \cos\left(kx_0 + \frac{2\pi}{3}\right) & \sin\left(kx_0 + \frac{2\pi}{3}\right) \end{pmatrix} \begin{bmatrix} F_x \\ F_z \end{bmatrix} \tag{5}$$

4. Experimental Setup and Hardware Description

Before the implementation of the control system designed in this work into the two-dimensional NanoPla, its validation is firstly performed in a separate experimental setup. In this manner, the experimental validation has been carried out in a metrology laboratory with standard conditions of temperature 20 ± 1 °C and humidity 50–70% controlled 24/7. The scheme of the experimental setup is shown in Figure 3. This setup installs one of the linear motors of the NanoPla and the same DMC Kit that will be implemented in the NanoPla. A pneumatic 1D-linear stage was used to imitate the frictionless motion of the NanoPla. The stator of the linear motor is mounted over the pneumatic linear guide, and the magnet array is fixed to the bridge part. The actuator is connected to the three-phase power stage of the control hardware, while the control card is connected to a computer by a USB port. As positioning sensor, a laser interferometer system has been used (i.e., laser head source and reflectors). The laser system is also connected to the computer. In addition, an oscilloscope has been used to monitor the signals of the control hardware.

As can be observed in Figure 3, in this preliminary setup, the stator is the moving part while the magnet array is static, in contrast to the design of the NanoPla. Nevertheless, the relative motion between parts is the same in both cases. Therefore, this does not affect the design of the control system nor the experimental validation.

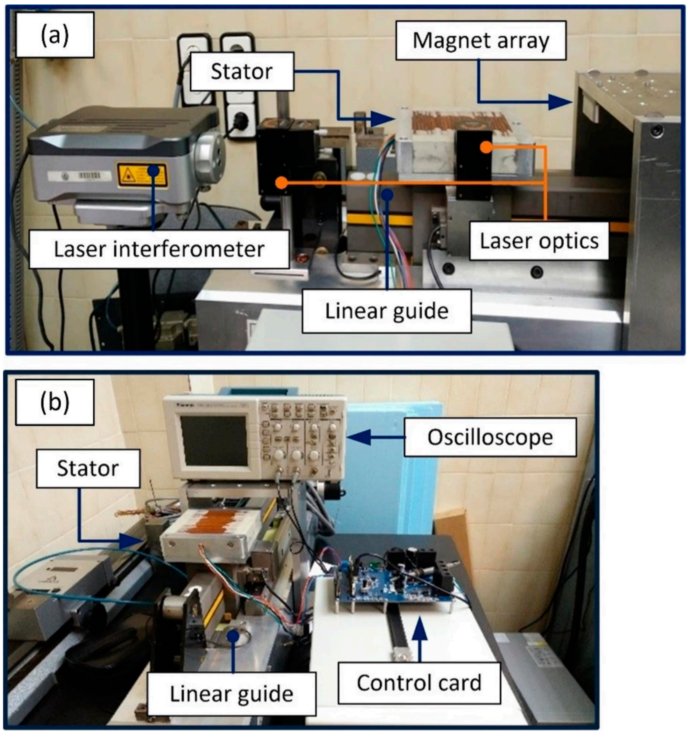

Figure 3. Lateral (**a**) and front (**b**) view of the experimental setup for the implementation of the control system of one linear motor.

As stated, this work proposes to facilitate the control issue by implementing a commercial solution for the control hardware. The selected device to perform the control is a DMC Kit (DRV8302-HC-C2-KIT) from Texas Instruments. This control hardware is designed to operate with generic rotary permanent magnet synchronous motors. It provides closed-loop digital control feedback, analogue integration and comprises a microcontroller unit (MCU) and the inverter stage that generates the phase voltages. The MCU is a C2000 microcontroller and is able to perform real time control by working with 32-bit data. The control hardware is able to generate three phase voltages. That means that in the NanoPla each motor will need one control DMC Kit.

A Renishaw XL-80 laser interferometer (Renishaw, Gloucestershire, UK) has been integrated to provide the position feedback. The readouts of the laser system are sent to the computer and then from the computer to the control card by a serial communication interface. The Renishaw XL-80 laser system has a resolution of 1 nm, and the measured noise under laboratory controlled conditions has a range of 400 nm. The purpose of this work is to develop, integrate and validate a 1D control strategy for one linear motor so that this control system can be implemented later in the four linear motors of the NanoPla for a 2D movement. Renishaw XL-80 laser system performance is similar to the laser system of the NanoPla, and it is perfectly suitable for this validation.

In contrast, the NanoPla includes a 2D laser system that belongs to the Renishaw RLE10 laser interferometer family. It consists of a laser unit (RLU), two sensor heads (RLD), two plane mirrors (one per axis), and an environmental control unit (RCU). In addition, an external interpolator improves the resolution to 1.58 nm. The measured noise of this system is 20 nm. In [26] an analysis of the performance of the NanoPla 2D laser system was presented and its suitability as positioning sensor was confirmed. This laser system will be used once the 2D positioning system is implemented in the NanoPla.

5. Dynamic Characterization

Now the driving actuators and the experimental setup have been described, in this section a dynamic characterisation of the system is performed. In other work that introduces the use of Halbach linear motors for metrology applications [20], electromechanical modelling was presented. In contrast, this section focuses on observing and understanding the dynamic behaviour of the motor under the electromagnetic forces that are generated when a DC current flows through the coils. This dynamic characterisation allows the definition of an open-loop control system, which will facilitate the design of the closed-loop control strategy described in the next section. Firstly, the conditions of the equilibrium of the system are studied. After defining the equilibrium state, a sensorless controller is developed. This controller moves the motor by varying the force distribution along the axis, and it does not require a positioning feedback sensor.

5.1. Equilibrium Position

In the system under study, the only forces that act on the motor are the orthogonal electromagnetic forces F_x and F_z, F_x being the only propulsion force that acts along the axis of movement. As mentioned in Section 3, when certain phase currents flow through the stator, F_x and F_z are generated, and their magnitude depends on the relative position between stator and magnet array. Figure 4 represents the sinusoidal shape of the horizontal force (F_x) and the vertical force (F_z) generated by certain phase current values along the axis of movement (x_s).

The motor will remain motionless once it arrives at a position x_0 where the propulsion force is null; that is, the equilibrium position. As can be observed in Figure 4, in each magnetic spatial period (pitch: $l = 29.778$ mm), there are two equilibrium positions. For instance, in the first pitch, F_x is equal to 0 N at the positions $x_s = 0$ mm and $x_s = 14.889$ mm. However, these two equilibrium positions have different characteristics. The second one, where the slope is negative, is a stable equilibrium position. As can be seen in Figure 4, if a perturbation displaces the motor from this stable equilibrium position, then the electromagnetic force pushes it forwards if the displacement is negative or backwards if the displacement is positive, always returning it to the stable equilibrium position. On the contrary, where the slope is positive, there is an unstable equilibrium position, where a small disturbance moves the motor away from its position to the nearest stable equilibrium position. According to Figure 4, at the stable equilibrium position, the value of the vertical force F_z is maximum and positive, while at the unstable equilibrium position, the value of F_z is minimum and negative.

In the NanoPla, once the motor arrives to the target or reference position ($x_s = x_{ref}$), it must remain motionless ($F_x = 0$). In addition, the magnet arrays are fixed to the moving part that is levitating by means of three air bearings. In order to leverage the vertical force generated by the motor, F_z, must be positive (Figure 2), favouring the levitation by lifting the magnet array. In other words, the target position must fulfil the conditions of a stable equilibrium position. For the experimental validation presented in this work, the target value of F_z has been defined as 1 N.

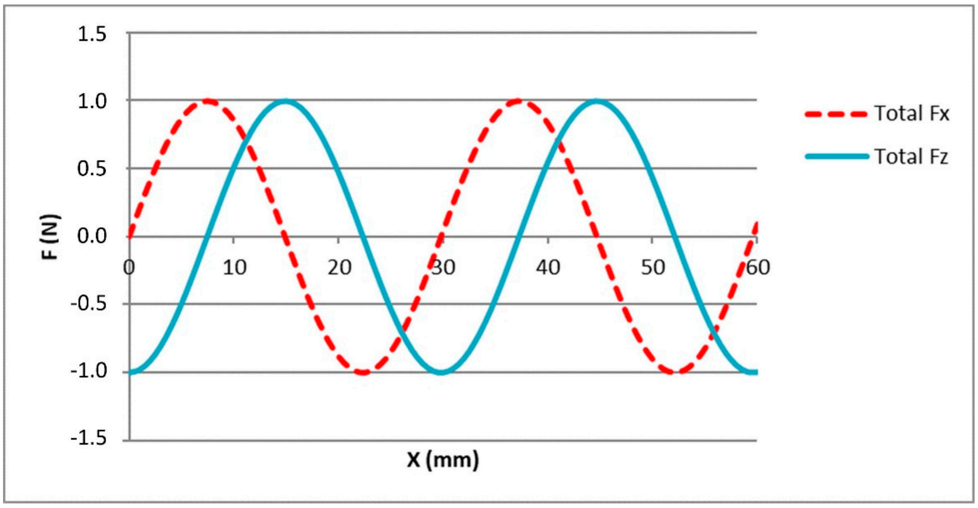

Figure 4. F_x and F_z along the axis of movement, for $I_a = 0$ A; $I_b = 0.3593$ A; $I_c = -0.3593$ A.

5.2. Electromagnetic Sensorless Controller

As stated in the previous subsection, according to the working conditions of the NanoPla, when the motor achieves the target position, it must be in a stable equilibrium state. By introducing the conditions of the stable equilibrium ($F_x = 0$ and $F_z = 1$ N) for a particular desired target position ($x_s = x_{ref}$) in the commutation law (Equation (5)), the required phase currents that create this state can be calculated. When these currents flow through the coils, the electromagnetic forces are generated. Therefore, by combining the phase currents, the equilibrium state can be created at any desired position. Then, the horizontal force moves the motor to the stable equilibrium position (x_{ref}) where it is maintained under small perturbations.

Thus, when the phase currents create a stable equilibrium state, the electromagnetic horizontal force acts as a controller, with the stable equilibrium position as the reference position. This system consists of the electromagnetic controller and the load elements of the plant, as represented in Figure 5. This electromagnetic controller does not require a positioning sensor.

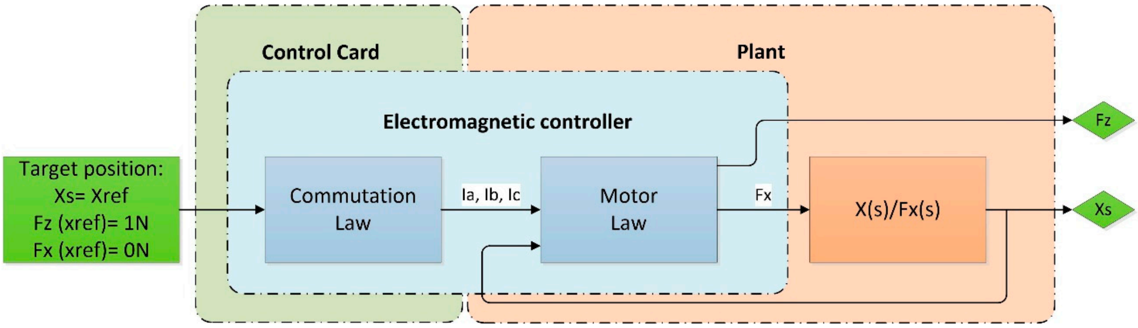

Figure 5. Scheme of the linear motor system in an open-loop system.

Nonetheless, this electromagnetic sensorless controller presents many limitations. The first one is the working range; it works only inside the range of 1 pitch (29.778 mm). That is because each combination of phase currents creates a sinusoidal distribution of the forces along the axis, with one stable equilibrium position in each pitch. Thus, the electromagnetic horizontal force takes the motor to the nearest stable equilibrium position, which may be in a maximum distance of ±14.889 mm. Another limitation of the electromagnetic controller is that it does not allow the tuning of the transient response. However, these two limitations can be overcome by introducing, as an input position (x_{ref}), a discrete ramp that moves the motor in small steps until it arrives at the target position. This allows control of the movement from the initial position to the target position, working in the full range of the linear motor.

The most significant disadvantage that cannot be overcome in this open-loop system is the positioning accuracy. The constant parameters k and A of the motor law (Equation (1)) have been determined theoretically and experimentally (Table 2). Nevertheless, the values of these parameters are an approximation. They may vary from point to point and from pitch to pitch as the motor is not ideal. Similarly, the generated phase currents may also present deviations. Hence, the electromagnetic controller will take the motor to the stable equilibrium position; however, due to these inaccuracies, the equilibrium position may not be exactly coincident with the target position.

6. One-Dimensional Control Strategy and Hardware Implementation

In the previous section, a dynamic characterisation was performed, and it was stated that the electromagnetic force could be defined to behave as a sensorless controller. Nevertheless, as mentioned, the electromagnetic sensorless controller presents many limitations: a working range of one pitch, positioning errors and uncontrolled transient response. Therefore, in order to detect the movement errors, a positioning sensor should be implemented. The readouts of this positioning sensor can be used as feedback for a proportional–integral–derivative (PID) position controller that compares them to the reference position and defines the action necessary to correct the error. Moreover, it will allow the full travel range of the motor to be used. Finally, by tuning the PID controller, it is also possible to adjust the transient response.

The resultant position control system has been represented in Figure 6. The reference position (x_{ref}) is the input to the PID controller, whose output is the required horizontal force (F_x*). Knowing the desired vertical force (F_{zref}) and the required horizontal force (F_x*), the commutation law calculates the required phase currents that are needed to generate those forces at the present position (x_s). The resultant phase currents are generated by the control hardware and, according to the motor law, the electromagnetic forces F_x and F_z are produced. The horizontal force F_x displaces the motor to the desired position while F_z favours the levitation. The real position of the motor is read by a positioning sensor and fed back to the PID controller where it is compared to the reference position and corrected. The positioning sensor readouts are also used as inputs to the commutation law.

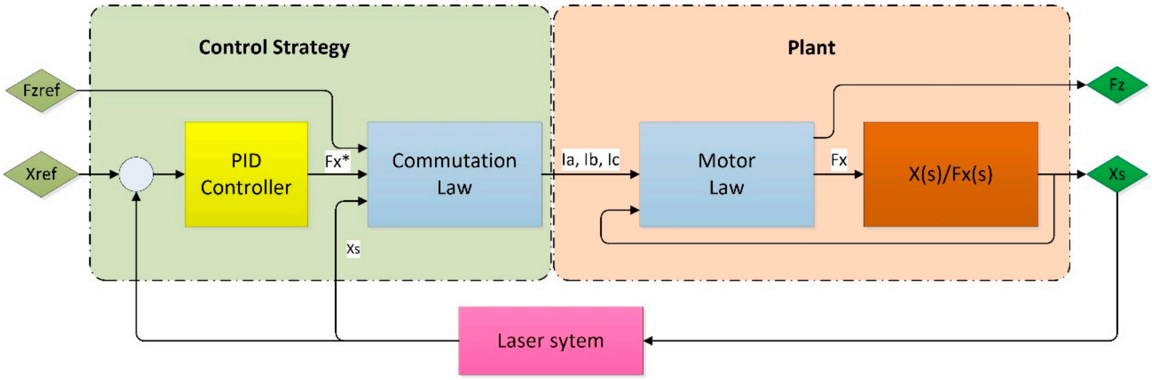

Figure 6. Position control scheme of the linear motor.

Once the 1D control strategy has been developed, it can be implemented in the control hardware and the positioning sensor that were presented in Section 4. The control hardware that has been chosen is a DMC Kit from Texas Instruments, and a Renishaw XL-80 laser system acts as positioning sensor. In this section, the implementation of the control system in the control hardware is presented and schematized.

The selected control hardware presents many advantages, such as being commercial, having a low cost and being suitable for this application. However, it is generic hardware for the control of rotary motors, where the main target is to control the rotation speed or the torque. Therefore, it has some limitations that need to be taken into account.

The first drawback is that the three phases must be wired, presenting a start connection. This constraint does not allow the introduction of an additional constraint of minimum power losses, as mentioned in Section 3.2, when the commutation law was defined.

In addition, the control hardware is not able to act on the phase currents directly as in [21,25], where hardware with current amplifiers was built for the control. Instead, it generates phase voltages by pulse wide modulation (PWM) [27]. The control program must calculate the duty cycles (DC) that are required to generate a desired phase voltage. Then, the transistor bridge generates the pulses of the PWM according to the DC, producing the corresponding voltages of each motor phase. The resulting phase currents flowing through the phases are constant, and their value depends on the phase voltages and the winding phase resistances that, in this case, are approximately 1 Ω for every phase. The DMC Kit from Texas Instruments includes high-resolution PWM (HRPWM) modules based on micro-edge positioner (MEP) technology which are able to extend the time resolution capabilities of the conventionally derived digital pulse [28]. The PWM working frequency must be higher than 10 kHz, according to the manufacturer. In order to get the best DC resolution, it was set to 14.64 kHz. The phase voltage resolution obtained when using the HRPWM modules at this frequency is 2.64×10^{-5} V.

Besides this, the control card is able to communicate in real-time with other peripherals, such as a computer, and transmit data through the serial communication interface (SCI).

Figure 7 presents the control system implementation in the control hardware, having the laser system as positioning sensor. The control strategy reference inputs are the desired position (x_{ref}) and the vertical force (F_{zref}). The outputs are the required phase currents (I_a*, I_b* and I_c*). As already mentioned, the control hardware does not act directly on the phase currents. Instead, it generates phase voltages by PWM. Hence, the PWM modules must generate the phase voltages that correspond to those phase currents. The required DCs must be calculated for the transistor bridge to generate these phase voltages. The voltage drop between the phase terminals and the neutral point of the motor creates the phase currents (I_a, I_b and I_c). Thus, by the motor law, two orthogonal forces (F_x and F_z) are generated, and their magnitude depends on the relative position between the stator and the magnet array (x_s). The motor position is measured by the laser system, and the readouts are extracted to the PC and directly sent to the control card through the SCI, together with the reference position command (x_{ref}). The control strategy is performed at the sampling speed of the positioning sensor. In this case, the fastest sampling speed of the laser system is 0.05 s.

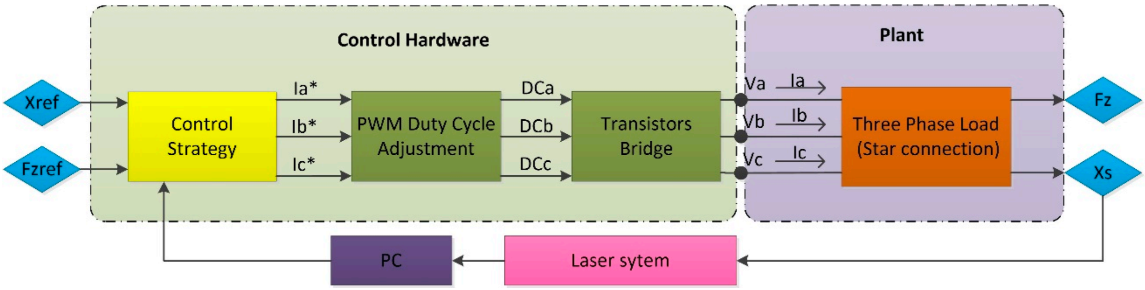

Figure 7. Implementation of the one-dimensional (1D) control strategy in the control hardware.

7. Experimental Results

This section presents and analyses the performance of the implementation of the developed electromagnetic sensorless controller and the 1D control system, which were previously described. The aim of the experiments is to confirm that the 1D control system fulfils the working conditions that the NanoPla design demands. For every experiment, the vertical force value defined as reference is 1 N, which defines the phase currents working range, that, in this case, is ±0.5 A.

7.1. Electromagnetic Sensorless Controller Results

Firstly, the electromagnetic sensorless controller that was presented in Section 5.2 was implemented and analysed. As expected, the electromagnetic controller is able to perform displacements inside a range of ±14.889 mm. The repeatability of the system when performing the same displacement of 5 mm inside the same pole 10 times is ±0.018 mm, and the average positioning error when reaching the position of 5 mm is 0.757 mm. The cause of this variation when performing the same displacement is that the electromagnetic controller displaces the motor to a certain position by creating a stable equilibrium state at this point. The stable equilibrium position is defined by the combinations of phase currents. Even though the command for these currents does not vary for the same target position, the real resultant phase currents may not be the same as they depend on other factors, such as the voltage generation noise and the winding resistor, which may vary with the temperature.

By introducing a stepped ramp as the input for the reference position, it was confirmed that the electromagnetic sensorless controller is able to work in the full range of 50 mm (Figure 8) as stated in Section 5.2. Nevertheless, as expected, this sensorless controller is unable to correct the positioning error, which increases the farther it moves away from the zero position. At the end of the travel range, when the reference position (blue line) is 50 mm, the real position (red line) of the motor is 48.920 mm, which supposes a positioning error equal to 1.080 mm. This positioning error is not acceptable for the NanoPla operation, and thus another control strategy approach is necessary, such as the one proposed below.

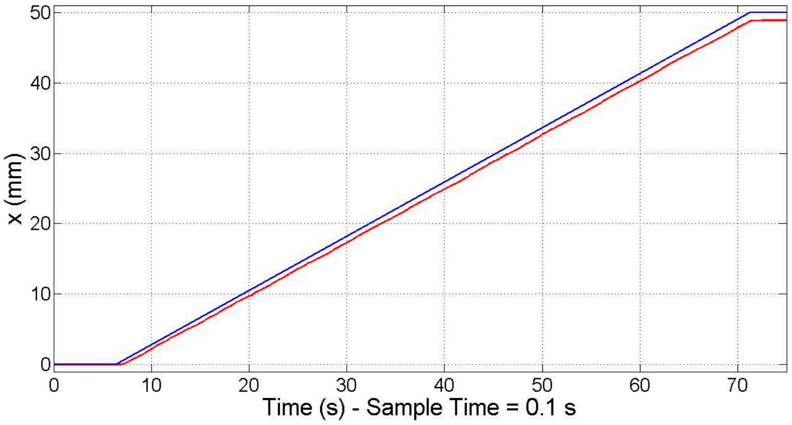

Figure 8. Electromagnetic sensorless controller: 50 mm travel range at constant speed.

7.2. One-Dimensional Control Strategy Results

The control system was implemented in the control hardware and its PID was experimentally tuned. As was done in the previous subsection for the electromagnetic sensorless controller, the repeatability of the system was measured by performing the same displacement of 5 mm 10 times. In this case, the system always reaches the target position; that is, its repeatability is equal to 0, and the average position error is 0 µm. Nevertheless, when the motor is at a stationary state, it slightly oscillates around the target position. This positioning noise has a root mean square (RMS) deviation of ±0.143 µm.

In order to confirm that the control system works along the travel range of 50 mm that is required in the NanoPla, the response to a 50 mm travel range input at a constant speed was recorded. As can be seen in Figure 9 the measured position (red line) follows the reference position (blue line) along the travel range, even doubling the sample time to 0.1 s.

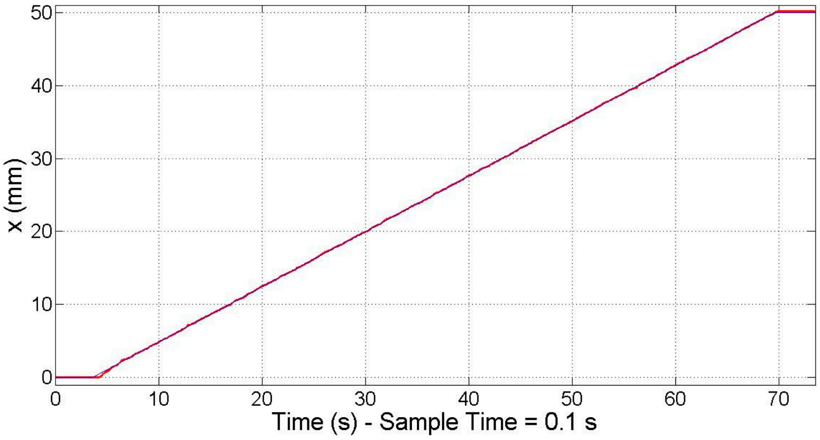

Figure 9. Closed-loop proportional–integral–derivative (PID) controller: 50 mm travel range at constant speed.

Moreover, it was verified that the motor is able to respond to the minimal required motion, that is, 10 µm, as stated in the Introduction. In Figure 10, the response (red line) to a 10 µm step (blue line) is represented.

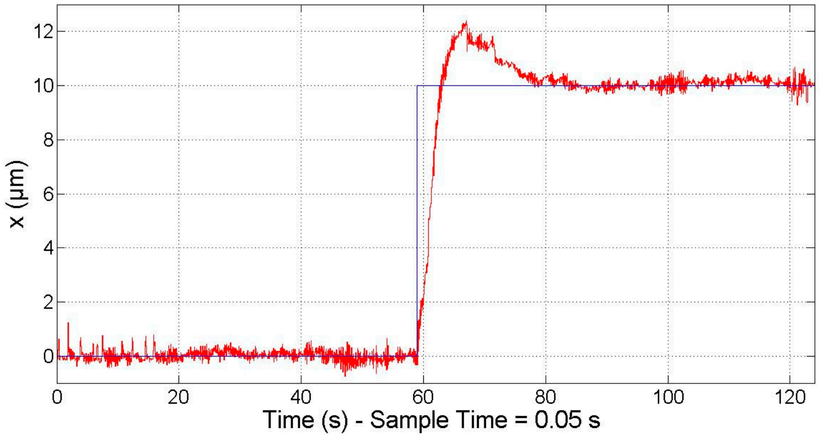

Figure 10. Closed-loop PID controller: 10 µm step response.

Besides this, the smallest step input that the motor can generate was also tested; that is, the minimum incremental motion. It must be noted that, in order to perform the motion, a change in the phase currents must occur. In turn, the variation of the phase currents is produced by a variation of the phase voltages that are controlled by the HRPWM module. As mentioned in the previous section, the minimum voltage variation that this module can perform is 2.62×10^{-5} V, which corresponds to a variation of approximately 2.62×10^{-5} A in the phase currents. Ideally, a change of this magnitude in the phase currents produces a displacement of approximately 600 nm. Nevertheless, the phase currents are also affected by the noise of the voltage source and the PWM signals. Therefore, the power stage is not able to work in the full range of the needed phase currents to perform a motion step in the submicrometre scale. However, the PID controller is fast enough to switch between two combinations of phase currents in order to reduce the positioning error, resulting in an improvement of the effective motion resolution. As shown in Figure 11, the system is able to respond to a staircase of 1 µm (reference position in blue and response in red). The magnitude of the positioning sensor measuring noise together with the resolution and noise of the voltage generation are the main contributors to the positioning noise of the control system. It must be taken into account that the laser system used for the experimental validation has a measuring noise in the range of 400 nm. In contrast, the laser system of the NanoPla has a measuring noise in the range of 20 nm. Therefore, better results are expected when the driving system is implemented in the NanoPla.

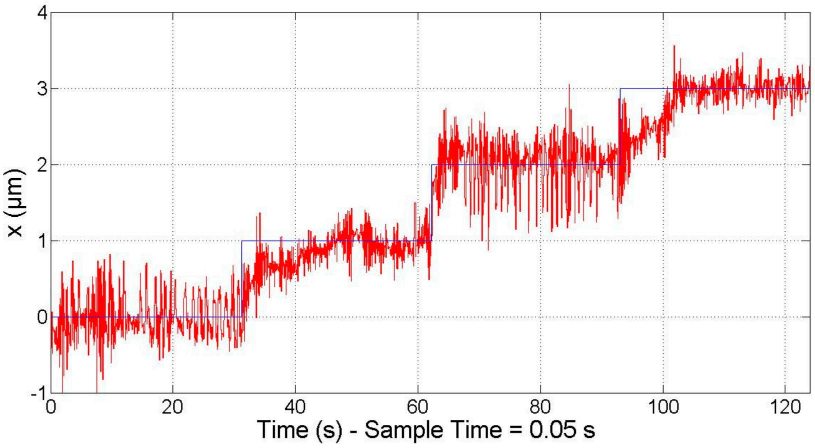

Figure 11. Closed-loop PID controller: 1 µm staircase response.

It should be noted that this results are for the motor under study, the design parameters of which are represented in Table 2. Experimental tests have shown that other motors having similar design parameters provide the same results. Nevertheless, for other values of k and A in the motor law (Equation (1)), the results could be different. The main aspect that should be taken into account when implementing this control system is the phase current's working range and the minimum variation in the phase current that the voltage generation module is able to perform. The phase current's working range is defined by the design parameters of the motor and the reference vertical force, while the minimum variation in the phase current is limited by the hardware.

In the control strategy, a reference value is also set for the generated vertical force (Figure 6). As mentioned, although the levitation of the moving platform of the NanoPla is performed by three air bearings, the design includes the use of the vertical force generated by the motors to favour the levitation. The inverted stators placed on the superior base of the NanoPla will attract the magnet arrays fixed to the moving platform. However, most of the load will be supported by the air bearings, and the linear motors will provide a levitation force of 1 N each. In the experimental setup, the vertical force generated by the motor was measured with a load cell. When the motor arrives to the target position, the vertical force is positive and constant, as required. However, when the motor moves from the initial position to the target position during the transient period, the vertical force varies slightly. It was observed that the transient response of the vertical force improves with the closed-loop control system compared to the open-loop system. During the transient response of the open-loop system, the value of F_z decreases by 18%. In contrast, in the closed-loop system, the value of F_z increases by 7%. According to the manufacturer of the air bearings, considering an air gap of 5 µm, they have a stiffness of 13 N/µm. Therefore, a change of 0.07 N in the load will compress the gap by 5 nm, which is acceptable for the application.

8. Conclusions

In this work, a control system for a Halbach linear motor in 1D has been designed, implemented and experimentally validated in commercial control hardware. The chosen hardware is a Digital Motor Control Kit from Texas Instruments. The usual application of this DMC Kit is the control of the rotation speed or the torque in rotatory motors. As a novelty, in this work it is used to control the position of a linear motor.

The developed control system will be implemented in the four Halbach linear motors that work as actuators in a 2D-nanopositioning stage (NanoPla). The NanoPla is currently in development at the University of Zaragoza. Halbach linear motors have been chosen as actuators because they allow movement along the moving axes and, also, in the orthogonal direction. Therefore, the 2D movement of the NanoPla is achieved in one plane. In addition, besides the propulsion force, Halbach linear motors generate a vertical force that favours the levitation of the moving part of the NanoPla. Developing the control system in a commercial hardware facilitates the future industrial applicability of the NanoPla.

Firstly, this work has proposed an open-loop control system that uses the electromagnetic horizontal force generated by the motor as a controller. Being a sensorless control system, it presents positioning errors that cannot be corrected. Consequently, a laser system has been chosen as a positioning sensor, and a closed-loop control system has been designed. Then, the developed control system has been implemented in the chosen hardware. The limitations of the commercial hardware have been overcome by optimizing the design.

Once the control system was designed and implemented, its performance was validated in the experimental setup. It has been verified that the system fulfils the working requirements of the NanoPla, which is a working range of 50 mm and a step response of 10 µm. It was also tested that the system is able to respond to steps of 1 µm. It must be noted that the laser system used in the experimental validation has a noise of 400 nm, while the laser system of the NanoPla has a noise of 20 nm. Therefore, the performance is expected to improve in the NanoPla. Additionally, the vertical force generated by the motor has also been measured, being constant at steady state and varying slightly (+7%) during the transient period; that is, when the motor is moving from the initial position to the target position. In the NanoPla, the main support of the levitation of the moving platform comprises three air bearings, while the motors favour the levitation with a force of 1 N each. Thus, a variation of 0.07 N does not affect the stability of the system.

The fact that the developed control strategy implemented in the chosen control hardware is able to operate according to the NanoPla design requirements, make unnecessary the use of more advance control devices. In future works, the control system that has been presented in this paper for one Halbach linear motor along one dimension will be implemented in the four NanoPla actuators to provide a two-dimensional travel range. One DMC Kit will be needed for each motor and the whole control strategy and experimental results will be obtained to assure the desired performance requirements of the NanoPla. At this point, different variants of the control strategy should be tested, in order to find the best performance. These variants could be for instance, operating at constant speed or applying a feedforward loop.

Author Contributions: M.T.G., J.A.A.G. and J.A.Y.F. conceived a preliminary design of the control strategy; L.C.D.P., M.T.G., J.A.A.G. and J.A.Y.F. optimized the control strategy for the implementation in the commercial hardware and performed the implementation; L.C.D.P. performed the experiments; L.C.D.P. wrote the manuscript. All authors contributed to the editing of the manuscript.

Funding: This project was funded by the Spanish government project DPI2015-69403-C3-1-R "MetroSurf" with the collaboration of the Diputación General de Aragón—Fondo Social Europeo. Appreciation is expressed to the FPU Program of the Ministerio de Educación, Cultura y Deporte of the Spanish government, which sponsored the first author.

Conflicts of Interest: The authors declare no conflict of interest. The founding sponsors had no role in the design of the study; in the collection, analyses, or interpretation of data; in the writing of the manuscript, and in the decision to publish the results.

References

1. Kramar, J.A.; Dixson, R.; Orji, N.G. Scanning probe microscope dimensional metrology at NIST. *Meas. Sci. Technol.* **2011**, *22*, 24001–24011. [CrossRef]
2. Manske, E.; Jäger, G.; Hausotte, T.; Füßl, R. Recent developments and challenges of nanopositioning and nanomeasuring technology. *Meas. Sci. Technol.* **2012**, *23*, 74001–74010. [CrossRef]
3. Gao, W.; Kim, S.W.; Bosse, H.; Haitjema, H.; Chen, Y.L.; Lu, X.D.; Knapp, W.; Weckenmann, A.; Estler, W.T.; Kunzmann, H. Measurement technologies for precision positioning. *CIRP Ann.* **2015**, *64*, 773–796. [CrossRef]
4. Sinno, A.; Ruaux, P.; Chassagne, L.; Topu, S.; Alayli, Y.; Lerondel, G.; Blaize, S.; Bruyant, A.; Royer, P. Enlarged atomic force microscopy scanning scope: Novel sample-holder device with millimeter range. *Rev. Sci. Instrum.* **2007**, *78*, 095107. [CrossRef] [PubMed]
5. Sato, K. Trend of precision positioning technology. *ABCM Symp. Ser. Mechatron.* **2006**, *2*, 739–750.
6. Fesperman, R.; Ozturka, O.; Hockena, R.; Ruben, S.; Tsao, T.; Phipps, J.; Lemmons, T.; Brien, J.; Caskey, G. Multi-scale alignment and positioning system—MAPS. *Precis. Eng.* **2012**, *36*, 517–537. [CrossRef]
7. Werner, C. A 3D Translation Stage for Metrological AFM. Ph.D. Thesis, Eindhoven University of Technology, Eindhoven, The Netherlands, 2010.
8. Klapetek, P.; Valtr, M.; Matula, M. A long-range scanning probe microscope for automotive reflector optical quality inspection. *Meas. Sci. Technol.* **2011**, *22*, 094011. [CrossRef]
9. Balasubramanian, A.; Jun, M.B.G.; DeVor, R.E.; Kapoor, S.G. A submicron multiaxis positioning stage for micro- and nanoscale manufacturing processes. *J. Manuf. Sci. Eng.* **2008**, *130*, 031112. [CrossRef]
10. Ducourtieux, S.; Poyet, B. Development of a metrological atomic force microscope with minimized Abbe error and differential interferometer-based real-time position control. *Meas. Sci. Technol.* **2011**, *22*, 094010. [CrossRef]
11. Jäger, G.; Hausotte, T.; Manske, E.; Büchner, H.J.; Mastylo, R.; Dorozhovets, N.; Hofmann, N. Nanomeasuring and nanopositioning engineering. *Measurement* **2010**, *43*, 1099–1105. [CrossRef]
12. Torralba, M.; Yagüe-Fabra, J.A.; Albajez, J.A.; Aguilar, J.J. Design optimization for the measurement accuracy improvement of a large range nanopositioning stage. *Sensors* **2016**, *16*, 84. [CrossRef] [PubMed]
13. Torralba, M.; Valenzuela, M.; Yagüe-Fabra, J.A.; Albajez, J.A.; Aguilar, J.J. Large range nanopositioning stage design: A three-layer and two-stage platform. *Measurement* **2016**, *89*, 55–71. [CrossRef]
14. Hansen, H.N.; Carneiro, K.; Haitjema, H.; De Chiffre, L. Dimensional micro and nano metrology. *CIRP Ann.* **2006**, *55*, 721–743. [CrossRef]
15. Kim, J.A.; Kim, J.W.; Kang, C.S.; Eom, T.B. Metrological atomic force microscope using a large range scanning dual stage. *Int. J. Precis. Eng. Manuf.* **2009**, *10*, 11–17. [CrossRef]
16. Liu, C.H.; Jywe, W.Y.; Jeng, Y.R.; Hsu, T.H.; Li, Y. Design and control of a longtraveling nano-positioning stage. *Precis. Eng.* **2010**, *34*, 497–506. [CrossRef]
17. Lu, X.; Usman, I.-U.-R. 6D direct-drive technology for planar motion stages. *CIRP Ann.* **2012**, *61*, 359. [CrossRef]
18. Hesse, S.; Schäffel, C.; Mohr, H.U.; Katzschmann, M.; Büchner, H.J. Design and performance evaluation of an interferometric controlled planar nanopositioning system. *Meas. Sci. Technol.* **2012**, *23*, 074011. [CrossRef]
19. Holmes, M.; Hocken, R.; Trumper, D. Long-range scanning stage: a novel platform for scanned-probe microscopy. *Precis. Eng.* **2000**, *24*, 191–209. [CrossRef]
20. Trumper, D.; Kim, W.; Williams, M. Design and analysis framework for linear permanent-magnet machines. *IEEE Trans. Ind. Appl.* **1996**, *32*, 371–379. [CrossRef]
21. Yu, H. Design and Control of a Compact 6-Degree-of-Freedom Precision Positioner with Linux-Based Real-Time Control. Ph.D. Thesis, Texas A&M University, College Station, TX, USA, 2009.
22. Torralba, M.; Albajez, J.A.; Yagüe-Fabra, J.A.; Aguilar, J.J. Preliminary modelling and implementation of the 2D-control for a nanopositioning long range stage. *Procedia Eng.* **2015**, *132*, 824–831. [CrossRef]
23. Kim, W.J.; Trumper, D.L.; Lang, J.H. Modeling and vector control of planar magnetic levitator. *IEEE Trans. Ind. Appl.* **1998**, *34*, 1254–1262.
24. Torralba, M.; Yagüe-Fabra, J.A.; Albajez, J.A.; Aguilar, J.J. Caracterización de motores lineales tipo Halbach para aplicaciones de nanoposicionado. In Proceedings of the 2014 Congreso Nacional de Ingeniería Mecánica (CNIM), Málaga, Spain, 24–26 September 2014.

25. Ruben, S. Modeling, Control, and Real-Time Optimization for a Nano-Precision System. Ph.D. Thesis, University of California, Los Angeles, CA, USA, 2010.
26. Díaz-Pérez, L.; Torralba, M.; Albajez, J.A.; Yagüe-Fabra, J.A. Performance analysis of laser measuring system for an ultra-precision 2D-stage. In Proceedings of the 17th International Conference & Exhibition, Hannover, Germany, 29 May–2 June 2017.
27. Texas Instruments. TMS320x2802x, 2803x Piccolo Enhanced Pulse Width Modulator (ePWM) Module, Reference Guide. Available online: http://www.ti.com/lit/ug/spruge9e/spruge9e.pdf (accessed on 18 August 2018).
28. Texas Instruments. TMS320x2802x, 2803x Piccolo High Resolution Pulse Width Modulator (HRPWM), Reference Guide. Available online: http://www.ti.com/lit/ug/spruge8e/spruge8e.pdf (accessed on 18 August 2018).

2.4. Electronics 2018

electronics

Article

Vector Control Strategy for Halbach Linear Motor Implemented in a Commercial Control Hardware

Lucía C. Díaz-Pérez [1,*], José A. Albajez [1], Marta Torralba [2] and José A. Yagüe-Fabra [1]

[1] I3A, University of Zaragoza, C/María de Luna 3, 50018 Zaragoza, Spain; jalbajez@unizar.es (J.A.A.); jyague@unizar.es (J.A.Y.-F.)

[2] Centro Universitario de la Defensa, Ctra. Huesca s/n, 50090 Zaragoz, Spain; martatg@unizar.es

* Correspondence: lcdiaz@unizar.es; Tel.: +34-976-762561

Received: 14 August 2018; Accepted: 3 October 2018; Published: 4 October 2018

Abstract: Halbach linear motors are selected as actuators in positioning stages because they present numerous advantages in precision engineering. These motors generate a horizontal and a vertical force. Whereas the horizontal force is used to perform the movement, the vertical force can be leveraged for the levitation of the moving part of the stage. This paper proposes a vector control strategy that enables the positioning of the motor while regulating the generated vertical force. In contrast to other research projects, this work implements the control strategy in a commercial control hardware. The use of commercial hardware facilitates the applicability and replication of the developed control strategy. The selected hardware is a generic Digital Motor Control Kit of Texas Instruments. The hardware implementation of the control strategy is analysed in detail in order to understand and optimize the control system. The developed control is first validated by simulation, where the error contributors are included. Then, an experimental validation is carried out. The results demonstrate that the control strategy enables the positioning of the motor along its complete operating range and the regulation of the vertical force when the motor is static, as well as while it is moving to a target position.

Keywords: Halbach linear motor; vector control; control hardware

---

1. Introduction

Positioning stages are critical in applications such as measuring at a nanoscale or nano-manufacturing, where they act as a supplementary unit for precisely positioning the sample or the tool [1,2]. The available options can be classified by their precision and their operating range. In addition, in 2D nano-positioning stages, the structure can be defined by its motion, i.e., either stacked or plane [3]. A plane structure is preferred in precision engineering applications [4]. The selection of the actuators directly depends on the positioning stage precision, operating range, and structure.

There are several types of actuators capable of generating linear motion. Thus, it is necessary to analyse their advantages and disadvantages to select the most suitable for each application. On one hand, piezoelectric transducers are capable of providing precise operation; however, they cannot carry out large travels [5,6]. On the other hand, electromagnetic linear motors are capable of transforming electrical energy into linear motion without the requirement for mechanical transmission elements. Within this category, brushless DC motors are among the most applied solutions. Each of these motors is a combination of a coil and a permanent magnet assembly that generates a relative, contactless motion. The absence of friction between the parts presents numerous advantages, e.g., absence of mechanical wear and less number of elements. However, these linear motors require a guiding system (e.g., linear rails), which introduces disadvantages such as friction. In addition, the guiding system, or even the motor design in certain cases (i.e., magnet array scheme), impedes the displacement of the motor along the orthogonal direction of its driving axes, which renders the implementation of planar motion unfeasible. Halbach linear motors designed by Trumper et al. [7] are considered to be a solution to this issue because the size of the effective winding area permits the interaction between the stator and magnet array in all the positions along the plane moving range.

Apart from enabling planar motion without contact between parts, Halbach linear motors present certain highly effective advantages in precision engineering. Therefore, they have been integrated in various high-precision nano-positioning stages that implement planar motion [8,9]. They have a large operating range that is limited only by the length of the stator winding. In addition, they generate a vertical force that can be leveraged to favour the levitation of the moving part. Although most nano-positioning stages using these motors [3,10,11] implement a hybrid suspension combing the magnetic suspension with air bearings, Halbach motors are capable of providing complete suspension of the moving platen [12].

The use of unguided Halbach linear motors is not yet widespread, and they are not commercialized. On the contrary, they are custom-made for each application. Consequently, a commercial solution to perform the control task of these motors is not available. That is [11,13], the authors specifically designed and developed the software and hardware of the control system consisting of linear transconductance power amplifiers that act directly on the phase currents of the motor.

This article proposes a vector control strategy that permits the positioning of the motor while regulating the generated vertical force. The control of the two orthogonal forces is decoupled by performing a Clarke–Park transformation, generally applied in rotative motors for decoupling the control of the magnetic flux and the torque. In contrast to other research projects, this work implements the control strategy in a commercial control-hardware. The selected hardware is a generic Digital Motor Control Kit for rotative permanent magnet synchronous motors of Texas Instruments. The two main functions of the hardware that define the performance of the system are the voltage generation and the current sampling. Therefore, they are analysed in detail in order to understand their effect and to optimize the implementation. It should be highlighted that the proposed vector control strategy is implemented in a commercial hardware without either any modification or additional custom-made electronics. The purpose of this is to facilitate the applicability and replication of the developed control strategy.

This paper is divided as follows: First, the operating principle and the dynamics of Halbach linear motors are analysed, and the experimental setup is described. Then, the proposed vector control strategy is presented. Following this, the implementation of the control strategy in the control hardware is described. The implementation of the control system in the hardware is simulated in order to be virtually analysed. Finally, the experimental results are obtained, and conclusions are drawn.

2. Halbach Linear Motor

The Halbach linear motor case of this study was developed by Trumper et al. [7] and custom-made in the University of North Carolina at Charlotte (U.S.A.). It consists of two main parts: A Halbach magnet array and the stator (see Figure 1). The Halbach magnet array comprises eight permanent magnets bounded into an aluminium housing. On the other side, the stator comprises three coils that are wrapped around an aluminium mandrel. It should be noted that the absence of a ferrous core eliminates the presence of the cogging force. When DC flows through the coils, this motor generates two orthogonal forces, as represented in Figure 1. In this section, first, the operating principle of Halbach linear motors is described. Then, the system is analysed and the experimental setup defined.

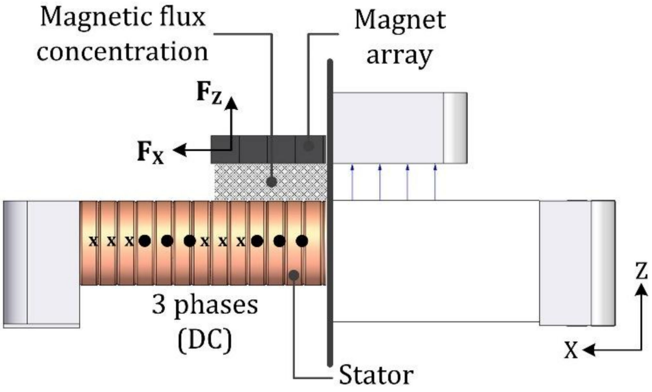

Figure 1. Orthogonal forces in Halbach linear motor.

2.1. Halbach Linear Motor Operating Principle

The operating principle of Halbach linear motors is based on the electromagnetic interaction between the magnetic field of the Halbach array and each of the currents flowing through the coils. Each phase generates two orthogonal forces: One horizontal and the other vertical. In Figure 2a, the horizontal forces along the X-axis (F_{x1}, F_{x2}, and F_{x3}) generated by the three different-phase currents (I_a, I_b, and I_c) have been represented. The sum of all the horizontal forces generated by the three phases is the total horizontal force F_x acting on the motor (continuous line graph). Similarly, the sum of all the vertical forces generated by the three phases is the total vertical force F_z acting on the motor (Figure 2b). This specific combination of currents generates a maximum total force (horizontal and vertical) of 1 N.

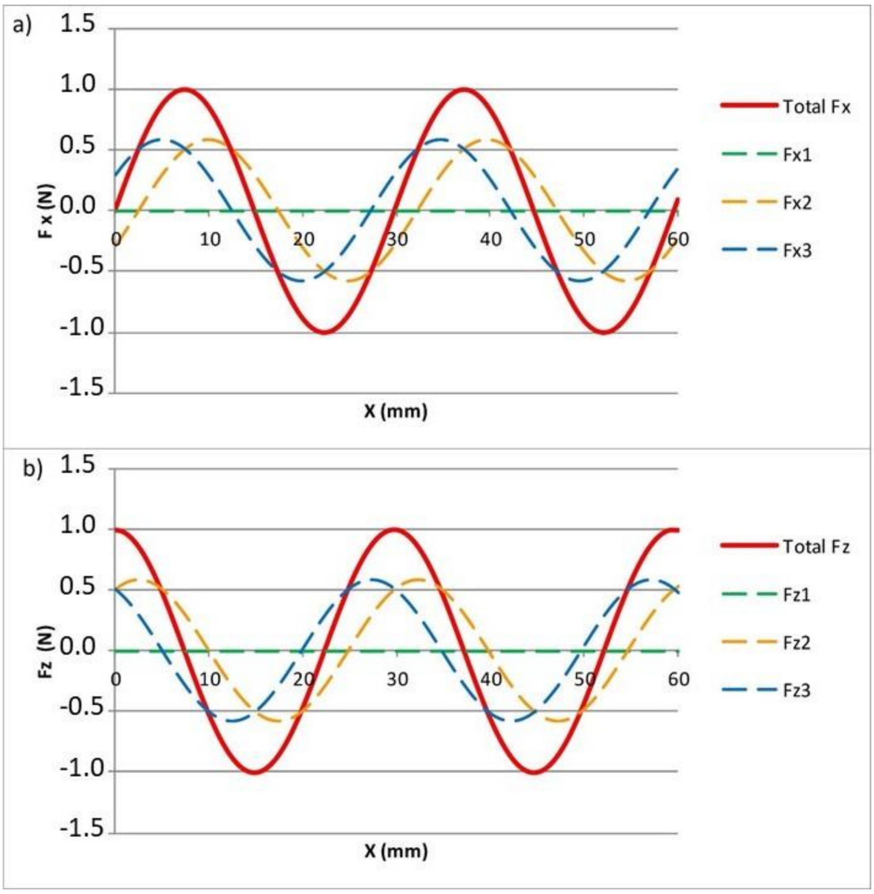

Figure 2. F_x (**a**) and F_z (**b**) along axis-of-movement for $I_a = 0$ A, $I_b = -0.3593$ A, and $I_c = 0.3593$ A.

Figure 2 illustrates that the magnitude of the generated forces is dependent on the relative position between the stator and magnet array, and it presents a sinusoidal shape. The period corresponds to one pitch of the motor (l). It is also apparent that the forces generated by each phase current exhibit a phase difference of $2\pi/3$. In addition, the total horizontal force (F_x) and the total vertical force (F_z) exhibit a phase difference of $\pi/2$.

$$\begin{bmatrix} F_x \\ F_z \end{bmatrix} = A \begin{bmatrix} \cos(kx_0) & \cos\left(kx_0 - \frac{2\pi}{3}\right) & \cos\left(kx_0 + \frac{2\pi}{3}\right) \\ \sin(kx_0) & \sin\left(kx_0 - \frac{2\pi}{3}\right) & \sin\left(kx_0 + \frac{2\pi}{3}\right) \end{bmatrix} \begin{bmatrix} I_a \\ I_b \\ I_c \end{bmatrix} \tag{1}$$

The motor law (Equation (1)) is the mathematical representation of the relationship between the total resultant vertical and horizontal forces and the phase currents, depending on the relative position between the stator and magnet array (x_0). In this equation, A is a constant that depends on the design parameters of the motor, as represented in Equation (2).

$$A = N_m \eta_0 \mu_0 M_0 G e^{-kz_0} \tag{2}$$

$$k = \frac{2\pi}{l} \tag{3}$$

In Equation (2), N_m is the number of spatial periods of the magnet array, η_0 is the winding density of the stator coil, $\mu_0 M_0$ is the remanence of the permanent magnets, G represents the effects of the motor geometry, k is the fundamental wave number, and z_o is the separation gap between the stator and the magnet array. The parameter k is calculated according to Equation (3), where l is the pitch or the spatial period of the array wavelength. The parameters A, k, and l can be experimentally calculated by measuring with a load cell, along the travel range of the motor, the vertical and horizontal force generated by certain known phase currents. Specifically, for the motor case of this study, A was experimentally calculated and is equal to 1.6067 N/A, while l is equal to 29.778 mm and, thus, k is equal to 211.0001 rad/m.

2.2. Servosystem

When functioning as a positioning actuator, the motor should move to the target position and remain motionless at this point ($F_x = 0$). It is feasible to identify the position where this condition is fulfilled, in Figure 3a. It is observed that when the slope of the horizontal force is negative, under marginal perturbations, the moving part returns to the target position. Therefore, the motor is at a stable equilibrium state.

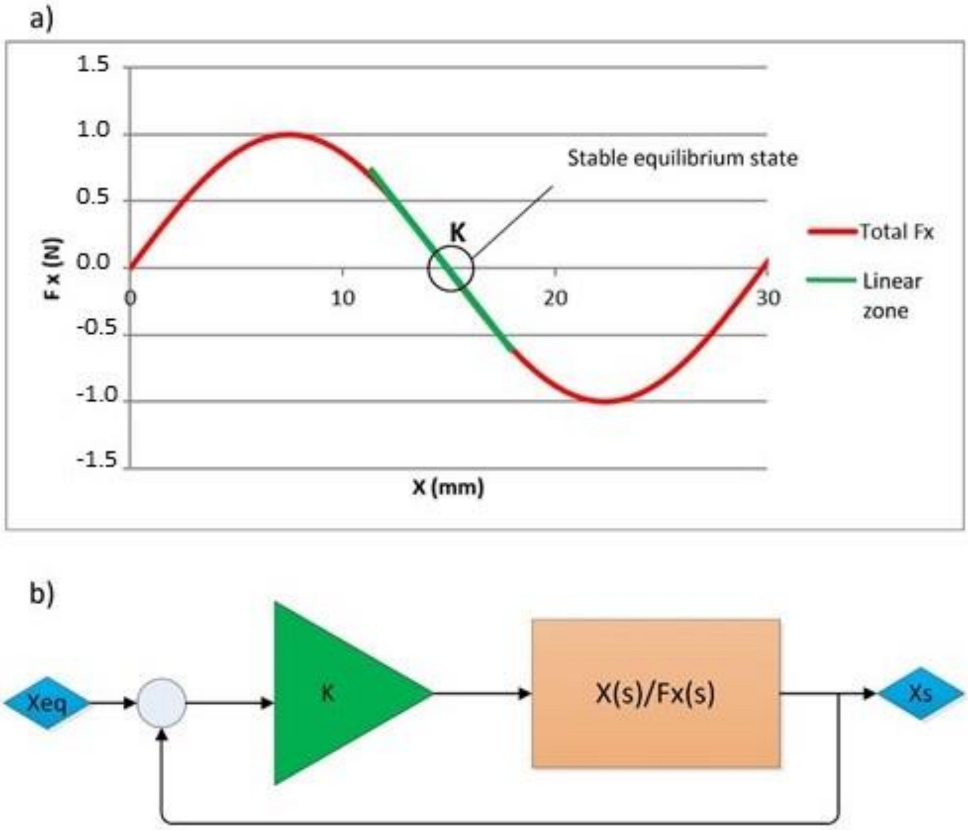

Figure 3. Linear zone around equilibrium position (**a**) and representation of the system in the linear zone (**b**).

Thus, around the stable equilibrium position, the open-loop system replicates a servosystem, with the stable equilibrium position as the reference position. This servosystem consists of the electromagnetic force that depends on the position, and of the load elements that depend on the setup. In addition, as is shown in Figure 3a, around the equilibrium position (X_{eq} = 0 mm) F_x is linear and behaves as a proportional controller (K). The value of the proportional constant K is calculated as the slope on the linear zone of the curve representing F_x as a function of the position. It depends on the magnitude defined for the vertical force at the target position. For example, when the value of F_z is set to 1 N at the target position as the initial condition, the electromagnetic proportional controller has a constant K of approximately 205 N/m. Figure 3b is a simplified representation of the system inside the linear zone.

The transfer function between the electromagnetic force generated by the motor $F_x(s)$ and the final position X(s) includes the mass of the moving part (m) and the viscous-friction elements of the setup (b), as expressed by Equation (4):

$$\frac{X(s)}{F_x(s)} = \frac{1/m}{s^2 + \frac{b}{m}s} \tag{4}$$

The closed-loop transfer function of this system relates the equilibrium position $X_{eq}(s)$ to the final position X(s) in the linear zone, and it is obtained as expressed by Equation (5):

$$\frac{X(s)}{X_{eq}(s)} = \frac{\frac{K}{m}}{s^2 + \frac{b}{m}s + \frac{K}{m}} \tag{5}$$

2.3. Experimental Setup

The experimental setup has been mounted in a metrology laboratory of the University of Zaragoza, as shown in Figure 4a. The stator of the linear motor is the moving part, and it is mounted over a pneumatic linear guide in order to facilitate frictionless movement. The magnet array is fixed to the arm of a coordinate measuring machine (CMM). In addition, a load cell has been placed between the magnet array and the CMM arm in order to measure the vertical force generated by the motor. The arm of the CMM is used only for positioning the magnet array above the stator, leaving a 400-µm air gap. Then, the arm stays static. The Renishaw XL80 laser system (Renishaw, Gloucestershire, UK) has been selected as the positioning sensor for its precision; it measures the position of the moving stator. A scheme of the setup has been represented in Figure 4b.

The control hardware is a Digital Motor Control Kit (DMC) of Texas Instruments, DRV8302-HC-C2-KIT (Dallas, TX, USA). The three-phase power stage of the control hardware is wired to the stator phases, and the control card is connected to a computer by USB.

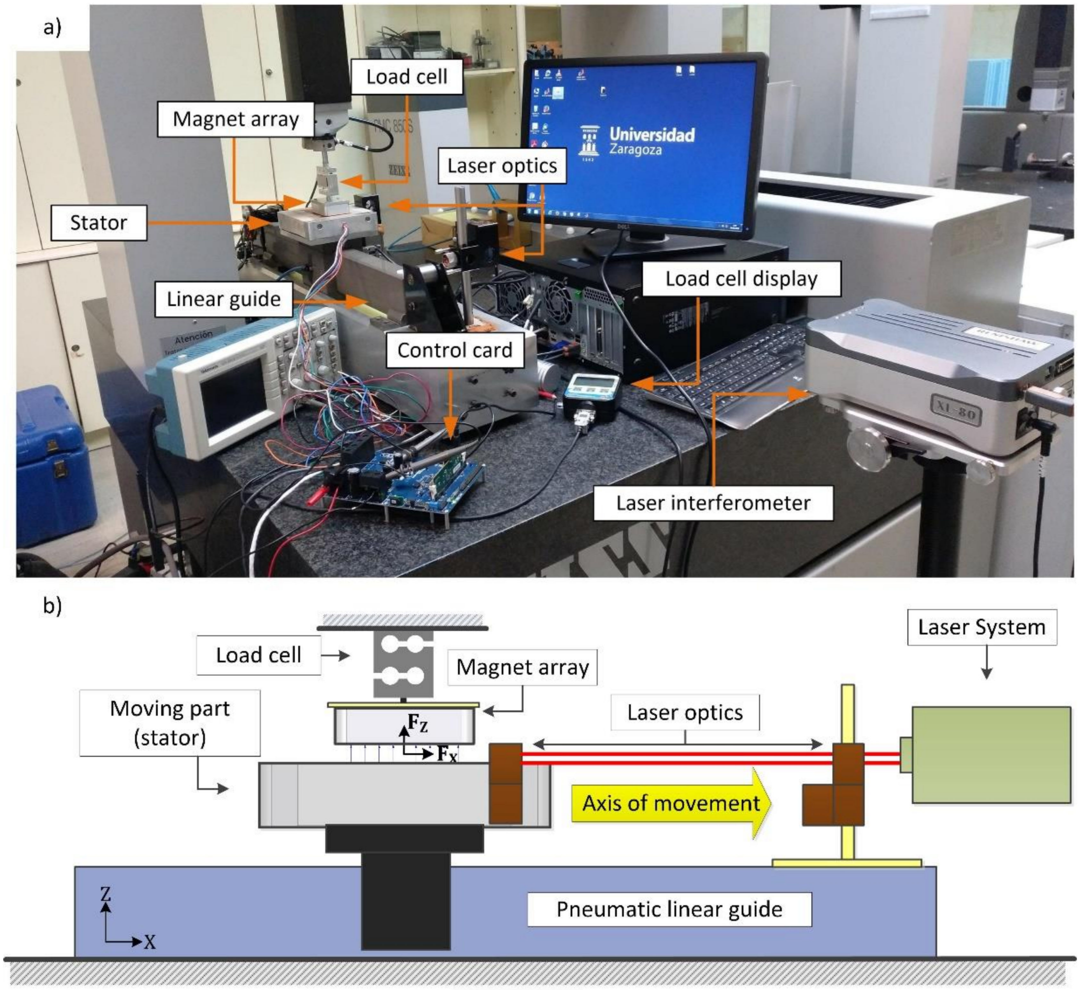

Figure 4. Experimental setup overview (**a**) and scheme (**b**).

According to the previous subsection, the transfer function between the horizontal force $F_x(s)$ and the final position X(s) includes the mass of the stator (m) and the viscous-friction elements of the setup (b). Therefore, by experimentally obtaining the transfer function, the viscous-friction elements of the setup can be estimated. For simplicity, the closed-loop transfer function (Equation (5)) has been assessed; this equation relates the equilibrium position $X_{eq}(s)$ to the final position X(s) in the linear zone. By acting on the phase currents and for a F_z set to 1 N, the equilibrium position has been displaced by

2 mm; the resultant movement of the motor has been recorded by the laser system. In Equation (5), the parameter K is known, and the viscous element b and the mass m can be experimentally adjusted until the simulated response matches the actual response of the system. The obtained values are b = 9.41 N·s/m and m = 3.75 kg.

3. Vector Control Strategy

Halbach linear motors are used for positioning in precision engineering; moreover, typically, there are two parameters that need to be regulated: The position of the moving part of the motor and the vertical force generated by the motor. It is important to regulate the vertical force generated by the motor because, in certain applications, it provides support for levitation [12]. This force could be either positive or negative depending on the design of the positioning stage, where the motor could be inverted, that is, the stator would be above the magnet array [3].

As described in the previous section, the position of the motor is defined by the horizontal force because it is the only force acting on the axis of movement. Therefore, in order to regulate the position and the vertical force separately, it is necessary to decouple the control of the vertical and the horizontal forces. However, on the basis of Equation (1), it is infeasible to regulate the two forces independently by acting directly on the phase currents.

In rotatory motors, a Clarke–Park transformation (Equation (6)) permits the decoupling of the rotor magnetizing flux and the torque. The Clarke–Park transformation defines the direct and quadrature (d–q) virtual axes that rotate with the spinning rotor at a speed identical to that of the rotating flux vector [14]. In these motors, the quadrature axis component (I_q) produces the torque, and the direct axis component (I_d) exerts a magnetising effect on the reference flux. Then, the common practice is to magnify the torque production and minimize the magnetic flux [15].

$$\begin{bmatrix} I_d \\ I_q \end{bmatrix} = \begin{bmatrix} \cos kx_0 & \cos\left(kx_0 - \frac{2\pi}{3}\right) & \cos\left(kx_0 + \frac{2\pi}{3}\right) \\ \sin kx_0 & \sin\left(kx_0 - \frac{2\pi}{3}\right) & \sin\left(kx_0 + \frac{2\pi}{3}\right) \end{bmatrix} \begin{bmatrix} I_a \\ I_b \\ I_c \end{bmatrix} \tag{6}$$

To understand the effect that the Clarke–Park transformation exerts on a Halbach linear motor, Equations (1) and (6) are combined to obtain:

$$\begin{bmatrix} F_x \\ F_z \end{bmatrix} = A \begin{bmatrix} I_d \\ I_q \end{bmatrix} \tag{7}$$

As implied by Equation (7), the direct axis component (I_d) is proportional to the horizontal force generated by the motor (F_x), as also is the quadrature axis component (I_q) to the vertical force (F_z) [16]. It must be highlighted that in a linear motor, the Clarke–Park transformation exerts a different effect than in a rotatory motor. The linear motor moves when F_x is non-zero; moreover, once it arrives at the target position, F_x should be zero for the motor to remain motionless. Thus, the reference input for I_d naturally tends to zero. The magnitude of F_z (I_q) does not affect the movement because it is orthogonal to the movement axis and it attains its maximum value when F_x is zero. On the contrary, in rotatory motors, I_q produces the torque that performs the movement. Moreover, in rotatory motors, the reference input of I_d is set to zero to optimize the torque production.

Therefore, in a Halbach linear motor, a Clarke–Park transformation permits the decoupling of the control of the two orthogonal forces; this is called vector control. This control can be performed by two independent proportional–integral (PI) controllers for I_d and I_q. The outputs of these two PI controllers are the direct and quadrature virtual voltages, V_d and V_q. Nevertheless, the phase voltages (V_a, V_b, and V_c) that correspond to V_d and V_q at a certain position, must be calculated. This can be achieved by performing an inverse Clarke–Park transformation. The inverse of Equation (6) has more than one solution (one degree of freedom). In the case of this study, the control hardware forces the star connection of the phases, which implies that the sum of the three phase currents must be zero (Equation (8)). Applying this constraint, Equation (9) is obtained:

$$I_a + I_b + I_c = 0 \tag{8}$$

$$\begin{bmatrix} V_a \\ V_b \\ V_c \end{bmatrix} = \frac{2}{3}\begin{pmatrix} \cos kx_0 & \sin kx_0 \\ \cos\left(kx_0 - \frac{2\pi}{3}\right) & \sin\left(kx_0 - \frac{2\pi}{3}\right) \\ \cos\left(kx_0 + \frac{2\pi}{3}\right) & \sin\left(kx_0 + \frac{2\pi}{3}\right) \end{pmatrix}\begin{bmatrix} V_d \\ V_q \end{bmatrix} \tag{9}$$

The resultant control strategy, implementing the vector control, is shown in Figure 5. The main proportional–integral–derivative (PID) controller has the desired position X_{ref} as the reference input and the real position X_s as the feedback; the output is the required horizontal force F_x. The two PI controllers regulate F_x and F_z independently and in real time. These controllers have I_{dref} and I_{qref}, respectively, as the reference input. I_{dref} is proportional to the output of the main PID controller (F_x). I_{qref} is proportional to the desired vertical force F_z. The outputs of the PI controllers are the voltages V_d and V_q, and, by an inverse Clarke–Parke transformation, the corresponding phase voltages that need to be generated for the current position can be calculated. The actual I_d and I_q currents must be fed back to the PI controllers to be compared to the reference inputs. Therefore, the control hardware must be capable of reading the phase currents and obtaining the values of I_d and I_q in real time by a Clarke–Park transformation. It must be noted that in order to perform the Clarke–Park transformation and its inverse, the position of the linear motor X_s as well as the value of the phase currents must be specified at each moment. The operating speed of the main PID is defined by the sampling speed of the positioning sensor, whereas the operating speed of the d–q controllers is defined by the sampling speed of the current sensors that is typically faster.

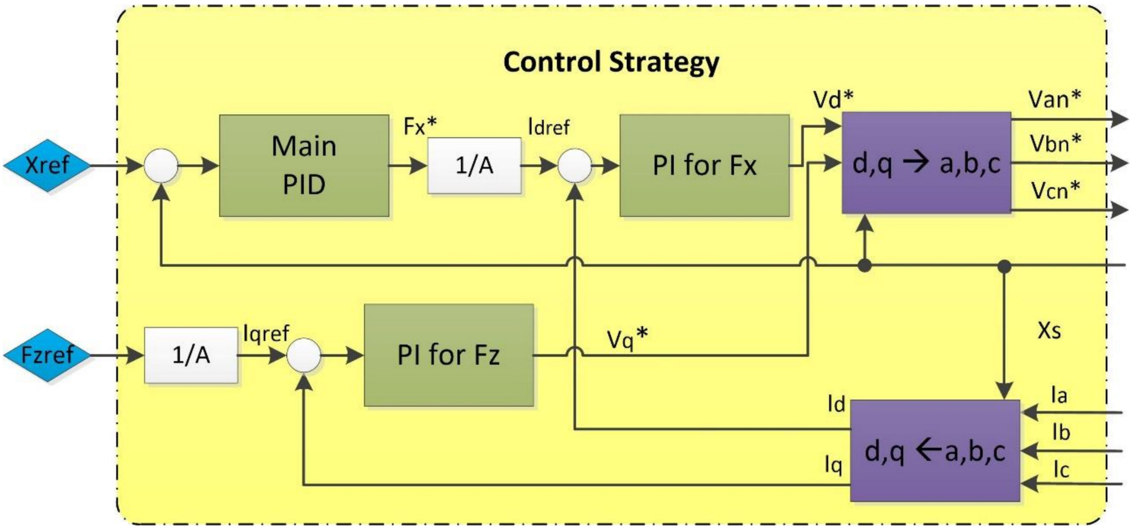

Figure 5. Vector control strategy for linear motor.

4. Control Hardware Implementation

This work proposes to facilitate control using a commercial hardware solution. The selected device is a Texas Instruments (DRV8302-HC-C2-KIT) Digital Motor Control Kit (DMC) designed for regulating generic three-phase rotative permanent magnet synchronous motors and brushless DC motors. The use of this hardware facilitates the implementation and reproducibility of the developed control strategy. Nevertheless, being a commercial control hardware for general purposes, it presents certain limitations when implementing it into our specific application. These limitations can be overcome or minimized by optimizing the control implementation.

The DMC comprises the 32-bit Digital Signal Processor (DSP) TMS320F28035 that executes the closed-loop digital control algorithm with the C2000 Micro Controller Unit (MCU), Analog to Digital Converters (ADC), and PWM outputs. The DMC also comprises current sense amplifiers and the required inverter stage for commutation.

The control program was developed in Simulink that includes a Texas Instruments Target Support Package for Embedded Code library. In addition, Texas Instruments library for MCU C2000 includes optimized blocks for fixed-point mathematical operations (IQ Math) and for digital motor control (DMC). It has been experimentally observed that although the processor is capable of operating with other 32-bit data types and math operation Simulink blocks, it operates faster with its optimized blocks and fixed point or integer data type. The units of the variables are adapted in order to minimize the dynamic range of the data values that the MCU has to process and thus, maximize the precision. Hence, the error derived from the use of the 32-bit data is negligible (<1 nm).

The implementation of the control system in the control hardware is represented in Figure 6. The controller setpoint parameters are the motor position (X_{ref}) and the required vertical force (F_{zref}). The selected hardware generates phase voltages in an inverter stage by pulse width modulation (PWM) of the required phase voltages (V_{an}*, V_{bn}*, and V_{cn}*). The voltage difference between the phase terminals and the neutral point of the motor (N) creates the phase currents (I_a, I_b, and I_c), from which the two orthogonal forces (F_x and F_z) are generated. According to the motor law, their magnitudes depend on the relative position between the stator and the magnet array (X_s). To perform the vector control, the phase currents must be measured by the analogue to digital converters (ADC). The hardware reads two of the phase currents and the third one is calculated according to Equation (8). Position is measured by an XL-80 Renishaw laser interferometer, transferred to Simulink, and directly transmitted to the control card through the serial communication interface (SCI) as 32-bit data, in conjunction with the reference position ($X_{ref)}$ and vertical force (F_{zref}) commands.

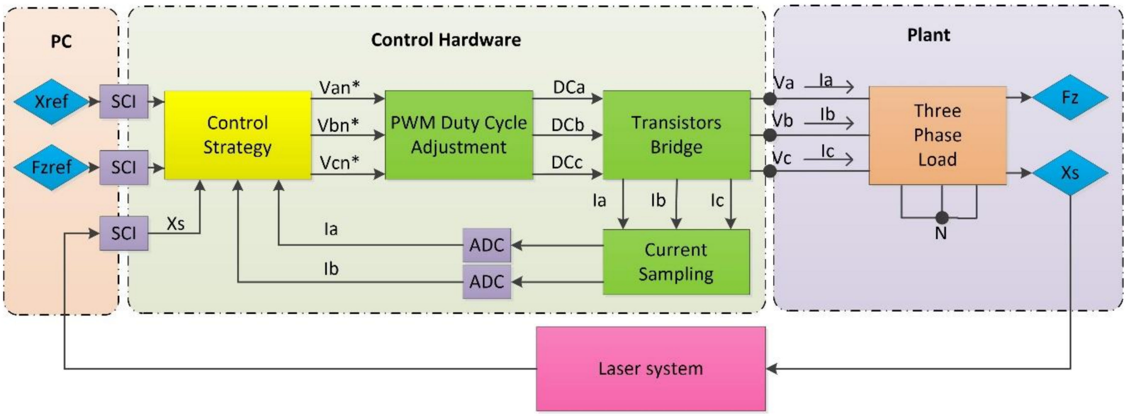

Figure 6. Implementation of control strategy in control hardware.

The movement of the motor is generated when the phase currents flowing through the coils of the stator are varied. The displacement is directly related to the magnitude of this variation. For example, for a reference vertical force set to 5 N, a displacement of 1 µm requires a variation in the phase currents of approximately 1×10^{-4} A. Thus, the precision of the positioning control depends on the precision with which the control hardware is capable of controlling the phase currents. There are two main functions of the hardware that affect the control of the phase currents: The voltage generation and the current sampling. In Sections 4.1 and 4.2, these two functions are described and analysed.

4.1. Voltage Generation

The selected control hardware generates phase voltages by pulse width modulation (PWM). For this application, the PWM signal frequency is constant and defined by the timer period. In contrast, the magnitude of the generated voltage varies and is defined by the duty cycle. When the neutral of the stator is floating, a duty cycle of 100% generates the maximum phase-to-neutral voltage, this is equivalent to half of the supply voltage (PVDD/2) that is being fed to the hardware. A duty cycle of 0% generates the minimum phase voltage (−PVDD/2) due to the inversion of the current flow.

In practice, a PWM signal produces undesirable current ripple. To minimize this ripple, the phase pulses must be center-aligned [17]. Therefore, the count is defined as up and down, which implies that in a period the timer base is counted two times (one-time up and one-time down) [18].

The resolution of the PWM depends on its timer period, which must be an integer of up to 16 bits. The higher the timer period is, the higher is its resolution. Nevertheless, the timer period is limited by the switching frequency. According to the manufacturer, setting the PWM switching frequency below 10 kHz is likely to adversely affect the inverter output and is not recommended. This implies that the highest timer period can be 2^{11} (2048), which corresponds to a lowest acceptable frequency of 14.64 kHz (up–down count). For that timer period, the PWM input is an integer of up to 11 bits and capable of defining the phase voltage with a resolution of PVDD/2048. In this study, the selected supply voltage is 12 V, and the PWM signal resolution is 0.006 V corresponding to 0.006 A in phase current for the 1 Ω resistance stator winding.

The DSP includes a high resolution PWM (HRPWM) function that is capable of extending the time resolution capabilities of the PWM module [19]. HRPWM is based on micro edge positioning (MEP) that divides each coarse step of the PWM into fine steps of 150 ps, which in our case corresponds to a resolution of 2.62×10^{-5} V. The digital input of the HRPWM is a 16-bit integer for the coarse steps and 8-bit fraction length for the MEP steps. As it was mentioned, owing to the PWM frequency requirements, the integer input has a maximum of 11 bits. Therefore, the input of the HRPWM is a fixed point of 19 bits (11 + 8 bits). This data type implies a resolution of 2.29×10^{-5} V. Hence, the resolution of the HRPWM is defined by the fine MEP steps, that is 2.62×10^{-5} V, rather than by the number of bits of the digital input. A disadvantage of the HRPWM is that it does not cover the complete duty cycle working range; i.e., the MEP is not operational for duty cycles near 0% and 100%. The reference value of F_z defines the operating range of the phase currents. In the case of this study, the vertical force is set to a maximum of 5 N. Therefore, the operating range of the phase currents is ±2.1 A, which corresponds to a duty cycle value between 32.5% and 67.5%. Therefore, the HRPWM function can be used in this application, which improves the resolution of the system, as it is shown in the virtual analysis, in Section 5.1.

4.2. Current Sampling

The phase currents are sensed by the shunt resistors that are placed in the inverter legs of the three-phase transistor bridge, where the phase current flows when the low-side switch is on. Therefore, the current sampling must be synchronized with the PWM. The MCU includes ADCs that convert the analog measurements into a 12-bit integer. Only two phase currents are read, and the third one is calculated.

The ADCs are based on start of conversion (SOC). Thus, the ADC modules are set to read once in each PWM signal period. In addition, in order to measure the average current, the shunt voltage must be sampled at the centre of the low-side on-period.

Considering that the maximum and minimum currents that the current shunt is capable of reading are 20.625 A (4095) and −20.625 A (0), respectively, the ADC resolution is 0.01 A. In a previous work [20], a current sampling stability analysis was performed, and the noise was measured for different current values. The observed noise was similar for all the currents within the operating range, exhibiting a root mean square deviation (RMSD) equal to ±0.022 A; moreover, the difference between the maximum and minimum recorded value in a sampling was 0.12 A. The deviations from the actual value are caused by the current sampling noise. This noise can be reduced by using a filter, similar to a rolling average. In this study, the average of 32 sampled values is determined. Applying this filter, the RMSD is reduced to ±0.0032 A, and the difference between the maximum and minimum recorded value in a sampling is reduced to 0.02 A.

5. Validation of Control System Performance

Once the control strategy has been defined and implemented in the control hardware, its performance can be validated. First, the whole system was virtually analysed in Simulink; the results obtained are presented in the first part of this section. In the second part of the section, the experimental verification of the performance of the implemented control system is described.

In this control system, the phase currents' operating range is defined by the reference value set for the vertical force. For all the experiments described in this section, the reference value for the vertical force is set to 5 N so that all the results are comparable.

5.1. Virtual Analysis

The system that is represented in Figure 6 has been completely simulated in Simulink. The plant was modelled according to the transfer function calculated in Section 2.3. In the model, the data type of the variables was set to be identical to that in the program compiled in the MCU. In addition, Texas Instrument's IQ Math and DMC blocks were used to perform the operations, similarly as in the compiled program. The sample times of the ADC and the positioning sensor were also taken into account apart from the errors and noise of the modules that could be characterized. The ADCs operate once in each switching period, i.e., every 68 µs. Renishaw XL80 laser system has a sample time of 0.055 s and a resolution of 1 nm, and its noise has a range of 400 nm. The sample time of the positioning sensor defines the speed of the outer loop, while the sample time of the ADCs defines the speed of the inner loops. In addition, the model includes the limitation of the resolution of the PWM modules and the resolution and noise of the current sensing. The simulation of the model permits us to determine the effects of each error that is introduced and of tuning the controllers in advance, which facilitates the task during the actual implementation.

As mentioned in Section 2.2, the electromagnetic horizontal force behaves as a servosystem, the target position of which is at an equilibrium state, wherein the horizontal force is zero. The equilibrium state of the motor is generated by a certain combination of the phase currents, which is different for each position inside a pitch. Therefore, the minimum incremental motion of the system is directly related to the phase current resolution. In turn, the resolution of the phase currents depends on the resolution of the voltage generation. The simulated model enables a better understanding of the system dependence on the voltage generation resolution, which is defined by the PWM module and the HRPWM function, if applied.

In order to study the effect of the voltage generation resolution in the system, the other error contributors were cancelled in the simulated model. First, the voltage generation resolution was set to be 0.006 V without using the HRPWM function. It was observed that when the system operates in an open-loop, the resultant minimum incremental motion is approximately 15 µm. This is owing to the fact that the inverter stage is not capable of generating the exact combination of the phase currents that generates a zero horizontal force in the intermediate positions. In Figure 7a, the response in open-loop (red) to a stair case of 10 µm steps (blue) has been simulated. It is observed that the system cannot react to the second step. Nevertheless, when the control strategy is implemented in the system, the positioning error is corrected. The simulation demonstrates that the controller switches between combinations of the phase currents, maintaining the motor at the target position. As a consequence, the motor does not remain motionless, but marginally oscillates around the target position. The amplitude of the oscillation depends on numerous variables such as the target position, the sample time of the positioning sensor and the reference vertical force. This is apparent in Figure 7b, which represents the response of the closed-loop system (red) to a stair case of 10 µm steps (blue). When the HRPWM function is applied, the voltage generation resolution improves to 2.62×10^{-5} V. This resolution is sufficient to perform a minimum incremental motion of approximately 700 nm in open-loop. Similarly, as in the previous case, the positioning error is corrected by implementing the closed-loop control strategy. Nevertheless, the controller switches between combinations of the phase currents that are closer to each other, and thus, the derived oscillation becomes imperceptible. Therefore, when using the HRPWM function, in closed-loop, the voltage generation resolution contributes negligibly to the positioning error. The response to the stair case of 10 μm steps (blue) when using the HRPWM function in closed-loop (red) is represented in Figure 7c. All the results are calculated for a vertical force set to 5 N. For other values it should be taken in to account that the higher the vertical force is, the higher is the dynamic operating range of the phase currents and the lower is the precision that is required.

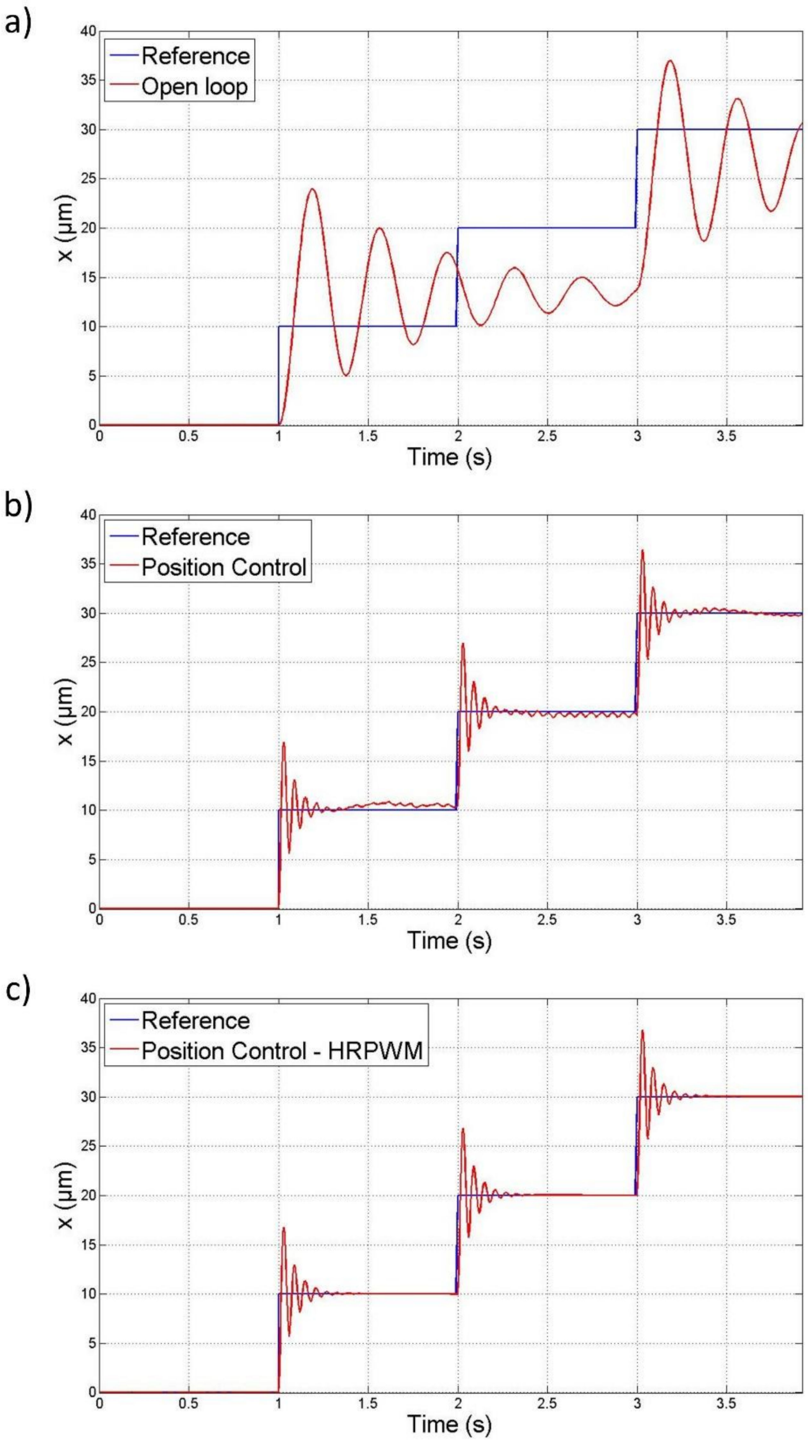

Figure 7. Simulated Response to 10 μm stair case in open loop (**a**), applying position control (**b**), and applying position control and high resolution pulse width modulation (HRPWM) function (**c**).

The simulation reveals that the two main contributors to the positioning error are the positioning sensor noise and the resolution and noise of the current sampling. The noise of the positioning sensor is not a subject of this work because it is external to the control hardware, and the selection of the positioning sensor does not affect the control system. The resolution of the ADCs is limited to 12 bits, and they present a noise that the previous section proposed to minimize by applying a rolling mean filter. It has been verified that the delay introduced by the filter does not affect the performance of the control system, due to the difference between the sample speed of the laser system (0.055 s per readout) and the sample speed of the ADCs (68 µs per readout). In addition, the simulation reveals that the rolling mean filter improves the resolution of the ADCs by approximately two additional bits. In this control hardware, the performance of the ADCs cannot be improved any further. If better results are required, another control card with higher performance ADCs should be selected.

The controllers were simulated and tuned in Matlab, taking into account all the error contributors and the sample times. The operating requirements that were taken into account when tuning the controllers were a maximum response time of 1 min to prevent oscillation. As mentioned in Section 2.2, around the equilibrium position, where the horizontal force is linear, the system behaves as a second-order servosystem. In order to facilitate the tuning of the controllers, the controllers were set to work in the linear zone by limiting the output in the saturation parameters.

5.2. Experimental Results

Once the system has been virtually validated, the control system is implemented in the hardware. The PID controller for the position and the PI controllers for I_d and I_q, which had already been tuned in the simulated system, have been experimentally fine-tuned in the setup. The saturation parameters have been also set to work in the linear zone.

One of the main advantages of Halbach linear motors is that the operating range is limited only by the design. The Halbach linear motor case of this study is designed to operate in a range of 50 mm. In order to verify that the control system is capable of operating in the complete operating range, the target reference was set to be a ramp that moves the motor 50 mm from the zero position. The response is represented in Figure 8, which shows that the position of the motor (red line) follows the reference position (blue line) along the whole working range at constant speed.

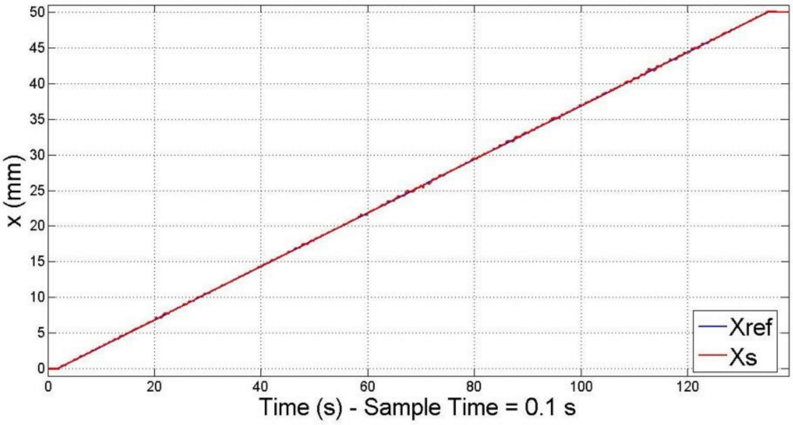

Figure 8. Experimental result: 50 mm travel range at constant speed.

Halbach linear motors are mainly applied in precision engineering, functioning as actuators in positioning stages. In Figure 9, the response to a 100 µm step is represented.

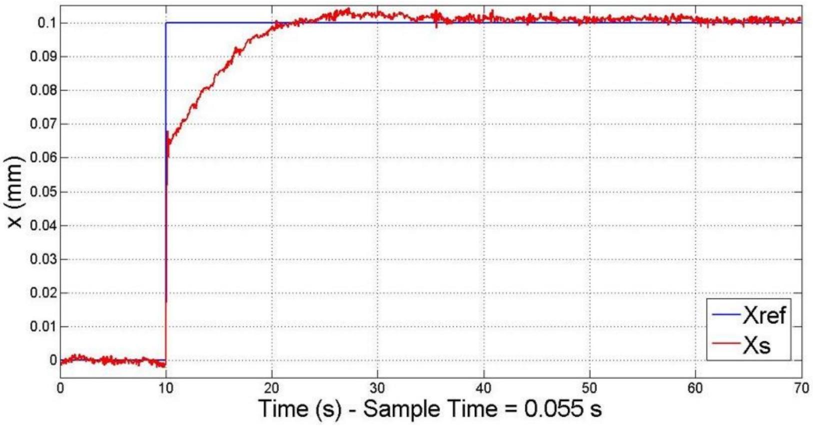

Figure 9. Experimental result: Response to 100 μm step.

In addition, in a positioning stage, the vertical force generated by the motors can be leveraged. As mentioned in the introduction, in most positioning stages, the levitation is performed by airbearings, whereas Halbach linear motors favour the levitation of the moving part [3,8,11]. Nevertheless, there are other designs that propose the vertical force of the linear motors as the only sustainable system for the levitation [12]. In both the cases, the vertical force should remain constant as the mass of the moving part does not vary. According to the motor law, the vertical force depends on the relative position between the stator and magnet array. Therefore, when the motor is moving to a target position (transient state), the vertical force varies marginally from its reference value. The vector control strategy that is proposed in this work enables the control of the transient response of the vertical force. In order to verify its performance, the vertical force was measured with a load cell fixed to the magnet array, as shown in Figure 4. The variation of the vertical force when the motor from being static moves to a target position having a separation of 5 mm has been represented in Figure 10a for three cases: Open-loop without applying any controller (dashed line), closed-loop with a position controller (dotted line), and closed-loop with the vector control strategy defined in this work (dash-dot line). Similarly, the displacement of the motor for each case has been represented in Figure 10b. In each case, the reference value for the vertical force was set to be 5 N (solid line). Nevertheless, if the vector control is not applied, the vertical force is not regulated, and its difference from the reference value is not corrected. As a result, in the first two cases, F_z does not attain its target value (5 N). As is evident, when the stator starts to move toward the target position (t = 1 s), the vertical force moves from its reference position. In the open-loop system, F_z decreases by 18%, whereas when a position controller is applied, it increases by 7%. This is owing to the fact that in both the cases, the vertical force is coupled to the horizontal force. A position controller acts on the horizontal force, and that explains the difference between the variation of the vertical force in the first two cases. When applying a vector control, the two forces are decoupled and regulated by separate controllers. The first consequence of this is that when vector control is applied, the measured value of the vertical force is coincident with its target value, i.e., the error is eliminated owing to the integral term of the controller. Moreover, as it can be observed, the effect on the position control result is minimal. In addition, the variation of the vertical force during the transient response can be adjusted by tuning its controller. As a consequence, the variation of the vertical force when applying vector control is smoother. In cases where the variation needs to be minimized, a derivative term could be added in the controller of the vertical force (I_q).

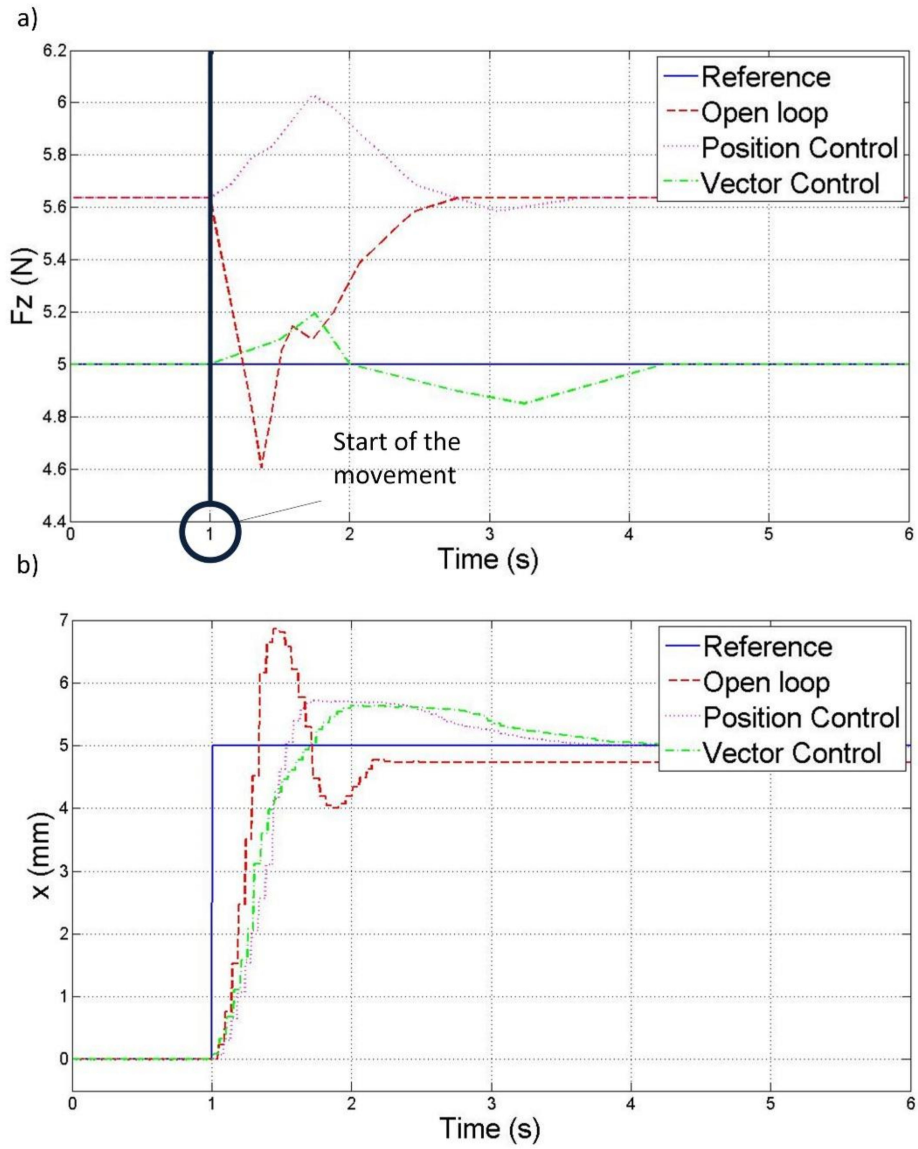

Figure 10. Experimental result: Variation of vertical force (**a**) and position (**b**) during movement of motor.

6. Conclusions

Halbach linear motors present numerous advantages in precision engineering. Consequently, they have already been implemented in a number of positioning stages. In these stages, the horizontal force that is generated by the motor is used for positioning and the vertical force for favouring the levitation of the moving part of the stage. In order to regulate these two forces separately, this work proposes a vector control that decouples the forces by applying a Clarke–Park transform. This control strategy includes a main PID controller for the position and a PI controller for each of the forces. In addition, the control strategy has been implemented in a commercial control hardware: A Digital Motor Control Kit of Texas Instruments. Using commercial hardware presents numerous advantages such as facilitation of the future replication of the system. Nevertheless, the control hardware presents certain constraints and limitations that need to be overcome by optimizing the system design.

The two main functions of the control hardware that affect the precision of the system are the voltage generation and the current sampling. These two functions have been analysed in detail in order to improve the performance. This work proposes the implementation of the HRPWM function in the voltage generation and a rolling mean filter in the current sampling, in order to improve the resolution and reduce the noise of the phase currents.

In addition, a virtual simulation of the whole control system has been carried out in Simulink using the transfer function obtained for the plant of the experimental setup. The simulation includes operations, data types, resolution, sample times, and noise identical to those of the actual system implemented in the control hardware. This simulation has enabled a better understanding of the system. In addition, the controllers have been tuned in the simulated plant, which has facilitated the task in the experimental setup.

The performance of the control system developed in this work has been verified in an experimental setup. The capability of the control system to operate in the complete operating range permitted by its design, that is 50 mm, and its suitability for precision engineering applications were tested. In addition, the vertical force has been measured with a load cell in order to verify the advantages that the vector control introduces. The variation of the vertical force when the motor is moving was compared to the variation of the vertical force in the open-loop system and that in the system with a positioning control albeit without vector control. The improvement is evident; vector control eliminates the difference between the generated vertical force and the reference value, and it was observed that the transient response of the vertical force can be adjusted by tuning its controller.

Author Contributions: J.A.A., M.T. and J.A.Y.-F. conceived a preliminary design of the control strategy; L.D, J.A.A.,M.T. and J.A.Y.-F optimized the control strategy applying vector control and performed the implementation; L.D. performed the experiments; L.D. wrote the manuscript. All authors contributed to the editing of the manuscript.

Funding: This project was funded by the Spanish government project DPI2015-69403-C3-1-R "MetroSurf" (MEC/FEDER, UE), with the collaboration of the DGA-FSE. Appreciations are due to the FPU Program of the Ministerio de Educación, Cultura y Deporte of the Spanish government, which sponsored the first author.

Conflicts of Interest: The authors declare no conflicts of interest. The funders had no role in the design of the study; in the collection, analyses, or interpretation of data; in the writing of the manuscript, and in the decision to publish the results.

References

1. Manske, E.; Jäger, G.; Hausotte, T.; Füßl, R. Recent developments and challenges of nanopositioning and nanomeasuring technology. *Meas. Sci. Technol.* **2012**, *23*, 74001. [CrossRef]
2. Gao, W.; Kim, S.W.; Bosse, H.; Haitjema, H.; Chen, Y.L.; Lu, X.D.; Knapp, W.; Weckenmann, A.; Estler, W.T.; Kunzmann, H. Measurement technologies for precision positioning. *CIRP Ann. Manuf. Technol.* **2015**, *64*, 773–796. [CrossRef]
3. Torralba, M.; Valenzuela, M.; Yagüe-Fabra, J.A.; Albajez, J.A.; Aguilar, J.J. Large range nanopositioning stage design: A three-layer and two-stage platform. *Measurement* **2016**, *89*, 55–71. [CrossRef]
4. Lu, X.; Usman, I.-U.-R. 6D direct-drive technology for planar motion stages. *CIRP Ann. Manuf. Technol.* **2012**, *61*, 359. [CrossRef]
5. Li, C.X.; Gu, G.Y.; Yang, M.J.; Zhu, L.M. Design, analysis and testing of a parallel kinematic high-bandwidth XY nanopositioning stage. *Rev. Sci. Instrum.* **2013**, *84*, 125111. [CrossRef] [PubMed]
6. Jywe, W.Y.; Jeng, Y.R.; Teng, Y.F.; Wang, H.S.; Wu, C.H. Development of the nano-measuring machine stage. In Proceedings of the IECON 2007 33rd Annual Conference of the IEEE Industrial Electronics Society, Taipei, Taiwan, 5–8 November 2007.
7. Trumper, D.; Kim, W.; Williams, M. Design and analysis framework for linear permanent-magnet machines. *IEEE Trans. Ind. Appl.* **1996**, *32*, 371–379. [CrossRef]
8. Fesperman, R.R. Multi-Scale Alignment Positioning System. Ph.D. Thesis, University of North Caroline, Charlotte, NC, USA, 2006.
9. Holmes, M.; Hocken, R.; Trumper, D. Long-range scanning stage: A novel platform for scanned-probe microscopy. *Precis. Eng.* **2000**, *24*, 191–209. [CrossRef]
10. Yu, H. Design and control of a compact 6-degree-of-freedom precision positioner with linux-based real-time control. Ph.D. Thesis, Texas A&M University, College Station, TX, USA, 2009.

11. Ruben, S. Modeling, control, and real-time optimization for a nano-precision system. Ph.D. Thesis, University of California, Los Angeles, CA, USA, 2010.
12. Kim, W.; Trumper, D.L. High-precision magnetic levitation stage for photolithography. *Precis. Eng.* **1998**, *22*, 66–77. [CrossRef]
13. Hu, T. Design and control of a 6-degree-of-freedom levitated positioner with high precision. Ph.D. Thesis, Texas A&M University, College Station, TX, USA, 2005.
14. Leonhard, W. *Control of Electrical Drives*, 2nd ed.; Springer-Verlag: Berlin, Germany, 1996.
15. Vas, P. *Sensorless Vector and Direct Torque Control, Monographs in electrical and electronic engineering Series 40*; Oxford University Press: New York, NY, USA, 1998.
16. Kim, W.J.; Trumper, D.L.; Lang, J.H. Modeling and Vector Control of Planar Magnetic Levitator. *IEE Trans. Ind. Appl.* **1998**, *34*, 1254–1262. [CrossRef]
17. Kazmierkowski, M.P.; Malesani, L. Current Control Techniques for Three-Phase Voltage-Source PWM Converters: A Survey. *IEE Trans. Ind. Electron.* **1998**, *45*, 697–703. [CrossRef]
18. Texas Instruments. *TMS320x2802x, 2803x Piccolo Enhanced Pulse Width Modulator (ePWM) Module*; Texas Instruments: Dallas, TX, USA, 2008.
19. Texas Instruments. *TMS320x2802x, 2803x Piccolo High Resolution Pulse Width Modulator (HRPWM)*; Texas Instruments: Dallas, TX, USA, 2009.
20. Díaz-Pérez, L.C.; Torralba, M.; Albajez, J.A.; Yagüe-Fabra, J.A. Current Sampling in a Control Strategy for a Linear Motor of a 2D Nanopositioning Stage Based on Vector Control. In Proceedings of the 18th EUSPEN conference & Exhibition, Venezia, Italy, 5 June 2018.

2.5. Sensors 2017

sensors

MDPI

Article

Geometrical Characterisation of a 2D Laser System and Calibration of a Cross-Grid Encoder by Means of a Self-Calibration Methodology

Marta Torralba [1], Lucía C. Díaz-Pérez [2,*], Margarita Valenzuela [3], José A. Albajez [2] and José A. Yagüe-Fabra [2]

[1] Centro Universitario de la Defensa, Ctra. Huesca s/n, Zaragoza 50090, Spain; martatg@unizar.es
[2] I3A, University of Zaragoza, C/María de Luna 3, Zaragoza 50018, Spain; jalbajez@unizar.es (J.A.A.); jyague@unizar.es (J.A.Y.-F.)
[3] Departamento de Ingeniería Industrial, Universidad de Sonora, Rosales y Blvd. Luis Encinas s/n, Hermosillo 83000, Mexico; margarita.valenzuela@unison.mx
* Correspondence: lcdiaz@unizar.es; Tel.: +34-97-676-2561

Received: 28 July 2017; Accepted: 28 August 2017; Published: 31 August 2017

Abstract: This article presents a self-calibration procedure and the experimental results for the geometrical characterisation of a 2D laser system operating along a large working range (50 mm × 50 mm) with submicrometre uncertainty. Its purpose is to correct the geometric errors of the 2D laser system setup generated when positioning the two laser heads and the plane mirrors used as reflectors. The non-calibrated artefact used in this procedure is a commercial grid encoder that is also a measuring instrument. Therefore, the self-calibration procedure also allows the determination of the geometrical errors of the grid encoder, including its squareness error. The precision of the proposed algorithm is tested using virtual data. Actual measurements are subsequently registered, and the algorithm is applied. Once the laser system is characterised, the error of the grid encoder is calculated along the working range, resulting in an expanded submicrometre calibration uncertainty (k = 2) for the X and Y axes. The results of the grid encoder calibration are comparable to the errors provided by the calibration certificate for its main central axes. It is, therefore, possible to confirm the suitability of the self-calibration methodology proposed in this article.

Keywords: nanopositioning; 2D-stage; self-calibration; calibration; plane mirror laser interferometer; grid encoder; uncertainty

1. Introduction

The nanotechnology field has grown over recent decades, and the importance of nanotechnology has rapidly increased with the demand for more accurate positioning systems and larger working ranges [1,2]. Positioning systems that operate at a nanometre scale are fundamental in devices used in nanotechnology applications such as nanomanufacturing machine tools or measuring machines. The performance and usage of these machines depend directly on the accuracy of these positioning systems and their working ranges [3]. Within this line of research, a novel 2D nanopositioning platform (NanoPla) has been developed [4,5] with a large working range (50 mm × 50 mm) and a submicrometre uncertainty.

Several sensor technologies currently exist that are suitable for addressing nanopositioning issues. Long-range positioning stages can integrate either 1D or 2D encoders or laser interferometer systems to provide displacement feedback. Spurious motions in out-of-plane positions are typically measured by short-range devices such as capacitive or inductive sensors [2,6]. As for the NanoPla, a laser sensor scheme based on plane mirror laser interferometers has been selected as the most suitable positioning sensor system. In large working ranges, these sensor systems achieve excellent accuracy and ensure direct traceability. When working at a nanometre scale, the accuracy of the positioning sensor system is crucial. The International Organisation for Standardisation (ISO) defines accuracy as the description of random and systematic errors [7]. Random errors can be quantified by taking numerous measurements and processing the resulting data by calculating averages and standard deviations in order to determine the measurement uncertainty. However, systematic errors can be corrected by using calibration methods; this is one of the goals of this paper.

When addressing error compensation techniques, several methods can calibrate positioning sensor systems depending on the type of sensors used, the accuracy required, the size of the working range and the available equipment. Direct calibration methods essentially measure a calibrated artefact in order to calculate the difference between the known and the measured position as the systematic error [8]. However, this procedure has a significant disadvantage when working at a submicrometre scale due to the difficulty in finding a reliable calibrated artefact. This artefact should be more accurate than the system to be calibrated, which can be complicated and costly when working at such a small scale. Self-calibration methods provide an alternative option [9] by relating views of a non-calibrated artefact; a calibrated artefact is not required, thus providing a clear advantage [10]. The only parameter that cannot be obtained through self-calibration is the absolute 1D length scale, which must be set independently.

This article focuses on the geometrical characterisation of a two-dimensional laser system used for X-Y positioning with submicrometre uncertainty. Even though the laser heads have already been separately calibrated by the manufacturer, the correction of the geometric errors existing between the laser detector heads and plane mirrors arrangement is required, especially for this 2D setup. The procedure proposed is based on self-calibration methods, and a non-calibrated artefact is therefore required. This study uses a commercial grid encoder as a non-calibrated artefact. A grid encoder is a 2D positioning sensor that has multiple applications in metrology and precision engineering; it utilises a scanning head that reads a geometric pattern (grid) encoded in a plate. The resulting accuracy is a function of the reference pattern quality. The grid encoder is partially calibrated; the manufacturer provides a calibration certificate with information on the measurement error along the main X and Y axes. When considering the various applications of the grid encoder, knowing its error not only along the main axes but also along the entire 2D working range is beneficial. By applying the proposed self-calibration procedure, the geometric errors of the 2D laser system setup are obtained, and, therefore, its measurements are corrected. Next, by comparing them to the grid encoder measurements obtained from the self-calibration procedure at the same positions, the measurement and squareness errors of the grid encoder can be calculated along the working range. The uncertainty of the laser system measurements can thus be determined after the grid encoder calibration is performed, making it possible to determine the calibration uncertainty of the grid encoder. A similar issue was addressed by Kim et al. in [11], where a self-calibration method was also applied to calibrate a 2D positioning system. However, the approach in this study is different because Kim et al. used additional capacitive sensors to perform the self-calibration.

This work initially describes the methods and materials used. The mathematical model of the 2D laser system is then analysed. This identifies the factors that must be calculated by means of the self-calibration algorithm to correct the laser system geometrical errors. The algorithm is initially tested using virtual data, thus verifying its performance within the working range. Once the actual measurements of the laser system and the grid encoder have been obtained experimentally, the geometric errors of the laser system arrangement are calculated. After the laser system has been geometrically characterised and the readouts corrected, the grid encoder error is calculated at each point evaluated. The calibration uncertainty of the grid encoder is then analysed. Finally, the results of the 2D laser system self-calibration and the error map of the grid encoder are illustrated in order to demonstrate the suitability of the self-calibration proposed methodology.

2. Description of the Methods and Materials Used for the Procedure

This work is based on a previous study [12] in which a 2D laser scheme was used as a reference system to characterise 2D grid encoder performance at different temperatures. The metrology frame used was manufactured in a very low thermal expansion glass ceramic material (Zerodur). The laser system was mathematically aligned by using the orthogonality of the grid encoder as the reference. Therefore, the squareness errors of the grid encoder were neglected. In contrast, the present study utilises a self-calibration of the 2D laser sensor system by using the grid encoder as an auxiliary element, and any squareness errors are explicitly considered in the algorithm. To verify this new procedure, a calibration is performed using an experimental setup where the laser system and the non-calibrated artefact are mounted on the same metrology frame as in [12]. The 2D laser system belongs to the Renishaw RLE10 laser interferometer family. It consists of a laser unit (RLU), two sensor heads (RLD), two plane mirrors (one per axis), and an environmental control unit (RCU). In addition, an external interpolator is used to reduce the expected resolution of the system from 10 nm to 1.58 nm. The non-calibrated artefact is a KGM 181 cross-grid encoder (Heidenhain GmbH) with a circular working range of 140 mm in diameter. The calibration is performed along an area equal to the working range of the NanoPla (50 mm × 50 mm).

Figure 1 represents a scheme of the work presented through the different sections of this article. The laser system is encompassed by two laser heads, which have been previously calibrated by the manufacturer. These laser heads are placed perpendicularly to each other in the setup that is described in the next part of this Section. To correct the geometrical errors of this 2D assembly (see Section 3), a self-calibration procedure was performed. A grid encoder is the non-calibrated artefact used, which has been calibrated by the manufacturer exclusively along its main axes. The laser system and the grid encoder take measurements simultaneously along a mesh of points in the considered working range, for different views of the grid encoder. The grid encoder readouts are mathematically aligned to the laser reference system, and then the self-calibration algorithm described in Section 4 is applied. Once the results are obtained (see Section 5), the geometric errors of the 2D laser system are compensated, and the corrected laser system readouts are used to calibrate the grid encoder along the whole working range. Additionally, the calibration uncertainty of the grid encoder is also calculated (see Section 6). Finally, the errors of the grid encoder along the main axes obtained after this calibration are compared to the ones provided by its calibration certificate.

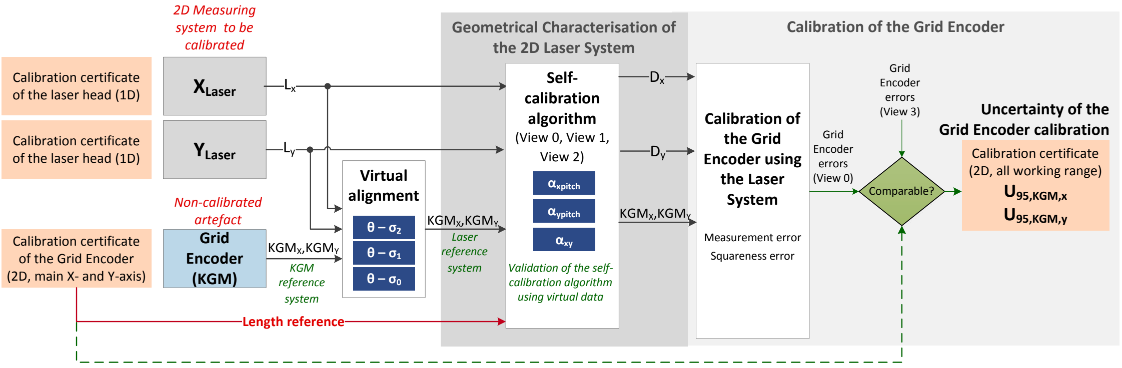

Figure 1. Scheme of the work presented in this article.

In Figure 1, L_x and L_y represent the laser readouts in X and Y axes, respectively. Similarly, KGM_x and KGM_y represent the KGM 181 cross-grid encoder readouts, and D_x and D_y are the real displacements. View 0, View 1 and View 2 are the different views used for the self-calibration and View 3 is an additional view measured only for the verification, and that was not used for the self-calibration procedure. $\theta - \sigma_j$ is the angular deviation between laser system and grid encoder in View j, for j = 0, 1,

2. Finally, α_{xpitch}, α_{ypitch} and α_{xy} are the geometric error of the 2D laser system. These parameters will be explained in detail in the following sections of this article.

In a calibration performed at a submicrometre resolution, the design of the experimental setup is crucial, because it can significantly affect the accuracy of the final result. Figure 2a is a block diagram of the connections between devices in the setup and Figure 2b represents a sketch of the setup used for the procedure. As it is shown in Figure 2a, the laser system and the grid encoder are connected to a host PC that records their readouts at each position. An auxiliary positioning machine is used to perform the X-Y displacements.

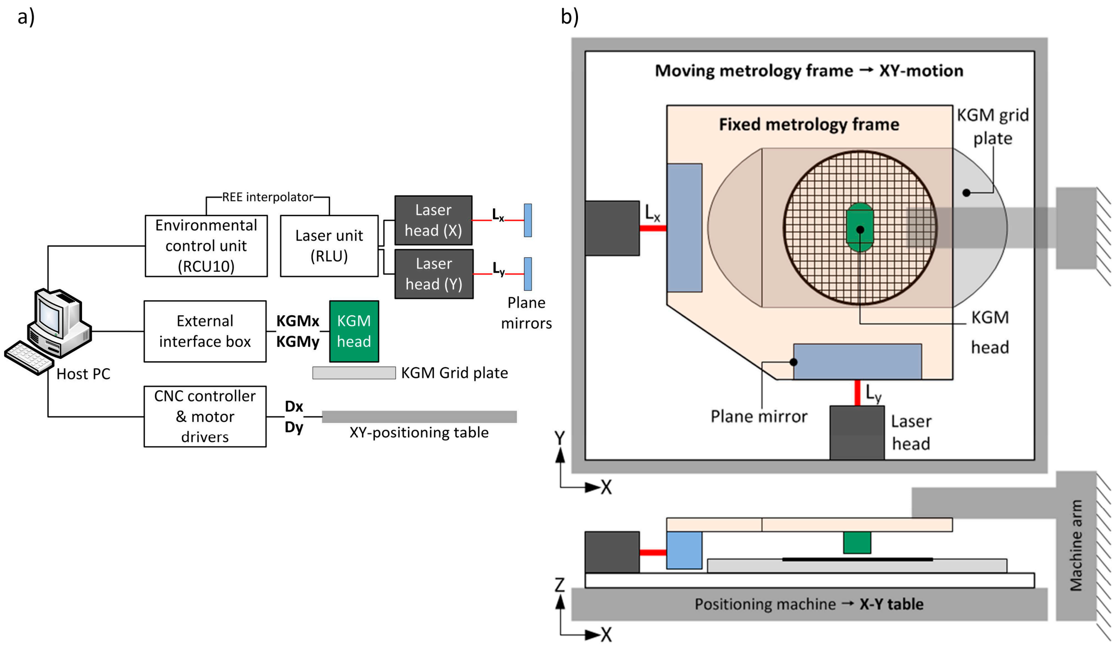

Figure 2. (**a**) Block diagram of the experimental setup connections; (**b**) Sketch of the experimental setup for the calibration procedure.

The metrology frame consists of two thermally stable parts with different relative motion. The plane mirrors and the grid encoder scanning head are installed in the upper metrology frame, which is attached to the arm of the positioning machine and remains static during the tests. The laser detector heads and the grid base of the 2D encoder are fixed to the lower metrology frame, which is placed on the X-Y table of the positioning machine. To minimise Abbe errors in the X and Y axes, the grid encoder scanning head and the X and Y laser sensors are aligned both in Z and, in advance, at the central position of the measuring range at the XY plane. Figure 3 shows photographs of the experimental setup.

Figure 3 (right) shows the following geometric relationships between the laser system, the grid encoder and the positioning machine for this arrangement: the angular deviation between the reference axes of the positioning machine and the laser system (θ), and the angular deviation between the reference system of the positioning machine and the encoder (σ). The angular deviation between the grid encoder and the laser system is the difference between θ and σ. The values of these angles depend on the assembly and are not expected to be higher than ± 0.01 rad.

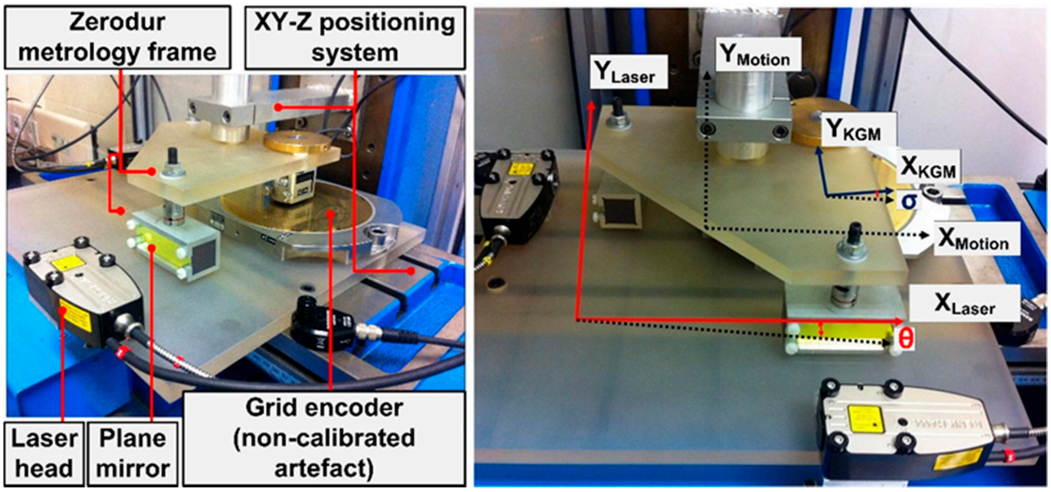

Figure 3. Experimental setup for the calibration procedure: main components (**left**); and defined geometric relationships between reference systems of the 2D sensors (**right**).

3. Mathematical Model of the 2D Laser System

This section analyses the mathematical model of the 2D laser system. The laser system essentially consists of two beams and two plane mirror interferometers (one per axis) that are theoretically orthogonal to each other and coplanar with the X-Y plane of movement. Based on this laser arrangement, two different geometric errors must be compensated. The first is a 1D error present in every plane mirror interferometer; it appears when the laser beam is not coplanar to the X-Y plane of motion. This study refers to this as pitch error (i.e., α_{xpitch}, α_{ypitch} shown in Figure 4). The second is a 2D error caused by the non-orthogonality of the X and Y plane mirror interferometers (α_{xy} in Figure 4). This study refers to this as squareness error, similar to [11]. As shown in Figure 4, the model assumes that the incident and reflected laser beams are coincident lines. In other words, each laser beam can be considered orthogonal to its respective plane mirror. This simplifies the problem by making it possible to describe it in a 2D level. This assumption is justified because the manufacturer defines a tight alignment tolerance between the laser beam and the normal vector of the plane mirror (±25 arc s). It applies to both pitch and yaw between laser beam and plane mirror. Considering 100 mm as the maximum possible distance between the mirror and the laser head in the setup, any deviations caused by the orthogonality error between the laser beam and plane are negligible (<<1 nm).

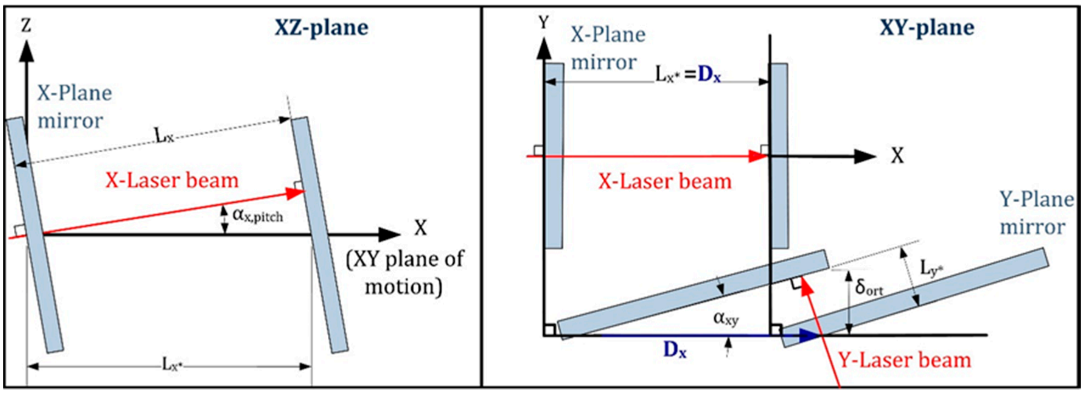

Figure 4. Geometric model of the 2D laser system.

In Figure 4, the angle α_{xpitch} represents the pitch error in the X-Z plane; similarly, there is a α_{ypitch} contained in the Y-Z plane. The angle α_{xy} represents the non-orthogonality between the X and Y plane mirrors, i.e., the squareness error. D_x and D_y are the actual displacements of the moving part, whereas L_x and L_y are the laser readouts of the X and Y axes, respectively. In Figure 4, there is a real displacement of the plane mirrors in the X direction ($D_x \neq 0$), but in the Y direction there is no movement ($D_y = 0$). However, after correcting the pitch error of the Y laser interferometer readout (L_{y*}), the squareness error (δ_{ort}) persists and requires correction. The geometric relations of the model are listed below, where the measurement errors in the X and Y axes are represented by δ_x and δ_y, respectively.

$$D_x = L_{x*} = \frac{L_x}{\cos(\alpha_{xpitch})} \tag{1}$$

$$D_y = \frac{L_{y*}}{\cos(\alpha_{xy})} + \delta_{ort} = \frac{L_y}{\cos(\alpha_{ypitch})\cos(\alpha_{xy})} + \delta_{ort} \tag{2}$$

$$\delta_{ort} = \frac{\tan(\alpha_{xy})L_x}{\cos(\alpha_{xpitch})\cos(\alpha_{ypitch})} \tag{3}$$

$$\delta_x = D_x - L_x = \left(\frac{1}{\cos(\alpha_{xpitch})} - 1\right)L_x \tag{4}$$

$$\delta_y = D_y - L_y = \left(\frac{1}{\cos(\alpha_{ypitch})\cos(\alpha_{xy})} - 1\right)L_y + \delta_{ort} \tag{5}$$

Therefore, the target values that should be obtained through the self-calibration are α_{xpitch}, α_{ypitch} and α_{xy}. Once these angles are known, it is possible to correct the laser system readouts.

4. Self-Calibration Procedure

Performing a calibration at a submicrometre scale presents difficulties. The most significant difficulty is determining a calibrated artefact at least one order of magnitude more accurate than the target accuracy of the laser system—ideally, the same size as the working range. The application of self-calibration techniques can solve this problem [9], thus making self-calibration a suitable procedure for optimising the performance of nanopositioning systems in a large working area [13,14]. A method based on reversal techniques is selected as the best option for this study, where the goal is to obtain submicrometre uncertainty along the working range.

A self-calibration procedure essentially consists of a non-calibrated artefact with measurement features whose geometrical relationships remain invariable. These features are measured by the system and calibrated by using different views. Because the non-calibrated artefact is assumed to be a rigid body, the pattern of the measurement features remains invariant over the different views [15]. The only calibrated pattern required is a 1D-length scale to correct the scale factor of the system to be calibrated [9]. To address this inconvenience, other authors have proposed a calibrated reference rod [16]. In the case of this study, the wavelength of the laser beam has already been calibrated by the manufacturer. Therefore, it is not necessary to correct the scale factor of the laser system. Nevertheless, a 1D scale reference is needed to measure the displacements of the grid encoder in the translation views, as it will be explained in the following subsection.

At any point, the observed error is, then, an addition of the system error and the non-calibrated artefact error. By combining the different equations for the three views, it is possible to isolate the laser system error. As a novelty, this paper selects a different approach based on the use of a measuring instrument as a non-calibrated artefact. In the following, the self-calibration algorithm is explained in detail, and its performance is verified using virtual data.

4.1. Definition of the Self-Calibration Algorithm

The case in this study is very specific, as the non-calibrated artefact is a grid encoder that uses a measuring grid and a scanning head instead of measuring features to provide X-Y coordinates.

The input data, then, become the readouts of the laser system and the grid encoder at the same positions. Nevertheless, these measurements are taken in different reference axes. Hence, these two axes must be virtually aligned to allow a comparison of both measurements. A measurement from point to point along each of the main axes of the grid encoder can be corrected by using the information from its calibration certificate. This measurement can be used during the calibration as an absolute length.

In a self-calibration procedure, the global error at each position is expressed as the addition of the positioning error of the calibrated system plus the intrinsic errors of the non-calibrated artefact plus the alignment errors of the non-calibrated artefact at each view. In this case, the alignment errors are not present because the grid encoder readouts are previously mathematically aligned to the laser system axes. For the initial view (View 0), the global error V_0 at each point is expressed as in Equation (6):

$$V_0(x_i,\ y_j) = M_0(x_i,\ y_j) + E_0(x_i,\ y_j) \tag{6}$$

where M_0 is the laser system positioning error at the point $(x_i,\ y_j)$ at its own reference axes, and E_0 is the grid encoder positioning error at the point $(x_i,\ y_j)$ rotated to the laser system reference axes ($\theta - \sigma$, in Figure 3) and displaced to the laser system origin. The grid has $N \times N$ points, thus $i, j = 1, 2, \ldots, N$.

As it can be observed in Equation (6), once the laser system positioning errors, M_0, are calculated by the self-calibration procedure, the grid encoder positioning errors, E_0, can also be deduced (Section 6).

According to the mathematical model presented in Section 3, three factors must be calculated by the self-calibration algorithm. At least three different views of the artefact are required to cancel the systematic errors of the non-calibrated artefact. In this particular case, a system of three equations is obtained by combining the expressions of the initial view and two additional translation views. Therefore, three different positions of the grid encoder are sufficient to perform this calibration (see Figure 5): the initial view (View 0), the X axis translation view (View 1) and the Y axis translation view (View 2). View 1 is obtained by moving the grid encoder approximately 5 mm (Δ_x) along its X axis, and View 2 is achieved by moving the grid encoder approximately 5 mm (Δ_y) along its Y axis (see Figure 5). The real value of these displacements (Δ_x and Δ_y) needs to be known, for this purpose, the calibrated main axes of the grid encoder are used. Given this particular setup, the relative position between the laser system and the positioning machine remains invariant for all the views as does the angular deviation θ between the positioning machine and the laser system. The relative position between the grid encoder and the positioning machine changes when the encoder is moved. Hence, the angular deviation σ between the positioning machine and the grid encoder may be slightly different for View 0, View 1 and View 2. As previously noted, the non-calibrated artefact provides coordinates for each measuring point. The displacement to reach the positions of each measuring point is given by the positioning machine that has been programmed to measure a mesh of points covering the entire working range. Due to the errors of the positioning machine and the variation of the σ angle from View 0 to View 1 and View 2, the points measured in each view may not be exactly the same. However, it has been observed that the maximum deviation between the points in different views is 0.05 mm. According to the calibration certificate of the grid encoder, nearby points have similar error values (with differences in the range of a few nanometres). Thus, it is possible to assume that the artefact errors can be compensated by relating the views.

A mesh of 11 × 11 points separated 5 mm from each other is measured for each view covering the working range. By combining Equations (4)–(6), the Expressions (7)–(10) are obtained, where V_{0x} and V_{0y} are the global errors for View 0 in X and Y axes, respectively. Similarly, V_{1x}, V_{1y} and V_{2x}, V_{2y} are the global errors in X and Y axes, for View 1 and View 2, respectively. In every case, the global errors of each view (V_0, V_1, V_2) are experimentally obtained. δ_x and δ_y are the laser system errors in X and Y axes. Likewise, E_x and E_y are the non-calibrated artefact errors in X and Y axes.

$$V_{0x}(x_i,\ y_j) = \delta_x(x_i) + E_x(x_i,\ y_j) \tag{7}$$

$$V_{0y}(x_i,\ y_j) = \delta_y(x_i,\ y_j) + E_y(x_i,\ y_j) \tag{8}$$

$$V_{1x}(x_i{+}\Delta_x,\ y_j) = \delta_x(x_i{+}\Delta_x) + E_x(x_i,\ y_j) \tag{9}$$

$$V_{1y}\ (x_i{+}\Delta_x, y_j) = \delta_y(x_i{+}\Delta_x, y_j) + E_y(x_i,\ y_j) \tag{10}$$

$$V_{2x}(x_i,\ y_j{+}\Delta_y) = \delta_x(x_i) + E_x(x_i,\ y_j) \tag{11}$$

$$V_{2y}(x_i, y_j{+}\Delta_y) = \delta_y(x_i, y_j{+}\Delta_y) + E_y(x_i,\ y_j) \tag{12}$$

View 0 and View 1 provide two linearly independent equations each, and View 2 just one because Equations (7) and (11) are linearly dependent, that is 5 linearly independent equations in total: (7)–(10) and (12). There are 5 unknown variables: the geometric errors α_{xpitch}, α_{ypitch} and α_{xy} and the systematic encoder errors E_x and E_y. Therefore, three views are enough to perform the calibration. It is worth noting that the squareness error of the laser system α_{xy} is decoupled from the squareness errors of the grid encoder that is considered in its systematic error $E(x,\ y)$.

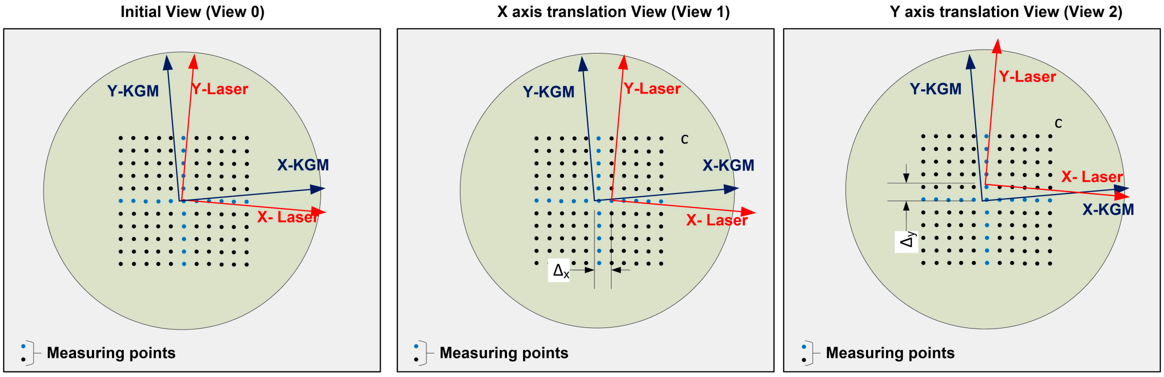

Figure 5. Schematic of the initial and translation views, including the reference systems and their geometric relationships and the mesh of the measuring points.

The global error at the initial view, consisting of the positioning error of the laser system and the grid encoder at a particular point, is compared to the global error at the translation view, consisting of the positioning error of the encoder at the same point and the positioning error of the laser system at a point displaced a distance equal to Δ. Therefore, the positioning errors of the grid encoder are cancelled, but not the ones of the laser system. The positioning errors of the laser system, δ_x and δ_y, are replaced by Equations (1)–(3). Finally, considering the following property, Equations (13)–(15):

$$L_x(x_i{+}\Delta_X) - L_x(x_i) = L_x(\Delta_x) \tag{13}$$

$$L_y(x_i{+}\Delta_x,\ y_j) - L_y\ (x_i,\ y_j) = L_y(\Delta_x,\ 0) \tag{14}$$

$$L_y(x_i,\ y_j{+}\Delta_y) - L_y\ (x_i,\ y_j) = L_y(0,\ \Delta_y) \tag{15}$$

The following equation system of three unknown variables (α_{xpitch}, α_{ypitch} and α_{xy}) and three equations is obtained:

$$V_{1x}(x_i^1{+}\Delta_x, y_j^1) - V_{0x}(x_i^0, y_j^0) = \left(\frac{1}{\cos\left(\alpha_{xpitch}\ \right)} - 1\right) L_x(\Delta_x,\ 0) \tag{16}$$

$$V_{1y}(x_i^1{+}\Delta_x, y_j^1) - V_{0y}(x_i^0, y_j^0) = \frac{\tan(\alpha_{xy})}{\cos\left(\alpha_{xpitch}\ \right)\cos(\alpha_{ypitch})} L_x(\Delta_x,\ 0) \tag{17}$$

$$V_{2y}(x_i^2, y_j^2+\Delta_y) - V_{0y}(x_i^0, y_j^0) = \left(\frac{1}{\cos(\alpha_{ypitch})\cos(\alpha_{xy})} - 1\right) L_y(0,\ \Delta_y) \quad (18)$$

where (x_i^0, y_j^0), $(x_i^1+\Delta_x, y_j^1)$ and $(x_i^2, y_j^2+\Delta_y)$ for i, j = 1, . . . , 11 are the coordinates of the points measured along the working range in View 0, View 1 and View 2, respectively, while $L_x(x_i,\ y_j)$ and $L_y(x_i,\ y_j)$ are the laser readouts in X and Y axes at those points.

4.2. Validation of the Self-Calibration Algorithm

The proposed method should work within all the expected ranges for the angles. Therefore, the values should be calculated with the required precision in order to obtain the actual displacements (D_x and D_y) with submicrometre uncertainty (see Table 1). As it was previously explained, before starting the self-calibration, the algorithm mathematically aligns the grid encoder readouts to the laser system reference axes. As long as the squareness error of the laser system is sufficiently small, this mathematical alignment does not have a significant effect on the estimation of the geometrical errors of the laser system. By mathematical simulations, the acceptable range has been defined to be $\pm 1 \times 10^{-2}$ rad. In order to achieve submicrometre uncertainty in the 2D positioning, α_{xy} should be determined with an error of $\pm 1 \times 10^{-6}$ rad. However, for the setup used for the experiment, the orthogonal error of the laser system, α_{xy} was measured and corrected using a CMM. The maximum accuracy achieved during the setup depends directly on this CMM and it was $\pm 5 \times 10^{-3}$ rad. Therefore, the proposed self-calibration procedure is needed to determine the value of α_{xy} with an uncertainty of $\pm 1 \times 10^{-6}$ rad. With regards to pitch errors, the proposed self-calibration procedure is able to calculate and correct them, even if the range of α_{xpitch} and α_{ypitch} is unbounded, independently of their value. To obtain the desired uncertainty, they should be determined with an error of $\pm 1 \times 10^{-3}$ rad.

Table 1. Factors of the considered 2D geometric model calculated by the self-calibration algorithm.

Parameter	Required Uncertainty	Description
α_{xy}	$\pm 1 \times 10^{-6}$ rad	Squareness error
α_{xpitch}	$\pm 1 \times 10^{-3}$ rad	Pitch error in X-axis
α_{ypitch}	$\pm 1 \times 10^{-3}$ rad	Pitch error in Y-axis
$\theta - \sigma$	$\pm 1 \times 10^{-4}$ rad	Angular deviation between the reference systems of the grid encoder and the laser system

Before beginning the experiment and measuring actual data, the proposed algorithm is validated using virtual data. To create the virtual data, the readouts of the grid encoder and the laser system at the same positions are simulated along the working range of 50 mm × 50 mm. The actual positions (D_x and D_y) are initially defined in a mesh of 11 × 11 points. The positioning machine movement is simulated with steps of 5 mm from −25 mm to +25 mm along the X and Y axes, covering the entire working range. The grid encoder readouts include linear errors of $[5 \times 10^{-5}]\cdot D_x$ and $[5 \times 10^{-5}]\cdot D_y$ in the X and Y components, respectively. The laser system readouts (L_x and L_y) are obtained according to the geometric relations of Figure 4 by selecting values inside the expected range for α_{xpitch}, α_{ypitch} and α_{xy}. Readouts for the three views (View 0, View 1 and View 2) are simulated, taking into account that the angle between the reference system of the laser system and the reference system of the grid encoder $(\theta - \sigma)$, which is different for each view because, as previously noted, σ is not constant. In a previous work [4], the random error of the laser system was calculated by considering the laser resolution, the wavelength instability, beam mixing, and environmental influences. The combination of these errors resulted in 7 nm. In this virtual validation of the algorithm, the laser system readouts, as well as the grid encoder readouts, include a random uniform error of 20 nm. The method used to validate the self-calibration algorithm proceeds as follows: firstly, the laser system readouts are corrected using the values obtained for α_{xpitch}, α_{ypitch} and α_{xy}; secondly, the grid encoder error is isolated and compared to the one set at the beginning; and finally, if both errors are equal the self-calibration algorithm is validated. This simulation verifies that the error of the grid encoder is linear along the X and Y axes as initially set. In addition, by defining different values for the random error, this simulation also provides a clear insight of the good theoretical repeatability of the system, in the range of ±25 nm. Therefore, the algorithm is considered to be valid.

By performing different simulations and including random errors of the expected order in the readouts of the laser system and the grid encoder, it is possible to estimate the expanded uncertainty (k = 2) of the resulting values given by the algorithm. It is observed that the accuracy depends on the value of α_{xy}; when its value is inside the expected acceptable range, the goal of submicrometre uncertainty is achieved (see Table 1).

5. Geometrical Characterisation of the Laser System Setup

Self-calibration can be performed once the setup used for the calibration is defined and the self-calibration algorithm has been explained and verified. Before starting the experiments, the stability of the laser system was studied by performing static repeatability tests inside the working range. A total of 9000 readouts were recorded at each point during 60 s. The resulting stability (2σ) was 24 nm, which was considered acceptable. During the calibration procedure, in order to minimise random errors of both, the laser system and the grid encoder, 100 readouts were recorded and averaged at each measured point.

To perform the self-calibration, it is necessary to know the real displacement of the grid encoder in the translation views (View 1 and View 2). The grid encoder has been calibrated by the manufacturer along its central X and Y axes. Therefore, this calibration is used as an absolute length reference to measure these translations in X and Y axes. The readouts of the laser system and the grid encoder are subsequently taken at the same time and the same positions in the defined mesh of 11 × 11 points. Once all the points are measured, the data obtained are the coordinates of 121 points in two different reference systems (the laser system and the grid encoder) and three different views (View 0, View 1 and View 2). Initially, the self-calibration algorithm mathematically aligns both reference systems; by applying Equations (16)–(18), the algorithm cancels the grid encoder systematic error and obtains the correction factors (α_{xpitch}, α_{ypitch} and α_{xy}) as well as the angle between the reference system of the laser system and the grid encoder ($\theta - \sigma$) for each View. The obtained results can be seen in Table 2. They are given with the required uncertainty specified in Section 2 and α_{xy} is inside the expected range of $\pm 5 \times 10^{-3}$ rad. To obtain the actual displacements (D_x and D_y), it is necessary to correct the laser system readouts (L_x and L_y) by applying the correction factors (α_{xpitch}, α_{ypitch} and α_{xy}) into Equations (1) and (2).

Table 2. Geometric parameter results of the experimental self-calibration procedure and virtual alignment.

Parameter	Required Uncertainty	Resulting Value	Description
α_{xy}	$\pm 1 \times 10^{-6}$ rad	4.010×10^{-3} rad	Squareness error
α_{xpitch}	$\pm 1 \times 10^{-3}$ rad	9×10^{-3} rad	Pitch error in X-axis
α_{ypitch}	$\pm 1 \times 10^{-3}$ rad	10×10^{-3} rad	Pitch error in Y-axis
$\theta - \sigma_0$ $\theta - \sigma_1$ $\theta - \sigma_2$	$\pm 1 \times 10^{-4}$ rad $\pm 1 \times 10^{-4}$ rad $\pm 1 \times 10^{-4}$ rad	-4.9×10^{-3} rad -4.6×10^{-3} rad -4.6×10^{-3} rad	Angular deviation between the reference systems of the grid encoder and the laser system

6. Calibration of the Grid Encoder

As previously explained, the grid encoder calibration certificate compares the central axes with the measurement of a calibrated laser interferometer. These calibrated axes have been used as a length reference to calculate the real displacements of the grid encoder in X and Y axes, for View 1 and View 2, before starting the self-calibration procedure. However, the grid encoder is used in many applications that require a high accuracy not only in the central axes but throughout the entire grid.

Some approaches for grid calibrations can be found in the literature, as the one presented in [17]. This work proposes an alternative solution to this issue; once the readouts of the laser system are corrected, it is possible to compare them with the grid encoder readouts in order to calculate the error of the grid encoder at each measured point. Thereby, the systematic error of the non-calibrated points that were not part of the main axes will be known. Additionally, this procedure validates the effectiveness of the self-calibration by comparing the error obtained for the central X and Y axes with the error provided in the calibration certificate by the manufacturer.

It is important to note that, even if the systematic errors of the grid encoder were present in Equations (7) to (12), they were cancelled by reversal techniques. Thus, they were not present in Equations (16) to (18), which were applied in the self-calibration algorithm. Once the laser system readouts are corrected, it is possible to use them to calculate the error of the grid encoder readouts.

The following sections initially explain how the grid encoder is calibrated and confirm the effectiveness of the self-calibration of the laser system. The error map of the grid encoder is then presented, and the uncertainty of its calibration calculated.

6.1. Calibration Procedure of the Grid Encoder Using the Laser System

Initially, the proposed procedure mathematically aligns the corrected laser readouts with the reference system of the grid encoder; the grid encoder error is then calculated as the difference between the two measurements. The rotation angle to align both reference systems is $\theta - \sigma$ (see Figure 3), as calculated in the previous section by means of an optimisation process. The grid encoder measurements may be affected by the grid squareness errors in addition to linear errors; therefore, the rotation angle is calculated by matching the X axis of the encoder to the X axis of the laser system, taking the orthogonality error of the grid encoder to its Y axis. For this reason, the Y component of the grid encoder errors is higher than the X component. This situation is illustrated in Figure 6. The mesh of points measured by the laser system after correction (Figure 6a) exhibits neither squareness nor linear errors, but the mesh of points measured by the grid encoder exhibits both (Figure 6b). Once the two meshes are aligned, and because the laser system measurements have already been corrected through self-calibration, the difference between the coordinates of the same point measured by the grid encoder and the laser system is the grid encoder error (see Figure 6c). By comparing these two meshes, it is also possible to determine the squareness error of the grid encoder.

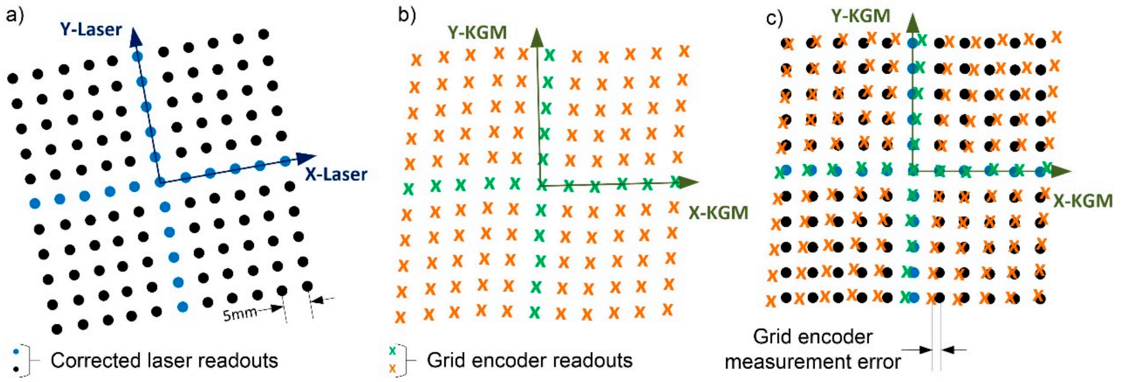

Figure 6. (**a**) Mesh of points measured by the laser system after correction; (**b**) Mesh of points measured by the grid encoder; (**c**) Their alignment and comparison.

The error of the grid encoder can be calculated by using the readouts of the initial view (View 0) or the translation views (View 1 and View 2). The results should be very similar in all the cases. However, it is expected that they are not coincident since the random errors of the laser system and the random error of the grid encoder are still present. In addition, as previously stated, the measuring points are slightly different in each view. The error maps of the grid encoder calculated for View 0 and View 1 and the difference between the two error maps are represented in Figure 7. It can be observed that both maps have similar error trends and orders of magnitude (the three maps use the same scale factor, equal to 1000), and in both cases, the error is smaller near the central axes. These presented results are similar to the error map calculated for View 2.

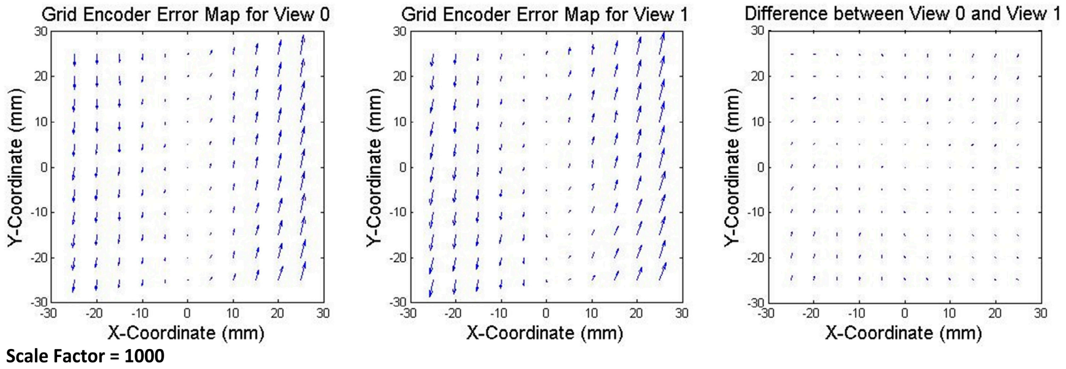

Figure 7. Error map of the grid encoder in View 0 (**left**); View 1 (**center**); and their comparison representing the difference (**right**). Scale factor equal to 1000.

To validate the calibration procedure, the errors of the grid encoder are also calculated in an additional view, named View 3, which was not used during the self-calibration procedure. View 3 is only used for this verification. The grid encoder errors should be similar to the ones calculated for the previous views because the grid encoder errors are independent of the views. In View 3, the grid encoder was rotated 180 degrees around its Z axis, and similarly to the other views, the measurements were taken simultaneously by the grid encoder and the laser system along the same mesh of 11 × 11 points separated 5 mm from each other. Because the setup of the laser system remains invariant, the readouts can be corrected using the parameters calculated in the self-calibration. In Figure 8, the error maps of the grid encoder in View 0 and View 3 are represented and compared (the three maps use the same scale factor, equal to 1000). It can be observed, as in the previous case, that both error maps have similar trends and orders of magnitude and the difference is due to the random errors of the laser system and the grid encoder and to the fact that the measured points are not the same in both views.

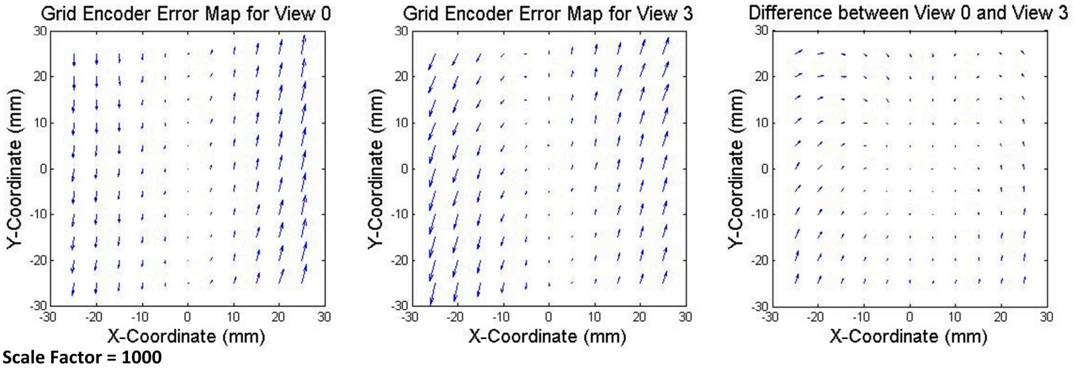

Figure 8. Error map of the grid encoder in View 0 (**left**); View 3 (**center**); and their comparison representing the difference (**right**). Scale factor equal to 1000.

The squareness error of the grid encoder calculated for View 0 is almost coincident with that calculated for View 1, View 2 and View 3: 1.36×10^{-4} rad. The resulting squareness error is very small and can be considered negligible in this working range with a submicrometre uncertainty.

The calibration certificate information includes the error along the two main axes in a range of 140 mm. The middle point, where the error is equal to zero, is coincident with the zero position in the experimental self-calibration, where the error is also equal to zero. The X component of the grid encoder error along the central X axis and the Y component of the error along the Y axis for View 0 and View 1 are represented in Figure 9. They can be easily compared to each other and to the error given by the calibration certificate of the grid encoder, also represented in Figure 9. The error provided by the calibration certificate is represented only for the working range of the laser system (±25 mm). It can be seen that the errors calculated experimentally for View 0 and View 1 and the errors provided by the calibration certificate are highly comparable, with the same linear trend and order of magnitude. Therefore, the self-calibration procedure for the grid encoder calibration can be considered validated.

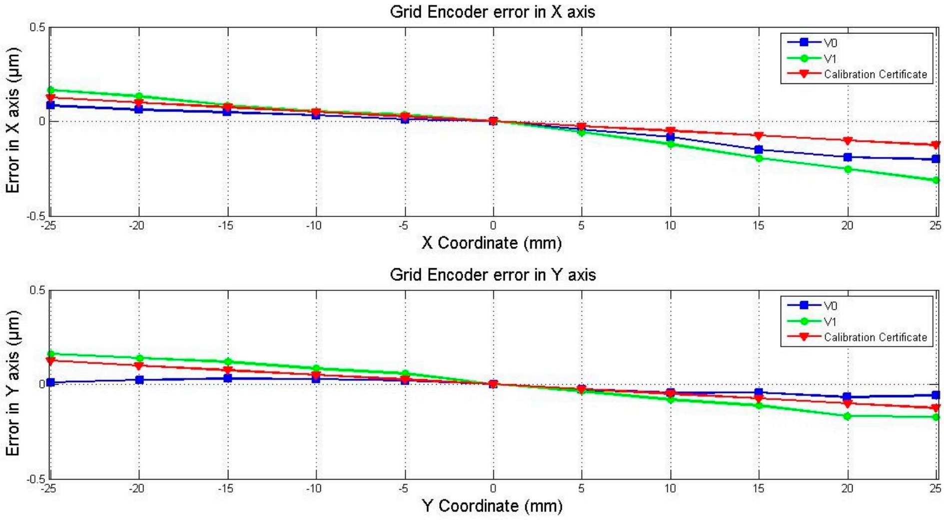

Figure 9. Error of the grid encoder along the main X and Y axes in the analysed range.

6.2. Calibration Uncertainty of the Grid Encoder

The error of the grid encoder at each point is calculated as the average between the resulting errors of View 0, View 1 and View 2. The expanded uncertainty of the calibration system (U_{95}) is evaluated according to [18]. All the error sources and their contributions to the uncertainty of the system are examined, and the uncertainty is calculated with a coverage factor of k = 2, thus providing a level of confidence of approximately 95%, as shown in Equation (19).

$$U_{KGM}(k=2) = k\sqrt{u_{laser}^2 + u_T^2 + \frac{S_{Cal.KGM}^2}{n_{Cal.KGM}} + u_{KGMResolution}^2 + u_{ResidualError}^2} \quad (19)$$

The standard uncertainty is calculated as the square root of the quadratic sum of the contributions of the uncertainty sources. These sources are listed below:

- The uncertainty of the calibration system, i.e., the laser sensors, represented as u_{laser}.
- The uncertainty of the expansion and contraction of the grid encoder due to small changes in the temperature u_T.
- The repeatability of the grid encoder measurements during the calibration $S_{Cal.KGM}$. The term $n_{Cal.KGM}$ represents the number of repetitions of each measurement.
- The uncertainty of the grid encoder resolution $u_{KGMResolution}$.
- The error that could not be corrected by the calibration is $u_{ResidualError}$ and is dependent on the distance of the calibrated point to the main central axes.

The uncertainty of the laser system is calculated according to Equation (20); its contributors are listed below:

$$U^2{}_{\text{Laser}} = u^2_{\text{estimatedLaser}} + \frac{S^2_{\text{Laser}}}{n_{\text{Laser}}} + u^2_{\text{mirrors}} + u^2_{\text{LaserResolution}} + u^2_{\text{SelfCalibration}} \quad (20)$$

- The standard uncertainty of the laser according to its manufacturer, denoted as the estimated uncertainty $u_{\text{estimatedLaser}}$.
- The repeatability of the laser measurements S_{Laser}. The term n_{Laser} represents the number of repetitions of each measurement.
- The uncertainty of the flatness of the mirrors u_{mirrors}.
- The uncertainty of the resolution of the laser $u_{\text{LaserResolution}}$.
- The uncertainty of the self-calibration procedure of the laser system $u_{\text{SelfCalibration}}$.

The estimated uncertainty of the laser system, as well as the uncertainty of the flatness of the mirrors and the laser resolution, were previously calculated in [12] for the same laser system. Therefore, the same values can be applied to this calculation. The repeatability of the laser system depends on the measurements taken during the calibration procedure of the grid encoder and is thus particular to this study. The uncertainty of the self-calibration procedure depends on the uncertainty of the calculation of the correction factors. As previously mentioned, a submicrometre uncertainty is achieved after the calibration; the uncertainty of the laser system measurements after applying the self-calibration is ±25 nm.

Once the uncertainty of the laser system is calculated, it is possible to proceed with the calculation of the expanded calibration uncertainty of the grid encoder. The calculation of the laser system uncertainty is represented in Table 3, and the contributions of the uncertainty sources of the grid encoder calibration and the resulting value are represented in Table 4.

Table 3. Calculation of the standard uncertainty of the laser system.

Uncertainty Source	Justification	X-Axis Contribution [nm]	Y-Axis Contribution [nm]
Estimated uncertainty of the laser system	According to the manufacturer, for a distance of 60 mm	76	76
Laser repeatability	Calculated for the readouts of this experiment	6	3
Planarity of the mirrors	According to the manufacturer	63	63
Laser resolution	Resolution of 1.58 nm, achieved by external interpolators	$1.58/\sqrt{12}$	$1.58/\sqrt{12}$
Self-calibration procedure	Self-calibration algorithm maximum error = ±25 nm, according to the virtual validation	$25/\sqrt{3}$	$25/\sqrt{3}$
Standard uncertainty of the laser system		**99**	**99**

As shown in Table 3, the expanded uncertainty (k = 2) is $U_{95,x}[\text{nm}] = 226 + 4\,x\,[\text{mm}]$ and $U_{95,y}[\text{nm}] = 410 + 15\,y\,[\text{mm}]$ for errors in the X and Y axes, respectively, in a working range of ±25 mm. The variables x and y represent the distance of the calibrated point to the X or Y main axes, respectively, and must be introduced in millimetres. The calibration certificate specifies that the position error along the entire range of the grid encoder (a circular area 140 mm in diameter) is ±2 µm, so it can be assumed that the position error inside the area of study (±25 mm) is approximately 0.8 µm. It is thus confirmed that the calibration procedure of the grid encoder performed in this study reduced the uncertainty of the grid encoder measurement. This reduction was achieved because the calibration was performed at every point of the mesh and the uncertainty sources were examined in detail.

Table 4. Calculation of the expanded calibration uncertainty (U95) of the grid encoder.

Uncertainty Source	Justification	X-Axis Contribution [nm]	Y-Axis Contribution [nm]
Laser system	Calculated in Table 3	99	99
Thermic variation	Thermal variation of ±0.40 °C during the experiment	48	48
Grid encoder repeatability	Calculated for the readouts of this experiment	5	3
Grid encoder resolution	Resolution of 1 nm	$1/\sqrt{12}$	$1/\sqrt{12}$
Residual error [nm]	Calculated by comparing the grid encoder error obtained in View 0, 1 and 2	24.5 + 2 x[mm] * * It is dependent on the position in X-axis expressed in mm	173 + 7.5 y[mm] ** ** It is dependent on the position in Y-axis expressed in mm
U95 of the grid encoder [nm]		226 + 4 x[mm]	410 + 15 y[mm]

7. Discussion and Conclusions

This study defined a self-calibration method and applied to the geometrical characterisation of a two-dimensional laser sensor system. Self-calibration eliminates the difficulty of finding a calibrated artefact with better accuracy than the system to be calibrated because the calibration is performed using a non-calibrated artefact. In this study, the non-calibrated artefact was a grid encoder. Thus, once the laser system was geometrically characterised, it was also possible to use it to calibrate the grid encoder.

The setup and the mathematical model of the 2D laser system were analysed in order to establish the geometrical errors that needed to be calculated through the self-calibration. The self-calibration algorithm and the setup were described in detail. After applying the calibration algorithm and correcting the readouts of the laser system, it was possible to determine the measurement error of the grid encoder at each measured point of the calibrated range by comparing the corrected laser readouts and the grid encoder readouts, obtained from the previous application of the self-calibration procedure. The calibration uncertainty of the grid encoder calibration was calculated, thus obtaining a result of $U_{95,x}[\text{nm}] = 226 + 4\,x\,[\text{mm}]$ and $U_{95,y}[\text{nm}] = 410 + 15\,y[\text{mm}]$ for errors in the X and Y axes, respectively. The suitability of the self-calibration procedure was verified in different ways in this work. First, the proper performance of the procedure was checked by using virtual data. Second, the experiment was carried out, and actual data were measured. The measurements were taken in three different views. Thus, once the laser system readouts were corrected, the grid encoder error map was calculated by using the readouts of the three views, verifying that the grid encoder errors remain invariant independently of the view. The error map of the grid encoder of one of the views used for the self-calibration procedure was compared to the error map calculated for an additional view that was not part of the self-calibration procedure, in order to validate the experimental procedure. Though the maps were not the same, they exhibited the same trend and order of magnitude. Their small differences could be due to random errors of the laser system and the grid encoder. Finally, in order to confirm the proper function of the self-calibration procedure with a different approach, the error calculated along the central axes was compared to the calibration certificate error; as expected, both were linear errors with the same trend and order of magnitude. Therefore, the self-calibration procedure described in this paper could be considered as valid and presents many advantages over direct calibration.

Acknowledgments: This work was supported by Spanish government projects DPI2010-21629-C02-01 "NanoPla" and DPI2015-69403-C3-1-R "MetroSurf", the UZCUD2016-TEC-09 project and DGA-FSE. We wish to thank the

FPU Program of the Ministry of Education, Culture and Sports of the Spanish Government, which sponsored the second author. We also offer special thanks to the "Consejo Nacional de Ciencia y Tecnología (CONACYT)" from the government of Mexico, which sponsored the third author.

Author Contributions: M.V., J.A.A. and J.A.Y.-F. conceived and designed the experiments; M.V. performed the experiments; M.T., J.A.A., J.A.Y.-F. and L.C.D.-P. conceived and developed the self-calibration technique; M.T. and L.C.D.-P. applied the technique and calculated the results; L.C.D.-P. wrote the manuscript. All authors contributed to the editing of the manuscript.

Conflicts of Interest: The authors declare no conflict of interest. The founding sponsors had no role in the design of the study; in the collection, analyses, or interpretation of data; in the writing of the manuscript, and in the decision to publish the results.

References

1. Kramar, J.A.; Dixson, R.; Orji, N.G. Scanning probe microscope dimensional metrology at NIST. *Meas. Sci. Technol.* **2011**, *22*, 24001–24011. [CrossRef]
2. Manske, E.; Jäger, G.; Hausotte, T.; Füßl, R. Recent developments and challenges of nanopositioning and nanomeasuring technology. *Meas. Sci. Technol.* **2012**, *23*, 74001–74010. [CrossRef]
3. Sato, K. Trend of precision positioning technology. *ABCM Symp. Ser. Mechatron.* **2006**, *2*, 739–750.
4. Torralba, M.; Yagüe-Fabra, J.A.; Albajez, J.A.; Aguilar, J.J. Design Optimization for the Measurement Accuracy Improvement of a Large Range Nanopositioning Stage. *Sensors* **2016**, *16*, 84. [CrossRef] [PubMed]
5. Torralba, M.; Valenzuela, M.; Yagüe-Fabra, J.A.; Albajez, J.A.; Aguilar, J.J. Large range nanopositioning stage design: A three-layer and two-stage platform. *Measurement* **2016**, *89*, 55–71. [CrossRef]
6. Fleming, A.J. A review of nanometer resolution position sensors: Operation and performance. *Sens. Actuators A Phys.* **2013**, *190*, 106–126. [CrossRef]
7. *BS ISO 5725-1. Accuracy (Trueness and Precision) of Measurement Methods and Results—Part 1: General Principles and Definitions*; International Organization for Standardization: Geneva, Switzerland, 1994.
8. Claverley, J.D.; Leach, R.K. A review of the existing performance verification infrastructure for micro-CMMs. *Precis. Eng.* **2015**, *39*, 1–15. [CrossRef]
9. Evans, C.J.; Hocken, R.J.; Estler, W.T. Self-Calibration: Reversal, Redundancy, Error Separation, and 'Absolute Testing'. *CIRP Ann. Manuf. Technol.* **1996**, *35*, 617–634. [CrossRef]
10. Jeong, Y.H.; Dong, J.; Ferreira, P.M. Self-calibration of dual- actuated single-axis nanopositioners. *Meas. Sci. Technol.* **2008**, *19*, 045203. [CrossRef]
11. Kim, D.; Kim, K.; Park, S.H.; Jang, S. Calibration of the straightness and orthogonality error of a laser feedback high-precision stage using self-calibration methods. *Meas. Sci. Technol.* **2014**, *25*, 125007. [CrossRef]
12. Yagüe-Fabra, J.A.; Valenzuela, M.; Albajez, J.A.; Aguilar, J.J. A thermally-stable setup and calibration technique for 2D sensors. *CIRP Ann. Manuf. Technol.* **2011**, *60*, 547–550. [CrossRef]
13. Zhu, Y.; Hu, C.; Hu, J.; Yang, K. Accuracy-and Simplicity-Oriented Self-Calibration Approach for Two-Dimensional Precision Stages. *IEEE Trans. Ind. Electron.* **2013**, *60*, 2264–2272. [CrossRef]
14. Wang, D.; Chen, X.; Xu, Y.; Guo, T.; Kong, M.; Zhao, J.; Zhu, B. Stage error calibration for coordinates measuring machines based on self-calibration algorithm. *Precis. Eng.* **2015**, *41*, 86–95. [CrossRef]
15. Ye, J.; Takac, M.; Berglund, C.N.; Owen, G.; Pease, R.F. Exact algorithm self-calibration of two-dimensional precision metrology stages. *Comput. Stand. Interfaces* **1999**, *21*, 187. [CrossRef]
16. Ekberg, P.; Stiblert, L.; Mattsson, L. A new general approach for solving the self-calibration problem on large area 2D ultra- precision coordinate measurement machines. *Meas. Sci. Technol.* **2014**, *25*, 055002. [CrossRef]
17. Haitjema, H. Iterative Solution of Lease-Squares Problems Applied to Flatness and Grid Measurements. Series on advances in mathematics for applied sciences. *World Sci. Publ.* **1996**, *40*, 161–171.
18. *ISO/TR 230-9. Test Code for Machine Tools. Estimation of Measurement Uncertainty for Machine Tools Test according to Series ISO 230, Basic Equations*; International Organization for Standardization: Geneva, Switzerland, 2005.

2.6. Procedia Manufacturing 2019

Available online at www.sciencedirect.com

ScienceDirect

Procedia Manufacturing 00 (2020) 000–000

Procedia
MANUFACTURING

www.elsevier.com/locate/procedia

8th Manufacturing Engineering Society International Conference

Positioning uncertainty of the control system for the planar motion of a nanopositioning platform

Lucía Díaz-Pérez *[,a] , Marta Torralba [b], José Antonio Albajez [a], José A. Yagüe-Fabra [a]

[a]*I3A – Universidad de Zaragoza, C/ María de Luna, 3, 50018, Zaragoza, Spain.*
[b]*Centro Universitario de la Defensa Zaragoza, Ctra. Huesca s/n, 50090 Zaragoza, Spain.*

Abstract

The novel nanopositioning platform (NanoPla) that is in development at the University of Zaragoza has been designed to achieve nanometre resolution in a large working range of 50 mm × 50 mm. The 2D movement is performed by four custom-made Halbach linear motors and a 2D laser system provides positioning feedback, while the moving part of the platform is levitating and unguided. As control hardware, this work proposes the use of a commercial solution, in contrast to other systems, where the control hardware and software were specifically designed for the purpose. In a previous work of this research, the control system of one linear motor implemented in the selected commercial hardware was presented. In this study, the developed control system is extended to the four motors of the nanopositioning platform to generate a 2D planar movement in the whole working range of the nanopositioning platform. In addition, the positioning uncertainty of the control system is assessed. The obtained results satisfy the working requirements of the NanoPla, achieving a positioning uncertainty of ±0.5 µm along the whole working range.

Peer-review under responsibility of the scientific committee of the 8th Manufacturing Engineering Society International Conference

Keywords: 2D positioning control; nanopositioning; Halbach linear motors; positioning uncertainty.

1. Introduction

In recent years, nanotechnology and nanoscience have increased their applications, demanding high accuracy positioning systems capable of working in large ranges at a nanometre scale. These positioning stages can be used for

---

* Corresponding author. Tel.: +34 976762561
E-mail address: lcdiaz@unizar.es

Peer-review under responsibility of the scientific committee of the 8th Manufacturing Engineering Society International Conference

measuring or nanomanufacturing applications by integrating different devices [1]. The performance of these processes is directly related to the accuracy of the positioning systems and their working range. Therefore, accurate positioning control in a large working range is one of the main necessities of nanotechnology applications [2].

At the University of Zaragoza, a novel 2D nanopositioning platform (NanoPla) is in development. The design of the NanoPla has been optimized to achieve nanometre resolution in a large working range of 50 mm × 50 mm [3,4]. The motion of the moving part of the NanoPla is performed by four custom-made Halbach linear motors. These motors directly transform electrical energy into linear motion. In addition, the motion is performed without any mechanical guidance between the stator and the permanent magnet array, allowing planar motion [5]. A commercial control solution for these custom-made linear motors is not available. In other works [6,7], a control hardware and software were specifically designed and built for control issues. In contrast, in this project, the use of a commercial control hardware for generic motors has been proposed as a novel solution to perform their control and drive. The purpose of this is to facilitate a future replicability of the system.

In a previous research [8], a positioning control strategy was designed and implemented in the selected commercial control hardware for one linear motor performing a 1D movement on a linear guide. The right performance of this control system, according to the established design requirements, was experimentally verified. In this work, the control strategy is optimized for the 2D movement and implemented in the NanoPla to control and drive the planar motion of a nanopositioning platform in a range of 50 mm × 50 mm. The positioning feedback is provided by a 2D laser system, which presents high accuracy in large working ranges and direct traceability. Subsequently, the positioning uncertainty of the proposed control system is analysed. A preliminary modelling of the 2D control positioning control was presented in [9]. Nevertheless, this previous work is prior to the implementation of the commercial hardware and considers that the phase currents are controlled independently, which is not possible with the commercial control hardware solution proposed.

This article is divided as follows; Firstly, an overview of the NanoPla is presented, and the Halbach linear motors, the positioning sensor and the hardware of the control system are described. Then, a positioning 2D control system is proposed and experimentally validated. The positioning uncertainty of the 2D positioning control system is assessed. Finally, conclusions are withdrawn.

2. Method and materials

In this section, firstly, the NanoPla design and application is described. Then, the control system hardware is defined, as well as the actuators, the positioning sensor and the connections between them.

2.1. 2D Nano-positioning platform (NanoPla)

The NanoPla design was presented in [3]. An exploded view of the NanoPla can be seen in Fig. 1. It has a three-layered structure that consists of fixed inferior and superior bases and a moving platform that is placed between them. The moving platform is levitated by three air bearings while four Halbach linear motors perform its motion. A Halbach linear motor has two parts, a permanent magnet array and the stator that consists of three-phase ironless coils. In the NanoPla, the magnet arrays of the four linear motors are fixed to the moving platform and the stators are assembled to the superior base, which minimizes the weight of the moving part and makes it wireless. A 2D laser interferometer system works as positioning sensor. The laser heads are positioned in the inferior base and the positioning mirrors are fixed to the moving platform. The aim is to embed an atomic force microscope (AFM) in the NanoPla. The AFM will be fixed to the moving platform that will position it in the XY-plane, above certain area of the sample to be measured, allowing the characterization of a large area of the sample (50 mm × 50 mm). Once the AFM is positioned, the moving platform will remain static (air-bearings off) in order to carry out the scanning task.

The NanoPla presents a two-stage scheme, that is, the XY-long range positioning of the moving platform is complemented by an additional piezo-nanopositioning stage that is fixed to the metrology frame of the inferior base. This second stage is a commercial piezo-nanopositioning device (part of the AFM system) with a working range of 100 µm × 100 µm × 10 µm, which will perform the motion of the sample during the scanning operation. Therefore, it has been decided that the position control system accuracy should have a positioning error at least one order of magnitude smaller than the maximum XY range of the commercial piezo-nanopositioning stage, i.e., 10 µm. So that, this error could be corrected by the fine motion of the piezo stage.

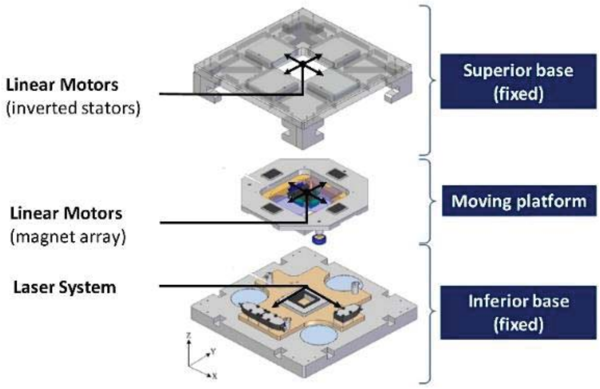

Fig. 1. Exploded view of the NanoPla

2.2. Components of the control system

Halbach linear motors have been selected as actuators in the NanoPla because of their many advantages in precision engineering due to the absence of mechanical transmission elements, like avoiding backlash. Similarly, the contactless unguided motion, prevents friction and allows planar motion. The Halbach linear motors used in the NanoPla were developed by Trumper et al. [5] and they are not commercialized. Therefore, they have been custom-made at the University of North Carolina at Charlotte, and the size of its winding area is large enough to allow planar movement in the 2D working range of the NanoPla. When DC current flows through the three-phase coils of a Halbach linear motor, the electric field interacts with the magnetic field of the magnet array, resulting in two orthogonal forces, one horizontal and the other vertical. The relation between the phase currents and the generated forces is defined by the motor law presented in [8]. The vertical forces of the four motors help to the moving platform levitation, while the horizontal forces perform the movement of the moving platform in the XY-plane.

A generic commercial control system for custom-made Halbach linear motors is not currently available. As a solution, other projects [6, 7] designed and built their own control hardware capable of acting directly on the phase currents. This project proposes to facilitate the 2D positioning control of the NanoPla by implementing a commercial control hardware. In contrast to the aforementioned custom-made control systems, generic motor control hardware acts on the phase voltages instead of acting directly on the phase currents. The selected device is the DRV8302- HC-C2-KIT Digital Motor Control (DMC) kit of Texas Instrument that is designed to operate with generic rotatory permanent magnet synchronous motors. It includes a 32-bit C2000 microcontroller unit (MCU). In addition, it has a power stage capable of controlling and generating three phase voltages by pulse width modulation (PWM). Thus, a DMC kit is required for the phase voltage generation of each linear motor of the NanoPla.

In a previous work [8], an experimental setup, external to the NanoPla, was assembled for the development and experimental validation of the control system of one Halbach linear motor in 1D. In that setup, the magnet array of the motor was fixed and the stator of the motor was the moving part, attached to a pneumatic linear guide. The control strategy was implemented in the DMC kit and a 1D interferometer laser system was used as positioning sensor. After that first validation, for the project presented in this paper, the four linear motors have been installed in the NanoPla and each of them connected to one DMC Kit. In turn, all the DMC kits are connected to the host PC that performs the coordination of the four motors. The movement is achieved while the moving platform is levitated by three air-bearings.

As mentioned, in the NanoPla, a 2D laser system is used as positioning sensor for the control system feedback. The laser system components belong to the Renishaw RLE10 laser interferometer family. It consists of a laser unit (RLU), three sensor heads (RLD), two plane mirrors (one per axis), and an environmental control unit (RCU). In addition, an external interpolator is used to reduce the expected resolution of the system from 9.88 nm to 1.58 nm. Besides the readouts of the three laser encoders, the system also provides the readouts of the RCU sensors: air temperature, material temperature and air pressure. The measurement of each signal takes approximately 0.04 seconds, thus, the maximum speed at which it is possible to record the six measurements is every 0.25 seconds.

Fig. 2a represents a scheme of the connections between the host PC, the positioning sensors, the control hardware and the linear motors. The input is the target position in X, Y coordinates, which is entered by the user in the host PC. The control strategy is computed in the PC that receives the position feedback from the laser system. Then, the PC computes the phase voltages that must be generated at the control hardware to drive the linear motors that produce the movement. The plane mirrors are the moving target of the 2D laser system, and the magnet arrays are the part of the linear motors that perform the relative movement respect to the stator that is fixed. The plane mirrors as well as the magnet arrays belong to the moving platform.

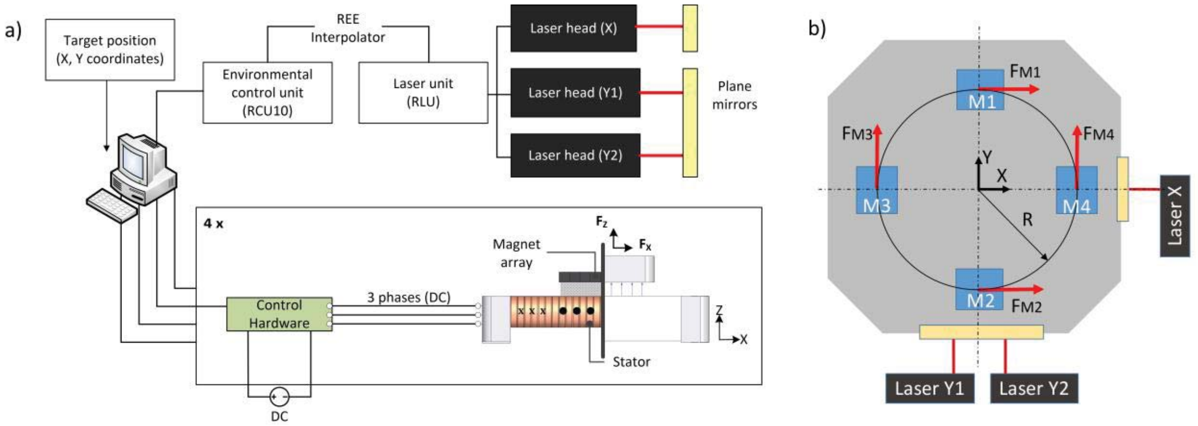

Fig. 2. a) Scheme of the connections between the host PC, control hardware and positioning sensor. b) Scheme of the forces that act on the moving platform

3. 2D positioning control

In this section, the 2D positioning control strategy for the NanoPla is presented and then, its performance is experimentally validated.

3.1. 2D Control strategy

In the NanoPla, the motors are placed in parallel pairs (Fig. 2b), thus, two motors, motor 1 and motor 2 (represented as M1 and M2 in Fig. 2b), generate forces in X-axis (F_{M1} and F_{M2}) that move the platform in X direction. Similarly, the other two parallel motors, motor 3 and 4 (M3 and M4) generate forces in Y-axis (F_{M3} and F_{M4}) that move the platform in Y direction. In addition, the four motors are placed at a distance R from the center of the platform and, thus, their forces generate a torque at the center of the moving platform, around Z-axis. The movement of the platform in X and Y-axes, X_s and Y_s, and the rotation around Z-axis, θ_{zs}, is monitored by the 2D laser interferometer system (Laser Y1, Y2 and X). The total forces in X and Y-axes and the torque around Z-axis (T_z) can be calculated as follows:

$$F_x = F_{M1} + F_{M2} \tag{1}$$

$$F_y = F_{M3} + F_{M4} \tag{2}$$

$$T_z = -F_{M1} \cdot R + F_{M2} \cdot R - F_{M3} \cdot R + F_{M4} \cdot R \tag{3}$$

Fig. 3a represents the scheme of the control system that has been implemented in this project. The input of the control system is the target position (X_{ref}, Y_{ref}) of the moving platform that is entered in the graphic user interface. In addition, for the laser system to read, the plane mirrors attached to the moving platform must remain perpendicular to the laser beams projected by the laser heads. Therefore, the rotation around the Z-axis should be kept minimal ($\theta_{zref}=0$). The control strategy is computed in Simulink®, in the host PC (Fig. 3b). Three independent PID controllers have as reference input X_{ref}, Y_{ref} and θ_{zref}, while the feedback input is the actual position of the moving platform, recorded by the laser system (X_s, Y_s, and θ_{zs}). The control strategy calculates the forces F_x and F_y needed to move the platform to the target position as well as the torque T_z, that is required to correct the platform misalignment. Then, considering symmetry of the moving platform, the horizontal forces that each of the linear motor needs to generate are computed. The phase currents that each linear motor requires to generate those forces are calculated according to the motor law. The output of the control strategy are the corresponding phase voltages that the control hardware must generate for each motor. These phase voltages are generated at the power stage of each DMC kit. Then, the interaction of the phase currents flowing through the stator coils with the magnetic field of the magnet arrays of the moving platform generate the horizontal forces that move the platform. This movement is recorded by the laser system and fed back to the control strategy.

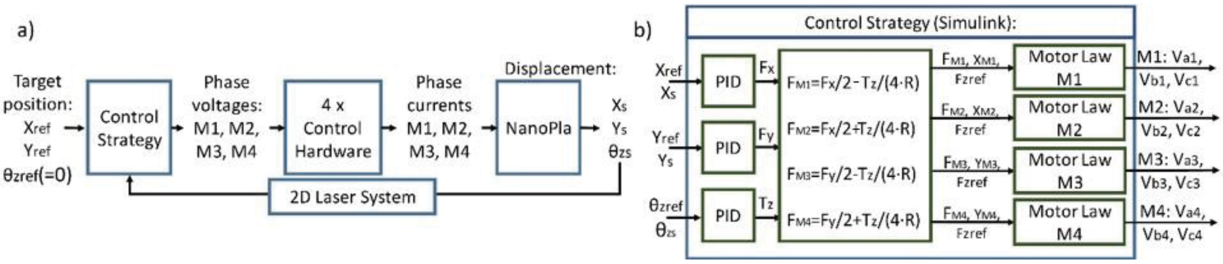

Fig. 3. a) Diagram of the control system. b) Detail of the control strategy.

3.2. Experimental results

The proposed control system has been implemented in the NanoPla and its correct performance has been experimentally verified. For these experiments, the vertical force generated by each motor has been defined to be 2 N, which limits the phase currents working range to ±0.83 A.

As it was mentioned, the NanoPla has a two-stage scheme. The moving platform performs the coarse movement in the large working range of 50 mm × 50 mm, once the moving platform has arrived to the target position, it will stay static (air bearings off) and a piezo-nanopositioning stage place on the inferior base will perform the fine displacement, required for the scanning task, in a range of 100 µm × 100 µm. Therefore, the performance of the control system has been tested when performing a displacement to a target position. Fig. 4a shows the response to a 100 µm displacement in X-axis, while Y-axis is kept static. When the platform reaches the target position at stationary state the positioning error is 0.038 µm and the root mean square (RMS) deviation positioning error is 0.11 µm. In addition, the proposed control system is capable of moving the platform in X and Y-axes simultaneously without losing the alignment of the laser beams and the plane mirrors, that is, keeping the rotation around Z-axis, θ_{zs}, minimal. In Fig. 4b, a displacement describing a 4-mm diameter circumference, moving simultaneously in the two axes, has been represented.

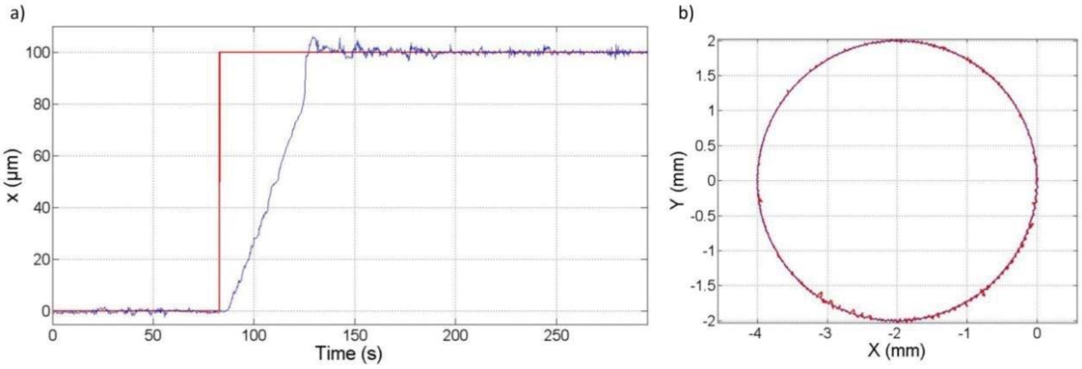

Fig. 4. a) 100 µm displacement in X-axis, while Y-axis is kept static. b) Simultaneous displacement in X and Y-axes describing a circumference.

4. Positioning uncertainty of the control system

The control system of the NanoPla has been optimized to reduce the positioning errors. Nevertheless, the computing operation in the control hardware is performed with finite numbers, which implies a rounding operation resulting in a truncation error that depending on its magnitude may not be negligible. In addition, the errors due to electronic devices noise cannot be completely eliminated and they result in a positioning noise. Thus, the positioning uncertainty of the control system is assessed and analyzed in this section.

In Fig. 5, the control system dataflow has been represented in a block diagram. The data type of the transmitted information is shown in colored arrows. The control strategy is computed in Simulink® (MATLAB®). X_{ref} and Y_{ref} are the desired positions in X and Y-axes. The real position of the NanoPla is measured by a 2D laser system and extracted by MATLAB into the Simulink program. The control strategy computed in the PC by Simulink uses a 64-bit double-precision floating point format (blue arrows) and, in this case, the rounding operation has no significant influence on the calculated results. The control strategy outputs are the required phase voltages, contained in a range of ± 6 V, and they are sent to the control hardware by a Serial Communication Interface (SCI) (green arrows). The MCU of the control hardware works with 32-bit data types, and the voltage values are transmitted as 32-bit fixed point with a 25-bit fraction length (red arrow). The resolution derived from the data type used for the voltages values is 0.0298 nV. These phase voltages are generated in the power stage of the control hardware by PWM. The DMC kit includes a High Resolution PWM (HRPWM) module that is capable of extending the time resolution capabilities of the PWM function. Thus, the resolution of the voltage generation is defined by the time resolution of the HRPWM module and is 26.1 μV. This resolution is sufficient to perform a minimum incremental motion of approximately 700 nm in open-loop. Therefore, the hardware is not able to generate the exact combination of phase currents for every target position. Nevertheless, when working in closed-loop, the positioning controller is capable of partially correcting this error by switching between combinations of phase currents [10].

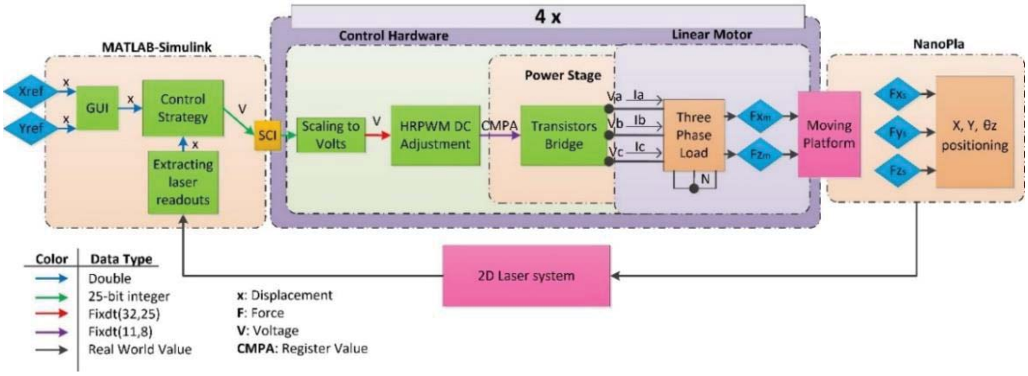

Fig. 5. Block diagram of the data flow in the control system of the NanoPla

In Fig. 5, the real world values are represented with black arrows. These values are the generated phase voltages, the derived currents and resultant forces. In addition, the 2D laser interferometer system measures the moving platform displacement The uncertainty of the laser system measurement also affects the positioning uncertainty of the control system.

It must also be taken into account that the PWM controlled phase voltages lead to a ripple in the phase currents. The current ripple is directly related to the inductance of the stator coils. The resistance and inductance of the coils have been experimentally measured and are 0.88 Ω and 0.24 mH in each phase coil. The electric circuit has been simulated in order to calculate the current ripple derived from the PWM generated phase voltages. The current ripple has a sawtooth waveform with a frequency of 29.28 kHz, which is the double of the PWM frequency. Moreover, the current ripple peak to peak value is dependent on the duty cycle (DC) of the PWM voltages, in this case of study the currents working range is ±0.83 A, which corresponds to a DC between 43.08% and 56.92%. For these values, the peak to peak value of the current ripple has a maximum magnitude of 0.09 A. The actual phase currents have been experimentally measured using a data acquisition system (DAQ) of National Instruments. This DAQ is able to record the measurements at a frequency of 500 kHz and with a resolution of approximately 2 mA. In Fig. 6a, an experimentally measured phase current is compared to the simulated one and, as shown, the current ripple in both cases is almost coincident. Nevertheless, the experimentally measured phase current includes an additional noise, that can be seen in Fig. 6b, where the difference between the measured and the simulated phase currents have been represented. This deviation has different sources, including the DAQ own noise. One of the contributors is the noise of the DC power supply that feeds the power stage of the control hardware. The noise of the DC power supply is imprinted in the PWM phase voltages and, thus, is transmitted to the phase currents. To minimize this contributor, a low noise power supply, with a peak to peak noise of 10 mV has been used.

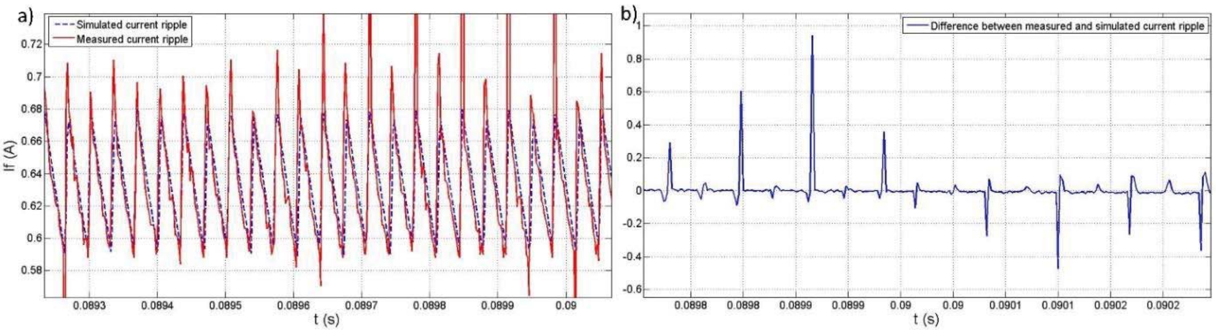

Fig. 6. a) Current ripple of the phase currents generated by PWM controlled phase voltage. b) Difference between the measured and the simulated phase currents.

In a previous work [11], a self-calibration procedure for the geometrical characterization of the 2D laser system of the NanoPla was proposed. The standard uncertainty of the calibrated laser system, after correcting the geometrical errors, was calculated to be 99 nm in X and Y-axes. The laser system resolution is 1.58 nm and the RMS deviation of the laser readouts of an axis is 6 nm. In addition, the stability of the 2D laser system integrated in the NanoPla was verified in [12].

In the control system of the NanoPla, the phase currents noise generates deviations in the forces that act on the moving platform, producing undesired vibrations of the platform. These vibrations are recorded by the laser system, added to the laser system own noise and fed back to the control strategy. This results in positioning noise of the moving platform that has been experimentally measured and computed as the RMS positioning error that is 0.11 µm in each axis. It has also been experimentally verified that the main contributor to the RMS positioning error is the phase currents noise.

In Table 1, the calculation of the positioning uncertainty according to [13] and its contributors has been represented. The resultant positioning uncertainty U_{XY} (k=2) in each axis and in all the working range of 50 mm x 50 mm is equal to 0.50 µm.

Table 1. NanoPla positioning uncertainty contributors and calculation

Source	Justification	Standard uncertainty	Relative contribution
Resolution at the HRPWM u_{HRPWM}	Resolution of 26.2 µV	0.7/√12 µm	65.1%
Laser system resolution u_{Lres}	Resolution of 1.58 nm	1.58/√12 nm	0.00%
Laser system calibration u_{Lcal}	Geometrical errors + measuring system calibration [12]	99 nm	15.6%
RMS positioning error u_{RMS}	Laser system noise + phase currents noise + NanoPla vibrations	0.11 µm	19.3%
Positioning uncertainty $U_{XY}(k=2)$	$U_{XY}(k=2)=k\sqrt{u_{HRPWM}^2+u_{Lcal}^2+u_{Lres}^2+u_{RMS}^2}$	0.50 µm	100%

In the Table, two types of contributors can be identified: the ones that add a constant positioning error (i.e. laser system resolution and calibration uncertainty) and the ones that contribute to the RMS positioning noise. The main contributor is the HRPWM module resolution and it contributes partially to both. That is, when the laser system detects this error, the controller acts on the horizontal force to correct it, resulting in oscillations. The phase currents noise is another main contributor to the positioning uncertainty. None of this errors can be corrected without additional electronics. Nevertheless, the resultant positioning uncertainty is much lower than the initial working requirements of the NanoPla, thus, the developed positioning control system is considered valid.

5. Conclusions

In this work, a positioning control system for a 2D nanopositioning stage has been designed and implemented in the NanoPla. The proposed control system drives four Halbach linear motors that allow planar motion while a 2D plane mirror laser interferometer system works as positioning sensor. The selected control hardware is a Digital Motor Control kit of Texas Instruments for generic rotative motors. The target is to obtain an accurate positioning control system that fulfils the NanoPla requirements by implementing the commercial hardware and without any additional electronics.

The NanoPla presents a two-stage scheme, which complements the XY-long range positioning of the moving platform (50 mm × 50 mm) with an additional commercial piezo-nanopositioning stage that is fixed to the inferior base. This second stage works in a range of 100 µm × 100 µm. Due to this, the position control system accuracy requirement of the NanoPla in X and Y-axes has been decided to be 10 µm. In addition, the rotation around Z-axis must be kept minimal in order to avoid the laser system misalignment. The correct performance of the proposed control system has been experimentally verified in the NanoPla. In addition, the positioning uncertainty of the control system has been computed and its contributors analysed. The obtained positioning uncertainty $U_X = U_Y = U_{XY}$ (k=2) is equal to ±0.50 µm in each axis and in all the working range of the NanoPla. Therefore, the resultant positioning uncertainty of the control system implemented in a commercial generic hardware and without additional electronics is much lower than the NanoPla required accuracy, broadening the applicability scope of the designed positioning system. In future works, possible alternatives to improve global uncertainty with additional electronics will be studied.

References

[1] W. Gao, S. Kim, H. Bosse, H. Haitjema, Y. Chen, X. Lu, W. Knapp, A. Weckenmann, W. Estler and H. Kunzmann. Measurement technologies for precision positioning. CIRP Annals 64 (2015) 773-796

[2] E. Manske, G. Jäger, T. Hausotte and R. Füßl. Recent developments and challenges of nanopositioning and technology. Measuring Science Technology 23 (2012) 74001–74010

[3] M. Torralba, M. Valenzuela, J.A. Yagüe-Fabra, J.A. Albajez, J.J. Aguilar. Large range nanopositioning stage design: A three-layer and two-stage platform. Measurement 89 (2016) 55–71.

[4] M. Torralba, J. A. Yagüe-Fabra, J. A. Albajez and J. J. Aguilar. Design Optimization for the Measurement Accuracy Improvement of a Large Range Nanopositioning Stage. Sensors 16/84 (2016)

[5] D. Trumper, W. Kim, M. Williams. Design and analysis framework for linear permanent-magnet machines. IEEE Trans. Ind. Appl. 32 (1996) 371–379.

[6] S. Ruben. Modeling, control, and real-time optimization for a nano-precision system. Ph.D. Thesis, University of California, Los Angeles, CA, USA, 2010.

[7] H. Yu, Design and Control of a Compact 6-Degree-of-Freedom Precision Positioner with Linux-Based Real-Time Control. Ph.D. Thesis, Texas A&M University, College Station, TX, USA, 2009.

[8] L.C. Díaz-Pérez, M. Torralba, J.A. Albajez, J.A. Yagüe-Fabra. One dimensional control system for a linear motor of a two dimensional nanopositioning stage using a commercial control hardware. Micromachines, 9 (2018) 421.

[9] M. Torralba, J. A. Albajez, J. A. Yagüe-Fabra and J. J. Aguilar. Preliminary modelling and implementation of the 2D-control for a nanopositioning long range stage. Procedia Eng. 132 (2015) 824–831.

[10] L.C. Díaz-Pérez, J.A. Albajez, M. Torralba, J.A. Yagüe-Fabra.Vector control strategy for a Halbach linear motor implemented in a comercial control hardware. Electronics 7 (2018) 232.

[11] M. Torralba, L.C. Díaz-Pérez, M. Valenzuela, J.A. Albajez, J.A. Yagüe-Fabra. Geometrical Characterisation of a 2D Laser System and Calibration of a Cross-Grid Encoder by Means of a Self-Calibration Methodology, Sensors 17/9 (2017) 1992.

[12] L. Díaz-Pérez, M. Torralba, J. A. Albajez and J. A. Yagüe-Fabra. Performance analysis of laser measuring system for an ultra-precision 2D-stage. Euspen's 17th International Conference & Exhibition, Hannover, Germany, 2017.

[13] ISO/TR 230-9. Test Code for Machine Tools. Estimation of Measurement Uncertainty for Machine Tools Test according to Series ISO 230, Basic Equations; International Organization for Standardization: Geneva, Switzerland, 2005.

Acknowledgements: Funded by the Gobierno de Aragón (Reference Group T56_17R) and co-funded with Feder 2014-2020 "Construyendo Europa desde Aragón" and the Spanish government project DPI2015-69403-C3-1-R "MetroSurf" with the collaboration of the Diputación General de Aragón – Fondo Social Europeo.

3. Summary

This section describes the aims, contributions and the methodology that has been followed in this thesis.

3.1. Aim

The importance of nanotechnology in the world of Science and Technology has been rapidly growing in the last decades. As a result, the demand for positioning systems capable of providing accurate positioning (nanometre resolution) in a large working range (from 10 mm up to 100 mm) has increased. In this line of research, this thesis deals with the development and implementation of the positioning control system of a large range nanopositioning platform stage. The design of a positioning control system is defined by its main components that are: actuators, positioning sensor and control hardware. Section 1.1 of this thesis presented a review of the state-of-the-art selection of these components for large range accurate positioning.

The choice of actuators is fundamental, because it defines the architecture of the positioning stage. The preferred architecture for accurate positioning is the one that allows planar motion and avoids stacked linear axes. Halbach linear motors present the best solution since they can be unguided, allowing the displacement along the orthogonal direction to its motion and, thus, they permit the implementation of planar motion. In addition, they are able to generate frictionless linear motion in a large range.

Nevertheless, unguided Halbach linear motors are not commercialised, thus, they are custom-made for each application. As a result, there is not a commercial control hardware available for these motors. Other works [59, 62, 70, 71] have specifically designed and built the software and hardware for controlling and driving these motors. The developed control hardware consists on an independent controlled current source for each motor phase. Nevertheless, using a commercial control hardware would increment the applicability and reproducibility of the control system and reduce its cost.

On the other hand, the amplitude of the working range and the architecture of the stage limits the selection of positioning sensors. That is, capacitive and inductive sensors can only be used in short range displacements, whereas linear encoders are not appropriate for planar designs. The combination of 1D plane mirror laser interferometer provide the best option for accurate 2D positioning sensing in a large range. In addition, they present direct traceability and permit XY-planar motion, although they restrict the rotation around Z-axis.

At the University of Zaragoza, a 2D nanopositioning platform (NanoPla) with a large range of 50 mm × 50 mm and submicrometre accuracy has been developed and its first prototype has already been manufactured and assembled [17]. The NanoPla actuators are four Halbach linear motors and it implements planar motion. Moreover, a 2D plane mirror laser interferometer system works as positioning sensor. One of the targets of the NanoPla is to implement commercial devices when possible. Therefore, a commercial control hardware has been selected to control and drive the Halbach linear motors.

An exploded view of the NanoPla is shown in Figure 3.1. As it can be seen, it consists of three main layers: a fixed inferior base, a moving platform and a fixed superior base. In addition, the metrology frame of the NanoPla has two parts: metrology frame (I) and metrology frame (II). The metrology frame (I) is fixed to the moving platform while the metrology frame (II) is fixed to the inferior base. The moving platform is levitated by three airbearings and performs frictionless planar motion along the whole working range of 50 mm × 50 mm. The NanoPla implements a two-stage architecture. That is, the coarse motion is performed by the moving platform and it is complemented by the fine motion of a commercial piezostage in the range of 100 µm × 100 µm × 10 µm.

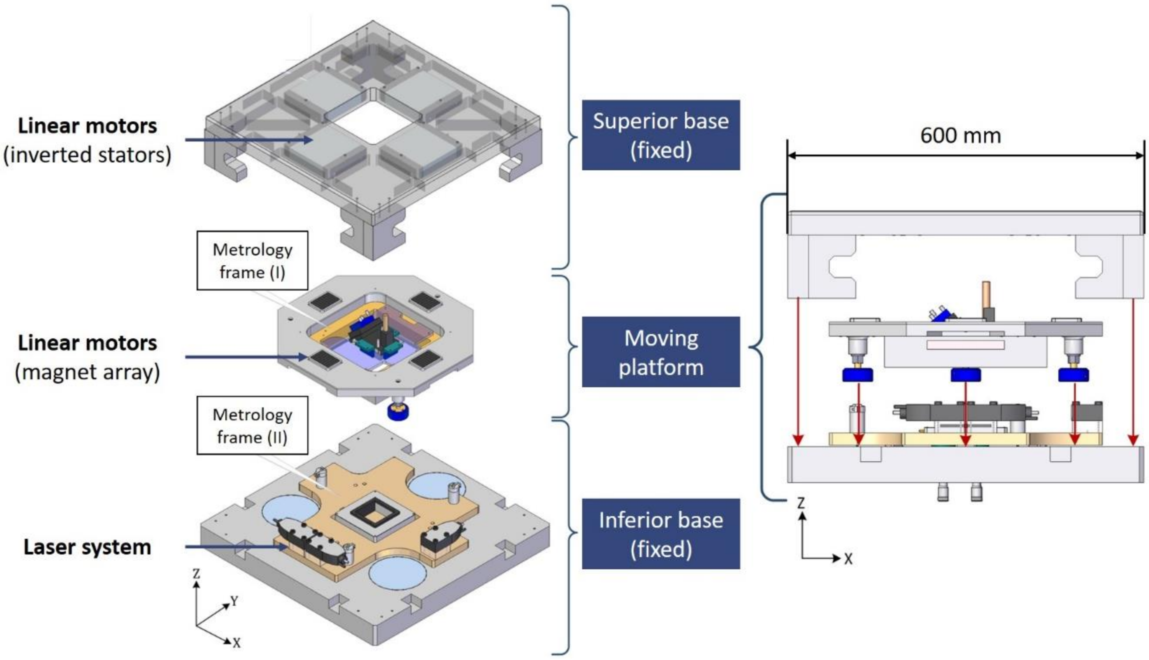

Figure 3.1. *Exploded and front view of the NanoPla. Adapted from [17].*

The linear Halbach motors used in the NanoPla consist of a three-phase stator and a magnet array. The stators are fixed to the superior base, while the magnet arrays, that are wireless, are fixed to the moving platform. The motors are placed symmetrically in parallel pairs, in a way that each pair provides motion in X and Y-axes respectively. The 2D laser system consists of the combination of three plane mirror laser interferometers. One laser beam is aligned to the X-axis and the other two beams, to the Y-axis, sharing plane mirror. Thus, apart from measuring motion in X and Y-axes, they also measure the rotation around Z-axis, θ_z. The three laser heads are placed on the metrology frame (II) fixed to the inferior base. The plane mirrors are attached to the metrology frame (I) of the moving platform. One of the design requirements of the NanoPla is to implement commercial devices when possible. Therefore, a commercial control hardware is preferred to perform the control and drive of the motors. The selected hardware is a Digital Motor Control Kit from Texas Instruments that has been design for generic control of three-phase permanent magnet synchronous motors.

The NanoPla positioning control system is fundamental to assure accuracy and high resolution and it must fulfil the NanoPla working requirements. That is, it must be able to work in a range of 50 mm × 50 mm, with a positioning error at least one order of magnitude smaller than the maximum XY range of the commercial piezostage, that is 10 µm. In addition, due to the fragility of some of the NanoPla components (e.g. Zerodur plane mirrors of the laser system), oscillations should be avoided.

The target of this thesis is to develop, implement and experimentally validate an accurate 2D positioning system for the NanoPla, having as actuators four Halbach motors, a 2D laser system working as positioning sensor and the DMC kit from TI as only control hardware, without additional electronics.

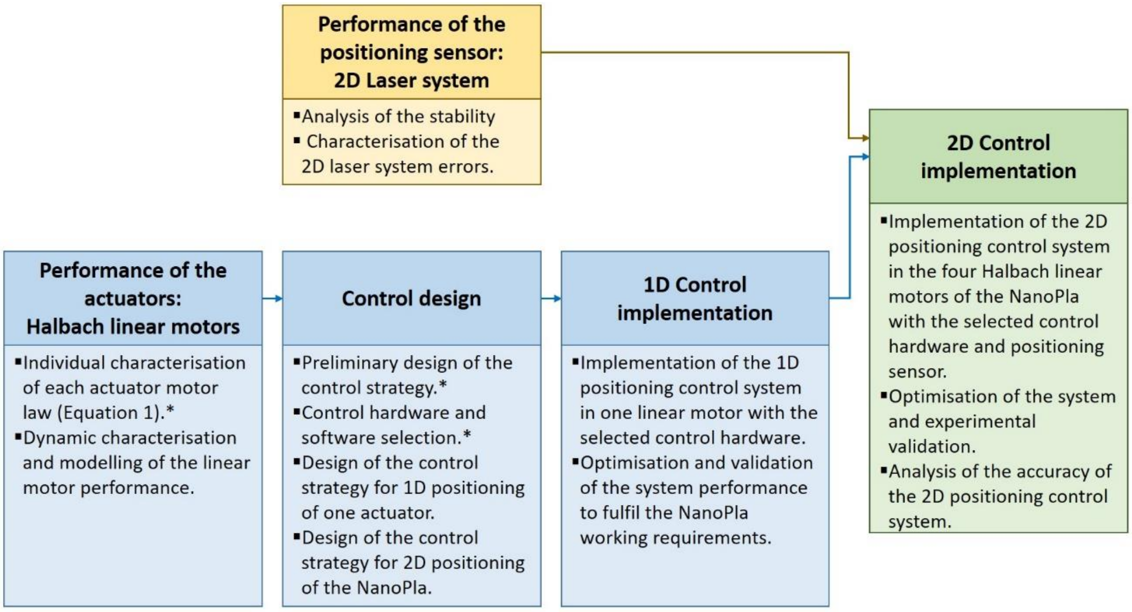

* Done in a previous thesis [17]

Figure 3.2. *Design and implementation process of the NanoPla positioning system.*

The design of the NanoPla positioning control system can be divided in the tasks represented in Figure 3.2. The first task is the characterisation and understanding of the performance of the NanoPla Halbach linear motors. The first step of this task was done in a previous work [17]: each motor was experimentally characterised in order to verify its performance and to experimentally obtain the constant parameters of the motor law (Equation 1) of each motor. The second step deals with the dynamic characterisation and modelling of the linear motor performance as actuator when implemented in a pneumatically levitated stage. The next task is the control design that includes the hardware and software selection and the design of the control strategy. A preliminary design of the control strategy was presented in [17] and a commercial DMC kit from Texas Instruments was selected to drive the motors of the NanoPla. TI provides a Target Support Package^{TM} for Embedded code that integrates MATLAB® and Simulink® with TI tools and the C2000 microprocessor that the DMC kit uses. Therefore, the software selected for the design of the control strategy is Simulink®, which is also able to compile the program and provide a graphic user interface. Once the control hardware and software are selected, a control strategy adapted to the hardware can be designed. Due to the complexity of the project and the absence of literature addressing the position control of Halbach linear motors with commercial control hardware, the project first focuses on the development of a 1D positioning control strategy for Halbach linear motors and its implementation in the DMC kit. This facilitates the 2D control strategy design and implementation and it presents a novelty in respect to the published literature. Concurrently, the performance of the 2D laser system that works as positioning sensor must be characterised and its errors corrected in order to improve its accuracy. Once it is verified that the performance of the 1D positioning control system and the 2D laser system are capable of fulfilling the NanoPla working requirements, the 2D control system is addressed. Therefore, the 2D control strategy is implemented in the control hardware and its performance optimised. Finally, the performance of the positioning control system needs to be experimentally verified and validated, based on the NanoPla working requirements.

This project can be divided in the following specific aims:

- Characterisation of the dynamic behaviour of a Halbach linear motor working as actuator in a pneumatically levitated stage. The characterisation of the dynamic behaviour of a Halbach linear motor has been performed in an experimental setup external to the NanoPla, consisting of a pneumatic linear guide, with the purpose of:
  - Defining the transference function of the system.
  - Developing a sensorless open-loop positioning control system.

- Development of a 1D positioning control strategy of a Halbach linear motor for the implementation in a commercial hardware. This includes:
  - Development of two alternative control strategies that act on the two orthogonal forces generated by the motor.
  - Optimisation of the control strategy for its implementation in the commercial control hardware.
  - Experimental validation of the 1D positioning control system based on the NanoPla working requirements.

- Characterisation of the geometrical errors of a 2D laser system and analysis of its performance stability.
  - Definition of the geometrical model of the 2D laser system assembly.
  - Development of a calibration procedure for the characterisation of the geometrical errors of the 2D laser system.
  - Compensation of the 2D laser system geometrical errors and calculation of the system uncertainty.

- Development and implementation of a 2D positioning control system for the NanoPla
  - Development of a 2D positioning control strategy that coordinates the four Halbach linear motors of the NanoPla and integrates the 2D laser system for positioning feedback.
  - Assessment and minimisation of the positioning uncertainty of the 2D positioning control system.
  - Analysis of the contribution of the trajectory definition errors to the final NanoPla positioning uncertainty when performing a trajectory of motion.

3.2. Contributions

This thesis is focused on the development of a 2D positioning control system for large range nanopositioning stages and, specifically, it is implemented in the NanoPla, a nanopositioning platform designed and built at the University of Zaragoza, subject to two prior theses: [16, 17]. The control system presented in this thesis is capable of providing accurate 2D positioning of the moving platform of the NanoPla along its working range of 50 mm × 50 mm with a positioning error uncertainty of ±0.5 µm. This thesis proposes the following contributions:

- In contrast to other works that analyse the electromagnetic model of Halbach linear motors, this thesis presents a dynamic modelling that allows:
    - Obtaining the transfer function of a positioning system where a Halbach linear motor works as actuator. Once the transfer function has been experimentally obtained, the control system can be simulated and analysed. The simulation of the model allows tuning the controllers in advance, which facilitates the task during the actual implementation.
    - Leveraging the dynamic properties of the Halbach linear motor to propose a sensorless open-loop positioning strategy. This open-loop positioning strategy defines the stable equilibrium position of the system and, then, it uses the horizontal force generated by the motor around this position as an electromagnetic sensorless controller. This strategy can be used for positioning the moving platform at an initial position, before the laser system is aligned, since it does not require position feedback.

- It develops two alternative positioning control strategies for a Halbach linear motor and implements them in a commercial control hardware for generic three-phase motors. The implementation in a commercial generic hardware facilitates the reproducibility of the control system and its future applicability, in contrast to other works that specifically designed and built the control hardware for the purpose. The configuration of the control hardware modules is optimised in order to obtain accurate positioning of the motor.
    - In the first strategy, the only controlled parameter is the position of the stage. This strategy is implemented in the DMC kit from Texas Instruments that acts on phase voltages by PWM. The positioning control system is able to achieve a minimal incremental motion of 1 µm.
    - The second is a vector control strategy that, apart from controlling the position of the stage, controls the vertical and horizontal force generated by the motor. The vertical force of the motor can be used to provide levitation to the moving part, and, thus, controlling it presents many advantages in magnetically levitated stages. The strategy is implemented in the DMC kit from Texas Instruments that includes a current sensing module, necessary to provide feedback in vector control.

- It proposes a novel self-calibration procedure for the geometrical characterisation of a 2D laser system assembly and, subsequently, a calibration procedure for a grid encoder. The self-calibration procedure is based on reversal techniques and it is performed with a non-calibrated artefact that eliminates the costly need of obtaining a calibrated artefact at a nanometre scale. Once the geometrical errors are known, the laser system readouts can be corrected and, thus, the accuracy of the system is improved. In addition, as non-calibrated artefact, a grid encoder has been used. Once the laser system errors are corrected, it is used to calibrate the grid encoder.

- It develops a 2D positioning control system that coordinates the forces generated by the four Halbach linear motors of the NanoPla to provide positioning in X and Y-axes and correct rotations around Z-axis. This work integrates the control strategies and the geometrical characterisation of the 2D laser system presented in the previous works and uses a DMC kit to drive the three-phase voltages of each motor. The developed positioning control system is capable of achieving a positioning uncertainty (k=2) of ±0.5 µm along the NanoPla working range of 50 mm × 50 mm. The obtained uncertainty is much lower than the NanoPla required positioning accuracy, broadening its applicability scope.

- It studies the contribution to the final positioning error of the NanoPla of the errors in the definition of a trajectory of motion by comparing the performance of traditional CAD/CAM system methods with novel algorithms for accurate curve fitting. This novel method with interest in Computer Aided Geometric Design (CAGD) allows high relative accuracy (HRA) in the computations of the representation of parametric curves, minimising the numerical errors. Curve fitting of a given set of points belonging to a parametric curve is performed by interpolation and least squares approximation by two different methods: CAD/CAM software method and a novel HRA method developed at the department of Applied Mathematics of the University of Zaragoza. The contribution of the obtained fitting errors to the final NanoPla positioning error is experimentally verified. The benefits of the HRA method that are shown in this work are that it is capable of performing accurate interpolation with a minimum quantity of data points, and, when performing a least squares approximation it is capable of obtaining an accurate approximation curve with a minimum number of control points. In addition, the number of obtained control points is independent of the size of the problem. Therefore, this work suggests that the implementation of the HRA method in CAD/CAM systems would be of great interest for nanomanufacturing applications in which a nanopositioning stage is required to follow a predefined trajectory with submicrometre accuracy.

3.3. Methodology

The articles **Micromachines 2018** and **Electronics 2018** presented in Section 2 of this thesis, characterise the dynamic model of a Halbach linear motor and, then, develop two alternative control strategies for 1D positioning of a pneumatically levitated stage actuated by a single Halbach linear motor. Similarly, in **Procedia Manufacturing 2019** a 2D positioning control strategy is developed and implemented in the NanoPla, actuated by four Halbach linear motors. The control strategies presented in these articles are implemented in the Digital Motor Control (DMC) kit from Texas Instruments, a generic commercial hardware for rotary motors that drives and generates the linear motors three-phase voltages. The benefit of using a commercial hardware without additional electronics is that it facilitates the reproducibility of the results and the future applicability of the system, in addition to its relatively low cost.

Therefore, in order to ensure the reproducibility of the results, this subsection presents a summary of the methodology that has been used for the programing of the developed control strategies. Moreover, the configuration of the control hardware module and its implementation in the NanoPla are described in detail and the experimental tests that have been performed to verify the capability of the positioning control system are shown and analysed. Finally, the contribution of the trajectory definition errors in the final uncertainty of the NanoPla is examined and the use of a novel high relative accuracy (HRA) method for trajectory definition is proposed.

3.3.1. Programing of the control strategies in the commercial control hardware

The process from control loop design to program execution in the DMC kit proceeds as follows: Firstly, the control model is created in Simulink® (MATLAB®) with Texas Instrument specific Target Support Package™ for Embedded Code library. This library includes blocks particular for the DMC kit control card, F28035, for the configuration of modules such as PWM, analogue to digital converters (ADC), and for host and board communication. In addition, it also includes optimised blocks for fixed-point mathematical operations (IQ Math) and for digital motor control (PID controller). Once the program is created, Embedded Coder toolbox of MATLAB® generates C code from it and an executable file. Code Composer Studio (CCS) program allows connecting to the target, loading the generated program to the device and run it. Moreover, while running, the control card is capable of communicating in real time with a Simulink® program through the host and board serial communication (SCI) blocks.

In the positioning control system, the movement is performed by acting on the phase voltages that vary the phase currents of each motor whose working range is ±0.83 A. Thus, the accuracy of the positioning system is directly related to the phase voltage and current generation resolution and noise. Although the performance of the voltage generation and current sampling modules of the DMC kit are described in the articles, the programing of the control card and the configuration of its modules is not addressed in detail. In order to facilitate the reproducibility of the results presented in this thesis, in this section, the control programs used in the control systems proposed in **Micromachines 2018**, **Electronics 2018** and **Procedia Manufacturing 2019** are presented and the configuration of the voltage generation and current sensing modules are described.

Program used in the 1D positioning control strategy

In **Micromachines 2018**, a 1D positioning control strategy of a Halbach linear motor was presented and implemented in the DMC kit from Texas instruments. In the experimental setup, the stator of the linear motor is the moving part and it is attached to a pneumatically levitated linear guide, whereas the Renishaw XL-80 laser interferometer provides positioning feedback. The laser interferometer includes an environmental compensator unit (XC80 compensator) that corrects the refractive index variations in real time.

In the proposed control system, the control strategy is computed in the control hardware, that is, the DMC kit, whereas the host PC works only as an interface between the user and the control hardware, and between the laser system and the control hardware. Nevertheless, additional electronics could also perform the interface function and replace the host PC. That means that the control system does not require to be connected to a host PC and could be run independently.

The process to move the stage proceeds as follows: The user introduces the target position (in X-axis) in a graphic user interface of Simulink®; in the same Simulink® program, the laser system readouts are extracted; the reference position command (X_{ref}) and the position feedback (X_s) are scaled to an integer data type and sent to the control card through a SCI transmit block from Texas Instruments library; the DMC kit computes the control strategy and generates the phase voltages in its power stage; the power stage terminals are connected to the three-phase coil of the stator that generates the force required to perform the movement. In Figure 3.3, the connection between the mentioned components have been represented.

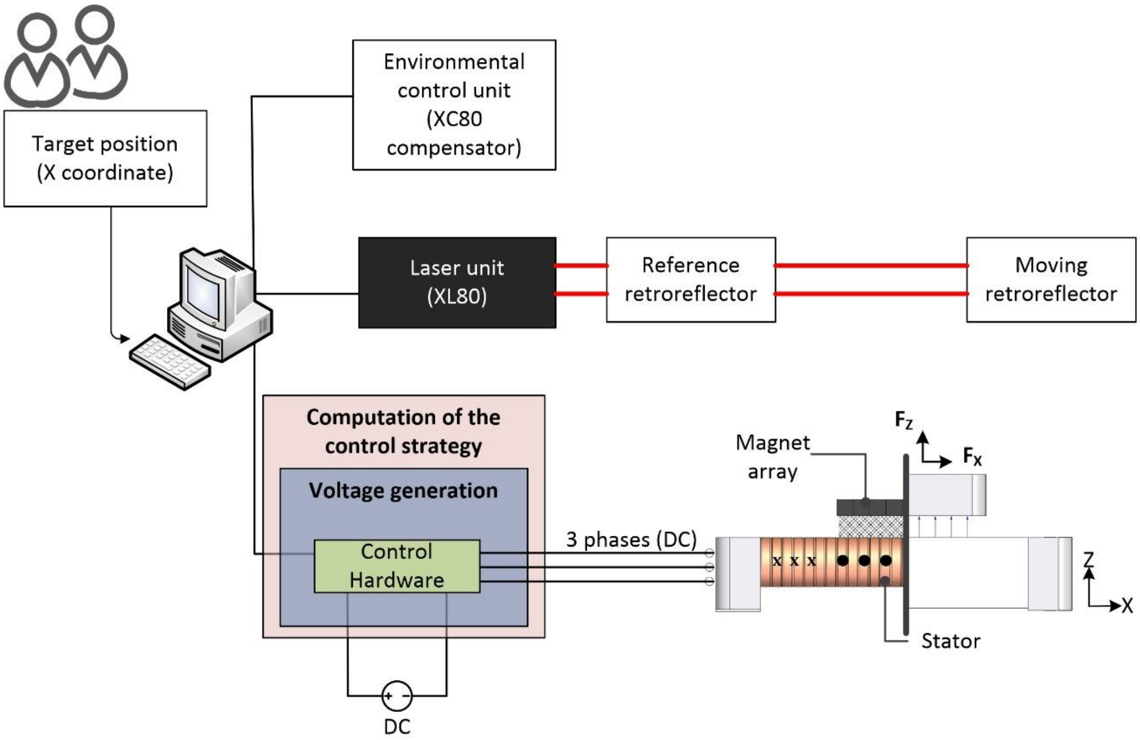

Figure 3.3. *Scheme of the connections between the host PC, control hardware and positioning sensor in the 1D positioning control system.*

Figure 3.4 shows the Simulink® model of the position control strategy presented in **Micromachines 2018**. As mentioned, this program is then executed in the control card. As it can be seen, the first block in the sequence is a SCI Receive block that provides serial communication between the target and the host PC. In this case, through this block the target receives the reference position (X_{ref}) and position feedback (X_s) that are send by another Simulink® model running in the host PC. This data is received as an integer that is then scaled to mm in a fixed point data type (second block). The reference position (X_{ref}) and position feedback (X_s) are the inputs of a 32-bit digital PID controller of the Texas Instruments library. This controller acts on the horizontal force and its output is limited to work in the linear zone around the stable equilibrium position referred in **Electronics 2018**. The required horizontal force and a constant vertical force, as well as the actual stage position (X_s) are input to the commutation law block that calculates the required phase currents to generate those forces at the stage position X_s. In the block, the phase voltages that correspond to those phase currents are also calculated. In the next block, the required phase voltages are scaled to be input in the PWM blocks. The PWM blocks configure the PWM module of the control card that is responsible of the voltage generation. Therefore, in this case, the DMC kit is used for computing the control strategy and as a power stage for the generation of the three-phase voltages.

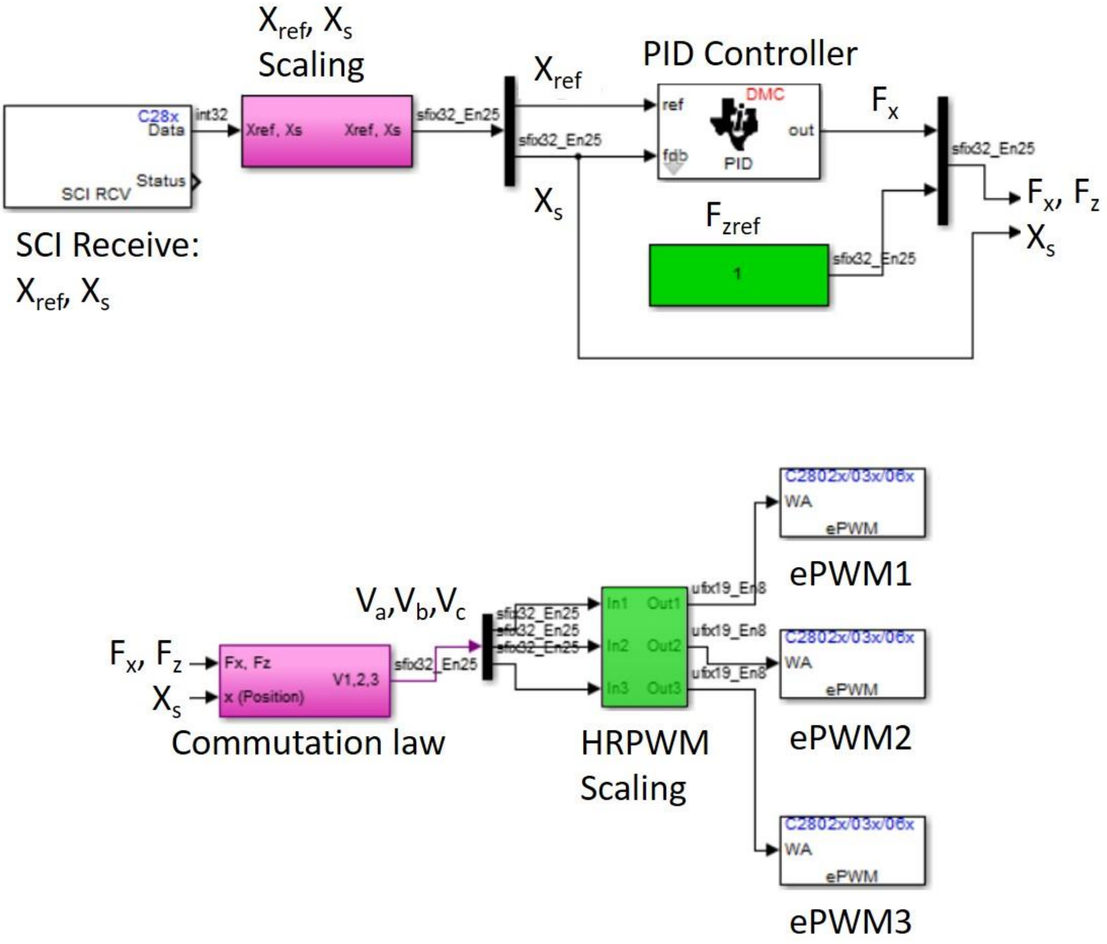

*Figure 3.4. Simulink® model of the position control strategy presented in **Micromachines 2018.***

The sample time of the system represented in Figure 3.4 is limited by the laser system sampling time. The validation of this control strategy was performed in a setup external to the NanoPla with Renishaw XL80 laser system, with a sample time of 0.1 seconds. Therefore, the SCI Receive block was set to work with that sample time. On the other hand, in the NanoPla, a 2D plane mirror laser system that belongs to the Renishaw RLE10 laser interferometer family is used. As mentioned, the sampling time of the system is 0.25 seconds when the variations of the refractive index are being corrected in real time and 0.12 seconds when they are not corrected and only the measurements of the three laser heads are being recorded. In addition, it has been experimentally observed that although the processor is capable of operating with 32-bit single-precision data type and math operation Simulink® blocks, it operates faster with its optimised blocks for fixed-point mathematical operations (IQ Math) and for digital motor control, or integer data type. The units of the variables are adapted in order to minimise the dynamic range of the data values that the MCU has to process and thus, maximise the precision. Hence, the error derived from the use of the 32-bit data is negligible (<1 nm).

Program used in the vector control strategy

In **Electronics 2018**, a vector control strategy for a Halbach linear motor was presented and implemented in the DMC kit from Texas instruments. The vector control strategy decouples the control of the vertical and horizontal forces generated by the linear motor. The horizontal force positions the motor whereas the vertical force can be leveraged for levitation. In the experimental setup, the stator of the linear motor is the moving part and it is attached to a pneumatically levitated linear guide. The magnet array is kept static and attached to a load cell in order to monitor the generated vertical force. The Renishaw XL-80 laser interferometer provides positioning feedback. The laser interferometer includes an environmental compensator unit (XC80 compensator) that corrects the refractive index variations in real time.

As in the previous case, the control strategy is computed in the control hardware, whereas the host PC is only used as an interface between the user and the control hardware, and between the laser system and the control hardware. Therefore, a graphic user interface of Simulink® is used to input the reference position (X_{ref}). The position feedback is extracted from the laser system (X_s) in the same program and the reference position and the real position are then sent to the control card through the SCI transmit block. The control hardware computes the control strategy and generates the three-phase voltages of the linear motor. The connections between components is the same as in the previous case (Figure 3.3)

Figure 3.5a shows the Simulink® model of the vector control strategy presented in **Electronics 2018** . As mentioned, this program is then executed in the control card. As it can be seen, the first blocks are the SCI Receive block, a scaling block and the position PID controller. The PID controller reference input is the reference position (X_{ref}) whereas, the actual stage position (X_s) is the feedback input, both received from the host PC through the SCI. Nevertheless, in this case, the position PID controller output is the virtual current I_{dref} (defined in **Electronics 2018**) that is required to correct the positioning error, proportional to F_x. Then, there is an ADC interrupt subsystem block that has as input the stage position (X_s), and the required virtual currents I_{dref} and I_{qref}, proportional to F_{zref}. It is worth mentioning that, in this program, the vertical force reference value F_{zref} is set constant (1 N), but it could also be an input command defined by the user. The function of the ADC interrupt block is to synchronise the current sampling function with the voltage generation, this will be explained in detail in the current sampling subsection.

Figure 3.5b shows the subsystem inside the ADC interrupt block. The subsystem first blocks are the PI controllers of the vector control strategy. These controllers have as input the required virtual currents I_{dref} and I_{qref} (reference input) and the actual current values I_d and I_q (feedback input). The controllers correct the deviations by acting on the virtual voltages V_d and V_q, respectively. Then, by an inverse Clarke-Park transformation, the corresponding phase voltages V_a, V_b and V_c are calculated in the "dq to abc" block, that, apart from V_d and V_q, it also has X_s as input. Then, as in the model of Figure 3.4, the phase voltages are scaled to be input in the PWM blocks. Additionally, in this subsystem IA-FB and IB-FB ADC channels readouts are also extracted. These channels convert the phase current sensing module readouts to a 12-bit integer data type. In the subsystem, the ADC outputs are scaled to amps. It is worth noting that having I_a and I_b, the third phase current I_c can be obtained through Equation 2. Then, I_a, I_b and I_c are transform to I_d and I_q, in the "abc to dq" block, to be input as feedback to the vector control PI controllers. Therefore, in this case, the DMC kit is used for computing the control strategy, for current sampling and as a power stage for three-phase voltage generation and the host PC only performs an interface function.

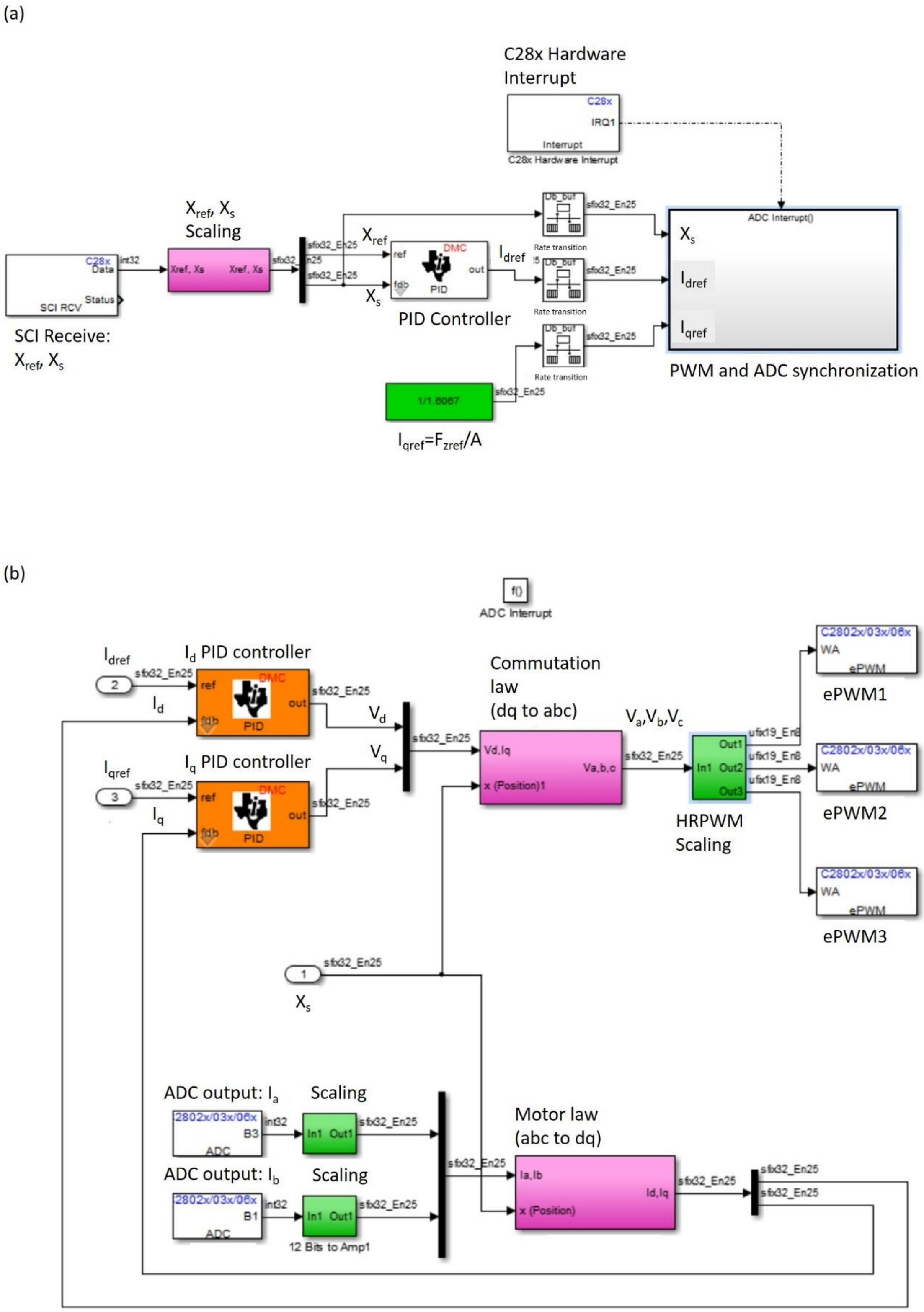

Figure 3.5. *Simulink® model of the position control strategy presented in* ***Electronics 2018****: (****a****) Parent system; (****b****) PWM and ADC synchronisation subsystem.*

As in the previous case, the SCI block works with the same sample time as the laser system that provides the positioning feedback. The positioning feedback sample time also determines the position controller sample time. Nevertheless, the ADC interrupt subsystem has a different sample time that is conditioned by the configuration of the ADCs for current sensing. As it will be explained in detail following, the phase currents are sampled once per PWM signal period.

Program used in the NanoPla 2D positioning control strategy

In **Procedia Manufacturing 2019** a 2D positioning control system for the NanoPla is presented. In the NanoPla positioning system, the motion is performed by four Halbach linear motors that are placed in parallel pairs. One pair generates a force in X-axis (F_x) and the other pair in Y-axis (F_y). In addition, a 2D plane mirror laser interferometer system works as positioning sensor. The laser system essentially consists of three laser beams, one for X-axis (X1) and two for Y-axis (Y1 and Y2), and two plane mirrors, one for X-axis and one for Y-axis. From these three measurements, the position of the platform in X and Y-axes (X_s and Y_s) and its rotation around Z-axis (θ_z) can be computed.

The control system positions the platform in X and Y-axes by acting on the total generated forces in X and Y-axes (F_x and F_y) and prevents the misalignment between laser beams and plane mirrors by acting on the total generated torque (T_z). Therefore, the control strategy needs to coordinate the performance of the four motors of the NanoPla, that are individually driven by a DMC kit each. For this reason, in contrast to the previous 1D positioning control systems, in this case, the control strategy is computed in the host PC. In the NanoPla it is necessary to coordinate the performance of other devices, such as the measuring device or the capacitive sensors, so that, it seems convenient to centralise their control in a host PC.

In a graphic user interface of Simulink®, the user introduces the reference position in XY coordinates (X_{ref}, Y_{ref}). In the same Simulink® program, the laser system readouts (X1, Y1, Y2) are also extracted and the position of the platform is calculated (X_s, Y_s, θ_Z). Then, the control strategy defined in **Procedia Manufacturing 2019** is computed. The output of this control strategy are the phase voltages (V_a, V_b and V_c) that each control card needs to generate for each motor. The connections between the host PC, the control hardware and positioning sensor have been represented in Figure 3.6.

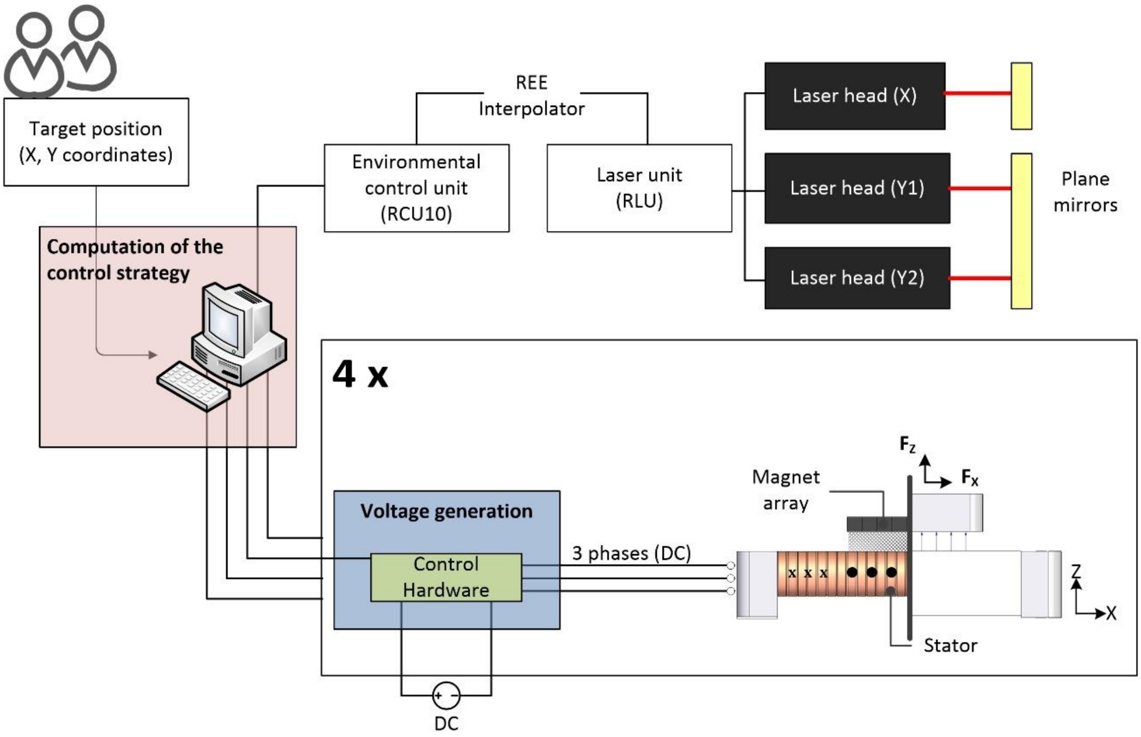

Figure 3.6. *Scheme of the connections between the host PC, control hardware and positioning sensor in the 2D positioning control system.*

Figure 3.7 shows the Simulink® model of the program that is executed in the control cards. As it can be seen, the first block is the SCI Receive block that receives the three-phase voltage command sent by the host PC. The data is received as an integer value and is then scaled to be input in the PWM blocks. In this case, the control hardware is only used for power generation, since the control strategy is computed in the host PC.

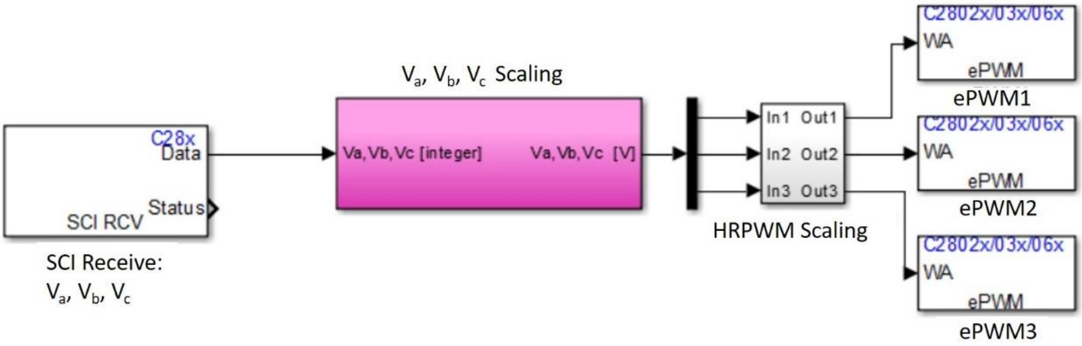

Figure 3.7. *Simulink® model of the control hardware program used in* ***Procedia Manufacturing 2019.***

Voltage generation configuration

In the control hardware, the phase voltages are generated by PWM at a three-phase inverter fed by the control hardware external power supply (PVDD). The inverter stage has two transistors (high and low) per phase (V_a, V_b and V_c) and, in each pair, one transistor works as the inverted version of the other. A simplified scheme of the inverter stage has been represented in Figure 3.8. Each phase pair of transistors (AH and AL; BH and BL; CH and CL) are driven by one

PWM block in the program. In all the control strategies proposed in this thesis, the voltage generation has the same configuration herein explained.

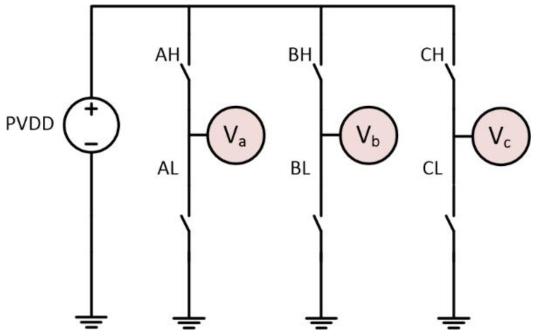

Figure 3.8. *Simplified scheme of the inverter stage of the control hardware.*

The configuration of the PWM modules is crucial for the final positioning accuracy of the control system because it defines the PWM signal frequency and its resolution, and, additionally, its configuration also affects the signal noise. The two main components that define the behaviour of a PWM voltage generation are the duty cycle and the frequency. In this application, the PWM signal frequency is kept constant and the generated voltage is controlled by varying the duty cycle. The duty cycle (DC) is defined as the fraction of one PWM signal period in which the signal is active (high-side switch ON and low-side switch OFF in Figure 3.8).

The frequency is determined by the cycle period that, in turn, depends on the time-base period (TBPRD) of the time-based counter, which is an integer up to 16 bits. The time-base counter has three modes of operation [102]:

- Up-down count mode: In this mode, the counter starts from zero and increments until the period value is reached, then, it decrements until it reaches zero. Then, the pattern repeats.
- Up-count mode: In this mode, the counter starts from zero and increments until the period value is reached. Then, it resets to zero and repeats the pattern.
- Down-count mode: In this mode, the counter starts from the period value and decrements until it reaches zero. Then, it resets to the period value and repeats the pattern.

In every case, the time increment for each step is defined by the time-base clock (TBCLK) which is a prescaled version of the system clock (SYSCLKOUT). It determines the rate at which time base counter increments or decrements. In this case, the time-base clock is set equal to the system clock (TBCLK=SYSCLKOUT) and it is 60 MHz. Therefore, the time-base clock together with the time-base period define the frequency of the PWM signal. It is worth noting that for the same time-base period and clock, in the up-down count mode the timer base is counted twice (once up and once down). Thus, for the same time-base period, the period of an up-down count is twice the period of an up or down count and it can be calculated according to Equation 14.

$$T_{PWM} = \frac{2 \times TBPRD}{SYSCLKOUT} \tag{14}$$

The counter value is compared to a compare value (CMP) and the digital output (ON or OFF) of the PWM module is changed when the counter matches the CMP value. Therefore, up-down count modes result in symmetric signals whereas up-count and down-count modes result in asymmetric signals. In symmetric signals the resultant current ripple is reduced [72] because they produce lower harmonic distortion, and, thus, in this application up-down mode is preferred.

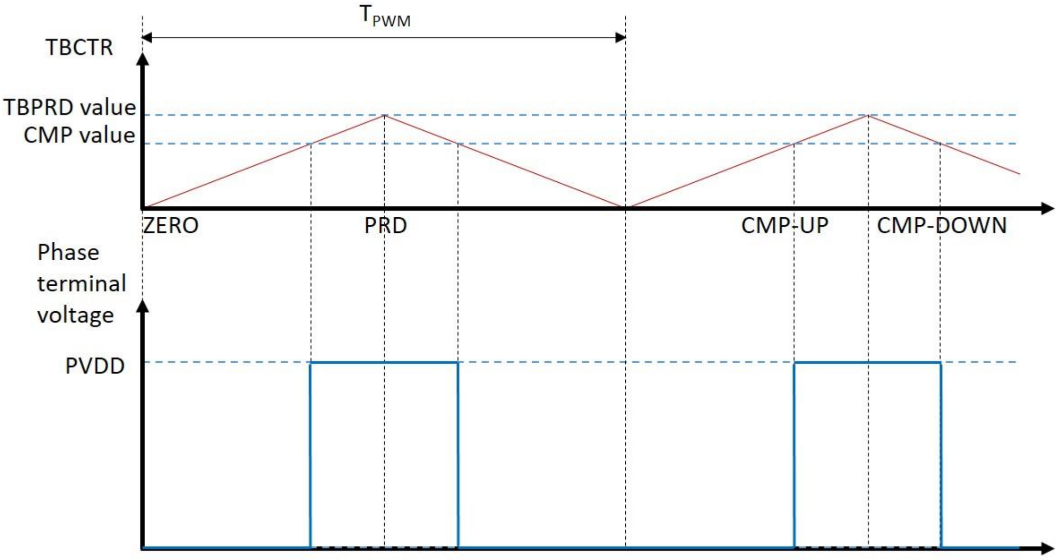

Figure 3.9. *Phase voltage generated at the control hardware terminal in a counter period, in an up-down operation mode for a given CMP value, in a star-connected configuration.*

Figure 3.9 shows the resultant phase voltage generated at the control hardware terminals with an up-down count mode, for a given compare value. The counter events have also been represented in the Figure. The duty cycle (DC) can be calculated as the compare value (CMP) divided by the time-base period (TBPRD), as shown in Equation 15, where TBPRD is an integer up to 16 bits. It is worth noting that, even though the voltage at the terminals is always positive or zero, the fact that the three phases are star-connected and the neutral point is not grounded allows generating positive and negative phase currents due to the inversion of the current flow. In addition, when the three phases are star-connected, the average value of the generated phase to neutral voltage of each phase can be calculated as shown in Equation 16.

$$DC = \frac{CMP}{TBPRD} \tag{15}$$

$$V_{phn} = DC \times PVDD - \frac{PVDD}{2} \tag{16}$$

A phase current ripple reduction can be achieved when the three phases of the motor are centred and symmetrical [72]. For this reason, the PWM counters of the three phases are synchronised and have the same time-base period, as shown in Figure 3.10. Therefore, the phase voltages of the three phases are centred and simmetrical in respect to PRD. Nevertheless, each phase voltage has a different average value, that is, the PWM module of each phase has a different duty cycle and, thus, differet compare value. In the Figure, tha voltage at the neutral point has also been represented.

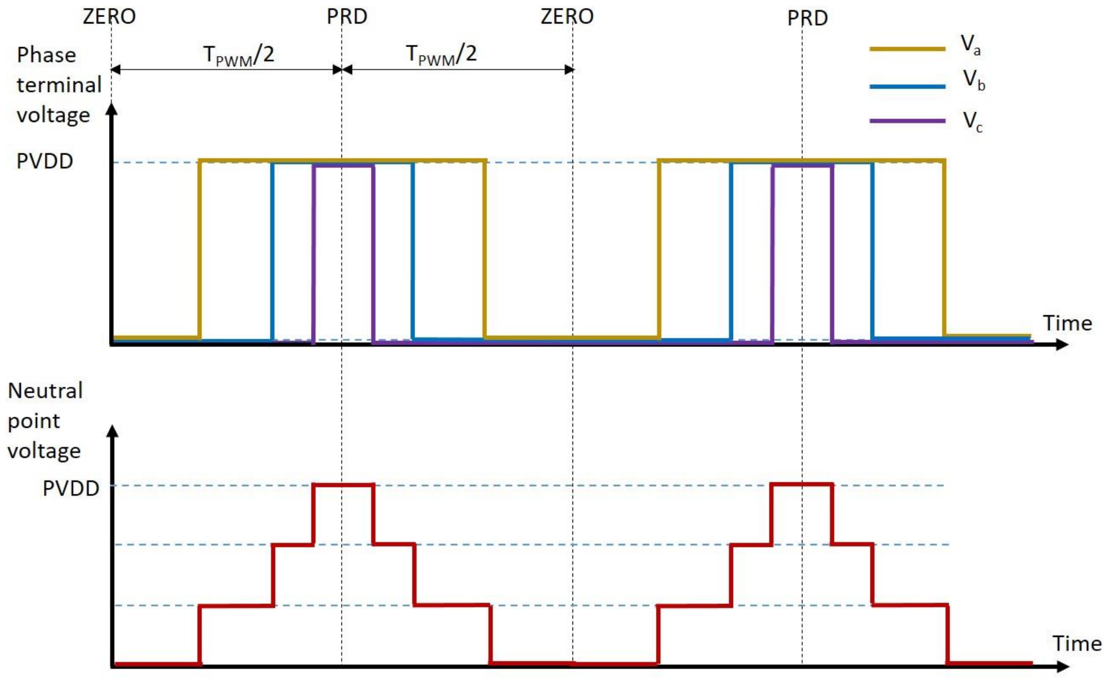

***Figure 3.10**. Synchronised and centred phase voltages and neutral point voltage at the terminals of the control hardware.*

From Equations 15 and 16 it can be deduced that the resolution of the PWM depends on the DC resolution and the supply voltage (PVDD). According to Equation 15, the higher the timer period is, the higher the DC resolution. Therefore, the timer period should be set as high as possible. Nevertheless, the timer period is limited by the switching frequency: the frequency decreases when the timer period increases. According to the manufacturer, setting the PWM switching frequency below 10 kHz may cause issues on the inverter output and is not recommended. Besides, when the frequency is lower than 10 kHz, the coils make a high-pitched whine that could annoy the user. Therefore, the switching frequency should be higher than 10 kHz. That means that the highest timer period can be 2^{11} (2048 counts) that corresponds to the lowest acceptable frequency that is 14.64 kHz (according to Equation 14, for up-down count). In addition, the digital signal processor includes a High Resolution PWM (HRPWM) function that extends the time resolution capabilities of the PWM module and, thus, improves its resolution. HRPWM is based on Micro edge positioning (MEP) technology that divides each coarse step of the PWM in fine steps of 150 ps (MEP_{res}). The digital input of the HRPWM (CMP value) is a 11-bit integer for the coarse steps, due to the PWM frequency requirements, and 8-bit fraction length for the MEP steps.

As mentioned, the voltage resolution of the control hardware depends on the generated voltage range, that is the magnitude of PVDD, and the time resolution according to which the duty cycle can be adjusted. As mentioned, the time resolution is defined by the HRPWM module. Thus, the supply voltage (PVDD) should be set as low as possible in order to improve the resolution. According to the control hardware specifications, the supply voltage must be between 8 V and 60 V. In the case of study, in order not to work too close to the lower limit, the chosen supply voltage is 12 V. Therefore, the final phase voltage generation resolution can be calculated as in Equation 17 and it is equal to 2.62×10^{-5} V.

$$V_{PWMres} = \frac{PVDD}{T_{PWM} / MEP_{res}} \tag{17}$$

The fact that the three-phase inverter is directly fed by the power supply means that the power supply noise is imprinted in the phase voltage. For this reason, an ultra-low noise switching power supply was selected for the purpose. In general, switching power supplies are more efficient and smaller than linear power supplies with the same capacity. Specifically, the selected power supply has a ripple noise of 10 mV peak to peak, an output voltage of 12V and an output power of 300 W. Thus, only one power supply is sufficient to serve the four motors of the NanoPla.

Phase current generation and current sampling configuration

In the motor coils, the phase voltages generated by PWM result in an average voltage at each phase that can be calculated according to Equation 16. The difference between the average and the actual PWM voltages is the source for the current ripple. In a three-phase inverter, the current ripple in each phase is influenced by the switching actions for all three phases. The current ripple is analysed in [103], where is stated that the current ripple in one PWM cycle has seven linear parts, as represented in Figure 3.11. Moreover, it can be observed that when the counter value is equal to ZERO and to PRD, the phase current is at its mean value. The current ripple peak to peak value is dependent on the phase currents working range, that, in this case of study, is ±0.83 A for the three phases, which corresponds to a DC between 43.08% and 56.92%. For these values, the peak to peak value of the current ripple has a maximum magnitude of 0.09 A.

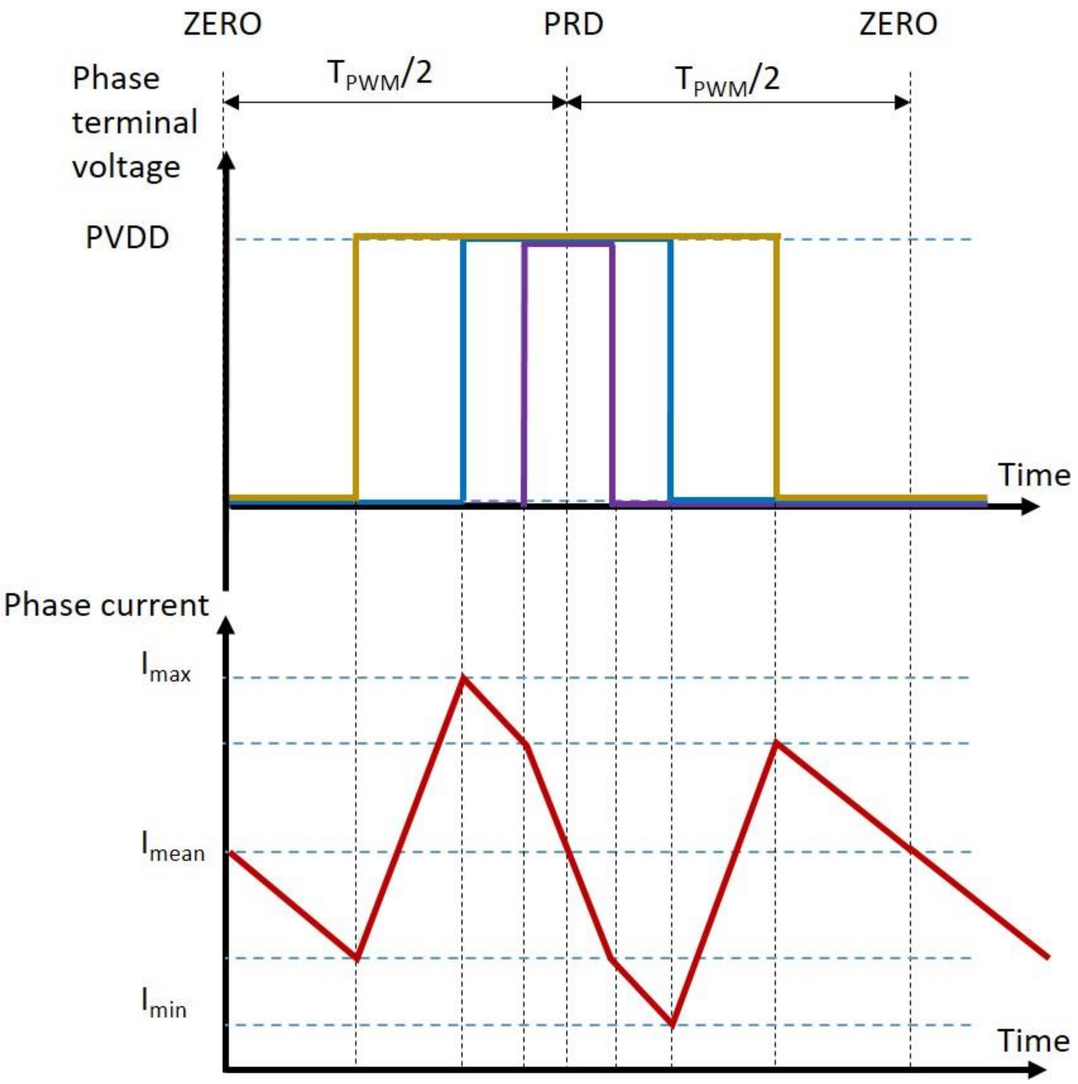

Figure 3.11. *Current ripple in one switching cycle. Adapted from [103].*

Texas Instrument control card includes three current shunt amplifiers that measure phase currents at the low-side inverter leg. The operational amplifier analogue output is converted to a 12-bit digital signal in Analogue to Digital Converter (ADC). Considering star connection, two leg inverter current sensing is sufficient to obtain accurate information of the three phase currents (Equation 2). Figure 3.12a represents a simplified scheme of two-shunt inverter leg current sensing. Current sampling has to be done when the current is flowing through the shunt resistor (R_{shunt}), that is, when the low-side switch is ON. Therefore, the current sampling module must be synchronised with the PWM module.

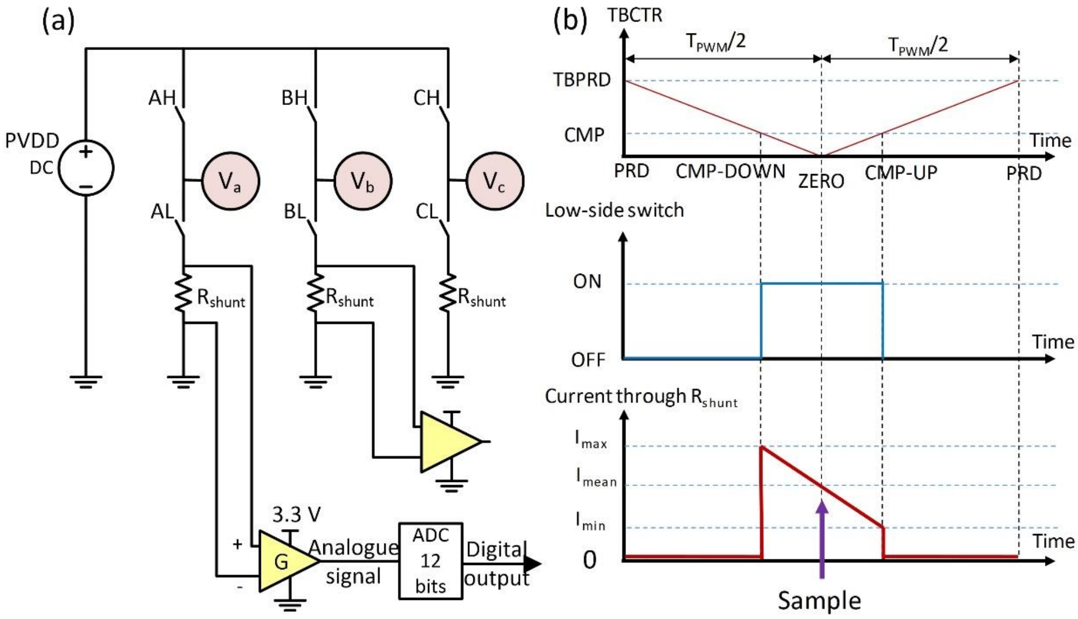

Figure 3.12. *Current sampling scheme: (**a**) Scheme of the low-side current sensing in the transistors bridge; (**b**) Phase current flowing through R_{shunt}.*

The current sensing modules can measure positive and negative values and they must be calibrated so half the range of the ADC (2048 counts) corresponds to 0 A. The highest count (4095) corresponds to the maximum current and the lowest count (0) represents the maximum negative current that can be measured. The current shunt amplifiers have two programmable GAIN settings, 10 or 40 V/V. The phase current value can be obtained by rescaling the ADC digital output (DO) according to Equation 18. The parameters of the current sensing module are known and they that have been represented in Table 3.1.

Table 3.1. Parameters of the phase-current sensing module

Component:	**R_{shunt}**	**Gain**	**Analogue ADC input**	**Digital ADC resolution**
Value:	0.002 Ω	40 or 10	3.3 V	12 bits

$$I_{ph} = (DO - 2048) \times \frac{3.3}{4096} \times \frac{1}{G \times R_{shunt}} \tag{18}$$

In addition, the resolution of the current sampling module can be calculated by dividing the phase current sampling range by the digital output ADC resolution. Thus, a better resolution is obtained with the highest value of the operational amplifier gain (G=40 V/V). The maximum and minimum phase currents that the ADC can read are 20.63 A (4095) and -20.63 A (0), respectively. Therefore, the current sampling has a resolution of 41.2/4096 = 0.01 A.

As it was previously noted, the current sampling has to be done when the low-side switch is ON, that is, when the low-side inverter leg is conducting. It must be noted that the phase current is measurable for a limited period of time that depends on the duty cycle of each phase voltage. Therefore, when the PWM is operating at a duty cycle near 100%, the current sampling will not be performed correctly. That could be solved by implementing a three-shunt current sensing technique that can bounce sampling between current signals selecting two out of three phases each period [104]. Nevertheless, that is not necessary in this specific case, because the phase currents working range in the NanoPla application correspond to a duty cycle between 43.08% and 56.92%, which results in a large enough sampling window.

Additionally, in order to measure the average value, the sample point has to be set when the counter is equal to ZERO, as represented in Figure 3.12b. The ADC are Start of Conversion (SOC) base, thus, the trigger source that starts the conversion can be configured to be “counter (CTR) equal to ZERO”.

In **Euspen 2018**, a current sampling stability analysis was performed and the noise was measured for different current values. The observed noise was similar for all the currents inside the working range, having a Root Mean Square (RMS) deviation equal to ±0.022 A, and the difference between the maximum and minimum recorded value in a sampling was 0.12 A. The deviations from the real value are caused by the current sampling noise. This noise can be reduced by using a filter, like a rolling average, at the cost of memory consumption. In this case of study, a quantity of 32 sampled values is averaged. Applying this filter, the RMS deviation is reduced to ±0.0032 A, and the difference between the maximum and minimum recorded value in a sampling is reduced to 0.02 A.

3.3.2. Implementation of the 2D control strategy in the NanoPla

The dynamic model of a Halbach linear motor working as positioning actuator in a pneumatically levitated linear stage was identified as a servosystem in **Electronics 2018.** In the system, the electromagnetic horizontal force generated around the stable equilibrium position acts as a proportional controller. The closed-loop transfer function that relates the equilibrium position to the final position of the stage was identified with a spring-mass-damper model (second order system). The NanoPla 2D positioning model is expected to present a similar second order transfer function in each axis of motion, since it uses the same actuators and the moving platform is also pneumatically levitated. The transfer function of the system can be obtained experimentally, which enables a better understanding of the system an allows tuning the controllers in advance, thus, it facilitates the task in the experimental setup. Once the 2D control strategy of the NanoPla was defined (**Procedia Manufacturing 2019**), the dynamic characteristics of the positioning system were determined. In addition, after the 2D control system defined in **Procedia Manufacturing 2019** was implemented in the NanoPla and its controllers tuned, the positioning capabilities of the system have been experimentally tested.

In the following, the NanoPla dynamic model is described and experimental results of the NanoPla positioning capabilities are shown and analysed.

<u>NanoPla dynamic model</u>

The moving platform is levitated by three airbearings and two parallel pairs of Halbach linear motors (M1 and M2; M3 and M4) generate the thrust force in X and Y-axes, respectively. The system model in X and Y-axes can be described as an inertia-damping system and the model transfer function in X-axis can be defined as:

$$\frac{X(s)}{F_x(s)} = \frac{1}{ms^2 + bs} \tag{19}$$

Where F_x is the total thrust force in X-axis generated by the two Halbach linear motors (M1 and M2), m is the mass of the moving part and b is the viscous-friction elements of the setup. Additionally, in [59], it was observed that the linear motors themselves produce eddy-current damping along their own axis, but not along their orthogonal axis. This damping effect is also included in b. The force generated by each Halbach motor around the stable equilibrium position (linear zone) can be defined as:

$$F_{M,x}(s) = K_M(X_{eq}(s) - X(s)) \tag{20}$$

where K_M is the slope of the thrust force generated by each Halbach linear motor around the equilibrium position. Considering that, in the system, the stable equilibrium position of the parallel pair of Halbach linear motors M1 and M2 are set at the same X-coordinate, the total force that each motor pair will generate around the stable equilibrium position will be twice the force defined in Equation 20. Thus, the transfer function that relates the final position of the stage X(s) with the defined stable equilibrium position $X_{eq}(s)$ is the following:

$$\frac{X(s)}{X_{eq}(s)} = \frac{\frac{2K_M}{m}}{s^2 + \frac{b}{m}s + \frac{2K_M}{m}} \tag{21}$$

Where m is the mass of the moving part and b comprehends the viscous-friction elements of the setup and the eddy-current damping of the motors. Additionally, $2K_M$ is the slope of the total thrust force generated by the pair of Halbach linear motors around the equilibrium position in X-axis. The forces along X-axis generated by the parallel motor pair M1 and M2 at the initial position have been represented in Figure 3.13a. The linear zone and the slope around the stable equilibrium position have also been represented in the Figure. Since the actuators distribution in the moving platform is symmetrical, the same equations are valid for Y-axis. The mass of the moving platform is known (13.25 kg) and the value of K_M depends on the maximum value of the electromagnetic force defined by the phase currents. This maximum value can be defined by varying the amplitude of the sinusoidal distribution of the force along the axis of motion, since the spatial period is defined by design (Figure 3.13a). Therefore, K_M and m are known, whereas b must be obtained experimentally.

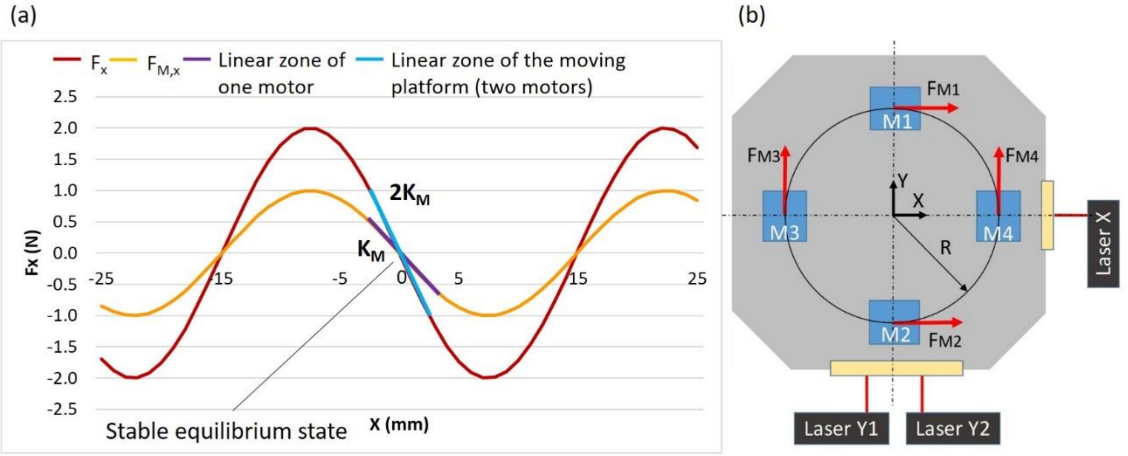

Figure 3.13. (***a***) *Generated forces by one and two motors along the X-axis of movement;* (***b***) *Scheme of the forces generation in the moving platform.*

On the other hand, rotation around Z-axis (θ_z) is generated by the torque acting on the central point of the moving platform. The torque (T_z) is the sum of the torques generated by each motor in the plane of motion (Figure 3.13b, where R is the distance from the motors to the moving platform central point, that is 169.9 mm). In **Procedia Manufacturing 2019**, it was defined that the control strategy distributes the torque generation symmetrically between the four motors and its target is to maintain the rotation around Z-axis null. As it was mentioned in **Sensors 2017**, the 2D plane mirror laser interferometer system restricts the rotation of the moving platform to a maximum of $\pm 1.2 \times 10^{-4}$ rad to prevent the misalignment between laser beam and plane mirror. Therefore, to rotate the moving platform an angle $\Delta\theta_z$, each motor would have to perform a displacement of the same magnitude, equal to $\Delta\theta_z \cdot R$, in the direction that favours that rotation. According to this, the torque generated by the four motors of the NanoPla to perform a rotation of $\Delta\theta_z$, can be calculated as follows:

$$T_z = 4K_m R^2 \Delta\theta_z \tag{22}$$

It is worth mentioning that the angular position θ_z is considered to be a stable equilibrium angular position when, at that angular position, the platform remains still and after a disturbance, it comes back to the same angular position. This stable equilibrium position is created when the moving platform is perfectly aligned in X and Y-axes, that is, $\theta_{z,eq}= 0$. Thus, as in the previous case, the transfer function that relates the final angular position of the stage $\theta_z(s)$ with the defined stable equilibrium angular position $\theta_{z,eq}(s)$ is defined by Equation 23, where b_θ is the viscous-friction element of the platform.

$$\frac{\theta_z(s)}{\theta_{z,eq}(s)} = \frac{\frac{4K_m R^2}{I_z}}{s^2 + \frac{b_\theta}{I_z}s + \frac{4K_m R^2}{I_z}} \tag{23}$$

The procedure for experimentally obtaining the transfer function in a linear stage was defined in **Electronics 2018**. This procedure has been adapted to the NanoPla, where a parallel pair (M1 and M2) generates the thrust force in X-axis, whereas the other parallel pair (M3 and M4) generates the force in Y-axis (Figure 3.13b). Firstly, the initial position is defined by implementing the electromagnetic sensorless controller (**Micromachines 2018**) in each motor of the NanoPla. Each parallel pair is set to have as stable equilibrium position the centre of the NanoPla working range in X and Y-axes (X_{ref}=0, Y_{ref}=0, $\theta_{z,ref}$=0). In order to obtain the transfer function in X-axis, the motor pair aligned in Y-axis are set to remain still at the stable equilibrium position in Y-axis (Y_{ref}=0, $\theta_{z,ref}$=0), acting as a guiding system that prevents the movement of the moving platform in Y-axis and its rotation around Z-axis. Then, the stable equilibrium in X-axis is displaced 1 mm inside the linear zone by using the electromagnetic controller defined in **Micromachines 2018**. The resultant movement of the moving platform is recorded by the laser system, and then, the spring-mass-damper model of Equation 21 is fit to the response. The same procedure is followed to obtained the transfer function in Y-axis. In Figure 3.14, the experimentally obtained 1-mm step response of the stage in X and Y-axes (X_s and Y_s) has been represented. The simulated response of the adjusted model is also shown (X_{sim} and Y_{sim}). The obtained values for m and K_m match the actual mass of the moving platform and the slope of the thrust force around the stable equilibrium position, respectively. The viscous-friction elements (b) have a value of 56.8 N·s/m in X-axis and of 63.07 N·s/m in Y-axis. The difference between axes can be due to the geometrical errors in the assembly and the fact that the moving platform is not perfectly symmetrical due to the presence of the plane mirrors, which are larger for Y-axis.

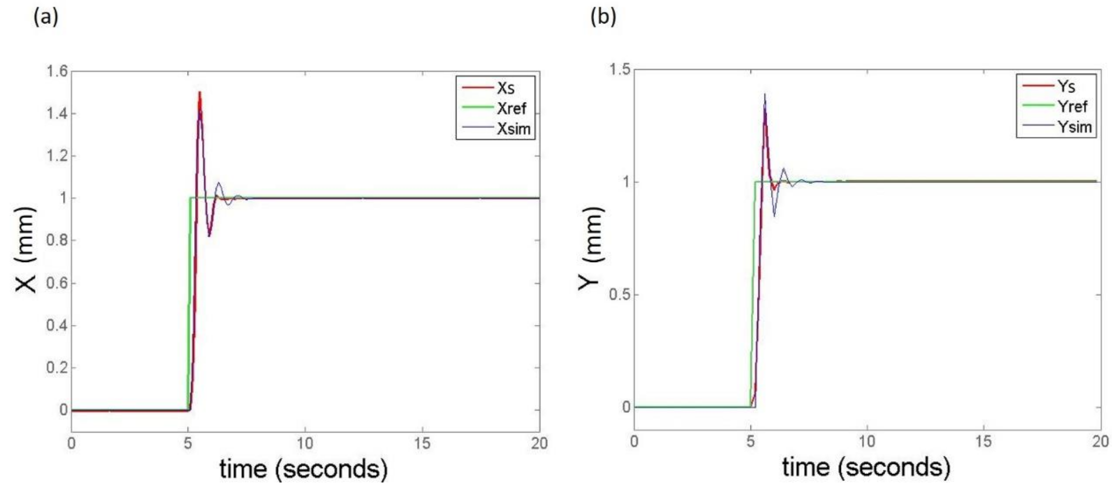

***Figure 3.14**. (**a**) 1-mm step response in X-axis of the stage in open loop and the simulation of the plant; (**b**) 1-mm step response in Y-axis of the stage in open loop and the of the simulation of the plant.*

In order to obtain the transfer function for the rotation around Z-axis, the four motors are set to displace from an initial position to the stable equilibrium position $\theta_{z,eq}= 0$. At this initial position the angular deviation is not null. In order to define the initial position, the four motors are displaced a distance $\Delta\theta_z \cdot R$, equal to 15 µm. In each motor pair, each motor displaces in an opposite direction to contribute to the rotation around the central point of the stage, generating an angular deviation of 8.83×10^{-5} rad, that is close to the maximum displacement allowed without losing the laser system alignment. The experimentally obtained values for I_z and K_m approximately match the actual inertia of the moving platform and the slope of the thrust force around the stable equilibrium position, respectively. Nevertheless, due to the limited range of the angular deviation and the short response time, the recorded response is not smooth enough to perfectly match the simulated plant. Figure 3.15 represents the experimentally obtained 8.83×10^{-5} rad step response of the stage around Z-axis (θ_s). The simulated response of the adjusted model is also shown (θ_{sim}).

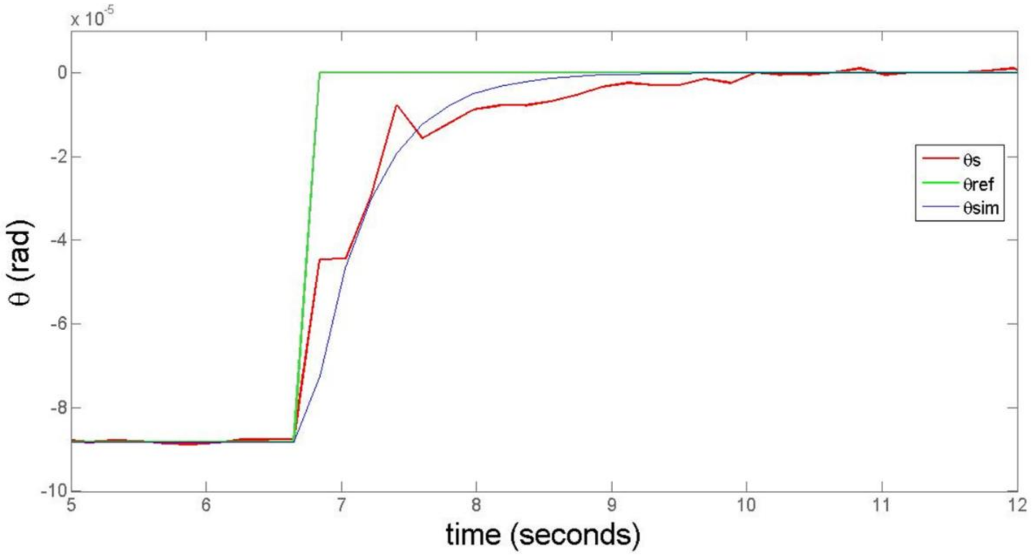

***Figure 3.15.** 8.83×10^{-5} rad step response around Z-axis of the stage in open loop and the simulation of the plant.*

In [59], control of out-of-plane motion was proven to be unnecessary due to the high stiffness of the airbearings. Similarly, in the NanoPla, the moving platform is levitated by three airbearings with an input pressure of 0.41MPa and an input vacuum of 15 mmHg, as recommended by the manufacturer. At this working conditions, the airbearings have a stiffness of 13 N/µm. As calculated in **Micromachines 2018,** the variation of the vertical force during motion has a maximum increment of 7%, which results in negligible vibrations of the moving platform. Therefore, control of out-of-plane motion is also unnecessary, although it will be monitored by three capacitive sensors.

Experimental analysis of the NanoPla positioning control system

After the implementation of the positioning control system and once the controllers have been tuned, the NanoPla position capabilities have been tested in the XY-plane. The NanoPla positioning control system initial requirement was to obtain a minimum incremental motion of 10 µm. However, as stated in **Procedia Manufacturing 2019**, the developed positioning control system is able to achieve a much lower positioning uncertainty (±0.5 µm). In this subsection, several experimental results are presented to demonstrate the capabilities of the system.

Stability of the system

For the positioning uncertainty presented in **Procedia Manufacturing 2019**, the root mean square (RMS) deviation positioning error was calculated to be 0.11 µm, that is the short-term stability (30 seconds) of the system. In this subsection, the stability of the positioning control system is examined for a longer period of time. The moving platform was set to remain still at the initial position during 30 minutes and it was experimentally verified that the position deviations are confined in ±1 µm. In Figure 3.16, a period of 400 seconds of this test is shown, the RMS deviation during this time is 0.28 µm. The results in Y-axis are similar, since the moving platform is symmetrical. During this period of time, the force generated by each linear motor variated between ±2 mN, that is, the system was working around the stable equilibrium position, as expected.

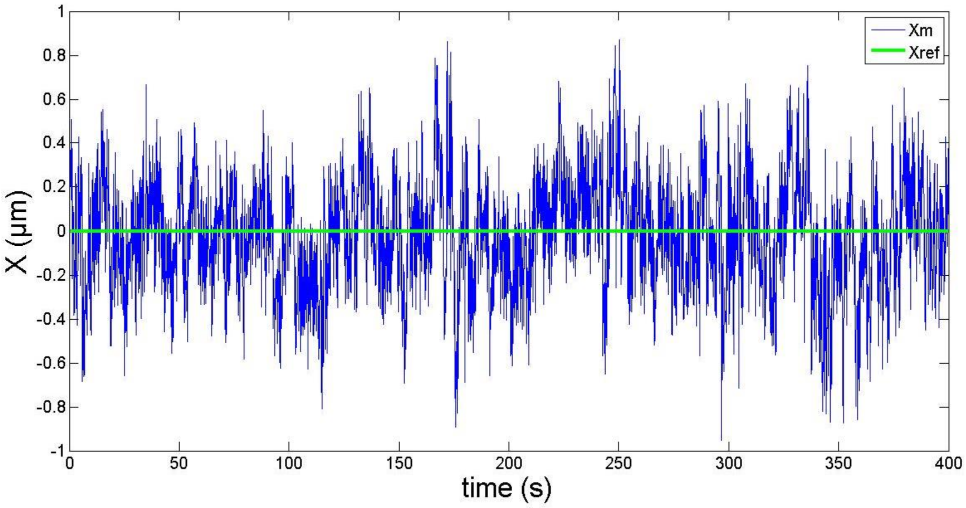

Figure 3.16. *Long term stability analysis of the developed positioning control system.*

In **Sensors 2017**, it was mentioned that the laser system manufacturer defined an alignment tolerance between laser beam and the normal vector of the plane mirror of ±25 arc s (±1.2 × 10^{-4} rad). During the experiments, the noise in each motor showed a peak to peak value of ±1 µm, that corresponds to an angular variation smaller than ±6 × 10^{-6} rad. For the laser system to lose the alignment the peak to peak noise in each motor should be ±20 µm. It has been experimentally verified that the positioning noise of the NanoPla at the motors does not reach this value.

In brief, the requirement of developing a 2D positioning control system capable of achieving a positioning error smaller than 10 µm has been achieved and surpassed. In future applications, when the AFM is integrated in the NanoPla, in working conditions, the moving platform would be set to move in a trajectory and stop at defined positions. Then, the moving platform would remain static while the AFM performs the scanning task and the piezostage is in charge of the fine positioning. Therefore, the moving platform would be required to maintain its position while the airbearings are shutting down, with a deviation smaller than 10 µm, so that the piezostage can correct it. It has been experimentally verified that when the airbearings are turned off, the final position of the stage does not deviate more than 3 µm from the target position, thus, the requirement is fulfilled.

Step responses

10-µm step responses were taken in the X- and Y-directions. At the same time, the perturbation to the other axis was also recorded, as shown in Figure 3.17. The settling time is less than 15 s, without steady-state error in X and Y-axes. The perturbed motions in the other axis demonstrate that there is a dynamic coupling between axes. This is unavoidable because there is only one moving part that is affected by the vibrations of the four motors. This perturbation generates a displacement in Y-axis of a maximum of 2 µm, which is considered acceptable. In addition, it has been observed that during the transient response, the maximum angular deviation is 1.5 × 10^{-5} rad, which is inside the tolerance of ±1.2 × 10^{-4} rad required for the laser system to read.

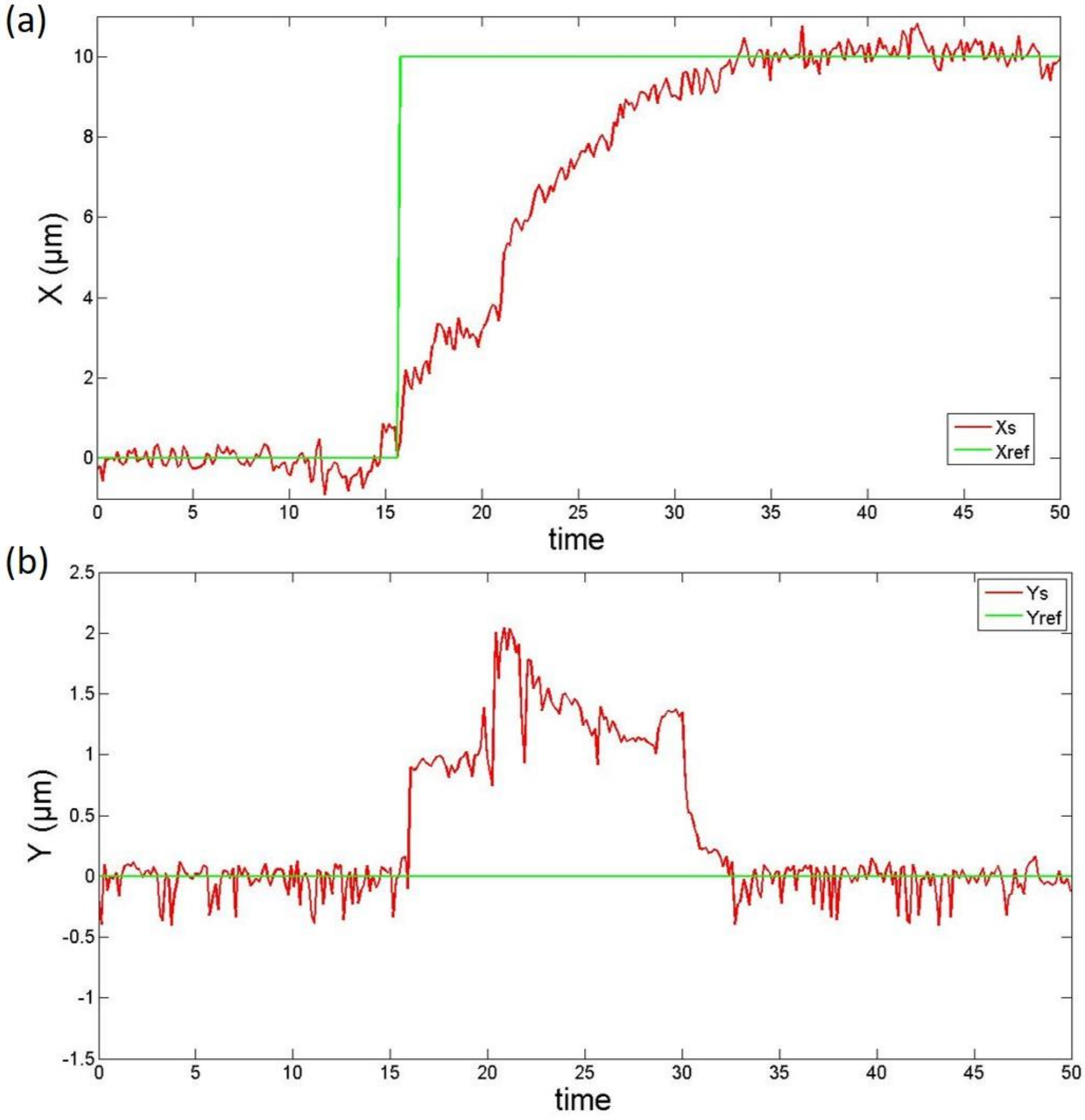

Figure 3.17. *10-µm step response in X-axis (**a**) and perturbation in Y-axis (**b**).*

Similarly, 100-µm step responses were taken in the X- and Y-directions while the perturbation to the other axis was also recorded, as shown in Figure 3.18. The settling time is less than 40 s, without steady-state error in X and Y-axes. As in the previous case, the displacement in one axis generates perturbations in the other axis. Nevertheless, this perturbation generates a displacement in Y-axis of a maximum of 7 µm, which is considered acceptable for a 100-µm step. In addition, it has been observed that during the transient response, the maximum angular deviation is 7.3 × 10^{-5} rad, which is inside the tolerance of ±1.2 × 10^{-4} rad required for the laser system to read.

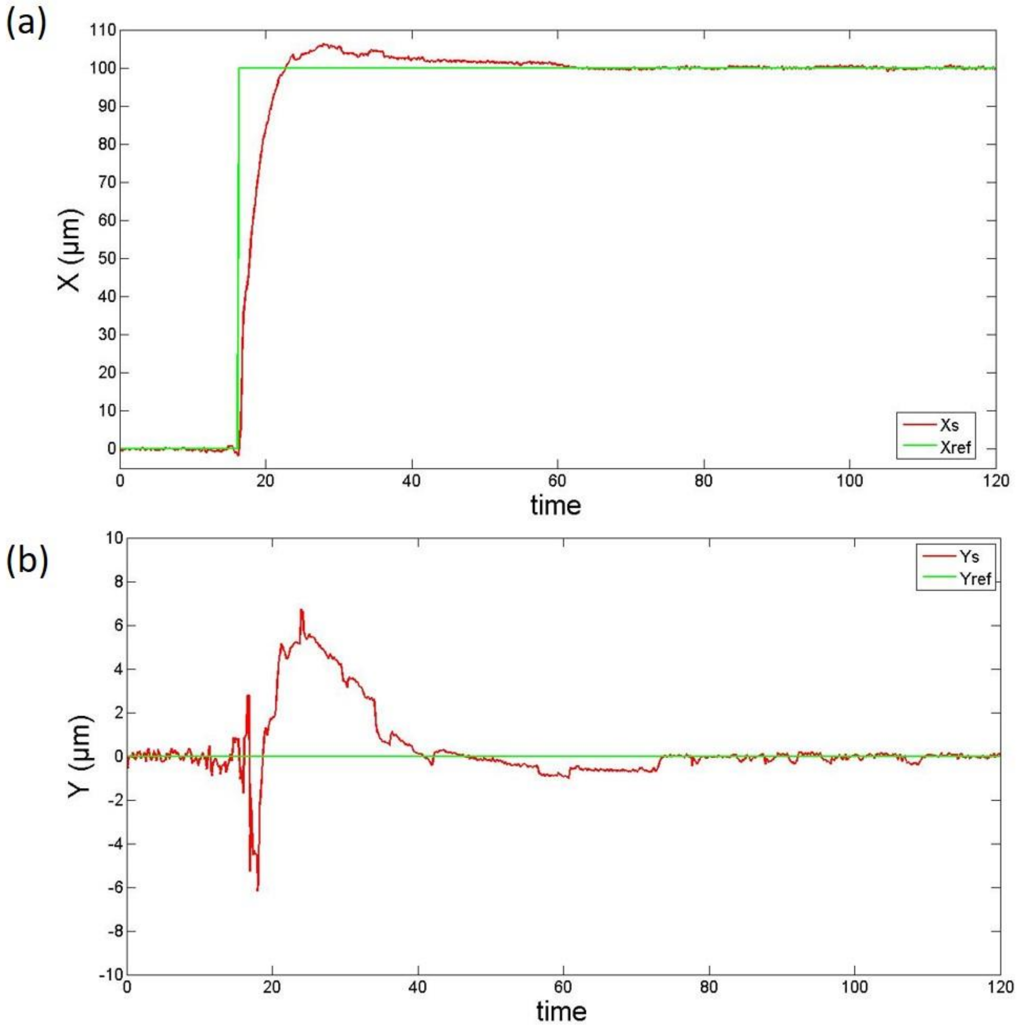

Figure 3.18. *100-µm step response in X-axis (**a**) and perturbation in Y-axis (**b**).*

It should be taken into account that the transient response can be adjusted depending on the requirements of the application by changing the parameters of the PID controller. In future works, the control strategy could be improved to minimise the coupling between axes during the movement.

Planar scanning motion

Planar scanning motion is a typical motion used in precision engineering such as nanomanufacturing and metrological characterisation. Several experimental results are presented to demonstrate the scanning capability of the developed positioning control system. Figure 3.19a shows a displacement in X-axis of the moving platform from the centre to one extreme of the working range, at constant speed. Similarly, Figure 3.19b shows a 1-mm forward and backward displacement in Y-axis.

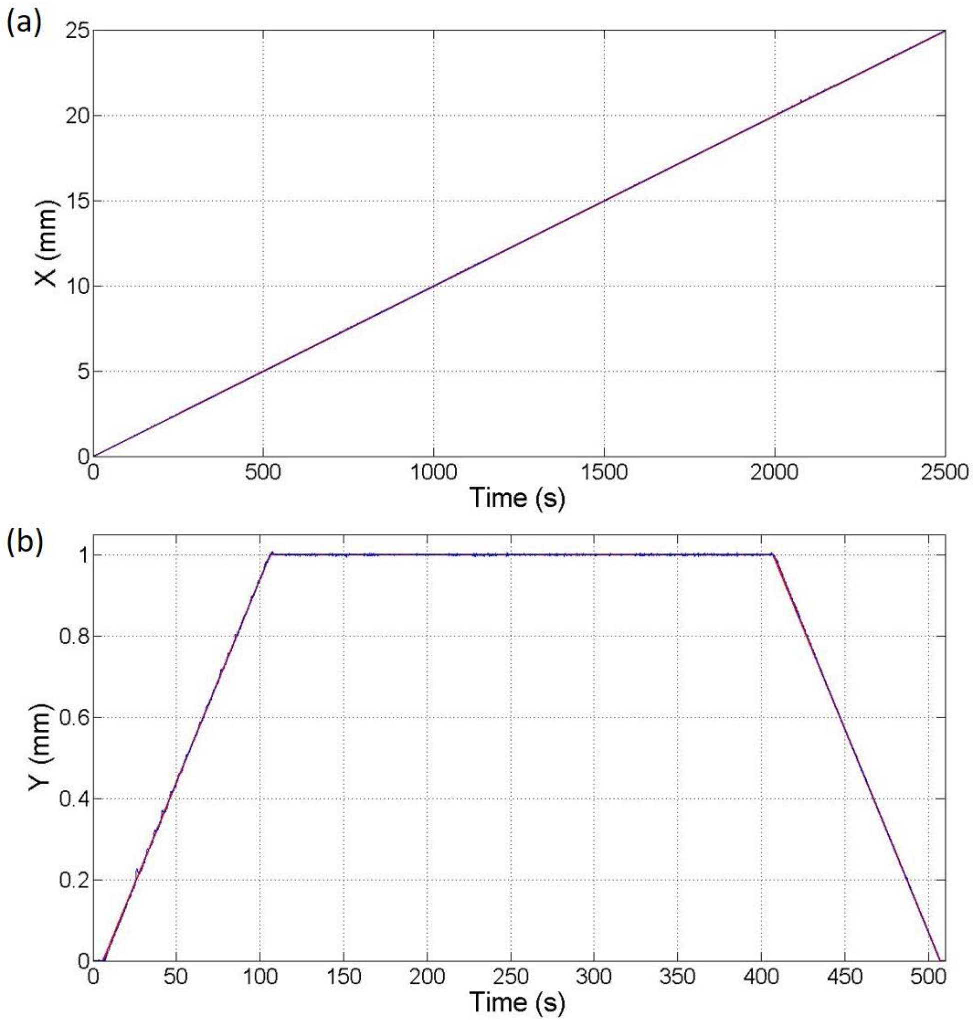

Figure 3.19. *(**a**) 25-mm displacement at constant speed in X-axis; (**b**) 1-mm forward and backward displacement at constant speed in Y-axis.*

In addition, it has been verified that the platform can perform simultaneous movement in X and Y-axes without losing the alignment between laser beam and plane mirrors. Figure 3.20 represents a circular motion performed simultaneously in X and Y-axes.

The target of this thesis was to develop a positioning system able to accurately position the moving platform along the whole working range. Nevertheless, the dynamic control of the motion of the moving platform while performing a trajectory is out of the scope of this work. In future works, in order to improve the dynamic performance of the moving platform, passive damping could be added to the in-plane motion (X, Y, and θ_z), by permanent-magnet eddy-current dampers.

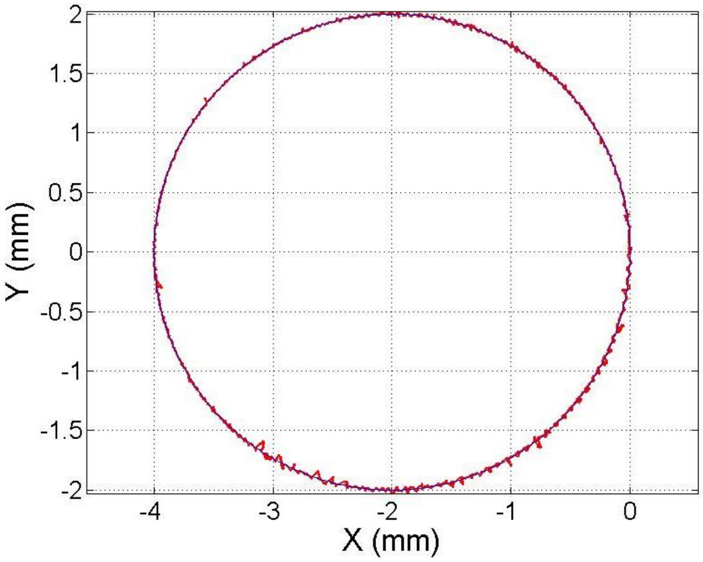

Figure 3.20. *Circular motion performed simultaneously in X and Y-axes.*

3.3.3.Trajectory definition of the NanoPla with high relative accuracy (HRA)

The NanoPla has been designed to work together with different kinds of tools and probes in various applications such as metrology or nanomanufacturing. In some nanomanufacturing applications, the NanoPla may be required to follow a predefined trajectory with a submicrometre precision. When working at submicrometre scale, errors in the definition of the trajectory can be a great contributor to the final positioning error of the NanoPla.

The definition of a trajectory in traditional manufacturing systems, like machine-tools, proceeds as follows: first the geometry is defined in a CAD program, then, this geometry is exported to a CAM program, where the machine and the toolpath generation conditions are defined. However, simpler geometries can be directly design in the CAM program. In addition, some applications include CAM and CAD functions in the same software. Finally, by means of a post-processor, the specific numerical control (NC) program is created [105]. Nevertheless, creating a complex curve in a CAD/CAM system is not always straight forward [106, 107, 108]. In CAD/CAM systems, complex curve trajectories are usually defined by curve fitting, having as input a set of points belonging to the nominal curve trajectory. The resultant fitting curve produces an equation that can compute points anywhere along the trajectory. This equation is determined by a set of control points together with the fitting method basis. However, trajectory definition by curve fitting in CAD/CAM systems results in fitting errors that, even though in traditional manufacturing systems are negligible, in nanopositioning stages like the NanoPla, can be of the same order or greater than the positioning control system error.

Other works focus on optimising the trajectory generation for a smooth interpolating motion in order to respect the machine kinematic feed rate and acceleration limits and to avoid fluctuation due to the discontinuity in the first derivatives along the tool path [109]. Spline-type interpolation is applied in high-speed machining to limit the discontinuities of speed while respecting the contour tolerance [110, 111]. The target of these works is to achieve a confined error and minimal machining time, this task becomes harder for more accurate tolerances. In the NanoPla application, speed and acceleration control is not as critical as accurately performing a predefined trajectory. Therefore, an accurate curve fitting method capable of offering high accuracy in the position definition along the whole trajectory is required.

The trajectory definition errors in CAD systems and their effect in the final positioning error of the NanoPla was the subject of a collaborative project with a research group of the Department of Applied Mathematics at the University of Zaragoza that is focused on Computer Aided and Geometrical Design (CAGD). This research group has developed a novel method for accurate curve fitting with shape preserving representations allowing high relative accuracy (HRA) in the computations. The proposed method, which will be called HRA method, is based on recent advances in Numerical Linear Algebra (see [112] and the references therein). The HRA method considerably improves the precision in curve fitting and, thus, minimises the contribution of the trajectory fitting errors in the total positioning uncertainty of a nanopositioning stage, like the NanoPla. The obtained fitting trajectories have continuous successive derivatives that can also be efficiently evaluated. In this subsection, the contribution of the novel HRA method fitting errors to the final positioning error of the NanoPla is compared with the contribution of the fitting errors obtained by traditional CAD/CAM systems, considering also the required computational efficiency due to the complexity of the resultant curve. For the comparison of this work, curve fitting is performed either by interpolation or by least squares approximation. The HRA method has been developed taking into account both problems. The relevance of the resultant fitting errors of each method has been experimentally analysed in the NanoPla.

Analysis procedure

This work analyses the errors in the definition of a trajectory that is determined by fitting a set of given data points $\{p_1, \ldots, p_{l+1}\}$. These given data points belong to a curve that was chosen to be a parametric curve so that the resultant trajectory can be compared to the nominal values of the curve. The selected parametric curve is a cycloid where the components x(t), y(t) take the form:

$$\begin{Bmatrix} x(t) = r(t - \sin t) \\ y(t) = r(1 - \cos t) \end{Bmatrix} \tag{19}$$

Cycloids are a commonly used geometry in manufacturing application (e.g. gear tooth geometry). The cycloid is a transcendental curve and, thus, it cannot be expressed by polynomials exactly. For this reason, cycloids cannot be incorporated into most commercial CAD systems [113]. Therefore, they are defined by curve fitting, that can be performed either by interpolation or least squares approximation.

Interpolation is a fundamental concept of CAGD. Given a basis $(u_0, \ldots, u_n)$ of functions defined on $t \in I$ and a set of data points $\{p_1, \ldots, p_{l+1}\}$, corresponding to parameters $\{t_1, \ldots, t_{l+1}\}$, it finds a curve $\gamma(t) := \sum_{i=0}^{n} P_{i+1} u_i(t)$, $t \in I$, that passes through the give data points, that is $\gamma(t_i) = p_i$ (see Figure 3.21).

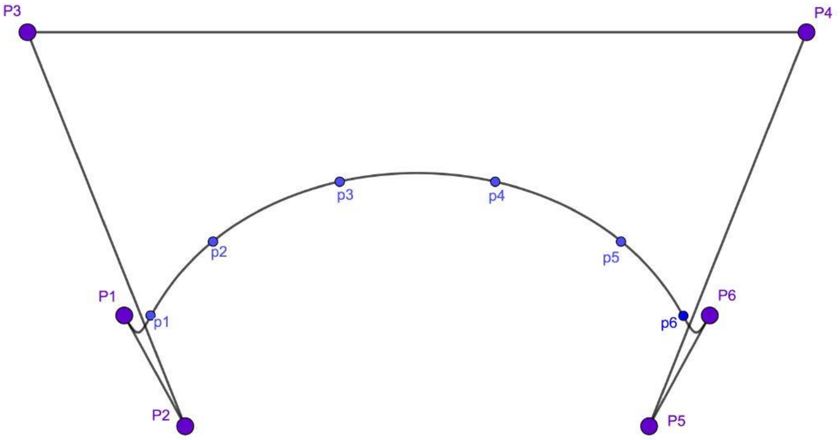

Figure 3.21. *Curve fitting by interpolation where* p_1, p_2, p_3, p_4, p_5, p_6 *are the given data and* P_1, P_2, P_3, P_4, P_5, P_6 *are the control points.*

It is worth noting that the number of control points $\{P_1, \ldots, P_{n+1}\}$ necessary to define the curve is equal to the number of interpolated data points (l=n). A better approximation to the curve to be fitted would be expected to be obtained by increasing the number of given data points. Nevertheless, increasing the number of data points increases the number of control points and, thus, the complexity of the curve and computations.

An approximating curve is a curve estimate that approximately fits the given data points, but does not necessarily includes them. The most common technique for finding such curves is known as least squares approximation. It should be noted that, in approximation the number of control points that define the approximate curve are fewer than the number of given data points ($l>n$). Therefore, when fitting the same set of given data points $\{p_1, \ldots, p_{l+1}\}$, an approximating curve requires less computational cost than an interpolating curve (see Figure 3.22).

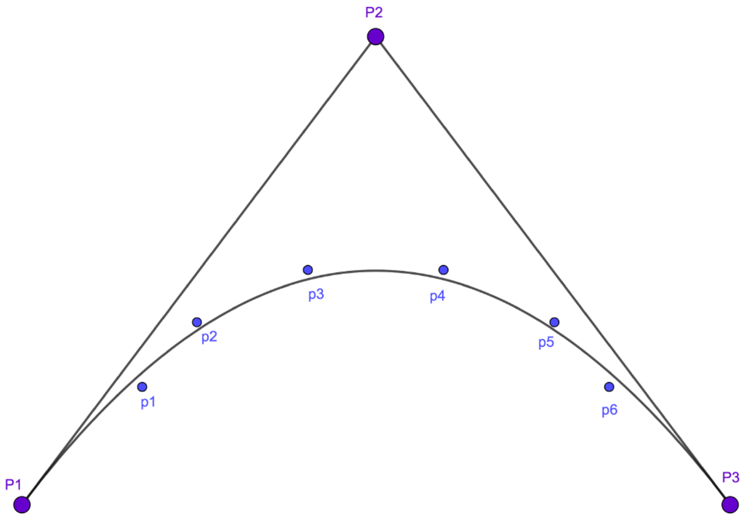

Figure 3.22. *Curve fitting by least squares approximation where* p_1, p_2, p_3, p_4, p_5, p_6 *are the given data and* P_1, P_2, P_3, *are the control points.*

Therefore, a trajectory has been defined by curve fitting a determined set of data points, $\{p_1, \ldots, p_{l+1}\}$, belonging to a cycloid of radius 1 mm, obtained for equidistant parameters of the interval $t \epsilon (0, 2\pi)$. Curve fitting has been performed by interpolation and least squares approximation using two different methods: the HRA method and commonly used commercial CAD/CAM software. The resultant curve obtained by linear interpolation, the most commonly used interpolation method in Numerical Control (NC), has also been included in the comparison. In addition, the number of control points required for the curve construction in each case is analysed due to its relation to the final complexity of the curve. Finally, the relevance of the curve fitting errors in the total positioning error of the NanoPla is experimentally studied. Figure 3.23 represents a diagram of the procedure that has been followed in this work.

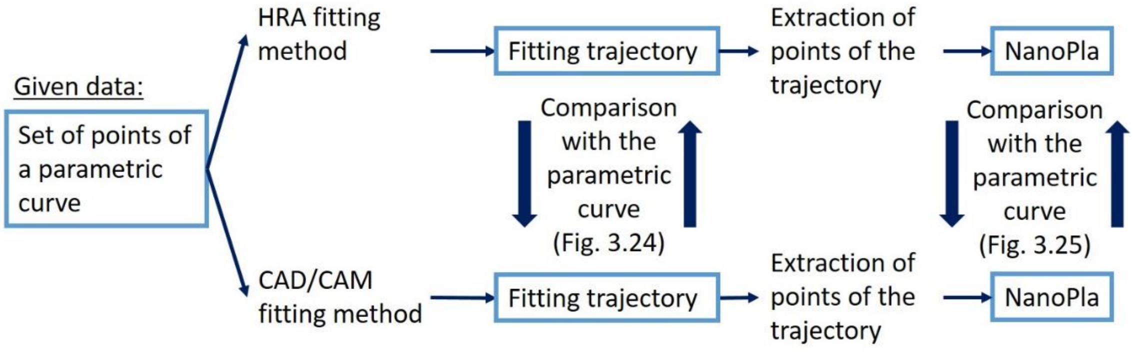

Figure 3.23. *Diagram of the procedure for the analysis of the curve fitting methods.*

Curve fitting

The NanoPla control system resultant positioning uncertainty in the XY-plane, U_{XY} (k = 2), was calculated to be 0.50 µm in all the working range of 50 mm × 50 mm (**Procedia Manufacturing 2019**). The error introduced by the definition of the NanoPla trajectory should not significantly increase the final positioning error. Thus, the trajectory definition error is required to be 0.05 µm or lower. A trajectory definition error of this magnitude would increase the final positioning error by less than 0.01 µm, which is considered acceptable for the NanoPla requirements.

Therefore, curve fitting has been performed by interpolation or least squares approximation, using the HRA method and CAD/CAM systems. The requirement has been to obtain a fitting error lower than 0.05 µm along the whole trajectory and without compromising the final complexity of the curve.

Curve fitting by interpolation

As previously noted, the problem of interpolation is to find a curve that passes through l + 1 data points $\{p_1, \ldots, p_{l+1}\}$. For this reason, when interpolating through a set of points using an exact method, the interpolation errors at these points are zero. Nevertheless, at non-data intervals (data between interpolation points), the interpolation errors can be calculated as the difference between the nominal parametric curve and the interpolated curve, when the equation of the nominal curve is known. In addition, in an interpolation problem, the number of control points (n+1) equals the number of given data points. For the comparison, the trajectory curve was generated by three exact interpolation methods: linear interpolation, CAD/CAM systems interpolation and the HRA method. The interpolation results of some commonly used CAD and CAM systems have been compared, and, even though their results slightly differ, the errors have similar magnitude, thus, the difference is not significant. Therefore, the results of a CAM software have been used as reference in this subsection. On the other hand, the interpolation with HRA method has been performed using two different fg-Bernstein bases. One of them is a polynomial basis, HRA interpolation with this basis will be called HRA IB1, and the other one is a trigonometric basis, HRA interpolation with this basis will be called HRA IB2.

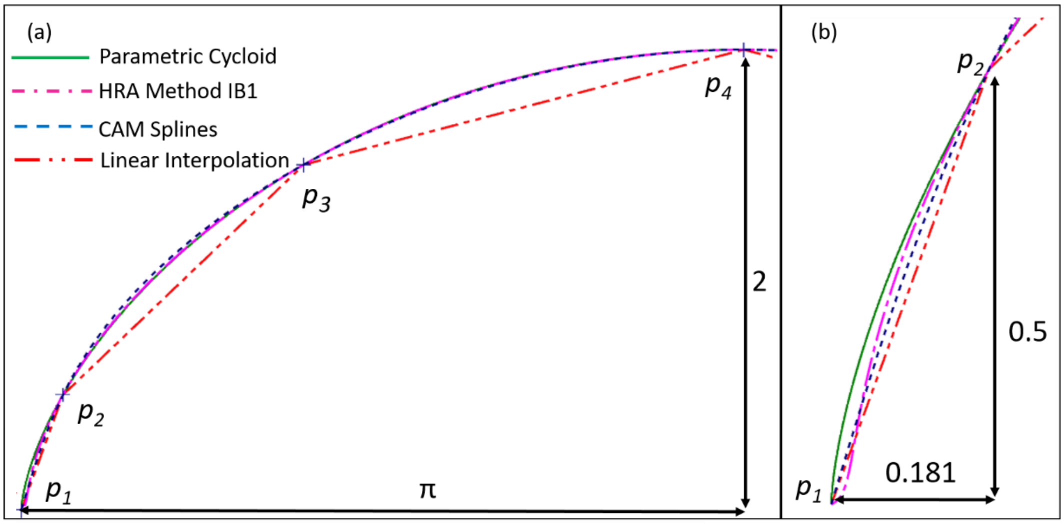

Figure 3.24. *(**a**) Resultant interpolated curves obtained for n+1=7, represented for tϵ (0, π); (**b**) Resultant interpolated curves obtained for n + 1 = 7, in the first non-data interval.*

Figure 3.24a shows the resultant curves for the three interpolation methods for n+1=7, that is, seven interpolation points and seven control points. For simplification and due to symmetry, only half of the curves have been represented. As it can be seen, the greatest interpolation errors occur when applying linear interpolation. With this method, the maximum interpolation errors appear at the middle zone of the intervals whose interpolating points are further from each other (interval between p_3 and p_4). Nevertheless, when applying CAM/CAD system splines interpolation and the HRA method, the interpolation errors are reduced. In both cases, the maximum interpolation errors appear at the middle zone of the first intervals. The first non-data interval has been represented in Figure 3.24b.

Table 3.2. Maximum interpolating errors for a curve generated based on a set of n+1 interpolation points, at the first and second non-data intervals, for different interpolation methods.

Data points	**Intervals**	**Linear**	**CAM**	**HRA IB1**	**HRA IB2**
n+1 = 7	(0,2π/6)	27.6 µm	18.0 µm	20.17 µm	17.85 µm
	(2π/6, 4π/6)	93.5 µm	17.1 µm	5.31 µm	5.60 µm
n+1 = 9	(0, 2π/8)	11.8 µm	8.0 µm	1.25 µm	3.95 µm
	(2π/8, 4π/8)	41.9 µm	8.5 µm	0.22 µm	0.93 µm
n+1 = 11	(0, 2π/10)	6.1 µm	4.0 µm	0.05 µm	0.94 µm
	(2π/10, 4π/10)	22.0 µm	4.5 µm	< 0.01 µm	0.18 µm
n+1 = 21	(0, 2π/20)	0.7 µm	0.5 µm	<< 1 nm	< 0.01 µm
	(2π/20, 4π/20)	2.8 µm	0.6 µm	<< 1 nm	<< 1 nm

CAD and CAM systems splines bases are usually unknown for the users. In other works [114], the interpolation algorithm had to be experimentally extracted to simulate the interpolation errors. In this work, the interpolation errors were calculated graphically in the CAM program. However, the interpolation errors of the other two methods were calculated analytically. In both cases, the errors of the interpolated curve from the cycloidal nominal have been obtained by computing the distance at equally distributed points along the profile curve. In Table 3.2, the errors of the interpolated curves for the number of points interpolated n + 1 = 7, 9, 11 and 21 were represented for the first and second non-data intervals, where they are greater for CAM system spline interpolation and the HRA method. As it can be seen, linear interpolation presents always the worst results. In addition, for the same number n + 1 of interpolation points, the HRA method presents a considerably smaller error than CAM system splines. When interpolating with the HRA method IB1 a number of interpolation points higher than 11, the resultant errors became negligible for the NanoPla application (< 0.05 µm) whereas in the HRA method IB2, 16 interpolation points are required. In contrast, it has been verified that more than 49 interpolation points are necessary to achieve an error lower than 0.05 µm at the non-data intervals, when interpolating with CAM/CAD system splines, and more than 250 interpolation points, when applying linear interpolation. Therefore, it can be inferred that the HRA method is capable of achieving accurate curve fitting by interpolating a smaller number of data points, in comparison with commonly used CAD/CAM systems.

Least squares approximation

Least squares approximation is not an exact method, that is, the resultant fitting curve does not necessarily contain the given data points, but approximately fits them. In an approximation problem, the number of control points can be externally defined and it is directly related to the fitting errors. As previously noted, the number of control points defines the complexity of the fitting curve. Typically, a greater number of control points results in a more complex curve but in smaller fitting errors. Nevertheless, control points can be redundant or inadequate. Redundant control points unnecessarily increase the computational complexity without decreasing the fitting errors. Whereas, inadequate control points increase the fitting errors and, thus, the curve fails to satisfy the precision requirements [111].

In an approximation problem, the fitting tolerance is defined as the maximum permitted error between the given data points and the resultant approximation curve. Nevertheless, the error between the approximation curve and the nominal curve can be greater at non-data intervals. For this reason, the number of points included in the set has to be large enough so that the fitting error does not increase significantly at the non-data intervals.

For the comparison, the trajectory curve was generated by two least squares approximation methods: CAD/CAM systems approximation and the HRA method. In CAD/CAM systems, when curve fitting by approximation, a tolerance for the fitting error must be defined by the designer. The smaller this tolerance is; the greater number of control points the approximation curve requires. Similar to the interpolation operation, the approximation operation has been performed in some of the most commonly used CAM/CAD systems and the results have been compared. Even though the obtained results are similar, some programs present to the user more information about the approximation function than others. For example, in some programs the approximation spline degree can be selected, they graphically show where in the curve the maximum fitting error occurs and they calculate its magnitude and the magnitude of the average fitting error along the whole curve. In this section, the results of a CAD software that calculates the maximum fitting error (confined error) and graphically shows its location has been used as reference. On the other hand, the least squares approximation with HRA method has been performed using two different fg-Bernstein bases, as in the interpolation operation. The first basis is polynomial, HRA least squares approximation with this basis will be called HRA LSB1, and the other one is a trigonometric basis, HRA least squares approximation with this second basis will be called HRA LSB2.

According to the positioning accuracy of the NanoPla, the fitting tolerance was set to be smaller than 0.05 µm for the approximation operation in every case. Table 3.3 represents the number of control points that are required to generate a fitting curve from a given set of data points, {p_1, …, p_{l+1}}, by least squares approximation with the reference CAD method and the HRA method. The resultant confined error (Ce) obtained for every method has been also represented in the Table 3.3. In the case of the CAD method, the confined error was calculated and provided by the software. For the HRA method, the confined error was analytically calculated by computing the maximum distance at equally distributed points along the profile curve. In addition, the results of the HRA method are shown for the two different bases (HRA LSB1 and HRA LSB2).

Table 3.3. Number of control points and maximum fitting errors (Ce) for a curve generated based on a set of l+1 given data points, using different least squares approximation methods.

Data points:	**CAM**		**HRA LSB1**		**HRA LSB2**	
	Control points	Ce	Control points	Ce	Control points	Ce
l+1 = 51	n+1=21	0.045 µm	n+1=10	0.004 µm	n+1=12	0.046 µm
l+1 = 101	n+1=38	0.006 µm	n+1=11	0.008 µm	n+1=13	0.037 µm
l+1 = 251	n+1=44	0.023 µm	n+1=11	0.013 µm	n+1=14	0.017 µm
l+1 = 501	n+1=34	0.046 µm	n+1=11	0.015 µm	n+1=14	0.021 µm
l+1 = 1001	n+1=38	0.036 µm	n+1=11	0.016 µm	n+1=14	0.023 µm

It can be observed that, in every case, for the same set of given data points, the HRA method is capable of obtaining an approximation curve within the tolerance of 0.05 µm with less control points than the CAD method, i.e. the HRA method requires less computational complexity. In addition, it is worth noting that, when the number of given data point increases, the number of control points required to fulfil the tolerance constraint is practically constant, in contrast to the CAD method. Thus, it can be inferred that the HRA method provides a better approximation requiring less number of data points and that it does not define redundant control points.

Experimental results

The NanoPla is required to displace to positions along a defined trajectory with the minimum positioning error. As it was assessed in **Procedia Manufacturing 2019**, the positioning uncertainty U_{XY}(k = 2) of the NanoPla is 0.50 µm. Therefore, the errors at defining the trajectory lower than 0.05 µm will be negligible. This work experimentally analyses the contribution of the trajectory definition errors in the final positioning error of the NanoPla. For this, the NanoPla trajectory is defined by interpolating a set of points using CAM/CAD system methods and the HRA method. Then, the position of the NanoPla at certain points of the trajectory defined by both methods is compared to the nominal curve position.

Previously, it was stated that the interpolating errors when calculating a cycloid (r=1 mm) based on 11 points, were lower than 0.05 µm when using the HRA method. Nevertheless, the errors were up to 4.5 µm, when interpolating with CAM system splines. In this experiment, the trajectory of the NanoPla was defined by the curves resulting from interpolating 11 points of a parametric cycloid (r=1 mm), separated by equal intervals of t ($\Delta t = 2\pi/10$ rad). The interpolation was performed by CAM system splines and by the HRA method, in order to verify the interpolating errors effect when implementing the trajectories in the NanoPla. Then, the NanoPla was set to maintain still (with the airbearings still on) in certain positions of the trajectories. The resultant XY positions of the NanoPla were experimentally recorded for 30 seconds, having one readout every 0.12 seconds. In Figure 3.25a, the experimentally recorded positions of the platform have been represented when the control system inputs are the coordinates of points belonging to the trajectory of the first non-data interval of the curve defined by the HRA method (p_{1HRA} and p_{2HRA}) and by CAM system splines (p_{1CAM} and p_{2CAM}). In Figure 3.25, the parametric curve of the cycloid has also been represented. The interpolating errors for p_{1HRA} and p_{2HRA} are 0.04 µm and 0.03 µm, respectively and, as it can be seen in Figure 3.25a, they are negligible in comparison to the NanoPla positioning uncertainty. On the contrary, the interpolating errors of p_{1CAM} and p_{2CAM} are 3.1 µm and 3.8 µm, respectively, and they have a significant effect in the total positioning error of the NanoPla, being the greatest contributor. Similarly, in Figure 3.25b, the position of the platform has been represented, when the control system inputs are points of the trajectory of the second non-data interval of the curves defined by the HRA method (p_{3HRA} and p_{4HRA}) and by CAM system splines (p_{3CAM} and p_{4CAM}). The interpolating error for p_{3HRA} and p_{4HRA} is 0.007 µm in both cases, and, as in the previous case, they are negligible in comparison to the NanoPla positioning uncertainty. The interpolating errors of p_{3CAM} and p_{4CAM} are 4.49 µm and 4.50 µm, respectively. As in the first interval, they are the greatest contributor to the NanoPla final positioning error.

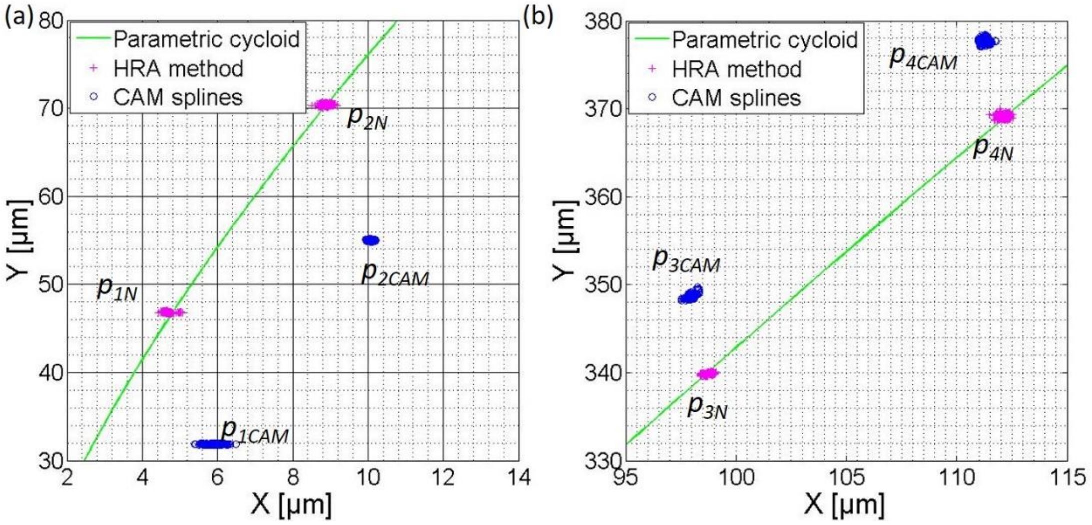

Figure 3.25. *Position of the platform at the first non-data interval (**a**) and at the second non-data interval (**b**).*

Conclusions

In nanopositioning systems like the NanoPla, the final positioning accuracy can be affected by errors in the definition of the trajectory. Hence, this work proposes the use of a novel method for the parametric representation of curves allowing curve fitting with high relative accuracy for the definition of curve trajectories. This method with collocation matrices of fg-Bernstein bases is applicable in CAGD and greatly improves the accuracy in trajectory definition by curve fitting compared to traditional CAD/CAM methods implemented in CAD/CAM software.

The positioning uncertainty of the NanoPla was calculated to be 0.50 µm. Thus, the trajectory definition errors are required to be lower than 0.05 µm in order not to significantly affect the final positioning accuracy of the system. Sets of given data points are curve fitted by interpolation and least squares approximation with the proposed HRA method and CAD/CAM software with the requirement of fulfilling the tolerance of 0.05 µm. The resultant fitting errors and the number of required control points are analysed for every case. In conclusion, the HRA method is capable of performing accurate interpolation with a minimum quantity of data points, and, when performing a least squares approximation it is capable of obtaining an accurate approximation curve with a minimum number of control points. In addition, the number of obtained control points is independent of the size of the problem. On the contrary, in CAD/CAM systems, a higher number of data points is required for an accurate curve fitting and the number of control points increases with the size of the problem, which may result in redundant or inadequate control points.

Finally, it was experimentally verified that, when defining the trajectory by interpolating a given set of 11 data points with the HRA method, the fitting errors at non-data intervals were negligible in comparison with the NanoPla positioning uncertainty. In contrast, when defining the trajectory with CAM splines with the same set of 11 interpolation points, the interpolation errors were the greatest contributors to the NanoPla final positioning error.

Therefore, implementing the high relative accuracy method in CAD/CAM systems would be of great interest for nanomanufacturing applications in which a nanopositioning stage is required to follow a predefined trajectory.

3.4. Conclusions

In this thesis, a 2D positioning control system for a large range nanopositioning stage was developed, implemented and experimentally validated in the NanoPla. In the positioning control system, four Halbach linear motors generate planar motion and a 2D laser system provides positioning feedback. In addition, a DMC kit from Texas Instruments was used as only control hardware, without additional electronics.

Firstly, the dynamic behaviour of a Halbach linear motor working as actuator in a pneumatically levitated stage was analysed. The system was identified with a mass-spring-damper model, whose stable equilibrium position can be defined by acting on the phase currents. This allowed the development of a sensorless open-loop 1D positioning control system which was implemented in the selected control hardware. Due to the generality of the control hardware, it acts on phase voltages, whereas other control systems specifically designed for the control of Halbach linear motors essentially consist in independently controlled current sources for each phase current. Nevertheless, the performance of the control hardware was optimised by configuring the voltage generation and current sampling modules in order to obtain precise positioning.

Once the correct performance of the open-loop positioning system was verified, the next step was to proceed with the development of a closed-loop 1D positioning control strategy. Two alternative control strategies that act on the two orthogonal forces generated by the motor were proposed. The first strategy is a 1D positioning strategy that acts on the thrust force generated by the motor in the axis of motion and leaves the levitation force in open-loop. The second strategy implements vector control, commonly utilised in rotary motors, to decouple the control of the thrust force and the levitation force. Both 1D positioning strategies were implemented in the control hardware and experimentally validated according to the NanoPla working requirements. A minimum incremental motion of 1 µm was achieved along the whole working range of the motor, that is 50 mm.

Before starting with the development and implementation of a 2D positioning control system in the NanoPla, a self-calibration procedure was developed in order to characterise the 2D laser system geometrical errors and correct them. The target of this procedure was to improve the final positioning accuracy of the 2D positioning control system. In a self-calibration procedure, the systematic errors of the laser system are isolated by relating different views of a non-calibrated artefact. Therefore, a self-calibration procedure eliminates the need of a calibrated artefact, which can be costly and difficult to obtain when working at a nanometre scale in a large range. In the developed procedure, a grid encoder was used as non-calibrated artefact and, once the laser system was calibrated, it was used to calibrate the grid encoder. The correct performance of this procedure was validated by comparing the obtained errors with the grid encoder calibration certificate of its main axes.

Finally, a 2D positioning control strategy for the NanoPla was developed and implemented. The developed control strategy coordinates the performance of the four Halbach linear motors and integrates the 2D laser system positioning feedback. The contributors to the final NanoPla positioning errors were analysed and the final positioning uncertainty (k=2) of the 2D control system was calculated to be ±0.5 µm. The resultant uncertainty is much lower than the NanoPla required positioning accuracy, broadening its applicability scope.

Nevertheless, the final positioning accuracy can be affected by errors in the definition of the trajectory of motion. Thus, in order not to significantly affect the final positioning accuracy of the system, it has been imposed that the trajectory definition errors must be lower than 0.05 µm. Hence, this work proposed the use of a novel method for the parametric representation of curves allowing curve fitting with high relative accuracy for the definition of curve trajectories. This method with collocation matrices of fg-Bernstein bases was developed by the Department of Applied Mathematics at the University of Zaragoza and it is applicable in CAGD. It was experimentally verified that the HRA method is capable of performing accurate curve fitting requiring less data points in the interpolation operation and with a minimum number of control points in a least squares approximation, in comparison with CAD/CAM systems.

3.5. Future work

Immediate future research should focus on the implementation of a measuring system in the NanoPla. As previously noted, the target application of its first prototype is surface topography characterisation at atomic scale of samples with relative big planar areas, using an atomic force microscope (AFM). Nevertheless, due to the fragile configuration of the AFM system, in [17], the implementation of an intermediate solution before integrating the AFM was proposed. In addition, for performing the measurements, the NanoPla two-stage architecture should be used as following: The NanoPla control system developed in this thesis performs the coarse motion to position the measuring instrument fixed to the moving platform, and the piezostage performs the fine motion of the sample during the scanning task. A contour standard artefact is proposed as first sample for testing the functionality of the NanoPla + measuring instrument system since it can be calibrated at a submicrometre resolution and it can have a length larger than the NanoPla working range. The initial tasks of this work are the development of a positioning control program for the piezostage, the selection of the measuring instrument and the characterisation of its performance. These tasks have already been completed. The guidelines to continue with the implementation of a measuring system in the NanoPla integrating the two-stage architecture are described below.

The commercial piezostage was selected in [17] and it is the model NPXY100Z10A from nPoint. It has a working range of 100 µm × 100 µm × 10 µm and a positioning noise of 0.5 nm in the XY-plane and 0.1 nm in Z-axis. The nPoint piezostage has been specifically design for scanning probe and optical microscopy. Motion along its three axes is controlled and driven by a C-300 controller that is connected to the host PC by a USB interface. The controller includes three channels, each channel is connected to an axis of the piezostage by a cable and it also includes analogue input and output BNC connectors for each axis (Figure 3.26a).

The C-300 controller can work in open-loop and closed-loop and computes the closed-loop control strategy with one PID controller per axis. The manufacturer includes a software that allows optimisation of the piezostage performance by adjusting the parameters of the PID controller inside the C-300 controller device. In addition, the software can also be used to command position changes and to monitor the system performance. Nevertheless, due to the fact that the positioning control system of the NanoPla has been developed in Simulink® (MATLAB®), it has been preferred to develop a Simulink® program that allows commanding position changes of the piezostage. In order to do that, it is required to include a data acquisition device (DAQ) with digital to analogue converters (DAC) to drive the analogue input (position command) and to receive the analogue output (position feedback) of the C-300 controller. The DAQ is connected to the Host PC by a USB and works as an interface between the Simulink® program and the C-300 controller. In Figure 3.26b a scheme of the connections between components is shown. It is worth mentioning that, even though the position commands are input in Simulink®, the closed-loop control strategy is still computed by the PID controllers inside the C-300 device.

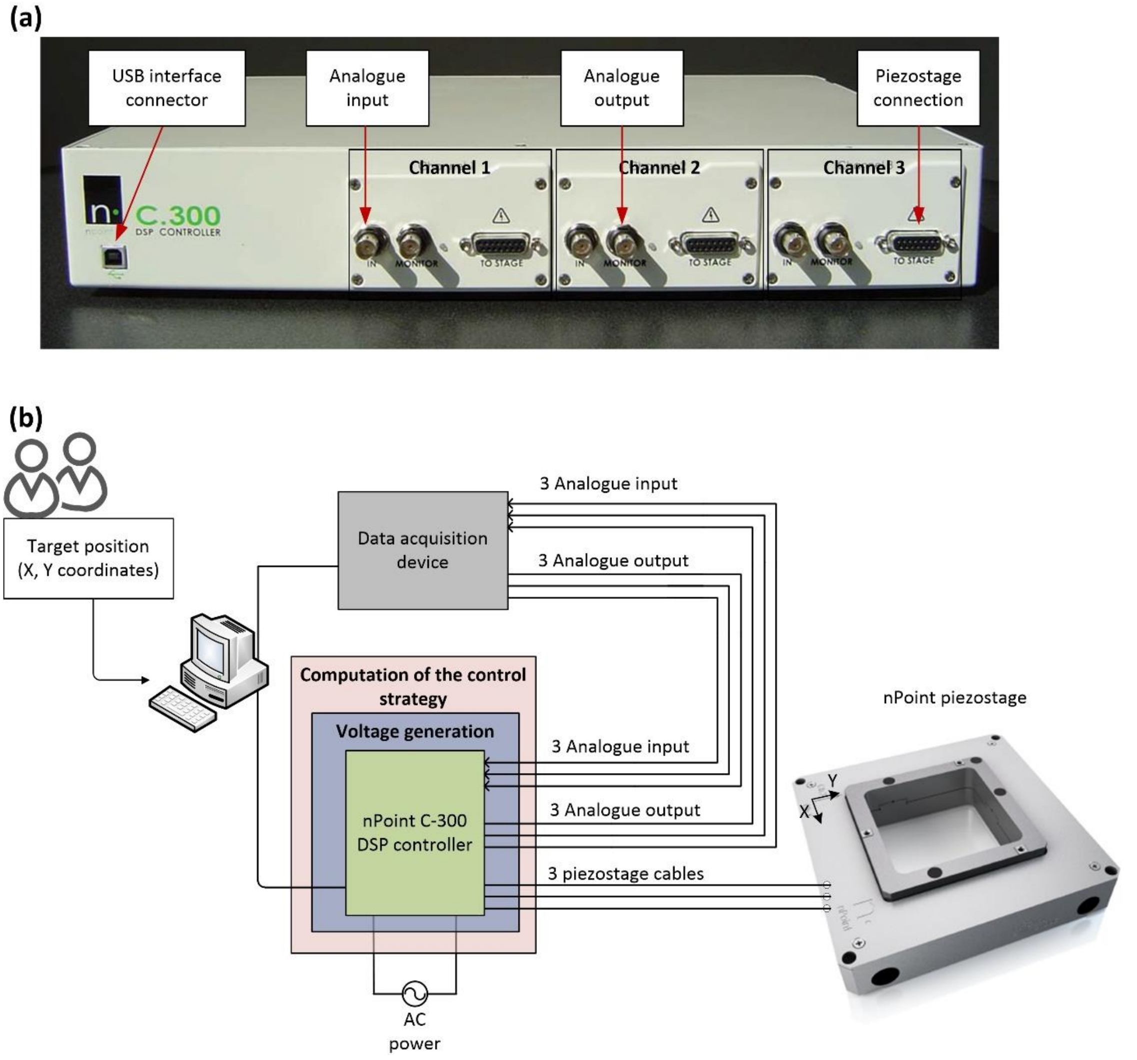

Figure 3.26. *(**a**) Front panel of the nPoint C-300 controller; (**b**) Scheme of the connections between the host PC, C-300 controller, DAQ and piezostage.*

On the other hand, a chromatic confocal point sensor, specifically the model CL4 with the magnifier MG 35 and the controller CCS Optima Plus from Stil, has been selected as the first measuring instrument to be implemented in the NanoPla. A confocal sensor performs a 1D measurement without contact with the target, which makes it suitable for measuring the contour standard as well as for characterising the NanoPla dynamics in Z-direction during the scanning task and during motion and optimise it prior to the AFM implementation. In addition, its measurements can be extracted in real time in MATLAB® and Simulink® and, thus, its control can be easily integrated in the same guide user interface of the piezostage and the NanoPla positioning control system. The confocal sensor performance has already been characterised in a metrological measuring setup that has been designed and manufactured for the purpose. The design of the metrological measuring setup minimises the effects of thermal variations in the measuring distance. The experimental setup is shown in Figure 3.27, in which the piezostage, its controller and the contour standard artefact have also been included. The correct performance of the confocal sensor has been verified by means of reference blocks along its measuring range of 4,000 µm. The manufacturer provides a measurement of the metrological characteristics of the instrument where specifies that the static noise at the centre of the measuring range is

99 nm. Nevertheless, this result is valid when the measurements are taken on a flat surface and with a 99% of light intensity. It has been experimentally verified that the light intensity depends on the sample material and roughness and can be optimised by adjusting the frequency and LED parameters. However, a 99% of light intensity cannot always be achieved. The static noise on the flat surface of a carbide contour standard with a 65% of light intensity is ± 244 nm.

Finally, in the experimental setup, the correct performance in the XY-plane of the piezostage has been verified by displacing the piezostage in X and Y-axes while measuring with the confocal sensor the height variations of a sloped surface of a contour standard placed on the piezostage. Similarly, the correct performance of the piezostage in Z-axis has been verified by displacing the piezostage in Z-axis while measuring with the confocal sensor the height variations of a horizontal surface of the contour standard.

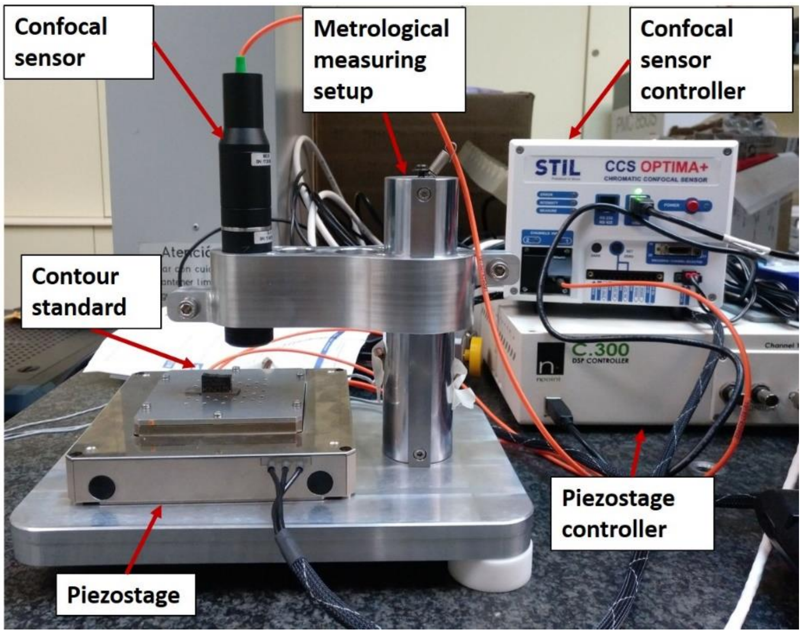

Figure 3.27. *Experimental setup for the characterisation of the confocal sensor performance.*

The next tasks for the implementation of the measuring instrument in the NanoPla should be the following: The contour standard artefact should be measured by the same measuring instrument in the NanoPla and in an external metrological setup, in order to characterise the errors that the NanoPla may introduce in the measurements, due to vibrations, thermal variations, etc. Moreover, a self-calibration procedure should be performed in order to calibrate the NanoPla + measuring instrument system. Afterwards, the confocal sensor should be used for characterising the dynamic properties of the NanoPla which should be optimised in order to facilitate the future integration of the AFM. Future developments should also include a thermal study of the NanoPla and the analysis of the NanoPla vibrations during motion and in static mode. As previously noted, the NanoPla has been designed to work together with different kinds of tools and probes in various applications such a metrology or nanomanufacturing. Therefore, the integration in the NanoPla of other application devices that require large range accurate positioning should be studied.

4. Spanish version

4.1. Resumen

La importancia de la nanotecnología en el mundo de la Ciencia y la Tecnología se ha incrementado en las últimas décadas. Consecuentemente, la demanda de sistemas de posicionamiento capaces de proporcionar posicionado preciso en un amplio rango de trabajo ha aumentado. En esta línea de investigación, la NanoPla ha sido desarrollada en la Universidad de Zaragoza. La NanoPla es un sistema bidimensional de posicionamiento, cuyo diseño ha sido objeto de dos tesis previas: [16, 17]. Ha sido fabricada y montada en la en la Universidad de Zaragoza. Está diseñada para alcanzar una precisión submicrométrica en su amplio rango de trabajo de 50 mm × 50 mm. La NanoPla tiene una estructura de tres niveles que consta de una base inferior y otra superior que están fijas, y una plataforma móvil situada en medio, como se puede ver en la Figura 4.1.

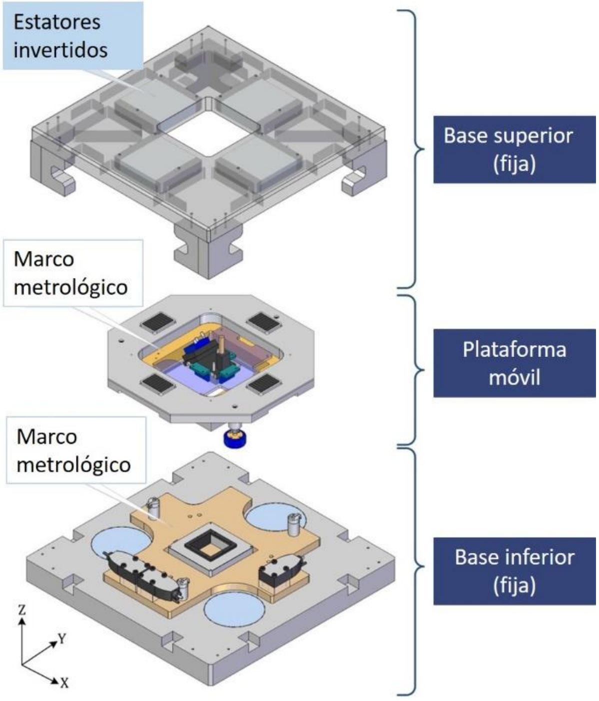

Figura 4.1. *Vista explotada de la NanoPla.*

La plataforma móvil del sistema levita gracias a tres cojinetes de aire y cuatro motores lineares Halbach conforman el sistema de actuación. Los estatores de los motores lineales están fijos a la base superior, mientras que los caminos magnéticos están situados en la plataforma móvil. Un sistema bidimensional de interferómetros láser es usado como sensor de posición, los cabezales de los láseres están situados en el marco metrológico de la base inferior, mientras que los espejos planos están fijos al marco metrológico de la plataforma móvil. Los sistemas interferómetros láser ofrecen una excelente precisión y trazabilidad directa. Además, usar espejos planos como retrorreflectores permite medir el desplazamiento coplanario de dos ejes.

La NanoPla implementa una estructura de dos etapas, es decir, el movimiento en amplio rango de la plataforma móvil es complementado por el posicionamiento más fino de una posicionadora comercial con actuadores piezoeléctricos. Esta posicionadora tiene un rango de trabajo de 100 µm × 100 µm × 10 µm. Por lo tanto, el sistema de control de posicionamiento de la plataforma móvil tiene que ser capaz de alcanzar una incertidumbre de posicionado de 10 µm o menor, para que, posteriormente, el error de posicionado pueda ser corregido por la posicionadora piezoeléctrica.

Uno de los principales criterios de diseño de la NanoPla es implementar tantos componentes comerciales como sea posible, con el objetivo de facilitar la futura aplicación industrial del sistema desarrollado. Aunque los motores lineales Halbach no guiados no son comercializados, han sido seleccionados como actuadores debido a que su diseño único permite la implementación de un movimiento plano que evita una estructura de ejes apilados. Además, estos motores proporcionan un movimiento sin contacto y están libres de holguras. Por lo tanto, los motores lineales Halbach han sido hechos a pedido expresamente para esta aplicación. Sin embargo, se ha preferido una solución genérica y comercial para el hardware. Debido a que no hay disponible ninguna solución comercial para el hardware de control de motores lineales Halbach, se ha optado por el “Digital Motor Control kit” de Texas Instruments. Este hardware de control se ha diseñado para el control genérico de motores trifásicos con imanes permanentes, en los que el objetivo suele ser el control de la velocidad de rotación o del par generado. El uso de un solo hardware comercial sin ningún tipo de electrónica adicional facilita la replicabilidad del sistema desarrollado, lo que está en línea con los criterios de diseño de la NanoPla. Sin embargo, el uso de un hardware genérico presenta limitaciones que se pueden superar mediante la optimización de la configuración de los módulos del hardware.

Esta tesis, primero, desarrolla dos estrategias alternativas de posicionado unidimensional para motores lineales Halbach y las implementa en el hardware de control comercial seleccionado. La implementación de un hardware comercial supone una novedad con respecto al resto de sistemas de control de motores Halbach desarrollados en otros trabajos, donde el hardware es diseñado y fabricado expresamente para cada aplicación. La configuración de los módulos del hardware de control es optimizada con el fin de obtener un posicionamiento preciso del motor. Además, para mejorar la precisión del posicionamiento, se propone un procedimiento de autocalibración para la caracterización de los errores geométricos del sistema bidimensional de interferómetros láser. Finalmente, se desarrolla un sistema de control de posicionamiento bidimensional en un amplio rango de trabajo y se implementa en la NanoPla. El sistema de control desarrollado coordina el funcionamiento de los cuatro motores Halbach de la NanoPla e integra el sistema láser bidimensional como sensor para la realimentación de la posición. Además, se analizan las contribuciones a los errores finales de posicionamiento de la NanoPla y se calcula la incertidumbre de posicionamiento (k=2) del sistema de control bidimensional, que resulta ser ±0.5 µm en todo el rango de trabajo. La incertidumbre de posicionamiento alcanzada es mucho menor que los requisitos iniciales que se habían impuesto a la NanoPla, lo que amplía su ámbito de aplicación.

4.2. Conclusiones

En esta tesis, se desarrolla un sistema de control de posicionamiento bidimensional para una plataforma de nanoposicionamiento de amplio rango y su funcionamiento se valida experimentalmente en la NanoPla. En el sistema de control, cuatro motores lineales Halbach generan las fuerzas necesarias para producir el movimiento planar y un sistema bidimensional de interferómetros láser proporciona realimentación de la posición. Además, como único hardware de control se utiliza el “Digital Motor Control kit” de Texas Instruments, sin ningún tipo de electrónica adicional.

Primero, se ha analizado el comportamiento dinámico de un motor Halbach cuando funciona como actuador en una plataforma lineal levitada por cojinetes de aire. El sistema se ha identificado con un modelo masa-resorte-amortiguador, cuya posición de equilibrio estable se puede definir a partir de las corrientes de fase. Esto ha permitido desarrollar un sistema de control de posicionamiento lineal en lazo abierto que no requiere de realimentación de posición que, posteriormente, se ha implementado en el hardware comercial. Debido a la generalidad del hardware de control, este actúa sobre las tensiones de fase, mientras que otros sistemas de control diseñados específicamente para motores lineales Halbach básicamente consisten en fuentes controladas de corriente para cada fase, independientes entre sí. Sin embargo, el funcionamiento del hardware de control ha sido optimizado mediante la configuración de los módulos de generación de tensión y muestreo de intensidades para obtener precisión en el posicionado.

Una vez se hubo verificado el funcionamiento del sistema de posicionado lineal en lazo abierto, el siguiente paso ha sido el desarrollo de una estrategia de control de posicionamiento lineal en lazo cerrado. Se han propuesto dos tipos de estrategia distintas que actúan sobre las dos fuerzas ortogonales, de empuje y de levitación, que genera el motor. La primera estrategia controla la posición actuando sobre la fuerza de empuje que produce el movimiento lineal mientras deja la fuerza de levitación en lazo abierto. La segunda estrategia implementa un control vectorial, comúnmente utilizado en motores rotativos que desacopla el control de la fuerza de empuje y la fuerza de levitación. Estas dos estrategias se han implementado en el hardware y su funcionamiento se ha validado experimentalmente según los requisitos de la NanoPla. Se ha conseguido realizar desplazamientos mínimos de 1 µm, a lo largo de todo el rango de trabajo del motor de 50 mm. Estos experimentos han sido realizados en un montaje externo a la NanoPla, en una plataforma lineal levitada neumáticamente, y un sistema interferómetro láser se ha usado para la realimentación de posicionamiento.

Antes de comenzar con el desarrollo y la implementación del sistema de control de posicionamiento bidimensional en la NanoPla, se ha desarrollado un procedimiento de autocalibración para caracterizar los errores geométricos del sistema láser bidimensional y corregirlos. Este procedimiento permite mejorar la precisión final del sistema de control de posicionado bidimensional. En un procedimiento de autocalibración, los errores sistemáticos del sistema a calibrar son aislados relacionando distintas vistas de un artefacto no calibrado. Por lo tanto, el uso de un procedimiento de autocalibración elimina la necesidad de un artefacto calibrado, que puede resultar costoso y difícil de obtener cuando se trabaja a escala nanométrica en amplio rango. En el procedimiento desarrollado, un encoder de malla se usa como artefacto no calibrado y, una vez se ha calibrado el sistema láser, sus medidas se usan para calibrar el encoder de malla. El correcto funcionamiento de este procedimiento se ha validado comparando los errores del encoder de malla obtenidos, con los proporcionados por su certificado de calibración para sus ejes principales.

Finalmente, se ha desarrollado e implementado el sistema de control de posicionamiento bidimensional en la NanoPla. El sistema desarrollado coordina el funcionamiento de los cuatro motores Halbach e integra la realimentación de posición del sistema láser bidimensional. Además, se han analizado las contribuciones a los errores finales de posicionamiento de la NanoPla y se ha calculado la incertidumbre de posicionamiento (k=2) del sistema de control bidimensional, que resulta ser ±0.5 µm en todo el rango de trabajo. La incertidumbre de posicionamiento que se ha alcanzado es mucho menor que los requisitos iniciales que se habían impuesto a la NanoPla, lo que amplía su ámbito de aplicación.

Sin embargo, la incertidumbre final de posicionamiento puede verse afectada por errores en la definición de la trayectoria de movimiento. Por consiguiente, para no afectar significativamente al error de posicionado final del sistema, se ha impuesto que los errores en la definición de la trayectoria deben ser menores que 0.05 µm. De esta manera, en esta tesis se propone el uso de un innovador método para la representación paramétrica de curvas que permite el ajuste de curvas con alta precisión relativa para la definición de trayectorias curvas. Este método de matrices de colocación de bases fg-Bernstein ha sido desarrollado por el Departamento de Matemática Aplicada de la Universidad de Zaragoza y es aplicable en diseño asistido por ordenador (CAGD). Se ha comprobado experimentalmente que el método propuesto ofrece una mejor precisión de posicionamiento que los métodos comúnmente usados en los programas CAD y CAM cuando se define una trayectoria por ajuste de curvas (por interpolación o aproximación por mínimos cuadrados), precisando un número menor de puntos de entrada en el caso de la interpolación y menos puntos de control en el caso de la aproximación por mínimos cuadrados.

5. Dissemination of results

Published articles

- **Sensors 2017**: "Geometrical characterisation of a 2D laser system and calibration of a cross-grid encoder by means of a self-calibration methodology". Marta Torralba, Lucía C. Díaz-Pérez, Margarita Valenzuela, José A. Albajez, José A. Yagüe-Fabra. Sensors, 2017, 17, 1992.
- **Procedia Manufacturing 2017:** "Implementation of the control strategy for a 2D nanopositioning long range stage". Lucía C. Díaz-Pérez, Marta Torralba, J.A. Albajez, J.A. Yagüe. Procedia Manufacturing, 2017, 13.
- **Micromachines 2018**: "One dimensional control system for a linear motor of a two dimensional nanopositioning stage using a commercial control hardware". Lucía C. Díaz-Pérez, Marta Torralba, José A. Albajez, José A. Yagüe-Fabra. Micromachines, 2018, 9, 421.
- **Electronics 2018**: "Vector control strategy for a Halbach linear motor implemented in a commercial control hardware". Lucía C. Díaz-Pérez, José A. Albajez, Marta Torralba, José A. Yagüe-Fabra. Electronics, 2018, 7, 232.
- **Procedia Manufacturing 2019**: "Positioning uncertainty of the control system for the planar motion of a nanopositioning platform". Lucía C. Díaz-Pérez, Marta Torralba, José A. Albajez, José A. Yagüe. Procedia Manufacturing, 2019, accepted.

Papers under review

- "Trajectory definition with high relative accuracy (HRA) by parametric representation of curves in nano-positioning systems". Lucía Díaz Pérez, Beatriz Rubio Serrano, José A. Albajez García, José A. Yagüe Fabra, Esmeralda Mainar Maza and Marta Torralba Gracia. Micromachines, 2019. Under review.

Conference contributions

- **Euspen 2016:** "A self-calibration methodology for a 2D-long range motion stage". Marta Torralba, Lucía Díaz, Margarita Valenzuela, José A. Albajez, José A. Yagüe, Juan José Aguilar. 16th euspen International Conference & Exhibition. **Poster**. Nottingham (United Kingdom). May 2016.
- **CNIM 2016:** "Auto-calibración del sistema de posicionamiento de una plataforma de movimiento en 2D". Marta Torralba, Lucía Díaz, Margarita Valenzuela, José A. Albajez, José A. Yagüe, Juan José Aguilar. XXI Congreso Nacional de Ingeniería Mecánica. **Oral presentation**. Elche (Spain). November 2016.
- **Euspen 2017**: "Performance analysis of laser measuring system for an ultra-precision 2D-stage". Lucía C. Díaz-Pérez, Marta Torralba, José A. Albajez, José A. Yagüe-Fabra. 17th euspen International Conference & Exhibition. **Poster**. Hannover (Germany). May 2017.
- **MESIC 2017:** "Implementation of the control strategy for a 2D nanopositioning long range stage". Lucía C. Díaz-Pérez, Marta Torralba, José A. Albajez, José A. Yagüe-Fabra. 7th Manufacturing Engineering Society International Conference. **Oral presentation**. Vigo (Spain). June 2017.

- **Euspen 2018**: “Current sampling in a control strategy for a linear motor of a 2D nanopositioning stage based on vector control". Lucía C. Díaz-Pérez, Marta Torralba, José A. Albajez, José A. Yagüe-Fabra. 18th euspen International Conference & Exhibition. **Poster**. Venice (Italy). June 2018.
- **Euspen 2019:** “2D positioning control strategy for a nanopositioning stage”. Lucía C. Díaz-Pérez, Marta Torralba, José A. Albajez, José A. Yagüe-Fabra. 19th euspen International Conference & Exhibition. **Poster**. Bilbao (Spain). June 2019.
- **MESIC 2019:** “Positioning uncertainty of the control system for the planar motion of a nanopositioning platform”. Lucía C. Díaz-Pérez, Marta Torralba, José A. Albajez, José A. Yagüe-Fabra. 8th Manufacturing Engineering Society International Conference. **Oral presentation**. Madrid (Spain). June 2019.

Research stay at DTU

Position: Visiting Scholar in the Department of Mechanical Engineering at the Technical University of Denmark (DTU)

Period: from September 1st to November 30th 2017 (3 months).

Supervisor: Associate professor Dr. Guido Tosello and PostDoc Dr. Ali Davoudinejad.

Purpose of the work: Collaboration in the research project ‘MICRO-AM’ (Micro 3D Additive Manufacturing and Integrated Process Chains) in the framework of the EU FP7 Marie-Curie research programme. Specifically, I studied the manufacturing capabilities of a micro additive manufacturing system applying state-of-the-art 3D microscopy and metrological methods.

Published articles

- “Additive manufacturing with vat polymerization method for precision polymer micro components production”. Ali Davoudinejad, Lucia C. Diaz-Perez, Danilo Quagliottia, David Bue Pedersen, José A. Albajez-García, José A. Yagüe-Fabra, Guido Tosello. Procedia CIRP, 2018, 75, 98-102.

Conference contributions

- “Geometrical shape assessment of additively manufactured features by direct light processing”. Lucia C. Diaz-Perez, Ali Davoudinejad, Danilo Quagliottia, David Bue Pedersen, José A. Albajez-García, José A. Yagüe-Fabra, Guido Tosello. 18th euspen International Conference & Exhibition. **Poster**. Venice (Italy). June 2018.
- “Additive manufacturing product and process quality control with vat polymerization method for precision polymer micro components production”. Ali Davoudinejad, Lucia C. Diaz-Perez, Danilo Quagliottia, David Bue Pedersen, José A. Albajez-García, José A. Yagüe-Fabra, Guido Tosello. 15th CIRP CAT Conference. **Oral presentation**. Milano (Italy). June 2018.

- “Geometric and feature size design effect on vat photopolymerization micro additively manufactured surface features". Ali Davoudinejad, Lucia C. Diaz-Perez, Danilo Quagliottia, David Bue Pedersen, José A. Albajez-García, José A. Yagüe-Fabra, Guido Tosello. 2018 ASPE and euspen Summer Topical Meeting, Advancing Precision in Additive Manufacturing. **Poster**. Berkeley (USA). July 2018.
- “Geometrical and feature of size design effect on direct stereolithography micro additively manufactured components". Ali Davoudinejad, Lucia C. Diaz-Perez, Danilo Quagliottia, David Bue Pedersen, José A. Albajez-García, José A. Yagüe-Fabra, Guido Tosello. 22nd European Conference on Fracture. **Oral presentation**. Belgrado (Serbia). August 2018.

Research stay at UNCC

Position: Visiting Scholar in the Center for Precision Metrology at the University of North Caroline at Charlotte (UNCC, USA)

Period: from September 1st to October 31st 2018 (2 months).

Supervisor: Dr. Stuart Smith and PhD student Masoud Arablu

Purpose of the work: Development and implementation of a two-axis Displacement Measurement Interferometer (DMI) using two Frequency-Modulated (FM) light sources. The method utilises modulation harmonics previously used for single-axis polydyne displacement interferometry [115]. The objectives of this work were to demonstrate two-axis displacement measurement with a single photodetector and that relative displacements between different axes can be directly extracted from the detector signal. The ultimate goal is to extend this technique for displacement measurement of an unlimited number of axes.

Conference contributions

- “Combined frequency-modulated signals for two-axis displacement measurement”. Lucia Diaz-Perez, Kumar Arumugam, Masoud Arablu, Stuart T. Smith. 19th euspen International Conference & Exhibition. **Oral presentation**. Bilbao (Spain). June 2019.

6. Appendix

6.1. Impact factor of publications

Micromachines 2018: The JCR journal impact factor of Micromachines in the year 2018 is 2.426. It is in the position 25 of 61 (Q2, T2) of the category "Instruments & Instrumentation".

Electronics 2018: The JCR journal impact factor of Electronics in the year 2018 is 1.764. It is in the position 154 of 265 (Q3, T2) of the category "Engineering, Electrical & Electronic".

Sensors 2017: The JCR journal impact factor of Sensors in the year 2017 is 2.475. It is in the position 16 of 61 (Q2, T1) of the category "Instruments & Instrumentation".

Procedia Manufacturing 2019: The SJR journal impact factor of Sensors in the year 2018 (last available at the moment) is 0.313. It is in the Q2 of the category "Industrial and Manufacturing Engineering”.

6.2. Co-authorship justification

This subsection describes the main contributions of the author in each of the publications of this thesis compendium:

Micromachines 2018 and Electronics 2018:

- Study of the state of the art.
- Contribution to the design of the control strategies and implementation in the control hardware.
- Configuration of the voltage generation and current sensing modules to optimise the performance of the control hardware in precision positioning.
- Programming of the control hardware.
- Contribution to the design of the experimental setups and performance of the experimental verification of the system.
- Analysis and discussion of the experimental results.
- Writing of the manuscript.

Sensors 2017:

- Study of the state of the art.
- Contribution to the development of the self-calibration procedure.
- Implementation and validation of the procedure for the calibration of the system.
- Analysis and discussion of the experimental results.
- Writing of the manuscript.

Procedia Manufacturing 2019:

- Study of the state of the art.
- Contribution to the design of the control strategy and implementation in the NanoPla.
- Programming of the control hardware.
- Performance of experimental tests for the system validation.
- Analysis of the positioning uncertainty contributors and optimisation of the system.
- Writing of the manuscript.

6.3. Acceptance letter for the pending publishing work

Procedia Manufacturing 2019: “Positioning uncertainty of the control system for the planar motion of a nanopositioning platform”. Lucía C. Díaz-Pérez, Marta Torralba, José A. Albajez, José A. Yagüe. Procedia Manufacturing, 2019.

MESIC
Madrid 2019

Madrid 22th July 2019

Dear Ms. Diaz,

I am pleased to inform you that your communication entitled ‘Positioning uncertainty of the control system for the planar motion of a nanopositioning platform ' has been accepted for its publication at the Procedia Manufacturing

Best regards.

Alfredo Sanz
Chair of Scientific Committee

Bibliography

[1] M. Roco and W. Bainbridge, "Societal implication of nanosciende and nanotechnology," *Journal of Nanoparticle Research,* vol. 7, pp. 1-13, 2001.

[2] W. Gao, S. Kim, H. Bosse, H. Haitjema, Y. Chen, X. Lu, W. Knapp, A. Weckenmann, W. Estler and H. Kunzmann, "Measurement technologies for precision positioning," *CIRP Annals,* vol. 64, pp. 773-796, 2015.

[3] A. Sinno, P. Ruaux, L. Chassagne, S. Topu, Y. Alayli, G. Lerondel, S. Blaize, A. Bruyant and P. Royer, "Enlarged atomic force microscopy scanning scope: Novel sample-holder device with millimeter range," *Review of Scientific Instruments,* vol. 78, p. 095107, 2007.

[4] R. Jain, S. Majumder, B. Ghosh and S. Saha, "Design and manufacturing of mobile micro manipulation system with a compliant piezoelectric actuator based micro gripper," *Journal of Manufacturing Systems,* vol. 35, pp. 76-91, 2015.

[5] P. Ouyang, R. Tjiptoprodjo, W. Zhang and G. Yang, "Micro-motion devices technology: The state of arts review," *The International Journal of Advanced Manufacturing Technology,* vol. 38, pp. 463-478, 2008.

[6] K. Sato, "Trend of precision positioning technology," *ABCM Symposium Series in Mechatronics,* vol. 2, p. 739–750, 2006.

[7] C. A. Werner, A 3D translation stage for metrological AFM, Ph.D. Thesis, Eindhoven University of Technology, 2010.

[8] A. Balasubramanian, M. Jun, R. DeVor and S. Kapoor, "A submicron multiaxis positioning stage for micro- and nanoscale manufacturing processes," *Journal of Manufacturing Science and Engineering,* vol. 130, no. 3, p. 031112, 2008.

[9] S. Ducourtieux and B. Poyet, "Development of a metrological atomic force microscope with minimized Abbe error and differential interferometer-based real-time position control," *Measurement Science and Technology,* vol. 22, no. 9, p. 094010, 2011.

[10] E. Manske, G. Jäger, T. Hausotte and R. Füßl, "Recent developments and challenges of nanopositioning and technology," *Measuring Science Technology,* vol. 23, p. 74001–74010, 2012.

[11] D. Dornfeld, S. Min and Y. Takeuchi, "Recent advances in mechanical micro-machining," *CIRP Annals,* vol. 55, no. 2, pp. 745-768, 2006.

[12] E. Brinksmeier, Y. Mutlugünes, F. Klocke, J. Aurich, P. Shore and H. Ohmori, "Ultra-precision grinding," *CIRP Annals,* vol. 59, no. 2, pp. 652-671, 2010.

[13] P. Shore, C. Cunnigham, D. Debra, C. Evans, J. Hough, R. Gilmozzi, H. Kunzmann and P. Morantz, "Precision engineering for astronomy and gravity science," *CIRP Annals,* vol. 59, no. 2, pp. 694-716, 2010.

[14] R. W. Johnson, A. Hultqvist and S. Bent, "A brief review of atomic layer deposition: From fundamentals to applications," *Materials Today,* vol. 17, no. 5, pp. 236-246, 2014.

[15] R. L. Donker, I. Widdershoven and H. A. M. Spaan, "Isara 400: Enabling ultra-precision coordinate metrology for large parts," in *10th euspen International Conference & Exhibition*, 2010.

[16] M. Valenzuela Galván, Diseño de una plataforma bidimensional con resolución nanométrica y amplio rango de desplazamiento, PhD Thesis, University of Zaragoza, 2013.

[17] M. Torralba, Development of a 2D positioning stage with submicrometric accuracy for metrological applications, PhD Thesis, University of Zaragoza, 2015.

[18] J.Minase, T.-F.Lu, B.Cazzolato and S.Grainger, "A review, supported by experimental results, of voltage, charge and capacitor insertion method for driving piezoelectric actuators," *Precision Engineering,* vol. 34, no. 4, 2010.

[19] K.-B. Choi and D.-H. Kim, "Monolithic parallel linear compliant mechanism for two axes ultraprecision linear motion," *Review of Scientific Instruments,* vol. 77, no. 6, p. 065106, 2006.

[20] L.-J. Lai, G.-Y. Gu and L.-M. Zhu, "Design and control of a decoupled two degree of freedom translational parallel micro-positioning stage," *Review of Scientific Instruments,* vol. 83, no. 4, p. 045105, 2012.

[21] Q. Yao, J. Dong and P.M. Ferreira, "Design, analysis, fabrication and testing of a parallel-kinematic micropositioning XY stage," *International Journal of Machine Tools and Manufacture,* vol. 47, no. 6, 2007.

[22] Q. Xu and Y. Li, "Analytical modeling, optimization and testing of a compound bridge-type compliant displacement amplifier," vol. 46, no. 2, pp. 183-200, 2011.

[23] J. G. Hui Tang, X. Chen, K.-M. Yu, S. To, Y. He, X. Chen, Z. Zeng, S. He, C. Chen and Y. Li, "Development and repetitive-compensated PID control of a nanopositioning stage with large-stroke and decoupling property," *IEEE Transactions on Industrial Electronics,* vol. 65, no. 5, 2018.

[24] J.-J. Kim, Y.-M. Choi, D. Ahn, B. Hwang, D.-G. Gweon and J. Jeong, "A millimeter-range flexure-based nano-positioning stage using a self-guided displacement amplification mechanism," *Mechanism and Machine Theory,* vol. 50, pp. 109-120, 2012.

[25] C. Li, G. Gu, M. Yang and L. Zhu, "Design, analysis and testing of a parallel kinematic high-bandwidth," *Review of Scientific Instruments,* vol. 84, p. 125111, 2013.

[26] W. Jywe, Y.-R. Jeng, C.-H. Liu, Y.-F. Teng, C.-H. Wu, T.-H. Hsieh and L.-L. Duan, "Development of a middle-range six-degrees-of-freedom system," *Proceedings of the Institution of Mechanical Engineers, Part B: Journal of Engineering Manufacture,* vol. 224, no. 4, p. 679–688, 2007.

[27] A. T. Elfizy, G. M. Bone and M. A. Elbestawi, "Design and control of a dual-stage feed drive," *International Journal of Machine Tools and Manufacture,* vol. 45, no. 2, pp. 153-165, 2005.

[28] A. Ghosh and B. Corves, Introduction to micromechanisms and microactuators, New Delhi, India: Springer, 2015.

[29] P. R. Ouyang, R. C. Tjiptoprodjo, W. J. Zhang and G. S. Yang, "Micro-motion devices technology: The state of arts review," *The International Journal of Advanced Manufacturing Technology,* vol. 38, no. 5-6, p. 463–478, 2008.

[30] J. Chen and I. Dwang, "A ballscrew drive mechanism with piezo-electric nut for preload and motion control," *International Journal of Machine Tools and Manufacture,* vol. 40, no. 4, pp. 513-526, 2000.

[31] Physik Instrumente (PI), Micropositioning, nanopositioning, nanoautomation: Solutions for cutting-edge technologies, Tustin, USA: Physik Instrumente (PI), 2001.

[32] G. J. Maeda and K. Sato, "Practical control method for ultra-precision positioning using a ballscrew mechanism," *Precision Engineering,* vol. 32, no. 4, pp. 309-318, 2008.

[33] C. Liu, W. Jywe, Y. Jeng, T. Hsu and Y. Li, "Design and control of a longtraveling nano-positioning stage," *Precision Engineering,* vol. 34, no. 3, pp. 497-506, 2010.

[34] T. Hu and W.-J. Kim, "Extended range six-DOF high-precision positioner for wafer processing," *IEEE/ASME Transactions on Mechatronics,* vol. 11, no. 6, pp. 682 - 689, 2006.

[35] H. Shinno, H. Yoshioka and K. Taniguchi, "A newly developed linear motor-driven aerostatic X-Y planar motion table system for nano-machining," *CIRP Annals - Manufacturing Technology,* vol. 56, no. 1, pp. 369-372, 2007.

[36] S. Verma, W.-J. Kim and H. Shakir, "Multi-axis maglev nanopositioner for precision manufacturing and manipulation applications," *IEEE Transactions on Industry Applications,* vol. 41, no. 5, pp. 1159 - 1167, 2005.

[37] A. E. Braun, "Nanotechnology: genesis of semiconductor's future," *Semiconductor International,* vol. 27, no. 12, pp. 45-52, 2004.

[38] T. Joo Teo, G. Yang and I.-M. Chen, "A flexure-based electromagnetic nanopositioning actuator with predictable and re-configurable open-loop positioning resolution," *Precision Engineering,* vol. 40, pp. 249-260, 2015.

[39] S. Lin, Y. Jia, I. P. Lei and Q. Xu, "Design and optimization of a long-stroke compliant micropositioning stage driven by voice coil motor," in *12th International Conference on Control Automation Robotics & Vision (ICARCV)*, Guangzhou, China, 2012.

[40] Q. Xu, "New flexure parallel-kinematic micropositioning system with large workspace," *IEEE Transactions on Robotics,* vol. 28, no. 2, pp. 478 - 491, 2012.

[41] N. K. Roy and M. A. Cullinan, "Fast trajectory tracking of a flexure-based, multiaxis nanopositioner with 50-mm travel," *IEEE/ASME Transactions on Mechatronics,* vol. 23, no. 6, pp. 2805 - 2813, 2018.

[42] J. Gieras and M. Godkin, "Status of permanent magnet linear motors in the US," in *3rd International Symposium on Linear Drives for Industry Applications*, Nagano, Japan, 2001.

[43] C. Yang, G. L. Wang, B. S. Yang and H. R. Wang, "Research on the structure of high-speed large-scale ultra-precision positioning system," in *3rd IEEE International Conference on Nano/Micro Engineered and Molecular Systems*, 2008.

[44] J. Kim, J. Kim, C. Kang and T. Eom, "Metrological atomic force microscope using a large range scanning dual stage," *International Journal of Precision Engineering and Manufacturing,* vol. 10, pp. 11-17, 2009.

[45] Q. Xu, "Design and development of a compact flexure-based XY precision positioning system with centimeter range," *IEEE Transactions on Industrial Electronics,* vol. 61, no. 2, 2014.

[46] X. Lu and I. Usman, "6D direct-drive technology for planar motion stages," *CIRP Annals Manufacturing Technology,* vol. 61, no. 1, p. 359, 2012.

[47] D. Trumper, W. Kim and M. Williams, "Design and analysis framework for linear permanent-magnet machines," *IEEE Transactions on Industry Applications,* vol. 24, pp. 371-379, 1996.

[48] W. Kim, D. Trumper and J. Lang, "Modeling and vector control of planar magnetic levitator," *IEEE Transactions on Industry Applications,* vol. 34, pp. 1254-1262, 1998.

[49] R. R. Fesperman, Multi-scale alignment positioning system, PhD Thesis, University of North Carolina, 2006.

[50] R. Fesperman, O. Ozturk, R. Hocken, S. Ruben, T. C. Tsao and J. Phipps, "Multi-scale alignment and positioning system - MAPS," *Precision Engineering,* vol. 36, no. 4, pp. 517-537, 2012.

[51] C. Schäffel, M. Katzschmann, H.-U. Mohr, R. Gloess, C. Rudolf, C. Mock and C. Walenda, "6D planar magnetic levitation system - PIMag 6D," *Mechanical Engineering Journal,* vol. 3, no. 1, pp. 15-00111, 2016.

[52] S. Hesse, C. Schäffel, H. Mohr, M. Katzschmann and H.-J. Büchner, "Design and performance evaluation of an interferometric controlled planar nanopositioning system," *Measurement Science and Technology,* vol. 23, p. 044011, 2012.

[53] S. Devasia, E. Eleftheriou and S. O. Reza-Moheimani, "A survey of control issues in nanopositioning," *IEEE Transactions on Control Systems Technology,* vol. 15, no. 5, pp. 802-823, 2007.

[54] M. Bazghaleh, S. Grainger and M. Mohammadzaheri, "A review of charge methods for driving piezoelectric actuators," *Journal of Intelligent Material Systems & Structures,* vol. 29, no. 10, pp. 2096-2104, 2018.

[55] J. Minase, T.-F. Lu, B. Cazzolato and S. Grainger, "A review, supported by experimental results, of voltage, charge and capacitor insertion method for driving piezoelectric actuators," *Precision Engineering,* vol. 34, no. 4, pp. 692-700, 2010.

[56] A. Sebastian and S. Salapaka, "Design methodologies for robust nano-positioning," *IEEE Transactions on Control Systems Technology,* vol. 13, no. 6, pp. 868-876, 2005.

[57] S. Derammelaere, M. Haemers, J. D. Viaene, F. Verbelen and K. Stockman, "A quantitative comparison between BLDC, PMSM, brushed DC and stepping motor technologies," in *19th International Conference on Electrical Machines and Systems (ICEMS)*, Chiba, Japan, 2016.

[58] C. Röhrig, "Optimal commutation law for three-phase surface-mounted permanent magnet linear synchronous motors," in *Proceedings of the 45th IEEE Conference on Decision and Control*, San Diego, USA, 2006.

[59] S. D. Ruben, Modeling, control, and real time optimization for a nano-precision system, PhD Thesis, University of California, 2010.

[60] S. Ruben and T.-C. Tsao, “Optimal commutation laws by real-time optimization for multiple motor driven systems,” in *Proceedings of the American Control Conference*, 2010.

[61] J. H. Choi and Y. S. Baek, "Theoretical analysis and its applications of a PM synchronous motor with minimized cogging force," *IEEE Transactions on Magnetics,* vol. 45, no. 10, pp. 4692 - 4695, 2009.

[62] W.-J. Kim, High-precision planar magnetic levitation, PhD Thesis, Massachusetts Institute of Technology, 1997.

[63] C. Röhrig, "Current waveform optimization for force ripple compensation of linear synchronous motors," in *42nd IEEE Conference on Decision and Control*, Maui, HI, USA, 2003.

[64] K. Tan, S. Huang and T. Lee, "Robust adaptive numerical compensation for friction and force ripple in permanent-magnet linear motors," *IEEE Transactions on Magnetics,* vol. 38, no. 1, pp. 221 - 228, 2002.

[65] W. Kim and D. Trumper, "High-precision magnetic levitation stage for photolithography," *Precision Engineering,* vol. 22, pp. 66-77, 1998.

[66] K.-B. Lee, H.-U. Shin and Y. Bak, "Chapter 11 - Basic control of AC motor drives," in *Control of Power Electronic Converters and Systems*, F. Blaabjerg, Ed., 2018, pp. 301-329.

[67] W. Leonhard, Control of electrical drives, Berlin, Germany: Springer-Verlag, 1996.

[68] P. Vas, Sensorless vector and direct torque control, monographs in electrical and electronic engineering, New York, NY, USA: Oxford University Press, 1998.

[69] X. Mo and B. Zhang, "Design and driving of a 3-DOF electromagnetic direct-drive nanopositioning stage with long stroke," in *IEEE International Conference on Manipulation, Manufacturing and Measurement on the Nanoscale (3M-NANO)*, 2017.

[70] T. Hu, Design and control of a 6-degree-of-freedom levitated positioner with high precision, PhD Thesis, Texas A&M University, 2005.

[71] H. Yu, "Design and control of a compact 6-degree-of-freedom precision positioner with linux-based real-time control," PhD Thesis, Texas A&M University, 2009.

[72] M. Kazmierkowski and L. Malesani, "Current control techniques for three-phase voltage-source PWM converters: A survey," *IEEE Transactions on Industrial Electronics,* vol. 45, no. 5, p. 697–703, 1998.

[73] H. Kunzmann, T. Pfeifer and J. Flügge, "Scales vs. laser interferometers performance and comparison of two measuring systems," *CIRP Annals,* vol. 42, no. 2, pp. 753-767, 1993.

[74] Y. Chen, R. Wu, F. Wang and J. Yen, "Sensor layouts for a long-stroke nano-positioning stage," in *Proceedings of the SICE Annual Conference (SICE)*, Sapporo, Japan, 2014.

[75] W. Gao, Precision nanometrology: Sensors and measuring systems for nanomanufacturing, Springer, 2010.

[76] A. Fleming, "A review of nanometer resolution position sensors: Operation and performance," *Sensors and Actuators A: Physical,* vol. 190, pp. 106-126, 2013.

[77] M. Kajima and K. Minoshima, "Calibration of linear encoders with sub-nanometer uncertainty using an optical-zooming laser interferometer," *Precision Engineering,* vol. 38, no. 4, pp. 769-774, 2014.

[78] Y. Hori, S. Gonda, Y. Bitou, A. Watanabe and K. Nakamura, "Periodic error evaluation system for linear encoders using a homodyne laser interferometer with 10 picometer uncertainty," *Precision Engineering,* vol. 51, pp. 388-392, 2018.

[79] W. Gao, S. Dejima, Y. Shimizu, S.Kiyono and H. Yoshikawab, "Precision measurement of two-axis positions and tilt motions using a surface encoder," *CIRP Annals,* vol. 52, no. 1, pp. 435-438, 2003.

[80] S. K. Ro and J. K. Park, "A compact ultra-precision air bearing stage with 3- DOF planar motions using electromagnetic motors," *International Journal of Precision Engineering Manufacturing,* pp. 115-119, 2011.

[81] C. Steinmetz, "Sub-micron position measurement and control on precision machine tools with laser interferometry," *Precision Engineering,* vol. 12, no. 1, pp. 12-24, 1990.

[82] J. Stone and S. Phillips, "Corrections for wavelength variations in precision interferometric displacement measurements," *Journal of research of the National Institute of Standards and Technology,* vol. 101, no. 5, 1996.

[83] V. Badami and P. J. de Groot, "Displacement measuring interferometry," in *Series in Optics and Optoelectronics*, Taylor & Francis, 2013, pp. 157-180.

[84] R. Loughridge and D. Y. Abramovitch, "A tutorial on laser interferometry for precision measurements," in *Proceedings of the American Control Conference*, Washington, DC, USA, 2013.

[85] H. J. Büchner and J. Jäger, "A novel plane mirror interferometer without using corner cube retroreflectors," *Measurement Science and Technology,* vol. 17, no. 4, pp. 746-752, 2006.

[86] ISO International Organization for Standardization, "BS ISO 5725-1. Accuracy (trueness and precision) of measurement methods and results—Part 1: General principles," Geneva, Switzerland, 1994.

[87] P. E. Ciddor and R. J. Hill, "Refractive index of air. 2. Group index," *Applied Optics,* vol. 38, no. 9, pp. 1663-1667, 1999.

[88] W. Gao, Y. Arai, A. Shibuya, S. Kiyono and C. HongPark, "Measurement of multi-degree-of-freedom error motions of a precision linear air-bearing stage," *Precision Engineering,* vol. 30, no. 1, pp. 96-103, 2006.

[89] S. Tang, Z. Wang, L. Zhong, J. Gao and J. Guo, "Error analysis of a plane mirror interferometer based on geometric optical paths," *Optics Express,* vol. 20, no. 5, pp. 5108-5118, 2012.

[90] M. Torralba, M. Valenzuela, J. A. Yagüe-Fabra, J. A. Albajez and J. J. Aguilar, "Large range nanopositioning stage design: A three-layer and two-stage platform," *Measurement,* vol. 89, pp. 55-71, 2016.

[91] M. Torralba, J. A. Yagüe-Fabra, J. A. Albajez and J. J. Aguilar, "Design optimization for the measurement accuracy improvement of a large range nanopositioning stage," *Sensors,* vol. 16, no. 84, 2016.

[92] J. Claverley and R. Leach, "A review of the existing performance verification infrastructure for micro-CMMs," *Precision Engineering,* vol. 39, pp. 1-15, 2015.

[93] P. Ekberg and L. Mattsson, "Traceable X,Y self-calibration at single nm level of an optical microscope used for coherence scanning interferometry," *Measurement Science and Technology,* vol. 29, no. 3, p. 03005, 2018.

[94] C. Evans, R. Hocken and W. Estler, "Self-calibration: Reversal, redundancy, error separation, and ‘absolute testing’," *CIRP Annals,* vol. 35, no. 2, pp. 617-634, 1996.

[95] Y. Jeong, J. Dong and P. Ferreira, "Self-calibration of dual- actuated single-axis nanopositioners," *Measurement Science and Technology,* vol. 19, p. 045203, 2008.

[96] Y. Zhu, C. Hu, J. Hu and K. Yang, "Accuracy-and simplicity-oriented self-calibration approach for two-dimensional precision stages," *IEEE Transactions on Industrial Electronics,* vol. 60, p. 2264–2272, 2013.

[97] D. Wang, X. Chen, Y. Xu, T. Guo, M. Kong, J. Zhao and B. Zhu, "Stage error calibration for coordinates measuring machines based on self-calibration algorithm," *Precision Engineering,* vol. 41, pp. 86-95, 2015.

[98] P. Ekberg, L. Stiblert and L. Mattsson, "A new general approach for solving the self-calibration problem on large area 2D ultra- precision coordinate measurement machines," *Measuring Science and Technology,* vol. 25, p. 055002, 2014.

[99] N. Roy and M. Cullinan, "Design of a flexure based XY precision nanopositioner with a two inch travel range for micro-scale selective laser sintering," in *Proceedings - ASPE 2016 Annual Meeting*, Portland, USA, 2016.

[100] J. A. Yagüe-Fabra, M. Valenzuela, J. A. Albajez and J. J. Aguilar, "A thermally-stable setup and calibration technique for 2D sensors," *CIRP Annals - Manufacturing Technology,* vol. 60, pp. 547-550, 2011.

[101] ISO International Organization for Standardization, "ISO/TR 230-9. Test code for machine tools. Estimation of measurement uncertainty for machine tools test according to Series ISO 230, Basic equations," Geneva, Switzerland, 2005.

[102] Texas Instruments, "TMS320x2802x, 2803x Piccolo enhanced pulse width modulator (ePWM) module," Dallas, TX, USA, 2008.

[103] D. Jiang and F. Wang, "Current-ripple prediction for three-phase PWM converters," *EEE Transactions on Industry Applications,* vol. 50, no. 1, pp. 531-538, 2014.

[104] Texas Instruments, "Current sensing with <1-µs settling for 1-, 2-, and 3-shunt FOC inverter reference design," Dallas, Texas, USA, 2017.

[105] P. Vavruska, "Machine tool control systems and interpolations of spline type," *Journal of Engineering Mechanics,* vol. 19, no. 4, p. 219–229, 2012.

[106] P. Božek, A. Lozkin and A. Gorbushin, "Geometrical method for increasing precision of machine building parts," *Procedia Engineering,* vol. 149, pp. 576-580, 2016.

[107] H. Fitter, A. Pandey, D. Patel and J. Mistry, "A review on approaches for handling Bezier curves in CAD for manufacturing," *Procedia Engineering,* vol. 97, p. 1155–1166, 2014.

[108] G. Hu, C. Bo, J. Wu, G. Wei and F. Hou, "Modeling of free-form complex curves using SG-Bézier curves with constraints of geometric continuities," *Symmetry,* vol. 10, p. 545, 2018.

[109] B. Sencera, A. Dumanlia and Y. Yamadab, "Spline interpolation with optimal frequency spectrum for vibration avoidance," *CIRP annals Manufacturing Technology,* vol. 67, no. 1, pp. 377-380, 2018.

[110] B. Msaddek, Z. Bouaziz, M. Baili and G. Dessein., "Influence of interpolation type in high-speed machining (HSM)," *International Journal of Advance Manufacturing and technology,* vol. 72, pp. 289-302, 2014.

[111] F. Lin, L. Shen, C. Yuan and Z. Mi, "Certified space curve fitting and trajectory planning for CNC machining with cubic B-splines," *Computer Aided Design,* vol. 106, no. 13, p. 29, 2019.

[112] E. Mainar and J. Peña, "Accurate computations with collocation matrices of a general class of bases," *Numerical linear algebra,* vol. 25, 2018.

[113] F. Higuchi, S. Gofuku, T. Maekawa, H. Mukundan and N. Patrikalakis, "Approximation of involute curves for CAD-system processing," *Engineering with Computers,* vol. 23, pp. 207-214, 2007.

[114] B. Msaddek, Z. Bouaziz, M. Baili, G. Dessein. and A. Mohsen, "A. Simulation of machining errors of Bspline and Cspline," *The International Journal of Advanced Manufacturing Technology,* vol. 9, pp. 3323-3330, 2017.

[115] M. Arablu and S. Smith, "Polydyne displacement interferometer using frequency-modulated light," *Review of Scientific Instruments,* vol. 89, p. 055007, 2018.

[116] J. Kramar, R. Dixson and N. Orji, "Scanning probe microscope dimensional metrology at NIST," *Measuring Science Technology,* p. 24001–24011, 2011.

[117] W. Gao, S. Dejima, H. Yanai, K. Katakura, S. Kiyono and Y. Tomita, "A surface motor-driven planar motion stage integrated with an XYθZ surface encoder for precision positioning," *Precision Engineering,* vol. 28, no. 3, 2004.

The importance of nanotechnology in the world of Science and Technology has rapidly increased over recent decades, demanding positioning systems capable of providing accurate positioning in large working ranges. In this line of research, a nanopositioning platform, the NanoPla, has been developed at the University of Zaragoza. The NanoPla has a large working range of 50 mm × 50 mm and submicrometre accuracy. The NanoPla actuators are four Halbach linear motors and it implements planar motion. In addition, a 2D plane mirror laser interferometer system works as positioning sensor. One of the targets of the NanoPla is to implement commercial devices when possible. Therefore, a commercial control hardware designed for generic three-phase motors has been selected to control and drive the Halbach linear motors.

This thesis develops 2D positioning control strategy for large range accurate positioning systems and implements it in the NanoPla. The developed control system coordinates the performance of the four Halbach linear motors and integrates the 2D laser system positioning feedback. In order to improve the positioning accuracy, a self-calibration procedure for the characterisation of the geometrical errors of the 2D laser system is proposed. The contributors to the final NanoPla positioning errors are analysed and the final positioning uncertainty (k=2) of the 2D control system is calculated to be ±0.5 µm. The resultant uncertainty is much lower than the NanoPla required positioning accuracy, broadening its applicability scope.